Structure and Dynamics of Supramolecular Assemblies Studied by Advanced Solid-State NMR Spectroscopy

Dissertation
zur Erlangung des Grades

„Doktor der Naturwissenschaften“

am Fachbereich Chemie und Pharmazie
der Johannes Gutenberg-Universität
in Mainz

Almut Rapp
geboren in Berlin

Mainz 2003

Jahr der mündlichen Prüfung: 2003

Contents

Introduction

Supramolecular chemistry has established itself during the last 35 years as one of the major fields in chemistry and is still advancing very rapidly [Lehn 95, Atwood 96, Steed 00, Ciferri 00]. Its first aims were to mimic biology but up to now a vast number of novel species have been synthesized, and the principles of supramolecular organization are increasingly used for designing new functional materials. The underlying principles are self-assembling processes via non-covalent interactions. Despite the knowledge gained so far about the design rules of supramolecular chemistry, many aspects of non-covalent interactions and the resulting self-organization are still poorly understood and yet to be discovered. Deeper insight can be gained by determining the structure as well as by identifying the structure-driving and structure-directing features of supramolecular systems, such as hydrogen bonds and molecular functional units capable of aggregating via π-π interactions. These questions represent important challenges for modern characterization techniques, where solid-state nuclear magnetic resonance (NMR) spectroscopy proves to be a very powerful tool, especially when a lack of long range order makes single-crystal investigations impossible, as is the case for many supramolecular systems. In addition to structural information, solid-state NMR can also elucidate dynamical properties of the materials.

Recent advances in homonuclear ^{1}H-^{1}H and heteronuclear ^{1}H-^{13}C dipolar recoupling techniques under fast magic angle spinning (MAS) [Schnell 01b, Saalwächter 01a, Saalwächter 02b] provide new means to investigate structure and dynamics in the solid state by NMR spectroscopy, without being reliant on isotopic enrichment. The NMR methods used in this work are all based on a selective suppression and/or measurement of ^{1}H-^{1}H and ^{1}H-^{13}C dipole-dipole couplings. Since dipole-dipole couplings act through space and depend on the distance between the coupled nuclei, as well as on the orientation of the coupling vector with respect to the magnetic field, they provide access to both structural and dynamic information about the material. Moreover, ^{1}H chemical shifts have been shown to be very sensitive to ring current effects of adjacent aromatic moieties and, in this way, serve as means to elucidate molecular packing arrangements [Brown 01b]. Dipole-dipole couplings are, however, also responsible for the poor resolution in ^{1}H solid-state spectra because they broaden the resonance lines significantly. A straight-forward approach to reduce dipole-dipole couplings in the solid state is MAS [Andrew 58, Lowe 59]. Spinning speeds of 30 kHz, which have become routinely available within the last few years, usually provide sufficient homonuclear dipolar decoupling to resolve the relevant ^{1}H resonances. While removing dipole-dipole couplings during the course of the experiment with MAS to achieve sufficient resolution, it is, at the same time, necessary to access the structural and dynamic information inherent to the individual dipole-dipole couplings. Therefore, selected homo- or heteronuclear dipole-dipole couplings are re-introduced by so-called recoupling techniques [Dusold 00]. A detailed description of the different homonuclear and heteronuclear dipolar recoupling NMR techniques employed in this work is found in Chapter 2.

Since the periodic arrangement of molecules in a crystal is induced by non-covalent interactions, molecular crystals can be understood as a supramolecular entity with an exceptionally high order [Desiraju 95b]. Due to the long-range order, an X-ray crystal structure can be easily determined. Chapter 3 deals with such a molecular crystal (Yellow Filter Dye molecule [Deroover]), which exists in two different morphologies and whose chromophore system induces π-shift effects. Due to the relatively small size of the molecule, a nucleus independent chemical shift (NICS) map can be calculated using density functional theory (DFT), which predicts the ^{1}H chemical shift effect induced by the π-electrons of the chromophore system at a certain location relative to the molecule. Since the two crystal structures are known, it is possible to relate the ^{1}H chemical shifts predicted by the NICS map to specific structural features and packing phenomena of the molecules in the two polymorphs. In this way, the applicability of the NMR experiments and the DFT calculations is tested.

Supramolecular helices and other columnar assemblies of molecules are well known from nature, one of the most famous examples being the Tobacco Mosaic Virus [Klug 83]. In addition, a lot of effort has been devoted to synthesizing novel columnar architectures, see e.g., [Bushby 02, Ciferri 02, Brundveld 01, Percec 98b, Chandrasekhar 98]. Such architectures are promising with respect to a variety of applications such as biocatalysis or optics and electronics. In Chapters 4 and 5 several related supramolecular dendritic molecules are investigated [Percec 98a, Percec 02b], which self-assemble in a columnar fashion below as well as above their glass transitions. The core of the nanometer-scale columns may be a polymer chain (Chapter 4) or consist of stacked polycyclic aromatic rings (Chapter 5), to which the dendrons are attached via a linker group (depicted schematically in Figure 0.1). The study is carried out over a representative selection of systems with characteristic differences, such as different polymer backbone or polycyclic aromatic core, size of dendritic groups or length and flexibility of linker units (Chapter 4). By solid-state NMR valuable information can be gained about the impact that different building blocks have on the self-assembly process and the resulting local structure and dynamics of the columnar arrangement. In particular, local dynamics of CH$_n$ groups are obtained and characteristic ^{1}H chemical shifts are analyzed in combination with NICS maps. In this way, the structure-driving and structure-directing moieties of the assembly can determined. It's to be noted that the dynamic properties of the polycyclic aromatic cores in the center of the columns (Chapter 5) are of special interest with respect to their promising optoelectronical properties, due to their significant charge-carrier mobility.

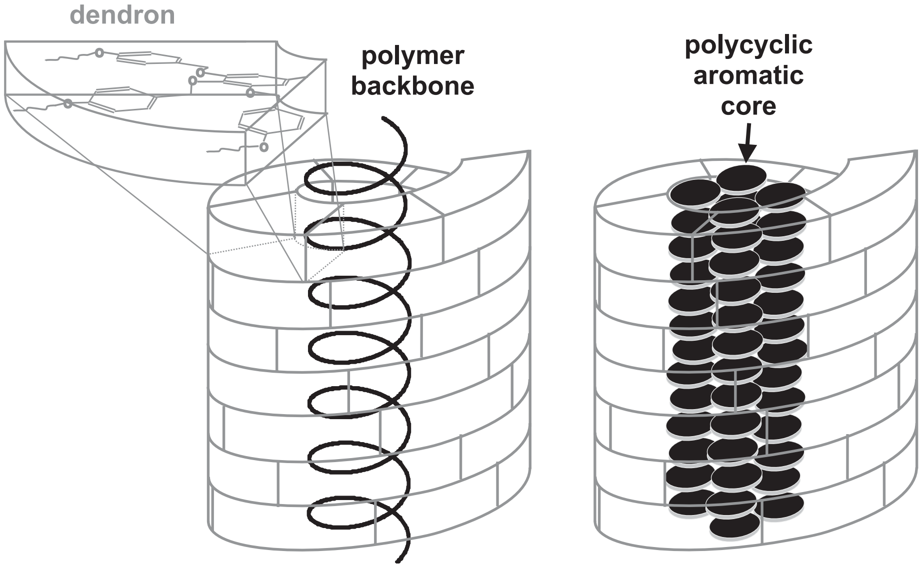

Figure 0.1: *Schematic representation of dendritic molecules which self-organize in a columnar fashion. The core of the column consists either of a polymer backbone (left) or a stack of polycyclic aromatic rings (right).*

Chapter 6 focuses on a quite different supramolecular columnar assembly where shape-persistent macrocycles with intra- and extraannular substituents stack on top of each other to build hollow nanotubes [Fischer 03]. To achieve a stable thermotropic liquid crystalline phase a correct balance of rigid and flexible parts in the molecule is required. The degree of segmental dynamics of the different moieties is determined by NMR, such that space requirements can also be estimated. In this way, the columnar phase and packing behavior can be understood on a molecular level.

Chapter 1

Fundamentals

Advanced solid-state nuclear magnetic resonance (NMR) methods are exceptionally well suited to give insight into the local structure and dynamics of rather large supramolecular systems. The fundamental aspects of supramolecular chemistry are discussed in the first part of this Chapter. The second part introduces the basic concepts of NMR spectroscopy, while the NMR methods used in this work are explained in detail in the following Chapter.

1.1 Supramolecular chemistry

Supramolecular chemistry is often referred to as the chemistry beyond the molecule or as J.-M. Lehn phrased it: “Supermolecules are to molecules and the intermolecular bond, what molecules are to atoms and the covalent bond.” [Lehn 95].[1] Hence, supramolecular chemistry deals with non-covalent interactions between different molecules, so that a certain kind of order is induced in a system, which can be solid, liquid crystalline or solubilized. In larger molecules these non-covalent interactions can also be intramolecular so that the molecule adopts a certain overall-structure. Well known examples of this kind are the helical arrangement of the Tobacco Mosaic Virus molecule [Klug 83] or the secondary structure (folding) of proteins, see for example [Branden 99, Fersht 99, Baldwin 90]. The process which leads to this spontaneous and usually reversible[2] association of different moieties of one or more molecules is called self-assembly, and the result is a well defined overall- or “supra”-structures. The initial aim of supramolecular chemistry was to become able to mimic biology. This makes an understanding of the nature and the strength of non-covalent inter-

---

[1] The term and concept of supramolecular chemistry was introduced in 1978 by J. M. Lehn. The first supermolecule was in fact the crownether synthesized in 1967 by C. J. Pedersen

[2] A class of irreversible supramolecular assemblies, so-called rotaxanes and catenanes, have been introduced by D. Philp and J. F. Stoddart in 1991 [Philp 91]

and intramolecular interactions vital. The non-covalent interactions can be divided into two classes: (i) the strong, anisotropic forces of longer range and (ii) the weak, isotropic forces of medium range. The latter are known as van-der-Waals interactions, while the class of strong interactions includes many different interactions: hydrogen bonding, π-interactions, metal-ligand interactions, hydrophobic and electrostatic interactions. Most investigations of supramolecular systems focus on hydrogen bonding [Sijbesma 99, Ciferri 02], metal-ligand [Sauvage 99, Haiduc 99] and π-interactions because these are the strongest, most specific and directional interactions and hence play the most significant role in self-assembly processes. A perfect understanding of the nature of these interactions and a correct assessment of their energetical plus spatial properties would enable us to predict supramolecular assemblies very accurately. As a result, organic chemistry would not only be able to mimic biology but also encompass novel species and processes as desired. Although substantial progress has already been made during the last 30 years by synthesizing a vast amount of different kinds of supramolecular systems and by investigating their interactions and properties thoroughly, many supramolecular algorithms are still poorly understood. A deeper understanding concerning non-covalent interactions is therefore vital and still a major aim in this field.

The study of the interactions involved in large supramolecular systems often is not easy. Therefore a lot of effort is devoted to studying molecular crystals. A crystal can be understood as a supramolecular entity with an exceptionally high long-range order, because its periodic arrangement is also induced by non-covalent interactions and formed spontaneously under certain conditions [Desiraju 95b]. The investigation of non-covalent interactions in crystals is a lot easier than in other (non-crystalline) supramolecular systems. While the latter usually lack long-range order and therefore diffraction techniques provide only limited insight, the three-dimensional X-ray structure of crystals is of course easily accessible. Large databases e.g. the Cambridge Structural Database (CSD) [CSD] contains crystal structures of more than 270000 compounds. Thus, it is possible to compare different non-covalent interactions inherent to building blocks of many different molecules with their overall crystal structure. In this way intermolecular interactions and recognition phenomena can be understood in the case of molecular crystals, which paves the way towards more general rules for the self-assembly processes and the interactions involved in (non-crystalline) supramolecular systems. In this way, G. R. Desiraju came up with three different types of arrangements for π-systems, depicted in Figure 1.1 [Desiraju 95b]: Face-face stacking, offset-stacking and herringbone arrangement. A face-face stacking is e. g. observed in the crystal structure of duroquinone (Figure 1.1a). This stacking can be explained by a maximum of intermolecular $C \cdots C$ contacts between the molecules and hence a maximum of van-der-Waals interaction energy. Due to π–π- repulsions in the face-face stacking, larger aromatic molecules, however, often prefer an offset stacking, where one ring is shifted laterally with respect to the other [Hunter 90]. Examples are [18]annulene (Figure 1.1b) or coronene. Benzene on the other hand prefers a herringbone arrangement (see Figure 1.1c), which can be explained in terms of a $C(\delta-) \cdots H(\delta+)$ interaction [Burley 86] or a C-H $\cdots$ π hydrogen bond [Steiner 95].

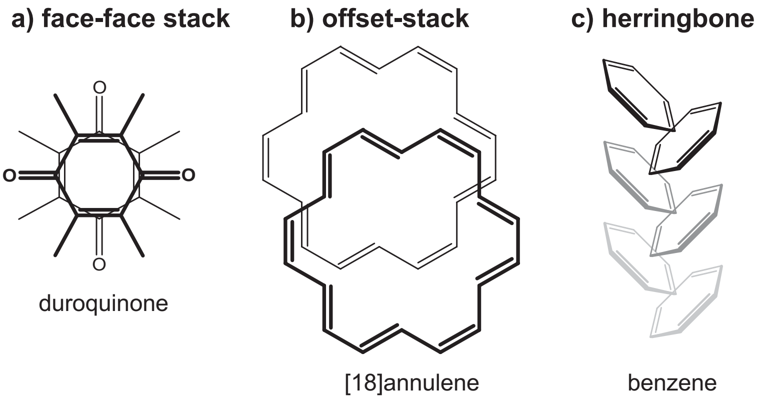

Figure 1.1: *π-systems can arrange in different fashions: a) face-face stacking of duroquinone, b) offset-stacking of [18]annulene and c) herringbone arrangement of benzene. [Desiraju 95b]*

Such effects have been employed in several studies in crystal engineering [Moulton 01, Desiraju 95a]. They are of course also of relevance in larger (non-crystalline) supramolecular assemblies, but to a limited degree. The larger the molecules are, the more non-covalent interactions as well as spatial attributes have to be taken into account. Hence, the self-assembly process follows more complicated rules than the ones just mentioned for molecular crystals. The supramolecular stacking of substituted Hexabenzocoronenes (HBCs), for example, has been studied thoroughly by solid-state NMR [Brown 00a, Brown 99, Fischbach 02]. The supramolecular arrangement depends strongly on the substituents and ranges from offset stacking, over sandwich like structures to herringbone arrangements and combinations of these. It becomes clear that the self-assembly process of such molecules is not governed by a few simple phenomena, but involves a combination of many different interactions and that their identification and characterization represents an important challenge for modern characterization techniques.

1.2 NMR Spectroscopy

Nuclear magnetic resonance (NMR) spectroscopy is used to study physical, chemical and biological properties of matter. NMR is a phenomenon which occurs when nuclei are immersed in a static magnetic field and are subject to a radio-frequency (rf) field. The nuclei must have a spin $\hat{\boldsymbol{I}} \neq 0$ and their magnetic moment is simply $\hat{\boldsymbol{\mu}} = \gamma \hat{\boldsymbol{I}}$, where γ is the magnetogyric ratio for a given isotope. The principle of NMR was discovered in 1946 independently by two groups: Purcell, Torrey, and Pound at Harvard [Purcell 46] and Bloch, Hansen, and Packard at Stanford [Bloch 46a, Bloch 46b]. Varian Associates made NMR commercially available already in 1952, but it was not until 1958 that a reliable spectrometer, the HR-60, was built taking full advantage of electronic shimming, and feedback stabilization. Since then NMR-spectroscopy has developed very rapidly, finding a multitude of applications in many different areas of science. The elucidation of organic chemical structure in solution or magnetic resonance imaging (MRI) in medicine are just two examples of routine use of NMR principles. In the solid-state, however, NMR is far from being a routine method. A lot of research is still dedicated to the improvement of existing methods and the development of entirely new ones. This is due to the overload of information available from solid-state NMR spectra, out of which the relevant or interesting pieces are often difficult to extract. In principle, solid-state NMR is capable of determining distances of mm ... Å and dynamics on timescales between 10^{-10}s ... 10s, but there are numerous difficulties which complicate such measurements, ranging from poor spectral resolution in proton dimensions to weak carbon signal-to-noise ratios, not to mention phenomena associated with quadrupolar nuclei. There are numerous textbooks and reviews covering various aspects of NMR [Abragam 61, Mehring 83, Ernst 87, Slichter 96, Schmidt-Rohr 94, Brown 01b], just to mention a few. This Section just outlines some of the underlying principles of solid-state NMR, which are essential for the understanding of the NMR methods used.

1.2.1 Interactions

The interactions encountered in NMR can be divided into external and internal interactions and are best described by the Hamiltonian

$$\begin{aligned} \hat{\boldsymbol{H}} &= \hat{\boldsymbol{H}}_{external} + \hat{\boldsymbol{H}}_{internal} \\ \hat{\boldsymbol{H}} &= (\hat{\boldsymbol{H}}_Z + \hat{\boldsymbol{H}}_{rf}) + (\hat{\boldsymbol{H}}_Q + \hat{\boldsymbol{H}}_{CS} + \hat{\boldsymbol{H}}_D + \hat{\boldsymbol{H}}_J) \end{aligned} \tag{1.1}$$

$\hat{\boldsymbol{H}}_Z$ represents the interaction between the magnetic moment of a nucleus $\hat{\boldsymbol{\mu}}$ and the magnetic field in z-direction (B_0 = $(0,0,B_0)$) and is called Zeeman interaction (named after the Dutch physicist Pieter Zeeman (1865-1943)).

$$\hat{\boldsymbol{H}}_Z = -\hat{\boldsymbol{\mu}} \cdot \mathrm{B}_0 = -\gamma\hbar \mathrm{B}_0 \cdot \hat{\boldsymbol{I}} \overset{\mathrm{B}_0 \| z}{=} -\gamma\hbar B_0 \cdot \hat{\boldsymbol{I}}_{\boldsymbol{z}} \tag{1.2}$$

It describes the splitting of the energy levels of a nucleus with spin I into 2I+1 levels in the presence of a static magnetic field. From solving the Schrödinger equation with the Hamiltonian above, one obtains the energy levels

$$E_m = -\gamma\hbar m B_0 \tag{1.3}$$

where m is the magnetic spin quantum number m = -I, -I+1, ... +I-1, +I, describing the 2I+1 energy levels, and ω_{Larmor} = γB_0 is the Larmor frequency.

$\hat{\boldsymbol{H}}_{rf}$ represents the interaction of a nucleus with the time-dependent transverse radio frequency field (B_1(t)). The internal interactions are described as follows:
$\hat{\boldsymbol{H}}_{Q}$ is the quadrupolar interaction for nuclei with a quadrupole moment, i. e. with I $>$ 1/2.
$\hat{\boldsymbol{H}}_{CS}$ represents the interaction between the nuclear spin and its electronic environment. The electrons surrounding a nucleus lead to chemical shielding, meaning that the nucleus only experiences an effective magnetic field. This in turn leads to a defined chemical shift for each nucleus depending on its environment.
$\hat{\boldsymbol{H}}_{J}$ describes the J-coupling, which is usually an isotropic indirect spin-spin coupling via electrons, hence through the bonds.
$\hat{\boldsymbol{H}}_{D}$ represents the purely anisotropic dipole-dipole coupling, a direct spin-spin coupling through space.

Quadrupolar interactions are not of significance in the following, because we only deal with spin I = 1/2 nuclei. Also we are not concerned with J-couplings, which are predominantly studied by solution-state NMR methods. In the solid-state J-couplings are usually not of much significance because they are a lot weaker than dipole-dipole couplings. Nevertheless, there have been attempts to identify J-couplings and hence through bond correlations in organic solids [Lesage 97, Lesage 99]. The majority of all solid-state NMR methods, however, are based on the effective suppression and/or the measurement of dipole-dipole couplings, as are the methods applied in this work, which are discussed in the following Chapter. The dipole-dipole coupling itself is explained in more detail below.

1.2.2 Dipole-dipole couplings

The dipole-dipole coupling is an anisotropic direct spin-spin interaction through space. It is present between all types of spin with I $>$ 0. When talking about homonuclear couplings in organic molecules we are usually only concerned with ^{1}H-^{1}H couplings, because ^{13}C-^{13}C or ^{15}N-^{15}N can only play a role in isotopically enriched substances (not dealt with in this work). The most common heteronuclear coupling in organic solids is obviously the ^{1}H-^{13}C coupling.

In NMR, dipole-dipole couplings effectively depend on both, the distance between the two spins involved as well as the angle between the internuclear vector and the B_0 field. The distance dependence of the coupling is contained in the dipolar coupling constant

$$D_{ij} = -\frac{\mu_0 \hbar \gamma_i \gamma_j}{4\pi r_{ij}^3}, \tag{1.4}$$

where r$_{ij}$ denotes the internuclear distance and $\gamma_{i,j}$ the magnetogyric ratios of the nuclei. The latter is a characteristic value of the isotope and is about four times larger for ^{1}H than for ^{13}C. Thus, the homonuclear ^{1}H-^{1}H dipolar coupling constant is about four times larger than the heteronuclear ^{1}H-^{13}C coupling constant. The angular dependence of the dipole-dipole coupling in the presence of a strong magnetic field, $\mathbf{B}_0$, reflects the anisotropy of the interaction. It is proportional to $(3cos^2\theta - 1)$, where θ is the angle between the internuclear vector and the $\mathbf{B}_0$ field. Due to the uniform distribution over all orientations in a powdered solid, a superposition of many lines, which correspond to different dipole-dipole couplings, is the result. Thus dipole-dipole interactions broaden the resonance lines, and spectral resolution is hampered in the solid state. This is illustrated in Figure 1.2. On the left, the two energy levels m = ± 1/2 of a single spin I = 1/2 are depicted, allowing one transition ω_0. On the right, the energy levels of a dipolar coupled spin pair are shown, with M = m$^{(i)}$ + m$^{(j)}$. Only four transitions are allowed, according to M = ± 1. This yields two resonance lines at ω_0 + ω_D and ω_0 - ω_D. ω_D depends on the strength of the dipolar coupling, which in turn depends on the orientation of the internuclear vector with respect to the $\mathbf{B}_0$ field. Thus it is clear that for a powdered solid (allowing all angles θ) a superposition of many lines is the result, causing a characterisitic broadening of the resonance line.

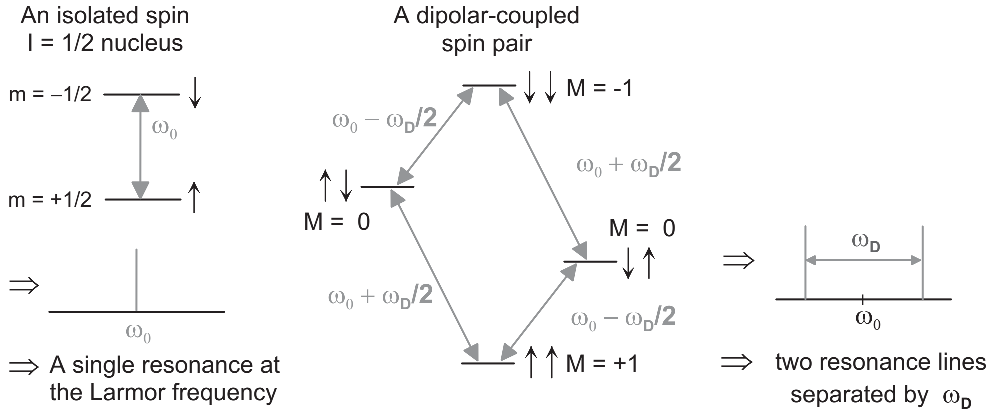

Figure 1.2: *Energy levels m of an isolated spin I =* $\frac{1}{2}$ *(left) and a dipolar coupled spin pair (right) in a magnetic field and their corresponding resonance frequencies* ω.

Altogether, the dipolar interaction for a spin pair i,j can be described by the dipolar Hamiltonian

$$\hat{\boldsymbol{H}}_D^{(ij)}(hom) = D_{ij} \cdot \left[\frac{3(\hat{\boldsymbol{I}}^{(i)} \cdot r_{ij})3(\hat{\boldsymbol{I}}^{(j)} \cdot r_{ij})}{r_{ij}^5} - \frac{\hat{\boldsymbol{I}}^{(i)} \cdot \hat{\boldsymbol{I}}^{(j)}}{r_{ij}^3} \right], \tag{1.5}$$

where D$_{ij}$ is the dipolar coupling constant (see eq. 1.4). In the secular approximation ($\hat{\boldsymbol{H}}_Z \gg \hat{\boldsymbol{H}}_D$) and after transformation from laboratory to polar coordinates the following expression for the dipolar Hamiltonian is left:

$$\begin{aligned}\hat{\boldsymbol{H}}_D^{(ij)}(hom) &= -D_{ij}\cdot\frac{1}{2}(3cos^2\theta-1)(3\hat{\boldsymbol{I}}_z^{(i)}\hat{\boldsymbol{I}}_z^{(j)}-\hat{\boldsymbol{I}}^{(i)}\hat{\boldsymbol{I}}^{(j)}),\\ \hat{\boldsymbol{H}}_D^{(ij)}(hom) &= -D_{ij}\cdot\frac{1}{2}(3cos^2\theta-1)(2\hat{\boldsymbol{I}}_z^{(i)}\hat{\boldsymbol{I}}_z^{(j)}-(\hat{\boldsymbol{I}}_+^{(i)}\hat{\boldsymbol{I}}_-^{(j)}+\hat{\boldsymbol{I}}_-^{(i)}\hat{\boldsymbol{I}}_+^{(j)})),\end{aligned} \tag{1.6}$$

where $(3cos^2\theta-1)$ denotes the space part of the Hamiltonian, mentioned above. The term $2\hat{\boldsymbol{I}}_z^{(i)}\hat{\boldsymbol{I}}_z^{(j)}$ describes one nuclear spin i in the magnetic dipolar field of the other spin j and $(\hat{\boldsymbol{I}}_+^{(i)}\hat{\boldsymbol{I}}_-^{(j)}+\hat{\boldsymbol{I}}_-^{(i)}\hat{\boldsymbol{I}}_+^{(j)})$ is the so-called "flip-flop" term describing the polarization exchange between the two spins i and j. Together, the two terms constitute the spin part of the Hamiltonian. The space part and the spin part of the dipolar Hamiltonian can be manipulated independently of each other. Magic angle spinning (MAS) (Section 1.2.4) for example affects solely the space part of the Hamiltonian, while the spin part can be manipulated by radio frequency (rf) pulse sequences.[3] A combination of both enables us to extract dipole-dipole couplings of interest while at the same time all other dipole-dipole couplings are suppressed, but we will return to this point in the following Chapter.

For a heteronuclear spin pair the "flip-flop" term can usually be neglected. The larger the difference of the resonance frequencies between the two nuclei, the smaller is their polarization exchange. Since the Larmor frequencies of a heteronuclear spin pair differ significantly, the polarization exchange tends to zero and the dipolar Hamiltonian can be reduced to

$$\hat{\boldsymbol{H}}_D^{(ij)}(het) = -D_{ij}\cdot\frac{1}{2}(3cos^2\theta-1)(2\hat{\boldsymbol{I}}_z^{(i)}\hat{\boldsymbol{I}}_z^{(j)}), \tag{1.7}$$

where $\hat{\boldsymbol{I}}^{(j)}$ is often denoted as $\hat{\boldsymbol{S}}$, to point out that two different isotopes are involved.

In general, motion reduces dipolar couplings. This is well known from liquids, where all dipole-dipole couplings are averaged due to an isotropic random motion of the molecules, which covers all possible angles θ. This corresponds to an integration of the space part of the dipolar Hamiltonian (eq. 1.6, 1.7) over a full sphere which is zero:

$$\int_0^{\pi}\int_{\pi}^{2\pi}\frac{1}{2}(3cos^2\theta-1)d\varphi sin\theta d\theta = 0. \tag{1.8}$$

Non-isotropic motion of molecular building blocks in solids causes a decrease in dipole-dipole couplings. Consequently, from the reduction factor of the dipolar couplings measured, the degree of mobility in a molecule can be extracted. This effect will be explained in more detail later.

---

[3] In the rotating frame a radio frequency pulse of length t describes the rotation of z-magnetization towards the transverse plane by an angle $\alpha = \omega_1(t)\cdot$t = $\gamma\mathbf{B}_1(t)\cdot$t, a pulse of α = 90° being called a 90° or π/2 pulse.

1.2.3 Line broadening

It was just mentioned that dipole-dipole couplings, in particular ^{1}H-^{1}H couplings, broaden the resonance lines of solid samples significantly and hence hamper spectral resolution. There are, however, several other factors contributing to the linewidth, too. In principle, line broadening effects can be divided into homogeneous and inhomogeneous contributions. An inhomogeneous broadening is caused by a superposition of a continuum of independent resonance lines due to the orientation dependence $(3cos^{2}\theta - 1)$ in solids with respect to the magnetic field. Inhomogeneous broadenings can efficiently be removed by magic angle spinning (MAS) (explained in the following Section). A straightforward example is the chemical shift anisotropy (CSA), shown in Figure 1.3. If MAS is applied, the CSA is refocused after each rotor period $(\int_{0}^{\tau_R} \hat{\boldsymbol{H}}_{CSA} dt = 0)$ and the inhomogeneous broadening is removed so that the shape of the line is mapped out by all the different resonances underneath. Other examples of inhomogeneous line broadening are magnetic field inhomogeneities, susceptibility gradients or spin-1 quadrupolar anisotropies.

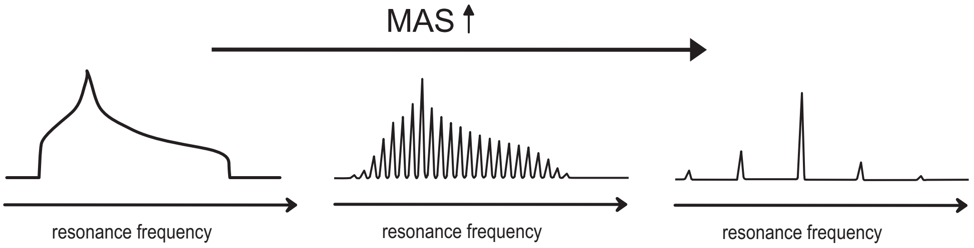

Figure 1.3: *Inhomogeneous line broadening. Schematic representation of the effect of MAS on the anisotropic CSA lineshape.*

Homogeneous line broadening is mainly due to dipolar couplings between multiple spins in solids, in particular for nuclei with high magnetogyric ratios and hence strong dipole-dipole couplings, such as ^{1}H or ^{19}F. Homogeneous line broadening can also be reduced by MAS, but there are no independent resonances underneath the broad line. Therefore the line no longer splits into a pattern of narrow sidebands, but is narrowed with increasing spinning speed. It should be noted that a two-spin dipole-dipole coupling is inhomogeneous not homogeneous. We saw in Figure 1.2 that a dipolar coupled spin-pair generates two distinct resonance lines. Thinking of a powdered solid as a sum of many spin pairs (not coupled to each other) a superposition of these pairs of lines would be the result, which essentially would correspond to an inhomogeneous line broadening. The conditions under which such a simplification is valid are explained in Section 1.2.8.

Clearly, it is necessary to reduce inhomogeneous and homogeneous line broadening as efficiently as possible to arrive at well resolved spectra of solids, which can be achieved for example by MAS. To which degree MAS is able to reduce the linewidth is discussed in the following Section. It should be noted, however, that an intrinsic linewidth always remains, even if all homogeneous and inhomogeneous line broadening effects were removed. This is inherent to the anisotropic magnetic susceptibility.

1.2.4 Fast Magic Angle Spinning

Magic angle spinning (MAS) [Andrew 58, Lowe 59] is used to average out anisotropic interactions that can be described by a second-rank tensor and, in this way, to enhance the resolution of NMR spectra. The sample is rotated around an axis which is inclined at an angle of $\theta = 54.7°$ (the so called “magic” angle) with respect to the magnetic field $\mathbf{B}_0$, so that the orientational dependence is canceled out: $(3cos^2\theta - 1) = 0$. In this way, anisotropic broadenings are averaged to zero. In the case of dipole-dipole couplings this process is called dipolar decoupling. A full cancellation, however, requires that the spinning frequency is larger than the linewidth, but the homogeneous linewidth of solid samples can reach 100 kHz for protons. Nevertheless, fast MAS at frequencies of 25–30 kHz is usually enough to achieve a sufficient line narrowing even for proton spectra. Recently, even spinning frequencies of up to 50 kHz have been reported [Samoson 01b, Samoson 01a], which can improve the resolution of rigid solid samples further. However, even at 50 kHz MAS the homogeneous linewidth of rigid solids is still a lot larger than the intrinsic one. Section 1.2.8 will explain why it is not necessary to reach MAS spinning speeds of 100 kHz and average out every single dipole-dipole coupling, but why MAS frequencies of 25–30 kHz suffice.

At this point it should be mentioned that there exist also various multiple-pulse experiments to reduce the linewidth in solid-state spectra. This approach was already introduced 35 years ago by Waugh, Huber and Haeberlen [Waugh 68, Haeberlen 68]. By applying a multiple-pulse sequence (WHH-4), the dipole-dipole interactions are decoupled through the spin part of the dipolar Hamiltonian. The pulse sequence brings about a rotation in spin space which complements the effect of a physical rotation. There have also been several approaches combining multiple-pulse experiments with MAS. A well known example is the Combined Rotation And Multiple-Pulse Spectroscopy (CRAMPS) experiment [Gerstein 77], applying slow MAS (2–3 kHz). An alternative approach is e.g. the Lee-Goldburg experiment [Lee 65] or the improved Frequency-Switch Lee-Goldburg (FSLG) experiment [Mehring 72, Bielecki 89, Levitt 93], both performing well at moderate MAS frequencies of 10–15 kHz. The most recent variation is the Phase-Modulated Lee Goldburg (PMLG) experiment [Vinogradov 99, Vinogradov 00], which also uses spinning speeds of 10–15 kHz. For a short overview of these pulse-sequences see for example [Brown 01b]. Multiple-pulse techniques in combination with MAS are capable of narrowing ^{1}H lines almost to the intrinsic linewidth, which is limited by the magnetic susceptibility of the sample, but experimentally these techniques are somewhat complicated and difficult to implement. From an experimental point of view “brute-force” fast MAS appears as a more direct approach, although it does not achieve as good line narrowing, but is a lot easier to apply. Besides, the resolution achieved with fast MAS (25–30 kHz) in combination with high magnetic fields (^{1}H 500–700 MHz) turns out to be sufficient for the structural and dynamical aspects under investigation in the following Chapters. It should be noted that the intrinsic linewidths in such supramolecular systems are considerably broader than in perfectly crystalline (well ordered) materials, due to the larger degree of inhomogeneity inherent to the samples.

1.2.5 Concept of Recoupling

Anisotropic interactions such as dipole-dipole couplings are problem and opportunity at the same time. On the one hand the above mentioned techniques (Section 1.2.4) are required for removing dipole-dipole couplings to provide spectral resolution and regaining isotropic chemical shift information. On the other hand we need to access information about molecular structure and dynamics, which is inherent to dipole-dipole couplings. This can be achieved by employing so-called recoupling techniques, which can recover anisotropic interactions during certain parts of the NMR experiment by manipulating the spin-part of the dipolar Hamiltonian. As shown in Figure 1.4 rotor-synchronized radio-frequency pulse-sequences are applied which invert the sign of the wave function every other half rotor period. Effectively, this induces a “counter-rotation” in spin space and compensates for the effect of MAS and, thus, selectively re-introduces homo- or heteronuclear dipole-dipole couplings during specific periods of the NMR experiment. All pulse-sequences used in this work rely on this recoupling technique. The most simple technique to illustrate the recoupling principle is the Rotational-Echo DOuble-Resonance (REDOR) pulse-sequence [Gullion 89b] explained in the following Chapter, which efficiently recouples heteronuclear dipole-dipole couplings by trains of π-pulses. Homonuclear ^{1}H dipole-dipole couplings in DQ experiments under fast MAS conditions are straightforwardly recoupled by the so-called “back-to-back” (BABA) pulse sequence [Sommer 95], also described in the following Chapter.

1.2.6 ^{1}H-decoupling in general

Of course there are many more dipolar decoupling techniques than the ones mentioned in Section 1.2.4. Homonuclear ^{1}H decoupling plays an important role in heteronuclear ^{1}H-X experiments, where ^{1}H decoupling pulse sequences are applied during the acquisition time (Figure 1.5), to average dipole-dipole couplings and J-couplings. In this way, the linewidth of the X-nucleus resonances is reduced and a better signal-to-noise ratio is achieved.

The most simple method for decoupling is continuous wave (cw) decoupling, where a continuous rf-pulse of fixed phase is applied for the duration of the acquisition of the free induction decay (FID). For efficient broadband decoupling a high rf-power is needed, which is

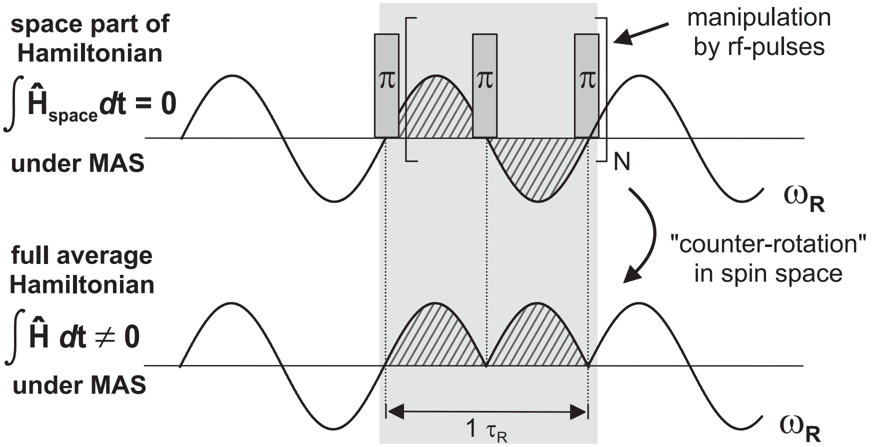

Figure 1.4: *Recoupling under fast MAS. The spin-space of the dipolar Hamiltonian is manipulated by applying π-pulses after half a rotor period. In this way the effective dipole-dipole coupling is reintroduced.*

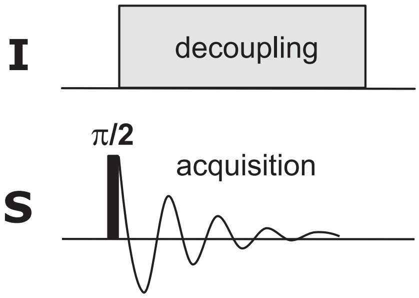

Figure 1.5: *One-pulse experiment on an S-spin heteronucleus (^{13}C, ^{15}N, ...) with decoupling on protons.*

technically not desirable. Therefore an improved composite pulse decoupling (cpd) is preferable.

If decoupling is needed during the experiment and not only during acquisition periods, cw or cpd decoupling are obviously not suited. It was mentioned in Section 1.2.4 that in these cases MAS is used for dipolar decoupling. One might think that under fast MAS no further decoupling is needed during the acquisition periods of the experiments, but it turns out that additional ^{1}H decoupling during the acquisition enhances the ^{13}C signal intensity significantly. This is not too surprising because we know that fast MAS alone (even at 50 kHz, [Ernst 01]) is not sufficient to obtain perfectly ^{1}H decoupled spectra in a powdered solid. Therefore additional rf-irradiation on the proton-channel during the detection is needed to average out the residual dipole-dipole couplings and the J-couplings. For decoupling under fast MAS the more recent two-pulse phase modulated (TPPM) decoupling sequence [Bennett 95] is most widely used. It achieves a strongly reduced linewidth as compared to cw, the reasons for which are explained in [Caravetta 00, Ernst 00]. Very recently two new types of decoupling were introduced by the group of B. H. Meier: the so-called XiX decoupling [Detken 02] and the low-power cw decoupling [Ernst 01]. XiX decoupling consisting of a windowless rf irradiation with a repeat of two pulses of equal width phase-shifted by 180°. For crystalline samples it usually performs a little better, otherwise it is comparable to TPPM, but more sensitive to an imperfect setup. Under very fast MAS ($>$ 40 kHz) or when low-γ nuclei (such as ^{15}N) are investigated under fast MAS ($\sim$30 kHz), the possibility of low-power cw decoupling instead of high power TPPM can be considered.

Just for completeness, some other decoupling sequences should be listed here, with a performance similar to TPPM, such as FMPM [Gan 97], $C12_2^{-1}$ [Eden 99], SPARC [Yu 98], SPINAL [Fung 00] or amplitude-modulated TPPM [Takegoshi 01]. Their particular advantages and disadvantages, however, will not be discussed here, as these are details which are of no significance to the studies presented in this work.

1.2.7 Coherence

A coherences in NMR describes the relationship between states of different transitions in a system. Coherence can be classified by a coherence order, p, which is an integer taking values 0, ± 1, ± 2, ± 3,... and is defined by the difference in the magnetic quantum numbers between the two states associated with the transition, ΔM. Recalling Figure 1.2 this can be illustrated. For a single nuclei (I = 1/2) only two energy levels are present and thus only one transition is possible which changes the spin-quantum number by ΔM = ± 1 and is therefore called a single-quantum coherence (SQC). For a dipolar coupled spin pair, four energy levels result. Transitions changing the spin-quantum number by ΔM = ± 1 again correspond to SQCs, while ΔM = ± 2 and ΔM = ± 0, correspond to double-quantum (DQC) and zero-quantum-coherences (ZQC), respectively. If more than two nuclei are coupled, also higher order coherences can be excited. Any coherence with the order $p > | \pm 1|$ can be termed multiple-quantum coherence (MQC). It should be noted, that only a single-quantum coherence gives rise to net magnetization which can be detected as an NMR signal. Any higher order coherence one might want to detect needs to be reconverted to a SQC by an appropriate pulse sequence. The concept of coherence can also be explained in terms of phase. Transverse magnetization is for example coherent, because its x and y component are precessing in the x-y plane with the same phase and thus are phase-coherent. A rf-pulse causes coherence to be transferred from one order to another order or even to several different orders. The precise outcome depends on the phase and flip angles of the pulses applied. Phase cycling is commonly used to select a specific coherence transfer pathway, ensuring that only magnetization of selected coherences contribute to the acquired signal.

1.2.8 Spin-pair approximation

In this Section the effect of MAS on homogeneous lines is discussed. We know that homogeneous line broadening in organic solids is due to a strongly dipolar coupled ^{1}H network. As mentioned above in Section 1.2.4, it is not possible with the current MAS technology ($\leq$ 50 kHz) to average out all ^{1}H dipole-dipole couplings in rigid organic solids. The homogeneous line broadening can therefore only partly be removed. However, it has been shown that spinning speeds of 25–30 kHz are sufficient to break up the strong dipolar coupled network among protons in such a way that it can be treated as a sum of spin-pair correlations [Filip 99, Schnell 01b]. This phenomenon is called spin-pair approximation. The idea behind the spin-pair approximation is illustrated in Figure 1.6. On the left a strongly homogeneous broadened proton line of a rigid organic solid is shown, with the corresponding ^{1}H dipolar coupling network schematically depicted below. Under fast MAS the broad line breaks down into several sidebands, shown on the left in Figure 1.6. With increasing spinning speed, the spectrum of a homogeneous multi-spin dipolar Hamiltonian, more and more approaches the features known from inhomogeneous MAS spectra, so that at high spinning speeds (25–30 kHz) MAS spectra of homogeneously broadened lines resemble features known from inhomogeneous interactions, such as isolated spin pairs. This phenomenon can be understood in terms of dipolar spin-pair interactions, which are inhomogeneous. Thus, with increasing spinning frequency, ω_R, dipole-dipole couplings to more distant spins become more and more negligible, so that spin systems with fewer and fewer coupled spins have to be taken into account. Ultimately, the fast spinning limit is reached for $\omega_D/\omega_R < 1$ where one strongest dipole-dipole coupling dominates, while more distant ones have been averaged out, so that the two-spin simulation becomes a good approximation. Of course this is an idealized picture, assuming that there is only one strongly coupled neighbor to each nucleus while all other nuclei

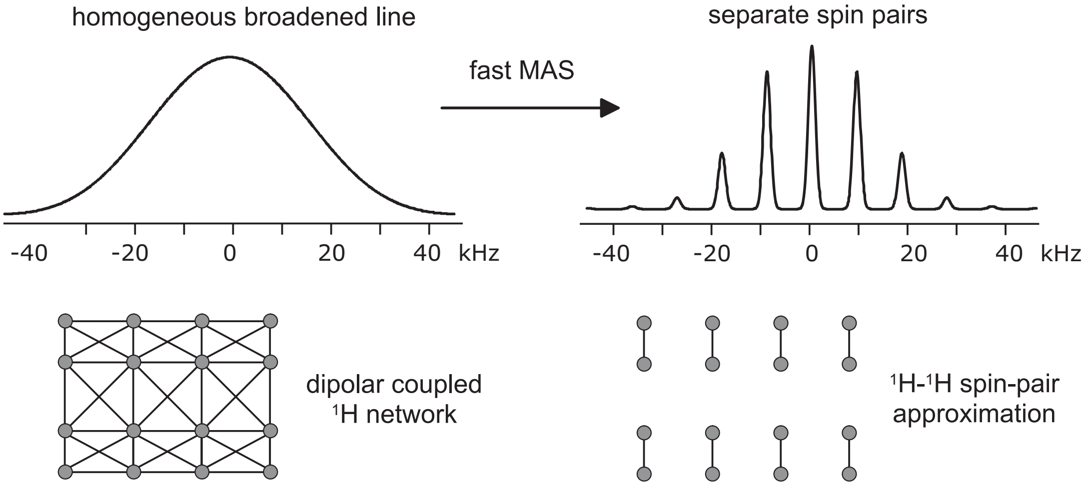

Figure 1.6: *^{1}H spectrum of a rigid organic solid: static (left) and under fast MAS (right). The dipole-dipole couplings present in the two cases are depicted schematically below the spectra.*

are more weakly coupled, so that all homogeneous line broadening is average out and only the inhomogeneous part due to the spin-pairs remains. This is of course not the full truth. The lines in MAS-spectra are still homogeneously broadened, which is not accounted for by the two-spin model. The sideband intensities in the fast spinning regime, however, are mainly determined by two-spin contributions. Therefore simulations using this spin-pair approximation agree surprisingly well with the experimental spectra [Filip 99, Graf 98].

1.2.9 Quantum Chemical description

Finally, the most fundamental quantum chemical terms and equations are introduced. For a more complete description the reader is referred to a number of excellent text books explaining this subject in great detail, for example [Slichter 96, Schmidt-Rohr 94, Harris 86, Hore 00].

Product operator formalism

First the product operator formalism is introduced, which can be used to easily describe systems with a small number of spins, I = 1/2. Looking at a single spin-1/2, just three operators are of importance to describe NMR experiments:

$$\hat{\boldsymbol{I}}_x, \qquad \hat{\boldsymbol{I}}_y, \qquad \hat{\boldsymbol{I}}_z. \tag{1.9}$$

They are usually called spin-operators and correspond to the x, y and z-magnetization of a single spin in the rotating frame. Through π/2 pulses they can be transformed into each other. In general a pulse with a flip angle β leads to the following transformations of I_z

$$\begin{aligned} \hat{\boldsymbol{I}}_z &\xrightarrow{\beta_x} \hat{\boldsymbol{I}}_z cos\beta - \hat{\boldsymbol{I}}_y sin\beta, \\ \hat{\boldsymbol{I}}_z &\xrightarrow{\beta_y} \hat{\boldsymbol{I}}_z cos\beta + \hat{\boldsymbol{I}}_x sin\beta, \end{aligned} \tag{1.10}$$

which can be easily understood in trigonometric terms. The transformation of $\hat{\boldsymbol{I}}_x$ and $\hat{\boldsymbol{I}}_y$ is analogous.

For a system of two coupled spin-1/2 nuclei, 16 product (or spin-) operators can be formed:

	$\frac{1}{2}$E	S_x	S_y	S_z
$\frac{1}{2}$E	$\frac{1}{2}$E	S_x	S_y	S_z
I_x	I_x	$2\mathrm{I}_x\mathrm{S}_x$	$2\mathrm{I}_x\mathrm{S}_y$	$2\mathrm{I}_x\mathrm{S}_z$
I_y	I_y	$2\mathrm{I}_y\mathrm{S}_x$	$2\mathrm{I}_y\mathrm{S}_y$	$2\mathrm{I}_y\mathrm{S}_z$
I_z	I_z	$2\mathrm{I}_z\mathrm{S}_x$	$2\mathrm{I}_z\mathrm{S}_y$	$2\mathrm{I}_z\mathrm{S}_z$

The operators are classified as inphase operators: I_x, I_y, I_z, S_x, S_y and S_z and antiphase operators: $2\mathrm{I}_x\mathrm{S}_z$, $2\mathrm{I}_y\mathrm{S}_z$, $2\mathrm{I}_z\mathrm{S}_x$, $2\mathrm{I}_z\mathrm{S}_y$ and $2\mathrm{I}_z\mathrm{S}_z$. While I_z and S_z correspond to longitudinal magnetization and $2\mathrm{I}_z\mathrm{S}_z$ to a “dipolar ordered” state, the x and y-components represent single quantum coherences (SQCs). The four operators in the middle $2\mathrm{I}_x\mathrm{S}_x$, $2\mathrm{I}_x\mathrm{S}_y$, $2\mathrm{I}_y\mathrm{S}_x$ and $2\mathrm{I}_y\mathrm{S}_y$ in contrast represent multiple-quantum coherences (MQCs). Taking I_x and $2\mathrm{I}_x\mathrm{S}_z$ as an example, the evolution under a dipole-dipole coupling Φ_{IS} for a period t is given as

$$\begin{aligned} \hat{\boldsymbol{I}}_x &\xrightarrow{\Phi_{IS}t} \hat{\boldsymbol{I}}_x cos\Phi_{IS}t + 2\hat{\boldsymbol{I}}_y\hat{\boldsymbol{S}}_z sin\Phi_{IS}t \\ 2\hat{\boldsymbol{I}}_x\hat{\boldsymbol{S}}_z &\xrightarrow{\Phi_{IS}t} 2\hat{\boldsymbol{I}}_x\hat{\boldsymbol{S}}_z cos\Phi_{IS}t + \hat{\boldsymbol{I}}_y sin\Phi_{IS}t. \end{aligned} \tag{1.11}$$

Density operator formalism

The density operator formalism is most conveniently used to describe the state of a system consisting of many spins. The magnetization we are dealing with in NMR experiments is the result of an ensemble of the many spins in a sample. Therefore each state $|\Psi\rangle$ of a system can be expressed as a linear combination of basis functions $|n\rangle$

$$|\Psi(t)\rangle = \sum_n c_n(t)|n\rangle, \tag{1.12}$$

where c_n are time-dependent coefficients. The expectation value of an observable $\hat{\boldsymbol{A}}$ is given by

$$\begin{aligned} \langle A\rangle &= \langle\Psi|\hat{\boldsymbol{A}}|\Psi\rangle \\ &= \sum_{n,m} c_n(t)c_m(t)^*\langle m|\hat{\boldsymbol{A}}|n\rangle. \end{aligned} \tag{1.13}$$

The dependence on $\mathrm{c}_n(t)c_m(t)^*$ leads to the definition of the density operator whose matrix representation is called the density matrix $\hat{\boldsymbol{\rho}}$

$$\langle\hat{\boldsymbol{\rho}}(t)\rangle = \sum_{n,m} \overline{c_n(t)c_m(t)^*}|m\rangle\langle n|. \tag{1.14}$$

The elements of the density matrix are given by

$$\langle \hat{\boldsymbol{\rho}}_{nm}(t) \rangle = \langle\, n | \hat{\boldsymbol{\rho}}(t) | m \,\rangle = \overline{c_n(t) c_m(t)^*}, \tag{1.15}$$

where the overbar denotes an ensemble average. Hence, the matrix elements describe the average over a large number of similar systems in different environments in the sample at a given time. Therefore, the density matrix fully describes the state of the spin system. The diagonal matrix elements $\hat{\boldsymbol{\rho}}_{nn} = \langle\, n | \hat{\boldsymbol{\rho}} | n \,\rangle$ denote the probability of a system to adopt its eigenstate $|n\,\rangle$, while the non-diagonal terms $\hat{\boldsymbol{\rho}}_{nm} = \langle\, n | \hat{\boldsymbol{\rho}}(t) | m \,\rangle$ (m $\neq$ n) represent coherent superpositions of the eigenstates $|n\,\rangle$ and $|m\,\rangle$.

The expectation value of an observable is always given by the trace of the product of the matrix representation of the operator and the density matrix:

$$\begin{aligned} \langle \hat{\boldsymbol{A}} \rangle &= \sum \langle\, n | \hat{\boldsymbol{\rho}} | m \,\rangle \langle\, m | \hat{\boldsymbol{A}} | n \,\rangle \\ &= \sum \langle\, n | \hat{\boldsymbol{\rho}} \hat{\boldsymbol{A}} | n \,\rangle \\ &= \mathbf{Tr}\{\hat{\boldsymbol{A}}\ \hat{\boldsymbol{\rho}}(\mathbf{t})\} = \mathbf{Tr}\{\hat{\boldsymbol{\rho}}(\mathbf{t}) \hat{\boldsymbol{A}}\}. \end{aligned} \tag{1.16}$$

Going back to to spin operators, it follows that the expectation value of a spin operator $\hat{\boldsymbol{I}}$, which corresponds to the observable signal in an NMR experiment, can also be represented as the trace of the product of the operator and the density matrix

$$\langle \hat{\boldsymbol{I}}_x \rangle = \mathbf{Tr}\{\hat{\boldsymbol{I}}_{\mathrm{x}} \hat{\boldsymbol{\rho}}(\mathbf{t})\}, \qquad \langle \hat{\boldsymbol{I}}_{\mathrm{y}} \rangle = \mathbf{Tr}\{\hat{\boldsymbol{I}}_{\mathrm{y}} \hat{\boldsymbol{\rho}}(\mathbf{t})\}, \qquad \langle \hat{\boldsymbol{I}}_{\mathbf{z}} \rangle = \mathbf{Tr}\{\hat{\boldsymbol{I}}_{\mathbf{z}} \hat{\boldsymbol{\rho}}(\mathbf{t})\} \tag{1.17}$$

For a spin-1/2 nucleus and two states i and j it follows

$$\begin{aligned} \langle \hat{\boldsymbol{I}}_x \rangle = \mathbf{Tr}\ \{\hat{\boldsymbol{I}}_{\mathrm{x}} \hat{\boldsymbol{\rho}}(\mathbf{t})\} &= \mathbf{Tr} \left\{ \begin{pmatrix} 0 & \frac{1}{2} \\ \frac{1}{2} & 0 \end{pmatrix} \begin{pmatrix} c_i c_i^* & c_i c_j^* \\ c_j c_i^* & c_j c_j^* \end{pmatrix} \right\} \\ &= \frac{1}{2}(c_i c_j^* + c_j c_i^*) = Re(c_i c_j^*) \\ \langle \hat{\boldsymbol{I}}_y \rangle = \mathbf{Tr}\ \{\hat{\boldsymbol{I}}_{\mathrm{y}} \hat{\boldsymbol{\rho}}(\mathbf{t})\} &= \mathbf{Tr} \left\{ \begin{pmatrix} 0 & -\frac{1}{2}i \\ \frac{1}{2}i & 0 \end{pmatrix} \begin{pmatrix} c_i c_i^* & c_i c_j^* \\ c_j c_i^* & c_j c_j^* \end{pmatrix} \right\} \\ &= \frac{1}{2}\, i\, (c_i c_j^* - c_j c_i^*) = -Im(c_i c_j^*) \\ \langle \hat{\boldsymbol{I}}_z \rangle = \mathbf{Tr}\ \{\mathbf{I_z} \hat{\boldsymbol{\rho}}(\mathbf{t})\} &= \mathbf{Tr} \left\{ \begin{pmatrix} \frac{1}{2} & 0 \\ 0 & -\frac{1}{2} \end{pmatrix} \begin{pmatrix} c_i c_i^* & c_i c_j^* \\ c_j c_i^* & c_j c_j^* \end{pmatrix} \right\} \\ &= \frac{1}{2}\, (c_i c_i^* - c_j c_j^*) \end{aligned} \tag{1.18}$$

showing that $\langle \hat{\boldsymbol{I}}_x \rangle$ and $\langle \hat{\boldsymbol{I}}_y \rangle$ correspond to the real and imaginary part of the free induction decay, respectively.

The time evolution of the density operator is best described by the Liouville von Neumann equation (eq. 1.19), which is basically the density matrix form of the time-dependent Schrödinger equation.

$$\frac{\delta \hat{\boldsymbol{\rho}}}{\delta t} = -i \left[\hat{\boldsymbol{H}}(t), \hat{\boldsymbol{\rho}}(t) \right]. \tag{1.19}$$

It describes the change over time of a system which is reflected by the density matrix $\hat{\boldsymbol{\rho}}$ and is subject to the Hamiltonian $\hat{\boldsymbol{H}}$. Hence, $\hat{\boldsymbol{\rho}}$ describes the properties of the system and $\hat{\boldsymbol{H}}$ all the forces acting on it. The Liouville von Neumann equation is readily solved when the Hamiltonian is constant with respect to the time t:

$$\hat{\boldsymbol{\rho}}(t) = e^{-i\hat{\boldsymbol{H}}t}\, \hat{\boldsymbol{\rho}}(t_0)\, e^{+i\hat{\boldsymbol{H}}t}. \tag{1.20}$$

Chapter 2

NMR methods and pulse sequences

This Chapter discusses the different homo- and heteronuclear solid-state MAS NMR techniques used in this work. They all rely on the effective suppression and/or measurement of homo- and heteronuclear dipole-dipole couplings. Fast MAS at rotation frequencies of 25-30 kHz and high B_0 fields (corresponding to a ^{1}H Larmor frequency of 700 MHz) are applied to ensure sufficient resolution even in ^{1}H spectra. Since under very fast MAS homo- and heteronuclear dipolar couplings are largely averaged out, the pulse sequences selectively recouple the dipole-dipole couplings of interest and, in addition, introduce rotor-encoding. In this way, the information on molecular structure and dynamics inherent to the homo- or heteronuclear couplings can be accessed. In the following, we will only deal with homonuclear ^{1}H-^{1}H and heteronuclear ^{1}H-^{13}C dipolar couplings. In principle, any other spin-1/2 nucleus could also be investigated (e.g. ^{15}N, ^{19}F or ^{29}Si).

With the aid of these multiple-pulse recoupling pulse sequences, it is possible to solve structural as well as dynamical problems in the solid-state using non-labeled samples. ^{1}H-^{1}H double quantum (DQ) spectra elucidate ^{1}H-^{1}H proximities up to about 3.5 Å, and two-dimensional ^{1}H-^{13}C spectra are well suited to show e. g. ^{1}H π-shifts. By means of homo- or heteronuclear MAS spinning sideband patterns, arising from the rotor-encoding of the recoupled dipolar Hamiltonian, site-specific information about the dynamics of different CH$_n$ building blocks of a molecule can be obtained on a time scale of about 10^{-6}–10^{-7}s.

2.1 Two dimensional experiments in general

The idea of two-dimensional (2D) NMR is more than 30 years old. It was first proposed by Jeener at a conference in 1971 [Jeener 71] and since then has triggered off a vast number of different experiments correlating for example chemical shifts of different nuclei or coupling constants with chemical shift etc. The intensity plotted in 2D spectra is always a function of two frequencies, ν_1 and ν_2. All 2D experiments are designed in a similar fashion depicted schematically in Figure 2.1.

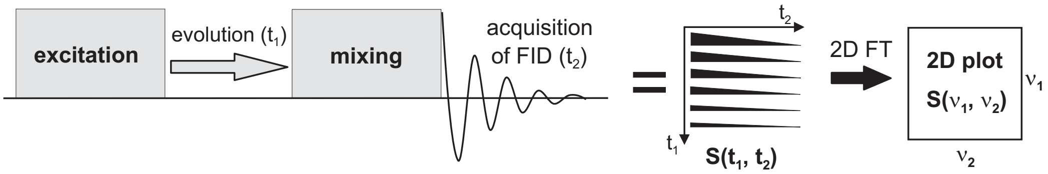

Figure 2.1: *Schematic representation of a two-dimensional NMR experiment.*

The key-element of a 2D experiment is the so-called evolution time, t_1, which is "inserted" into the pulse sequence between the so-called excitation and mixing period. During the excitation the coherence of interest is excited by one or more pulses. The resulting magnetization then evolves during t_1. It is followed by the mixing procedure and finally the acquisition time, defined as t_2. Hence, the free induction decay (FID) detected during the acquisition is a function of both times, i.e. $S(t_1, t_2)$. t_1 is incremented (starting with $t_1 = 0$), therefore the pulse sequence is repeated for increasing values of t_1 and for each step an FID is recorded. A double fourier transform (FT) then converts the data to a 2D spectrum which is a function of two frequency variables, $S(\nu_1, \nu_2)$:

$$S(t_1, t_2) \xrightarrow{FT\ in\ t_2} S(t_1, \nu_2) \xrightarrow{FT\ in\ t_1} S(\nu_1, \nu_2) \tag{2.1}$$

The exact nature of the excitation and mixing procedure, of course, determines the information obtainable from the spectrum.

2.2 2D ^{1}H Double-Quantum Spectroscopy

Two-dimensional double-quantum (DQ) MAS spectroscopy [Schnell 01b] is based on homonuclear dipole-dipole couplings and provides information about through-space ^{1}H-^{1}H proximities. A ^{1}H 2D DQ MAS spectrum is recorded in a rotor-synchronized fashion in t_1, where t_1 is incremented in steps of full rotor periods, $t_1 = N\tau_R$. The creation of a double-quantum coherences (DQC) (Section 1.2.7) between two protons relies on the existence of a sufficiently strong dipole-dipole coupling between them. Since the intensity of the DQC depends on the strength of the dipole-dipole coupling, which in turn depends on the internuclear distance r_{ij} (see eq. 1.4), it is clear that spatial proximities of protons can be directly inferred from the observed DQ signals.

Figure 2.2 schematically shows such a DQ spectrum. The sum projection in the single quantum dimension corresponds to a DQ-filtered spectrum. The double-quantum dimension elucidates the ^{1}H-^{1}H proximities in the sample. DQCs between like (AA) spins give rise to a so-called auto-peak, a single peak on the "DQ" diagonal of the spectrum at (ν_A, ($\nu_A + \nu_A$)), referring to the position in the (SQ, DQ) dimension, respectively. For DQCs between unlike (AB) spins two so-called cross peaks are observed at ν_A, ($\nu_A + \nu_B$) and ν_B, ($\nu_A + \nu_B$). The resonance frequency of a given DQC is simply the sum of the two SQ frequencies of the two spins involved.

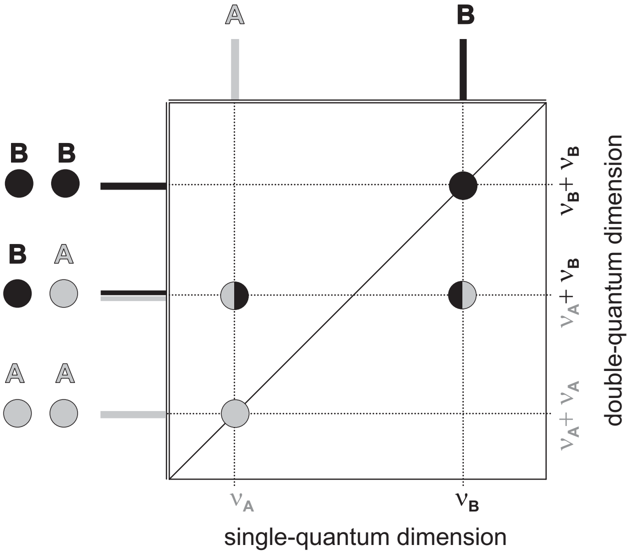

Figure 2.2: *Schematic representation of a DQ spectrum. A and B protons with different resonance frequencies, ν_A and ν_B, respectively. The cross-peaks refer to an A-B proximity and the auto-peaks to A-A and B-B proximities.*

The back-to-back (BABA) pulse sequence [Feike 96, Schnell 01b], depicted in Figure 2.3, is used in 2D DQ MAS experiments, because it is very robust and suitable for fast MAS (25–30 kHz). During the excitation time, τ_{exc}, DQCs are created, which evolve during the evolution time t_1 under the influence of the dipolar interactions in the sample. Since DQCs cannot be detected directly, they need to be converted back to SQCs during the mixing time of the experiment, which is therefore called reconversion time, τ_{rec}. Usually the excitation time equals the reconversion time, τ_{exc} = τ_{rec}, and both are integer multiples of the rotor period: $\tau_{exc,rec}$ = Nτ_R. The easiest way to excite DQCs are two π/2 pulses phase shifted by 180°(x and -x in Figure 2.3). The maximum separation of these two pulses under MAS conditions, however, is half a rotor period. Since the rotor modulation under MAS inverts the space part of the dipolar Hamiltonian for the second half of a rotor-period, a time reversal would be induced and no DQC would be left after τ_R. Therefore, two additional π/2 pulses with 90° shifted phase are applied during the second half of the rotor period (y and -y in Figure 2.3), effectively inverting the sign of the wave-function and, in this way, recoupling the DQC. This recoupling technique can be viewed as a "counter-rotation" in spin space compensating for the effect of MAS (see also Section 1.2.5). The reconversion corresponds to an inversion in time, hence the average Hamiltonian describing the reconversion has the opposite sign than the Hamiltonian of the excitation ($\hat{\boldsymbol{H}}_{rec} = -\hat{\boldsymbol{H}}_{exc}$). This can be accomplished by a phase shift of the pulses by φ = 90°. However, it turns out, that in the case of even-order coherences (m) no special care has to be taken with respect to the phases, because the change in sign of the Hamiltonian results in a phase factor $e^{im\pi}$ = (-1)^m, showing that reconversion not only takes place for $\hat{\boldsymbol{H}}_{rec} = -\hat{\boldsymbol{H}}_{exc}$, but also for $\hat{\boldsymbol{H}}_{rec} = \hat{\boldsymbol{H}}_{exc}$ [Schnell 99]. Finally, a suitable phase cycle must be applied to ensure the selection of the coherence transfer pathway $0 \rightarrow \pm 2 \rightarrow 0 \rightarrow -1$, depicted in Figure 2.3, and in this way guaranteeing that solely DQCs contribute to the observed signal.

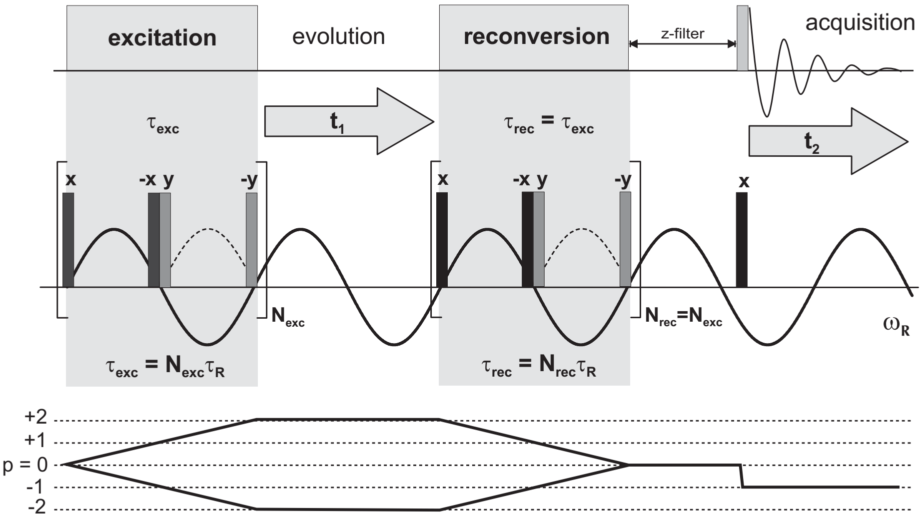

Figure 2.3: *Back-to-back recoupling pulse sequence with coherence transfer pathway below. The sinusoidal curve visualizes the rotor modulation, with the dashed line indicating the effect of the pulse sequence.*

In the limit of short recoupling times and for an isolated spin-pair, it can be shown that the signal intensity, I$_{ij}^{DQ}$ is directly proportional to the dipolar coupling constant D$_{(ij)}$ squared. The intensity of a DQ signal is hence given by:

$$I_{ij}^{(DQ)} \propto \left(D_{(ij)}\right)^2 \cdot \tau_{exc}^2 + \ldots \tag{2.2}$$

$$\propto \frac{\tau_{exc}^2}{r_{ij}^6} \tag{2.3}$$

The dependence on the internuclear distance to the sixth power explains why usually only proton-proton distance of $<$ 3.5 Å can be detected. A more quantitative measurement of homonuclear couplings and internuclear distances is provided by DQ spinning sideband patterns, which are explained in Section 2.4.

The 2D DQ MAS experiment bears some similarities with the INADEQUATE [Bax 81] and the NOESY experiment, both known from solution-state NMR. The INADEQUATE technique also excites DQCs, but uses isotropic J-couplings for the creation of DQCs and therefore only probes through-bond proximities. The NOESY experiment provides information about through-space proximities, but correlates spins in an incoherent fashion via cross relaxation and the nuclear Overhauser effect (NOE), not coherently via DQCs.

2.3 Heteronuclear experiments

The heteronuclear NMR experiments conducted in this work are also recorded under fast MAS (25–30 kHz). They are based on REDOR-type recoupling to re-introduce the heteronuclear dipole-dipole couplings, while homonuclear ^{1}H-^{1}H couplings can usually be safely neglected due to the decoupling performance of fast MAS. The 2D REPT-HSQC [Saalwächter 01a] experiment (Section 2.3.2) is a type of HETCOR experiment, correlating dipolar coupled ^{13}C and ^{1}H. REPT stands for REcoupled Polarization Transfer, which in this case is a ^{1}H→^{13}C transfer. Skipping the ^{1}H dimension of a 2D REPT-HSQC experiment yields the TEDOR experiment [Hing 92], explained in Section 2.3.3. It proves particularly useful to get a qualitative idea about the dynamics of CH_2 groups. For a more quantitative investigation of the dynamics of different CH_n groups in a molecule, heteronuclear experiments generating MAS spinning sideband are best to be used, such as REPT-HDOR or REREDOR (see Section 2.4). First of all, however, the REDOR (Rotational-echo double resonance) experiment is explained (Section 2.3.1), as introduced by Gullion in 1989 [Gullion 89b]. It builds the basis for all heteronuclear recoupling pulse sequences described in the following. The actual REDOR experiment itself, however, was not applied in this work.

2.3.1 REDOR

The rotational-echo double resonance (REDOR) [Gullion 89b, Gullion 89a, Gullion 98] is a one-dimensional experiment under MAS for measuring dipole-dipole couplings between heteronuclear spin-pairs by relating the signal intensity (S_r) to the signal intensity of a reference experiment (S_0). The reference experiment is a spin-echo sequence, depicted in Figure 2.4 (left), where the π pulse is applied on the S-channel after a full rotor period to simply refocus the isotropic chemical shift. The dipole-dipole coupling has no primary effect on the detected signal amplitude, because it is averaged to zero over each rotor period. Therefore, the acquired signal, S_0, is the full signal. In the actual experiment (Figure 2.4, right) π pulses are not only applied on the S-channel after full rotor periods but also on the L-channel, at half-integer multiples of τ_R, i.e. $1/2\tau_R$ and $3/2\tau_R$. Therefore, the sign of the average local dipolar field is inverted every other half rotor period and thus does not get averaged to zero after each rotor period. This effect is known as recoupling (see also Section 1.2.5). Hence, the S-spin magnetization is not refocused at the beginning of data acquisition, but is reduced to S_r due to a net dipolar dephasing of the S-spin.

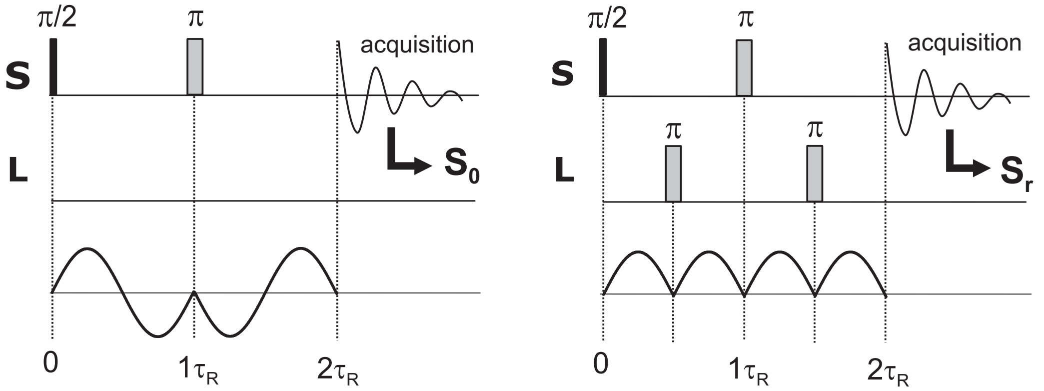

Figure 2.4: *Model of a REDOR experiment for two rotor periods. On the left the spin echo sequence of the reference experiment is depicted, leading to full signal intensity* S_0*, on the right the actual REDOR experiment is shown, giving a reduced signal intensity* S_r*, depending on the product of the evolution time and the heteronuclear dipolar coupling.*

For an isolated spin pair the ratio S_r/S_0 depends solely on the product of the evolution time and the heteronuclear dipolar coupling. Since dipole-dipole couplings depend on the internuclear distance to the inverse cube power, the distance between heteronuclear spin pairs can also be determined with REDOR experiments. The complete REDOR experiment over N rotor periods is shown in Figure 2.5. The cross polarization (CP) enhances the S signal. The CP is followed by a S-L dipolar evolution period for N rotor cycles and proton dipolar decoupling. Since the REDOR experiment is based on the existence of isolated spin-pairs, selective isotopic labeling or, alternatively, pair selection via frequency-selective pulses is needed. Typical heteronuclear spin-pairs under investigation are e.g. ^{13}C–^{15}N or ^{13}C–^{19}F. Below, methods are described which do not rely on isotopic labeling and in addition detect multiple heteronuclear dipole-dipole couplings at once, as suppose to only one in the REDOR experiment.

2.3.2 2D REPT-HSQC

The REcoupled Polarization Transfer - Heteronuclear Single Quantum Correlation (REPT-HSQC) experiment [Saalwächter 01a, Saalwächter 01b] is a two dimensional experiment correlating the chemical shifts of two different nuclei, usually ^{1}H and ^{13}C, through dipole-dipole

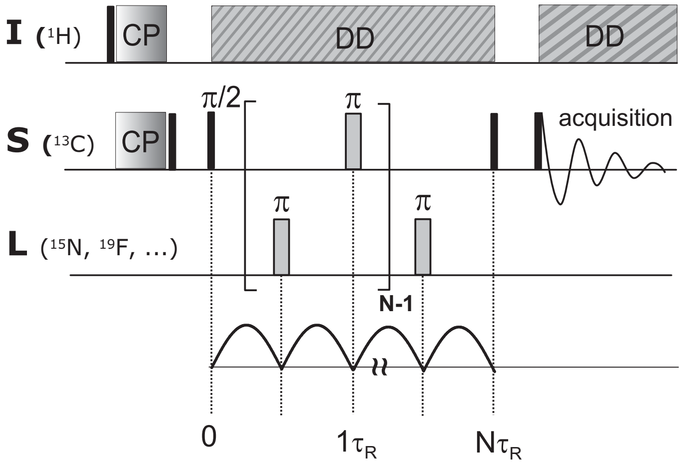

Figure 2.5: *The REDOR pulse sequence for N rotor periods.*

couplings. The experiment is carried out under fast MAS, so that only ^{13}C-^{1}H couplings need to be considered, while ^{1}H-^{1}H dipole-dipole couplings can be neglected as far as coherent effects are concerned. The influence of homonuclear dipole-dipole couplings is basically restricted to the residual ^{1}H linewidth. REDOR recoupling is applied to selectively recouple heteronuclear dipole-dipole couplings by creating a single quantum coherence (SQC), which evolves during t_1. It is similar to the HSQC experiment [Bodenhausen 80] known from solution-state NMR, apart from the fact that the latter relies on J-couplings rather than dipole-dipole couplings.

Figure 2.6 shows the pulse sequence and the corresponding coherence transfer pathway of a REPT-HSQC experiment. A more general expression is chosen for the excitation and the reconversion time known from the ^{1}H DQ experiment (Section 2.2), namely first recoupling time, $\tau_{rcpl,1}$ and second recoupling time, $\tau_{rcpl,2}$. Similar to the 2D DQ experiment, the two times are set equal, $\tau_{rcpl,1} = \tau_{rcpl,2}$ and the evolution time must be incremented in multiple integers of the rotor period, $t_1 = N\tau_R$. This rotor-synchronization of the evolution results in a modulation of the t_1 signal by the isotropic chemical shift Ω_I of the I-spin. The peak intensities in the spectrum are determined by the underlying dipolar coupling strength and the the number of recoupling cycles applied [Saalwächter 02b]. Therefore, the recoupling conditions can be chosen to cover only short-range or also longer-range C-H interactions. For $\tau_{rcpl} = 1\tau_R$ only signals of ^{1}H-^{13}C pairs with a direct chemical bond are observed in the spectra, while $\tau_{rcpl} = N_{rcpl}\tau_R$ with $N_{rcpl} > 1$ also allows for ^{1}H-^{13}C polarization transfer to carbons without directly attached protons. In addition, REPT-HSQC spectra allow a better resolution and assignment of ^{1}H resonances which overlap in 1D ^{1}H spectra by taking advantage of the much greater resolution in the ^{13}C dimension due to the larger chemical shift range and inherently narrower linewidth of ^{13}C resonances.

In a REPT-HSQC experiment initial ^{1}H magnetization is used directly for the excitation of a heteronuclear single quantum coherence (SQC) state, which is monitored during t_1, and

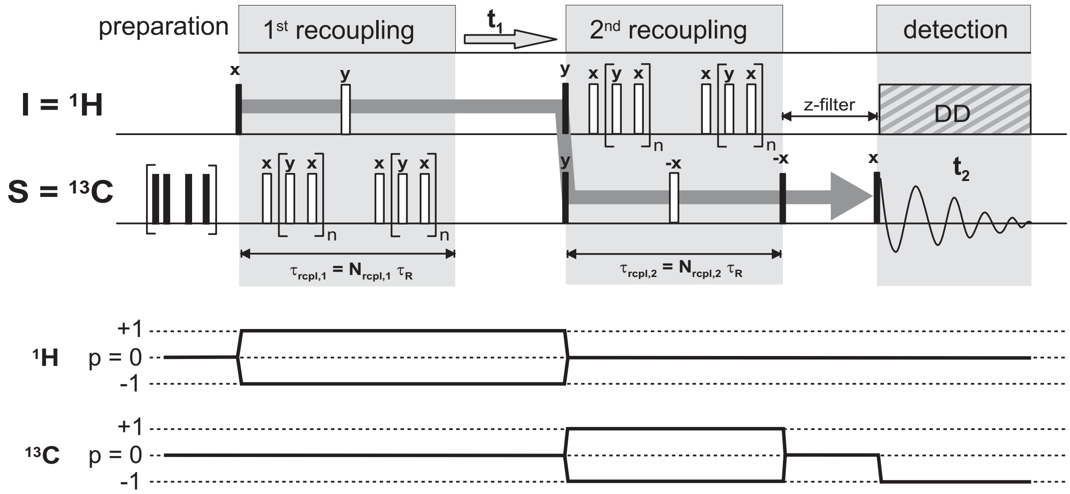

Figure 2.6: *Pulse sequence and coherence transfer pathway diagram for the* ^{1}*H-*^{13}*C REPT-HSQC experiment. The large dark grey arrow represents the magnetization transfer in the experiment. 90° and 180° pulses are depicted in black and white, respectively. (It should be noted that n = 0 corresponds to a recoupling time of 2* τ_R*, while for 1* τ_R *recoupling also the first* π*-pulse of each train needs to be omitted.)*

then transferred from the protons to the carbons, where it is finally read out. The large dark grey arrow in the pulse sequence in Figure 2.6 indicates the transfer of magnetization. Since MAS averages out dipole-dipole couplings, recoupling must by applied, which is achieved by the π-pulse trains on the ^{13}C and the ^{1}H channel during the first and the second recoupling period, respectively. The magnetization transfer can be explained in terms of product operators taking only IS spin-pairs into account. Looking at Figure 2.6, the experiment starts with a train of π-pulses on the ^{13}C- channel (preparation-time). These pulses saturate S-magnetization, so that no IS-coherence is present at the start of the experiment and a pure -I$_y$ state is created by the first 90°$_x$ pulse applied on the proton channel.

$$\hat{\boldsymbol{I}}_z \xrightarrow{(90^\circ_x)_I} -\hat{\boldsymbol{I}}_y \tag{2.4}$$

Due to free precession of -$\hat{\boldsymbol{I}}_y$ in the xy-plane for a time t = $\tau_{rcpl}/2$ at a resonance offset Ω the following expression results, which accounts for the isotropic chemical shift:

$$-\hat{\boldsymbol{I}}_y \xrightarrow{\Omega_I t} -\hat{\boldsymbol{I}}_y cos\Omega_I t + \hat{\boldsymbol{I}}_x sin\Omega_I t \tag{2.5}$$

Taking into account also the evolution under the recoupled heteronuclear dipole-dipole coupling, N$_{rcpl,1}\Phi_0$, between a ^{1}H-^{13}C spin pair we arrive at:

$$\begin{aligned}
&-\hat{\boldsymbol{I}}_y cos\Omega_I t + \hat{\boldsymbol{I}}_x sin\Omega t\\
&\xrightarrow{N_{rcpl,1}\Phi_0} \quad -\hat{\boldsymbol{I}}_y cos\Omega_I t\ cosN_{rcpl,1}\Phi_0 + 2\hat{\boldsymbol{I}}_x\hat{\boldsymbol{S}}_z cos\Omega_I t\ sinN_{rcpl,1}\Phi_0\\
&\qquad\qquad + \hat{\boldsymbol{I}}_x sin\Omega_I t\ cosN_{rcpl,1}\Phi_0 + 2\hat{\boldsymbol{I}}_y\hat{\boldsymbol{S}}_z sin\Omega_I t\ sinN_{rcpl,1}\Phi_0, \qquad (2.6)
\end{aligned}$$

where N$_{rcpl}$ denotes the number of rotor cycles the recoupling period lasts and Φ_t is the average phase factor for a two-spin system and a full rotor cycle, with t describing the dependence on the initial rotor phase, ω_Rt, such that

$$\begin{aligned}
\Phi_0 &= \frac{-D_{IS}}{\omega_R}\, 2\sqrt{2}\, sin2\beta_{IS}\ sin(\gamma_{IS}),\\
\Phi_t &= \frac{-D_{IS}}{\omega_R}\, 2\sqrt{2}\, sin2\beta_{IS}\ sin(\omega_R t + \gamma_{IS}). \qquad (2.7)
\end{aligned}$$

D$_{IS}$ is the dipolar coupling constant in units of angular frequency, β_{IS} and γ_{IS} (in polar coordinates) are the Euler angles defining the orientation of the internuclear C-H vector with respect to the rotor axis and $\omega_R t_1$ defines the rotor modulation.

A $(180^\circ_y)_I$ pulse follows in the middle of the excitation-period, which refocuses the isotropic chemical shift by changing the sign of all I$_x$ and I$_z$ operators

$$\begin{aligned}
&-\hat{\boldsymbol{I}}_y cos\Omega_I t\ cosN_{rcpl,1}\Phi_0 + 2\hat{\boldsymbol{I}}_x\hat{\boldsymbol{S}}_z cos\Omega_I t\ sinN_{rcpl,1}\Phi_0\\
&+\hat{\boldsymbol{I}}_x sin\Omega_I t\ cosN_{rcpl,1}\Phi_0 + 2\hat{\boldsymbol{I}}_y\hat{\boldsymbol{S}}_z sin\Omega_I t\ sinN_{rcpl,1}\Phi_0\\
&\xrightarrow{(180^\circ_y)_I} \quad -\hat{\boldsymbol{I}}_y cos\Omega_I t\ cosN_{rcpl}\Phi_0 - 2\hat{\boldsymbol{I}}_x\hat{\boldsymbol{S}}_z cos\Omega_I t\ sinN_{rcpl}\Phi_0\\
&\qquad\qquad -\hat{\boldsymbol{I}}_x sin\Omega_I t\ cosN_{rcpl}\Phi_0 + 2\hat{\boldsymbol{I}}_y\hat{\boldsymbol{S}}_z sin\Omega_I t\ sinN_{rcpl}\Phi_0,
\end{aligned}$$

$$(2.8)$$

so that an evolution under the isotropic chemical shift Ω_I for a second time t = $\tau_{exc}/2$ gives

$$\begin{aligned}
&-\hat{\boldsymbol{I}}_y cos\Omega_I t\ cosN_{rcpl,1}\Phi_0 - 2\hat{\boldsymbol{I}}_x\hat{\boldsymbol{S}}_z cos\Omega_I t\ sinN_{rcpl,1}\Phi_0\\
&-\hat{\boldsymbol{I}}_x sin\Omega_I t\ cosN_{rcpl,1}\Phi_0 + 2\hat{\boldsymbol{I}}_y\hat{\boldsymbol{S}}_z sin\Omega_I t\ sinN_{rcpl,1}\Phi_0\\
&\xrightarrow{\Omega_I t} \quad -\hat{\boldsymbol{I}}_y cos\Omega_I t\ cosN_{rcpl,1}\Phi_0 t\ cos\Omega_I t + \hat{\boldsymbol{I}}_x cos\Omega_I t\ cosN_{rcpl,1}\Phi_0\ sin\Omega_I t\\
&\qquad\qquad -2\hat{\boldsymbol{I}}_x\hat{\boldsymbol{S}}_z cos\Omega_I t\ sinN_{rcpl,1}\Phi_0\ cos\Omega_I t - 2\hat{\boldsymbol{I}}_y\hat{\boldsymbol{S}}_z cos\Omega_I t\ sinN_{rcpl,1}\Phi_0\ sin\Omega_I t\\
&\qquad\qquad -\hat{\boldsymbol{I}}_x sin\Omega_I t\ cosN_{rcpl,1}\Phi_0\ cos\Omega_I t - \hat{\boldsymbol{I}}_y sin\Omega_I t\ cosN_{rcpl,1}\Phi_0\ sin\Omega_I t\\
&\qquad\qquad +2\hat{\boldsymbol{I}}_y\hat{\boldsymbol{S}}_z sin\Omega_I t\ sinN_{rcpl,1}\Phi_0\ cos\Omega_I t - 2\hat{\boldsymbol{I}}_x\hat{\boldsymbol{S}}_z sin\Omega_I t\ sinN_{rcpl,1}\Phi_0\ sin\Omega_I t\\
&\quad = \qquad -\hat{\boldsymbol{I}}_y cosN_{rcpl,1}\Phi_0 - 2\hat{\boldsymbol{I}}_x\hat{\boldsymbol{S}}_z sinN_{rcpl,1}\Phi_0, \qquad (2.9)
\end{aligned}$$

revealing that the chemical shift is indeed refocused at the end of the excitation period due to the $(180^\circ_y)_I$ pulse. The magnetization which evolved under the recoupled dipolar interaction, however, has not been refocused and hence an antiphase magnetization with SQC character on the I-spin side $-2\hat{\boldsymbol{I}}_x\hat{\boldsymbol{S}}_z$ is present. (The $\hat{\boldsymbol{I}}_y$ coherence can be omitted because it does not evolve into detectable S-spin magnetization). This SQC now is subject to the chemical shift evolution of the I-spin during t$_1$, $\Omega_I t_1$, while the S-spin chemical-shift has no effect on a $\hat{\boldsymbol{S}}_z$ state.

$$\begin{aligned} -2\hat{\boldsymbol{I}}_x\hat{\boldsymbol{S}}_z sinN_{rcpl,1}\Phi_0 \xrightarrow{\Omega_I t_1} & -2\hat{\boldsymbol{I}}_x\hat{\boldsymbol{S}}_z sinN_{rcpl,1}\Phi_0\ cos\Omega_I t_1 \\ & -2\hat{\boldsymbol{I}}_y\hat{\boldsymbol{S}}_z sinN_{rcpl,1}\Phi_0\ sin\Omega_I t_1. \end{aligned} \tag{2.10}$$

By applying a procedure for phase sensitive detection (TPPI = time proportional phase increment [Marion 83, Marion 89]), the real and the imaginary part are alternatingly selected for each increment in t$_1$. It starts with the real part for t_1 = 0 (first slice). Thus, the simultaneous application of a 90°_y pulses on the I- and S-channel at the end of the evolution time gives

$$-2\hat{\boldsymbol{I}}_x\hat{\boldsymbol{S}}_z sinN_{rcpl,1}\Phi_0\ cos\Omega_I t_1 \xrightarrow{(90^\circ_y)_I,(90^\circ_y)_S} 2\hat{\boldsymbol{I}}_z\hat{\boldsymbol{S}}_x sinN_{rcpl,1}\Phi_0\ cos\Omega_I t_1, \tag{2.11}$$

which describes the transfer of magnetization from the protons to the dipolar coupled carbons. During the second recoupling time this antiphase coherence now evolves back into observable S-spin magnetization. The second recoupling period works analogously to the first one, but affects the S-nuclei. The chemical shift of the S-spins, Ω_S, is refocused by a $(-180^\circ_x)_S$ pulse in the middle of the recoupling period so that the spin system again only evolves under the dipolar coupling, N$_{rcpl,2}\Phi_{t_1}$

$$\begin{aligned} & 2\hat{\boldsymbol{I}}_z\hat{\boldsymbol{S}}_x sinN_{rcpl}\Phi_0\ cos\Omega_I t_1 \\ & \xrightarrow{N_{rcpl,2}\Phi_{t_1}} 2\hat{\boldsymbol{I}}_z\hat{\boldsymbol{S}}_x sinN_{rcpl,1}\Phi_0\ cos\Omega_I t_1\ cosN_{rcpl,2}\Phi_{t_1} \\ & \qquad\qquad + \hat{\boldsymbol{S}}_y sinN_{rcpl,1}\Phi_0\ cos\Omega_I t_1\ sinN_{rcpl,2}\Phi_{t_1}. \end{aligned} \tag{2.12}$$

The (-90$^\circ_x$)$_S$ pulse at the end of the second recoupling period converts the $\hat{\boldsymbol{S}}_y$ state into $\hat{\boldsymbol{S}}_z$, while the $\hat{\boldsymbol{I}}_z\hat{\boldsymbol{S}}_x$ term is unaffected and can therefore be omitted. After a dephasing delay (z-filter) and a final $(90^\circ_x)_S$ read-out pulse, S$_y$ magnetization is detected during t$_2$, which is defined as the expectation value of $\hat{\boldsymbol{S}}_y$

$$S_y(t_1) = \langle cos\Omega_I t_1\ sinN_{rcpl,1}\Phi_0\ sinN_{rcpl,2}\Phi_{t_1}\rangle, \tag{2.13}$$

where the brackets ⟨...⟩ denote the powder average. When the imaginary part of the expression in equation 2.10 is selected by TPPI (every second slice) the $\hat{\boldsymbol{S}}_x$ component determines the signal

$$S_x(t_1) = \langle sin\Omega_I t_1 \;\; sinN_{rcpl,1}\Phi_0 \; sinN_{rcpl,2}\Phi_{t_1}\rangle. \tag{2.14}$$

During the acquisition TPPM dipolar decoupling (see Section 1.2.6) is applied on the proton channel. After fourier transform (FT) over t_2 the first slice (t_1 = 0) represents the HSQC filtered S-spin (^{13}C) spectrum. A second FT over t_1 reveals the I-spin (^{1}H) chemical shift information in the second dimension of the spectrum. It should be noted that the phases of the pulses just described, must of course by cycled to select the desired SQC and remove artifacts from imperfect pulses. The appropriate phase cycle can be found in [Saalwächter 01a].

2.3.3 TEDOR

Skipping the ^{1}H dimension of the 2D REPT-HSQC experiment yields the TEDOR (Transferred-Echo, Double Resonance) experiment [Hing 92, Hing 93]. It is particularly useful for obtaining qualitative information about the mobility of CH_2 groups. The ^{13}C signal of rigid CH_2 groups disappears for recoupling times $\tau_{rcpl} \geq 60\mu$s under fast MAS which corresponds to two or more rotor periods ($\tau_{rcpl} \;\geq 2\tau_R$) at MAS frequencies $\leq$ 30 kHz. The reason for this are interfering effects of the two C–H couplings in the CH_2 group. Figure 2.7 shows calculated signal intensities for a CH (dashed line) and a CH_2 group (solid line) as a function of recoupling time. The maximum signal intensity for CH_2 and CH groups is observed at 30 and 40 μs, respectively (40 μs = 1 τ_R at 25 kHz MAS). While the signal intensity for the CH group oscillates around 0.8 of the (theoretical) full intensity for longer recoupling times, the signal intensity of the CH_2 group sharply decreases and reaches its minimum ($\sim$ 0.0) at 80 μs which corresponds to a recoupling time τ_{rcpl} = $2\tau_R$ at 25 kHz MAS. At longer recoupling times not much of the signal intensity recovers. This means that the signal of a rigid CH_2 group disappears from a ^{1}H-^{13}C TEDOR spectrum, when MAS $\leq$ 30 kHz and $\tau_{rcpl} \;\geq 2\tau_R$ are applied.

Dynamic processes, however, may lead to an orientational averaging and, thus, to a motional reduction of the C-H dipole-dipole couplings in the CH_2 group, which is then reflected in the spectra by the re-appearance of the respective ^{13}C resonance for $\tau_{rcpl} \;\geq 2\tau_R$. Effectively, ^{1}H-^{13}C TEDOR spectra of this type straightforwardly provide semi-quantitative information of the local mobilities of CH_2 groups: If the ^{13}C signal of a CH_2 group is observed at $\tau_{rcpl} \geq 2\tau_R$, the CH_2 group must be somewhat mobile, while the disappearance of the ^{13}C resonance points at a rather immobile CH_2 group.

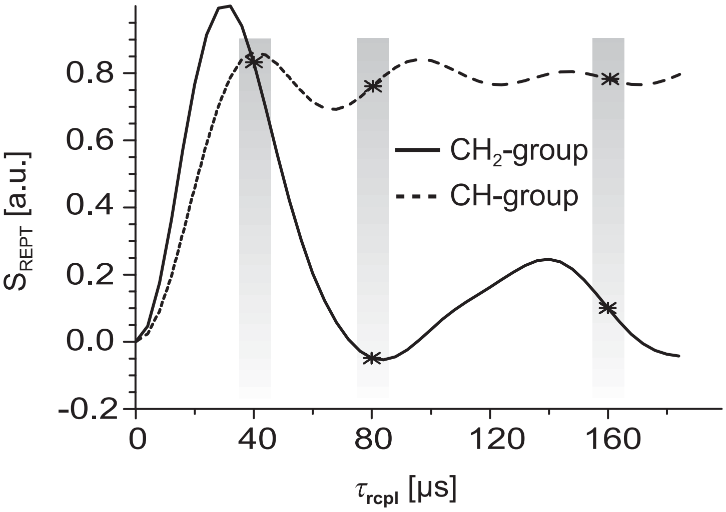

Figure 2.7: *Signal intensities of ^{13}C resonance lines of rigid CH (dashed line) and CH_2 groups (solid line) in TEDOR and REPT-HSQC experiments as a function of the duration of the ^{1}H-^{13}C recoupling period (τ_{rcpl}) [Fischbach 02]. The grey bars indicate the signal intensities expected for a CH and CH_2 group when τ_{rcpl} = 1, 2, 4 τ_R is applied under MAS at 25 kHz.*

2.4 Spinning sideband patterns

The pulse-sequences described in this Section aim at a quantitative and site-selective determination of homonuclear and heteronuclear dipole-dipole couplings by correlating ^{13}C-^{1}H or ^{1}H-^{1}H coupling information with the corresponding ^{13}C or ^{1}H chemical shifts, respectively. Fast MAS at 25–30 kHz is applied to provide sufficient proton decoupling and line narrowing. Two variants of heteronuclear recoupling techniques are discussed: Firstly, the REPT-HDOR experiment [Saalwächter 01a] where, similar to the TEDOR/ REPT-HSQC approach, the ^{1}H polarization is transferred to ^{13}C during the recoupling periods and, secondly, the REREDOR pulse sequence [Saalwächter 02b] where a t_1 dimension is inserted in the standard REDOR pulse sequence. To determine homonuclear ^{1}H-^{1}H couplings a variation of the ^{1}H DQ pulse sequence (discussed above in Section 2.2) can be applied [Schnell 01b]. The dipole-dipole couplings are measured by means of MAS spinning sideband patterns, which arise in the indirect dimension of the 2D experiments as a result of rotor-encoding the dipolar interaction. While the experiments mentioned above in Section 2.2 and 2.3.2 were carried out in a rotor-synchronized fashion ($\Delta t_1 = \tau_R$), t_1 now is incremented in fractions of a rotor period ($\Delta t_1 < \tau_R$), which increases the spectral width and, in this way, gives rise to MAS spinning sideband patterns. These spinning sidebands, however, have nothing to do with "mapping out" anisotropic interaction, because we deal with isolated spin pairs in the spin-pair approximation and hence no anisotropic evolution is present in t_1. Instead, the origin of the sidebands lies in the t_1-dependent change of the dipolar Hamiltonian that is active during the second recoupling period relative to the one active during the first recoupling period. The two average Hamiltonians differ by an amplitude factor $\propto$ D$_{ij}$cos(ω_Rt$_1$), where D$_{ij}$ denotes the dipole-dipole coupling constant and ω_R the MAS frequency. This phenomenon is known as Reconversion Rotor Encoding (RRE) [Friedrich 98]. Accordingly, the signal intensities are modulated along t$_1$, and Fourier transformation yields a pattern of MAS-induced sidebands along the F$_1$ frequency axis. Examples of such sideband patterns are shown in Figure 2.8 for DQ, REPT-HDOR and REREDOR experiments, calculated for a dipole-dipole coupling of 10 kHz and different recoupling times at a MAS spinning frequency of 30 kHz.

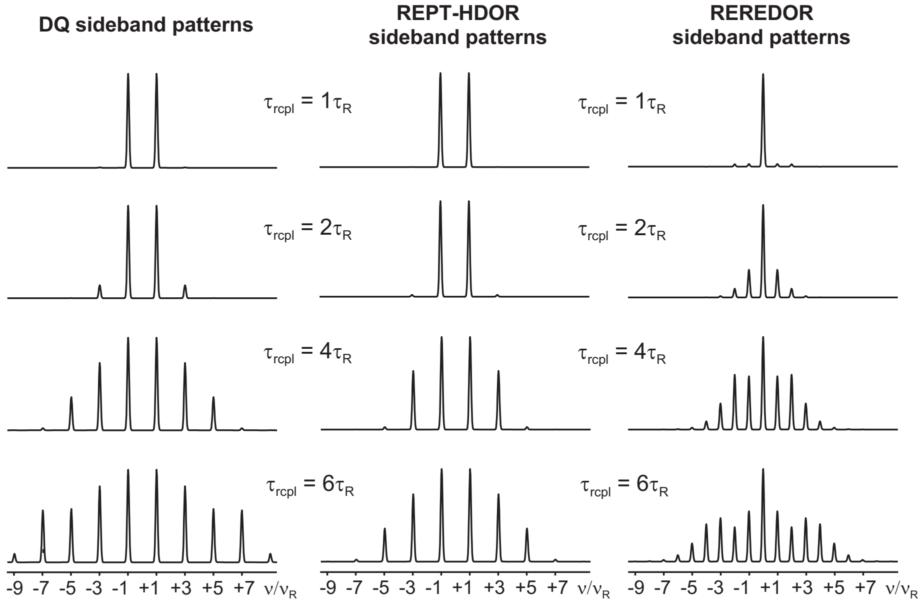

Figure 2.8: *Spinning sideband patterns of homonuclear DQ and heteronuclear REPT-HDOR and REREDOR experiments, calculated for a dipole-dipole coupling (D_{ij}) of 10 kHz and different recoupling times (τ_{rcpl}) under a MAS frequency of 30 kHz (corresponding to a rotor period of τ_R = 33.3 μs).*

The distribution of the sideband intensities over the pattern is only determined by the product of the underlying dipole-dipole coupling and the recoupling time applied in the experiment, D$_{ij}$ τ_{rcpl}. Hence, for a given dipole-dipole coupling a longer recoupling time leads to higher order sidebands, as shown in Figure 2.8. From the relative intensity of these sidebands the dipolar coupling constant can be extracted to a high degree of accuracy. It should be noted that the overall intensity of the sidebands is unaffected by the recoupling time, it is just spread over more sidebands if τ_{rcpl} is increased. Comparing the sideband patterns of the three experiments, the sidebands for HDOR and DQ spin pairs are very similar, in fact they just differ by a scaling factor 1.5 of the coupling constant, which reflects the difference in the homonuclear and heteronuclear dipolar Hamiltonians. The REREDOR spinning sideband patterns clearly show sidebands not only at odd order multiples of the MAS spinning frequency but also at even order ones. The reason for this is explained below in Section 2.4.2.

The strength of the dipole-dipole coupling between two given nuclei (i = ^{1}H and j = ^{1}H or ^{13}C) only depends on their distance r_{ij}, given that the molecular moiety under investigation is immobile on the NMR time scale

$$\frac{D_{ij}}{2\pi} \propto \frac{\gamma_i}{\gamma_i}\frac{\gamma_j}{\gamma_i} \cdot \frac{1}{r_{ij}^3} \tag{2.15}$$

In the presence of molecular motions faster than about 10^{-6}s, dipole-dipole couplings, however, get reduced. This is due to the anisotropy of the interaction in the presence of a magnetic field B_0, which is proportional to (3cos$^2\theta$-1). A dynamic order parameter, S, can be defined for individual segments by relating the measured (reduced) dipolar coupling to the one calculated for the immobile case, so that for an immobile segment S = 100$\%$ results. Effectively, the parameter S reflects the motion of the internuclear vector (C-H or H-H) in terms of its reorientation with respect to the external magnetic field vector B_0. In particular ^{1}H-^{13}C dipole-dipole couplings for directly bonded C-H pairs can provide much insight into site-specific molecular motion, e. g. aromatic ring-flips or alkyl chain motion [Wind 02, Rapp 03, Fischer 03]. By measuring ^{1}H-^{1}H dipolar couplings, either dynamical processes can be investigated for example of aromatic building blocks [Rapp 03] or precise proton-proton distances can be determined [Percec 02b, Schnell 02a, Brown 01c, Brown 00a]. Clearly, MAS sideband patterns, generated by homonuclear and heteronuclear dipolar recoupling schemes, allow the precise and selective determination of local order parameters through site-specific dipole-dipole couplings and, in this way, elucidate the local molecular dynamics. This enables the identification of structure-directing moieties within supramolecular architectures.

2.4.1 REPT-HDOR sideband patterns

The REPT-HDOR (REcoupled Polarization Transfer - Heteronuclear Dipolar ORder) and REPT-HSQC (see Section 2.3.2) experiment are very similar. In REPT-HDOR the evolution time is incremented in fractions of a rotor period (not in integer multiples as in REPT-HSQC) to generate spinning sideband patterns. The pulse sequence itself only differ in the position of one 90° pulse. In both cases transverse ^{1}H magnetization, $-I_y$, evolves under the heteronuclear dipolar coupling producing a heteronuclear single quantum coherence, $2I_xS_z$, at the end of the first recoupling period. While in HSQC this $2I_xS_z$ state evolves during t_1 and a $(90^\circ_y)_I$ pulse follows **after** the evolution time (see Figure 2.6), in HDOR a $(90^\circ_y)_I$ pulse is placed **before** the evolution time. Thus, a two-spin dipolar ordered state, $\hat{\boldsymbol{I}}_z\hat{\boldsymbol{S}}_z$, is created, which does not evolve under either ^{1}H or ^{13}C chemical shift during t_1. Therefore, the time domain signal of a ^{1}H-^{13}C spin pair, $S(t_1)$ "lacks" the cos$\Omega_I t_1$ term:

$$S(t_1) \propto \langle sinN_{rcpl,1}\Phi_0 \; sinN_{rcpl,2}\Phi_{t_1}\rangle, \tag{2.16}$$

where $\langle ... \rangle$ denote the powder average and $N_{rcpl,1}$ and $N_{rcpl,2}$ give the number of rotor periods during which the first and the second recoupling period, respectively, is applied. The phase angles Φ_0 and Φ_{t_1} remain the same as in REPT-HSQC (eq. 2.7)

$$\begin{aligned} \Phi_0 &= \frac{-D_{IS}}{\omega_R}\, 2\sqrt{2}\, sin2\beta_{IS}\, sin\gamma_{IS} \\ \Phi_{t_1} &= \frac{-D_{IS}}{\omega_R}\, 2\sqrt{2}\, sin2\beta_{IS}\, sin(\omega_R t_1 + \gamma_{IS}). \end{aligned} \tag{2.17}$$

The loss of chemical shift information in the ^{1}H dimension is usually not a problem but rather an advantage, because in principle only one rotor period needs to be recorded in t_1, $t_1 = 0...1\tau_R$. In this way, the total time of the experiment is reduced significantly. The acquired signal in the indirect dimension, $S(t_1)$, must then be catenated and multiplied by a weighting function to introduce an artificial line broadening, before it is Fourier transformed and gives spinning sideband patterns (see Figure 2.8) in the indirect dimension of the experiment. It is, however, advantageous to actually record $t_1 = 0...2\tau_R$ or even $0...3\tau_R$, not only $0...1\tau_R$ (with $\Delta t_1 \ll \tau_R$), because the time span of the signal in t_1, $N\cdot\tau_R$, determines the frequency resolution of the sideband patterns, $\Delta f = 1/N\tau_R$. Hence, for $t_1 = 0...1\tau_R$ the so-called correlated noise only appears at the positions of the sidebands, while for $t_1 = 0...2\tau_R$ it appears also at half rotor period intervals, such that the contribution of noise to the sidebands is less and can be better estimated.

No matter how many rotor cycle are recorded in t_1, reconversion rotor-encoding, of course, always takes place during the evolution time due to the incrementation of t_1 by Δt_1, in fractions of the rotor period, so that

$$\Delta t_1 = \frac{1}{2 \cdot \nu_R \cdot n} = \frac{1}{sw}, \tag{2.18}$$

where ν_R is the MAS spinning frequency, n is the highest order spinning sideband one wants to observe and sw is the resulting spectral width in the indirect dimension. Hence, the number of slices, N_{slice}, that needs to be recorded in the indirect dimension for one rotor cycle, τ_R, is given by

$$\frac{1}{\nu_R} = \tau_R = \Delta t_1 \cdot N_{slice}. \tag{2.19}$$

If the ^{1}H chemical shift information in the indirect dimension is needed, the same type of rotor encoding, just described for REPT-HDOR, can equally be introduced into the REPT-HSQC experiment. Like in HDOR, the t_1 evolution time is then incremented in fractions of a rotor period (not in multiple integers as for a ^{1}H-^{13}C correlation experiment, Section 2.3.2). In this way, the spectral width is increased in the indirect dimension of the HSQC experiment so that spinning sideband patterns are observed which are identical to the HDOR spinning sideband patterns. Due to the ^{1}H-^{13}C correlation information contained in the REPT-HSQC experiment the sidebands are, however, shifted in the F_1 dimension according to the chemical shifts of the corresponding ^{1}H resonance. The price for this additional information is a significantly longer experimental time. Due to the ^{1}H chemical shift evolution in t_1, several rotor periods must of course be recorded in the indirect dimension as opposed to only one in the HDOR experiment.

For the sake of completeness, inverse REPT techniques [Schnell 02b, Schnell 01a, Goward 01] are shortly mentioned here, although they have not been applied in this work. “Inverse” refers to the fact that the signal is detected on the ^{1}H channel rather than the X-channel. Similar to REPT-HSQC inverse REPT experiments can be carried out rotor-synchronized to yield a heteronuclear correlation spectrum, or spinning sideband patterns can be generated by incrementing t_1 in steps of $\Delta t_1 < \tau_R$. In principle, an improvement in signal-to-noise ratio is expected from inverse detection. A problem, however, is to extract the ^{1}H signal of interest (arising from ^{1}H-X nuclei couplings), while suppressing all other ^{1}H signal intensity. This can be either achieved with appropriate phase cycles or more efficiently by pulse field gradients. Essentially, the inverse REPT technique is very useful for the investigation of labeled samples, e.g. ^{15}N, to determine ^{1}H-^{15}N dipolar couplings.

2.4.2 REREDOR sideband patterns

REPT methods usually fail when dipolar couplings of rather rigid CH_2 groups are to be determined. As was explained for TEDOR experiments in Section 2.3.3, the signal intensity for rather immobile CH_2 groups vanishes at recoupling times $\tau_{rcpl} \geq 60$ μs in all REPT experiments. To be able to determine the residual dipolar couplings of rather rigid CH_2 groups the so-called Rotor-Encoded REDOR (REREDOR) experiment [Saalwächter 02b] is applied, which does not suffer from this signal intensity loss. The REREDOR pulse sequence is very similar to REDOR. As shown in Figure 2.9, a variable delay $0 \leq t_1 \leq \tau_R$ is inserted into the π-pulse train of a REDOR-type recoupling pulse sequence, so that a first and a second REDOR-type recoupling time result. In this way rotor-encoding of the recoupled dipolar Hamiltonian is implemented during t_1, creating MAS spinning sideband patterns in the indirect dimension of the experiment, as was explained above for the REPT-HDOR experiment. The second t_1 time inserted at the end of the pulse sequence as well as the π-pulse placed on the S-channel in the middle of the first and second recoupling time, serve to refocus the S spin chemical shift evolution. A CP at the beginning of the experiment creates the initial ^{13}C polarization.

The signal of the spinning sidebands observed in the t_1 dimension of a REREDOR ex-

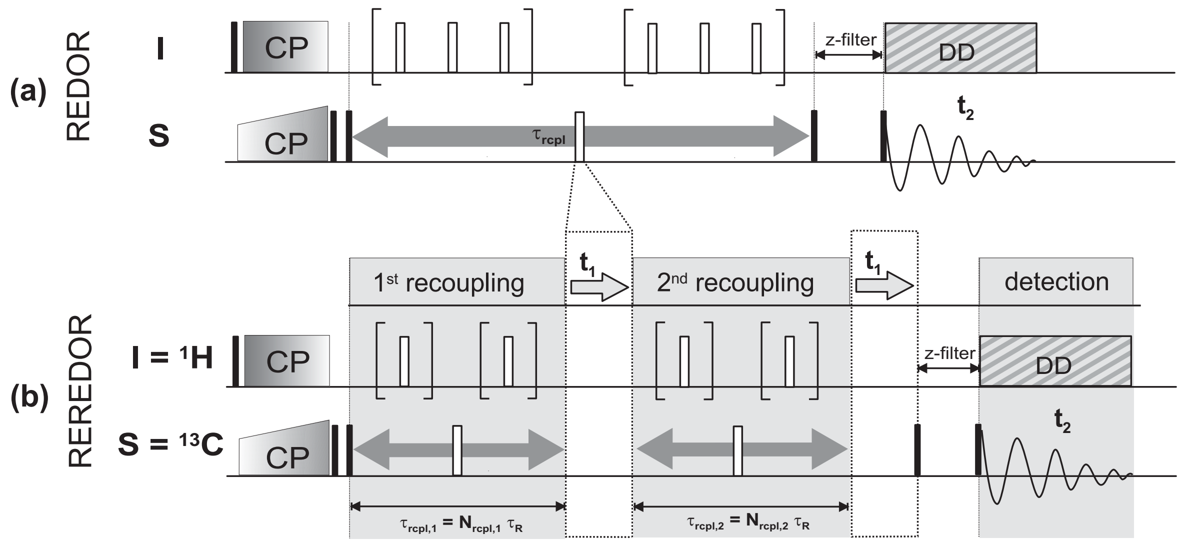

Figure 2.9: *Pulse sequence of the (a) REDOR and (b) REREDOR experiment, showing the insertion of a t_1 evolution time which is incremented in fractions of a rotor period so that rotor-encoding of the recoupled dipolar Hamiltonian takes place and MAS spinning sideband patterns can be generated in the indirect dimension of the REREDOR experiment. 90° and 180° pulses are depicted in black and white, respectively.*

periment under fast MAS can also be described in terms of individual ^{13}C-^{1}H couplings:

$$S(t_1) \propto \langle sinN_{rcpl,1}\Phi_{IS,0}sinN_{rcpl,2}\rangle + \langle cosN_{rcpl,1}\Phi_{IS,0}cosN_{rcpl,2}\rangle. \tag{2.20}$$

Comparing this expression with the one determined for REPT-HDOR spinning sidebands in eq. 2.16, it is apparent, that a cos-cos term is added to the signal. The expression for the phase factors Φ_0 and Φ_{t_1} remains the same (see eq. 2.17). It was mentioned above that REREDOR spinning sidebands appear at odd and even order multiples of ν_R, while in REPT-HDOR experiments only odd order spinning sidebands are observed. It becomes clear that the sin-sin term leads to odd order spinning sidebands, while the cos-cos term generates even order sidebands.[1] The REREDOR experiment generates more sidebands than REPT-HDOR using the same recoupling times (see Figure 2.8). Therefore a shorter recoupling time can generally be used in REREDOR experiments, “pumping” already a sufficient number of sidebands to extract the underlying residual coupling reliably. Also, at first sight, more sidebands should mean a higher sensitivity of the pattern to the underlying dipole-dipole coupling, but practically more sidebands also mean that the signal is spread over more peaks, which reduces the overall signal-to-noise ratio. As mentioned above, the signal of REREDOR experiments does not suffer from signal cancellation effects for CH$_2$ groups, which is due to its additional

---

[1] A so-called RELM (Rotor-Encoded Longitudinal Magnetization) experiment [De Paul 00], not further discussed here, solely relies on the cos-cos term and therefore only creates even order sidebands.

cosine dependence. Therefore it is particularly useful when couplings of relatively rigid CH_2 groups need to be measured.

The REREDOR experiment is rather similar to the more traditional SLF (separated local field) technique conducted under MAS [Munowitz 82, Terao 86, Roberts 87, Hohwy 00] or a more recent variation by Frydman and coworkers [McElheny 00], simplifying the SLF approach. SLF experiments, however, usually fail if coupling constants become small due to molecular motion. With the MAS spinning sideband patterns of REREDOR experiments, also weak dipole-dipole couplings can be determined by increasing the recoupling time τ_{rcpl} = N_{rcpl} τ_R and, in this way, "pumping" sidebands (see Figure 2.8).

2.4.3 DQ sideband patterns

The same type of reconversion rotor encoding as in REPT-HDOR and REREDOR experiments can equally be introduced into the ^1H-^1H DQ MAS experiments (described in Section 2.2), by also incrementing the t_1 dimension in steps of $\Delta t_1 < \tau_R$, [Schnell 01b]. The sideband patterns arising in the indirect dimension are then shifted according to the chemical shifts of ^1H-^1H double-quantum resonances. The signal intensity, $S(t_1)$, determined for REPT-HDOR sidebands (see eq 2.16), applies equally to ^1H-^1H DQ-sidebands

$$S(t_1) = \langle sinN_{exc}\Phi'_0 \; sinN_{rec}\Phi'_{t_1}\rangle, \tag{2.21}$$

where only the average phase factors, Φ_0' and Φ_{t_1}', need to be scaled by a factor 3/2 due to different tensor scaling factors of homo- and heteronuclear interactions [Schnell 01b].

$$\begin{aligned}\Phi'_0 &= \frac{-3D_{ij}}{\omega_R}\sqrt{2}\,sin2\beta_{ij}\;sin\gamma_{ij}\\ \Phi_{t1}{}' &= \frac{-3D_{ij}}{\omega_R}\sqrt{2}\,sin2\beta_{ij}\;sin(\omega_R t_1+\gamma_{ij}).\end{aligned} \tag{2.22}$$

The brackets $\langle ... \rangle$ again denote the powder average, and i and j refer to the two coupled protons. Quite clearly, identical sideband patterns are generated by REPT-HDOR and DQ experiments, which just differ in their intensity by a factor 3/2, as can be also be inferred from Figure 2.8.

In this way, ^1H-^1H dipole-dipole couplings can be sensitively measured, which provides access to ^1H-^1H internuclear distances or, in the case of a known distance, to motional order parameters for molecular segments.

2.4.4 Calculating spinning sideband patterns

MAS Spinning sideband patterns for homo- and heteronuclear spin-pairs can easily be calculated analytically, [Schnell 01b, Saalwächter 01b]. For multiple spin systems an analytical solution becomes difficult, so that rather time-consuming numerical calculations have to be carried out, using programs such as Simpson [Bak 00]. It has been shown that the two-spin approach gives very accurate results, as long as one (strongest) dipole-dipole coupling dominates [Schnell 01b, Saalwächter 01a, Brown 01c]. In such cases the weaker dipolar couplings can be neglected because they are largely averaged out by fast MAS so that basically a spin-pair remains.

Figure 2.10 shows experimental REPT-HDOR spinning sideband patterns of the ^{1}H-^{13}C couplings of a pyrene ring recorded with different recoupling times (black lines). The grey lines show the corresponding analytical two-spin calculations. Neglecting the first order sidebands and only fitting the higher orders, all three recoupling times, as expected, yield the same ^{1}H-^{13}C dipole-dipole coupling of $D_{CH}/2\pi$ = 21.0 kHz. This value corresponds to a rigid C-H group with a internuclear distance of about 1.13 Å. The fact that the first order sidebands are too high is attributed to the influence of secondary couplings involving coherences of distant protons. Their couplings are, however, so weak that their contribution is restricted to the first order sidebands. The result is therefore a heterogeneous superposition of the primary C-H coupling and secondary contributions (restricted to the first order). Looking at Figure 2.10 it is apparent that the intensity of the first order sidebands with respect to the other sidebands gets larger with longer recoupling times. On the one hand this shows the increasing contribution of secondary couplings of more distant protons at longer recoupling times. On the other hand it makes clear that sidebands of higher order (> 1) can still safely be fitted in terms of spin-pairs. The height of the first order sidebands with respect to the calculated one thus gives an idea about the degree of multi-spin effects involved.

In REREDOR experiments secondary couplings mainly affect the centerband of the sideband pattern, as long as short recoupling times are used. The intensity of the centerband is, however, strongly affected by relaxation processes. Therefore it cannot give any idea about the strength of the secondary dipolar couplings, but is simply excluded from the fit.

^{1}H-^{1}H DQ spinning sideband patterns, in principle, behave similarly to REPT-HDOR patterns. As long as one strongest ^{1}H-^{1}H dipole-dipole coupling is present, the sideband pattern can be evaluated in terms of a spin-pair and weaker secondary couplings to more distant protons only affect the intensity of the first order sidebands. There are, however, some cases where it becomes necessary to consider more than two spins. Looking for example at the ^{1}H-^{1}H couplings in a pyrene ring, it is quite obvious that the distance from one proton to its next neighbor on the right is about the same than to the left. In such a case a two-spin approach cannot be valid any more. Figure 2.11a shows an analytical two-spin fit, while 2.11b depicts the result of a numerical four-spin simulation. Calculating DQ spinning sideband patterns for

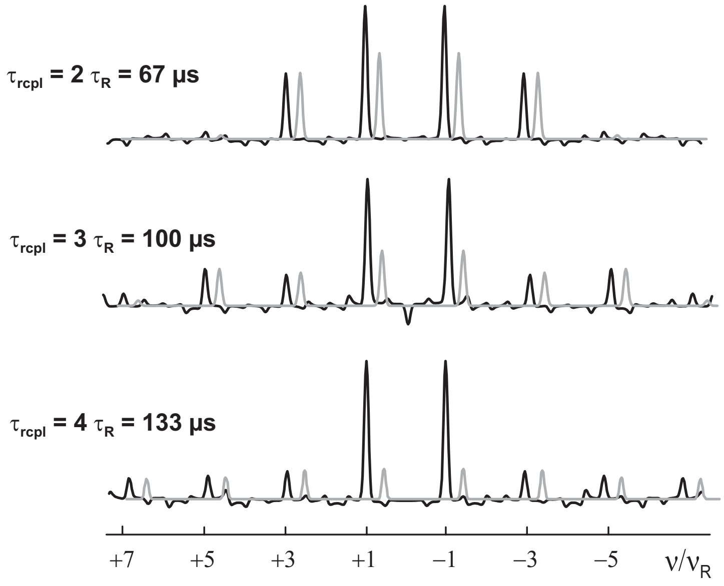

Figure 2.10: *REPT-HDOR spinning sideband patterns of pyrene, recorded with different recoupling times, τ_{rcpl} = 2, 3, 4 τ_R at 30 kHz MAS (black line). The patterns depicted in grey are analytically calculated for ^{1}H-^{13}C spin-pairs with a dipole-dipole coupling of $D_{CH}/2\pi$ = 21.0 kHz at the corresponding recoupling times.*

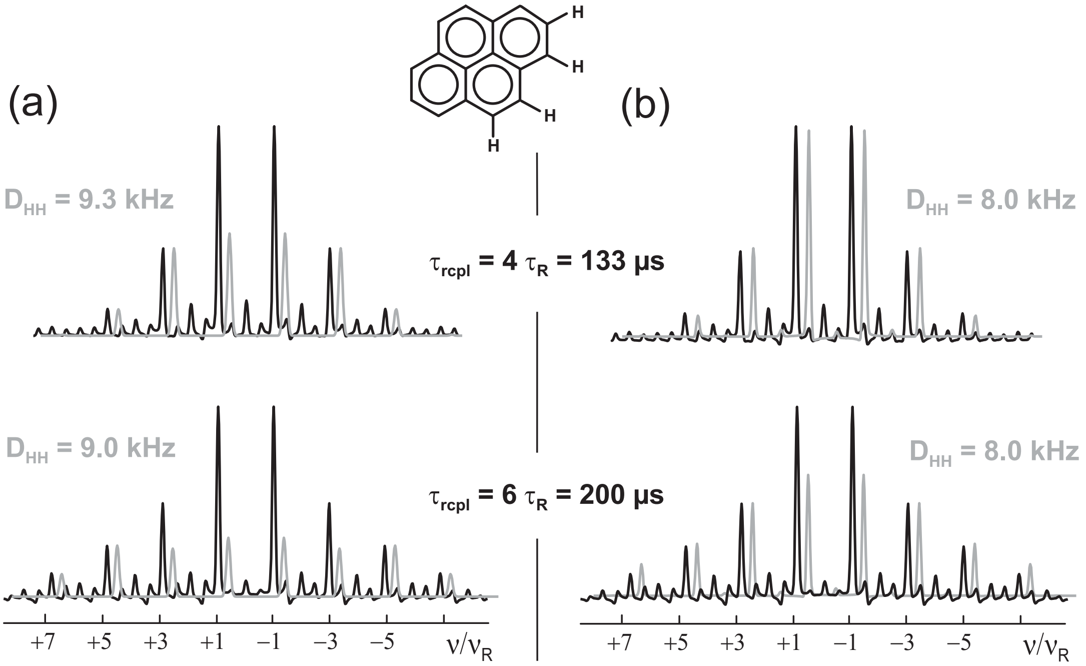

Figure 2.11: *DQ spinning sideband pattern of pyrene, recorded at a recoupling time of, τ_{rcpl} = 4 τ_R and τ_{rcpl} = 6 τ_R at 30 kHz MAS (black sidebands). The patterns depicted in grey are the result of (a) an analytical calculation of a ^{1}H-^{1}H spin pair and (b) a numerical ^{1}H four-spin calculation using the Simpson program [Bak 00].*

^{1}H spin-pairs, it becomes clear that no pattern exists which matches all experimental sidebands recorded for a pyrene molecule. Assuming secondary couplings and, thus, omitting the first order sidebands, the spin-pair calculations yields a dipolar coupling of D_{HH} = 9.3 kHz for τ_{rcpl} = 4 τ_R (Figure 2.11a). This is not a very reasonable result, because it would assume an average ^{1}H-^{1}H distance in a pyrene ring of 2.35 Å, which is rather short. Turning to the sideband pattern recorded with τ_{rcpl} = 6 τ_R, either 5^{th} and 7^{th} order can be fitted (Figure 2.11a) or 3^{rd} and 5^{th} order, but not all three together. Clearly, the spin-pair approach fails in the case of ^{1}H couplings in a the pyrene ring, because each proton is coupled equally to two neighboring protons. Turning to a ^{1}H four-spin system and calculating the DQ sideband intensities numerically, the interpretation of the patterns is straight forward. At a recoupling time of 4 τ_R the calculated sideband pattern perfectly matches the experimental one and yields a dipolar coupling of D_{HH} = 8.0 kHz. When applying a recoupling time of 6 τ_R and excluding the first order sidebands also a dipolar coupling of D_{HH} = 8.0 kHz results. (To account for the full height of the first order sidebands also more distant couplings and hence more spins need to be considered.) A ^{1}H dipolar coupling of D_{HH} = 8.0 kHz is what we expect for an immobile pyrene ring assuming an internuclear ^{1}H-^{1}H distance of 2.47 Å [Ochsenfeld 02].

When investigating the heteronuclear dipolar couplings of CH_2 or CH_3 groups, we need to consider of course also more than just two spins. Luckily, the theoretical treatment of one ^{13}C-spin to multiple ^{1}H-spins is straight forward [Goetz 97]. It allows an independent evaluation of the dipolar evolution of each ^{13}C-^{1}H pair in a CH_2 or CH_3 group, and the signal can be calculated analytically using product operator theory explained in detail in reference [Saalwächter 02a].

2.5 ^{1}H NMR shift calculations

^{1}H chemical shifts are known to be affected by aromatic ring-current effects and to be indicative of supramolecular organization [Brown 01b]. It has been shown that by means of quantum-chemical calculations ^{1}H chemical-shifts resulting from supramolecular organization can be assigned quantitatively to specific molecular packing arrangements [Brown 01a, Ochsenfeld 01, Ochsenfeld 02, Sebastiani 02]. A more general approach is the computation of so called nucleus-independent chemical-shift (NICS) maps [Schleyer 96]. With such model calculations characteristic ^{1}H shift-effects can be related to local structural features with a remarkable degree of accuracy. An example is given in Figure 2.12, showing the NICS map of a phenol ring [Sebastiani 03, Rapp 03], which is a key building block of many supramolecular structures.

A NICS map is a generalization of the atom-specific chemical shift tensor. It is defined as the trace of the shielding tensor computed at every point in space, as opposed to the traditional chemical shielding value which is only calculated at the position of the nucleus. The map shows how much the chemical shift of a fictitious nuclear spin would be changed by the presence of a particular molecule. Technically, the electronic linear response to the external magnetic field is calculated, which results in an electronic current density. This quantum current induces an additional magnetic field within a range of several Ångstroms, which is the basis of the NICS maps. Taken at the actual positions of the atoms, we would find their absolute chemical shielding values. In this calculation, no explicit probe atom is incorporated, such that the picture is quantitative only in the limit of non-interacting molecules. However, as long as the electronic wavefunctions do not overlap with those of neighboring molecules, it can be assumed that the electronically induced magnetic fields are essentially unchanged.

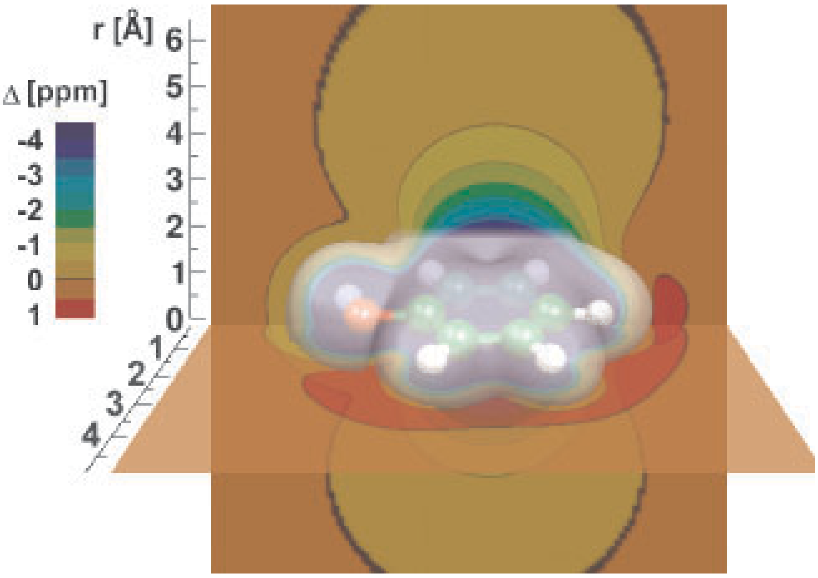

Figure 2.12: *Nucleus-independent chemical-shift (NICS) [Schleyer 96] map of a phenole ring, calculated using density functional theory with the BLYP exchange-correlation functional9 and the CPMD code [CPMD]. The color code reflects the chemical-shift change a nucleus would experience when placed at the respective position relative to the phenol ring. The white-shaded surface around the phenol molecule represents the effective exclusion volume where no other atom can be placed without strongly interfering with the phenol electrons.*

The calculations were performed in the framework of density functional theory with the BLYP exchange-correlation functional [Becke 88] using the CPMD code [CPMD]. The electronic orbitals were expanded in plane waves with a cut-off of 70 Ry, and Goedecker-type pseudopotentials [Goedecker 96] were used for all atoms. The system was put in a large unit cell of 20 Å^3 in order to eliminate interactions between periodic images. The magnetic response properties were calculated using the method described in [Sebastiani 01]. Prior to calculating the NICS map, the geometry of the molecule was fully optimized under the same computational setup.

The resulting map (see Figure 2.12) displays the theoretical chemical-shift displacement that a nuclear spin would experience when placed at a given position relative to a phenole molecule. Such rings represent key building blocks of the dendrons investigated in Chapter 4 and 5. In their environments, characteristic chemical-shift pattern are thus expected with a large and long-ranged π-shifts (to lower frequencies) above and below the ring, as well as a weak and localized inverse effect beside the ring. Based on the map in Figure 2.12, the shift effect experienced by a proton can be used in a semi-quantitative fashion to locate the proton relative to the aromatic ring. The shift effects are determined by comparing ^{1}H NMR spectra of dilute solutions (with negligible aggregation of the solubilized molecules) with solid-state data. For example, a proton in the condensed phase that is shifted to lower frequency by $\Delta = \delta_{solid} - \delta_{solution} = -2$ ppm can be expected within a distance range of 2–3 Å above or below the center of a phenyl ring. A proton shifted to higher frequency by $\Delta = \delta_{solid} - \delta_{solution} = +1$ ppm is expected within the rather confined (red) region around the phenyl ring. In this way, the ^{1}H chemical shift can provide distance constraints for the structure, which are remarkably precise given the simplicity of the approach. In biological solid-state NMR, such ^{1}H chemical-shift constraints have already been used successfully in a study of bacteriochlorophyll aggregates [Rossum 01].

However, one limiting factor of such constraints is the non-uniqueness of ring-current effects: A given shift displacement could be caused by a single phenyl ring as well as by two phenyl rings with the same orientation at a larger distance (about 1.5 times larger). This slightly reduces the accuracy of distance constraints that can be derived from π-shifts, but they still contain significant information, so that the principal approach is not affected. Moreover, it should also be noted that a spin can experience different frequency shifts if it is subject to molecular motion. In this case an average shift-displacement is observed.

Chapter 3

Homo- and heteronuclear solid-state NMR investigation of a Yellow Filter Dye molecule

In this Chapter, a Yellow Filter Dye molecule (Figure 3.1) used for color film materials is investigated [Deroover]. It is a rather rigid and planar molecule due to its extended conjugated π-system that represents the chromophore. It crystallizes in two different morphologies depicted in Figure 3.2 [Deroover], a rhombic one and a needle shaped one. The formation of the rhombic and the needle polymorph are thermodynamically and kinetically controlled, respectively. The aromatic and the isoxazol-5-on moiety of the molecule are coplanar to allow delocalization of the π-electrons. In this way, a chromophore system is built and the molecule can act as a filter dye. The absorption wavelengths, however, are significantly different for the two morphologies. Therefore, the absorption cannot depend solely on the chemical structure but must be influenced by the crystal packing of the molecules [Deroover]. This is investigated in detail in this Chapter using dipolar ^{1}H-^{1}H and ^{1}H-^{13}C recoupling NMR methods under fast MAS.

The lack of control of crystal growth and morphology is a major problem in the development of dyes used for color films. The main challenge to control crystal properties is to understand the interrelation between (i) molecular properties, (ii) crystal properties and (iii) crystal structure. So, on the one hand, we would like to know why a molecule crystallizes in a given way and how we can alter that packing by modifying the molecular structure. On the other hand, we would also like to understand how a given packing defines the properties of the system. Controlling this complex interplay is one of the ambitious aims in material science and can of course not be solved here. However, some insight in this respect can be gained from the comparison of the properties and crystal structures of the two Yellow Filter Dye polymorphs.

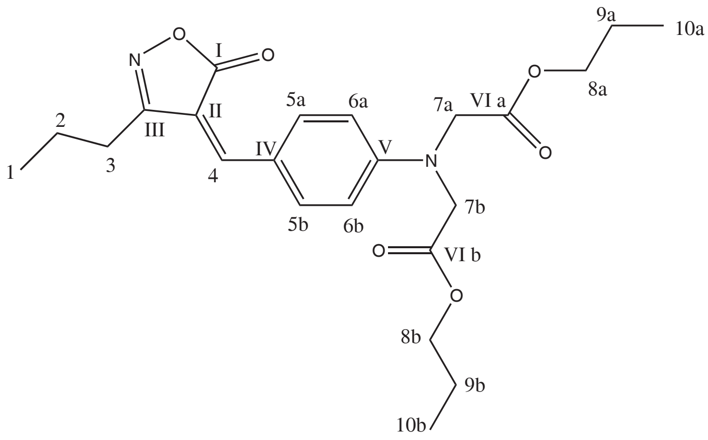

Figure 3.1: *Yellow Filter Dye.*

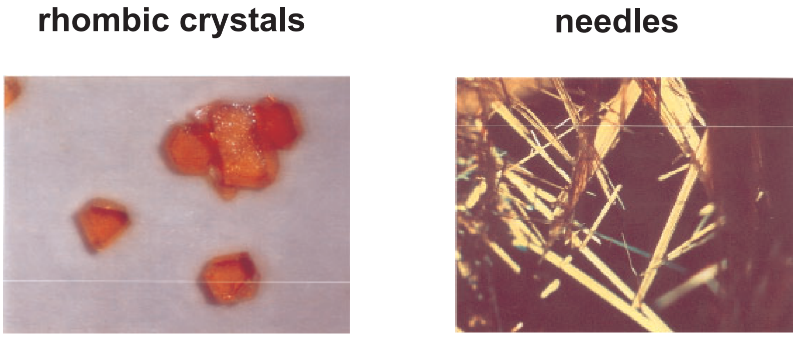
rhombic crystals

needles

Figure 3.2: *Morphologies of Yellow Filter Dye [Deroover].*

For this purpose, a variety of different analytical techniques can be applied, with solid-state NMR being a very promising approach. In the following it is shown that solid-state NMR is capable of distinguishing the two different polymorphs and, in this way, elucidate some correlations between crystal structure and system properties. More importantly, the Yellow Filter Dye molecule serves as a kind of "test-molecule" for the more complex supramolecular systems discussed in the following Chapters. Supramolecular chemistry basically pursues the same aims as mentioned above, meaning the understanding of and the control over the interrelation between (i) molecular properties (ii) bulk properties and (iii) supramolecular assembly. The Yellow Filter Dye molecule is well suited for testing characterization methods due to small size and the known crystal structures. In this way, it is possible to relate the measured solid-state NMR data directly to the structure adopted by the molecule in the crystal, where of course the packing and hence the interaction between neighboring molecules have a major effect. Most important in this respect are π-shifts induced by the conjugated π-electrons of the chromophore system of the molecule. With density functional theory calculations based on BLYP exchange correlation functional [Becke 88, Lee 88] and the CPMD code [CPMD] it is possible to calculate the local field values induced by the electrons of the Yellow Filter Dye molecule. In this way, a nucleus independent chemical shift (NICS) map can be generated, which reflects the chemical-shift changes a nucleus would experience when placed at the respective position in the proximity of a Yellow Filter Dye molecule [Sebastiani 03]. In addition, the dynamical properties of the Yellow Filter Dye molecule are investigated with solid-state NMR. This can easily be done by means of heteronuclear spinning sideband patterns. The structural and dynamical information is very valuable not only with respect to the system itself but also in general, because it shows the variety of detailed structural and dynamical information solid-state NMR can provide.

In the following Section some general remarks are made about the properties of pigments used in color films, such as the Yellow Filter Dye. In Section 3.2 the solid-state NMR results of the rhombic crystals are compared with the X-ray crystal structure and the ^{1}H chemical shifts taken from the chemical shift maps. This shows that solid-state NMR is able to give very valuable information about intra- and intermolecular interactions of the molecules. These are in very good agreement with the crystal structure from X-ray diffraction. In the following Section 3.3 the NMR-results of the needle crystals are shown. Significant differences to the NMR-results of the rhombic form are observed, which shed some light into the different stacking of the Yellow Filter Dye molecule in the different crystal structures. Finally, the local dynamics of the aromatic and the aliphatic moieties are investigated in Section 3.4 for both polymorphs.

3.1 Color film dyes and their properties

Color film materials are multi-layered systems with up to sixteen different layers. In practice, water-based layers are coated simultaneously. Formulating the dyes as dispersions is one established way to prevent diffusion from one layer to the other. Control over particle size of the dispersions is essential, because layer thickness varies and the particles should of course be smaller than the layer. Moreover, light scattering needs to be prevented which requires a particle size below 200 nm. Dispersion by precipitation is one of the preferred methods to obtain nanoparticles, but keeping them stable is by no means trivial. The most important performance criteria for organic dye dispersions are: primary particle size and aggregation state, application properties like dispersibility, dispersion stability and rheological properties, diffusion properties and recrystalization stability, optical properties and processing properties such as dissolution and bleaching. The conventional approach to achieve these properties is the repeated synthesis of new compounds, until the desired dispersion properties are accomplished. The overall performance of a particular pigment does, however, not only depend on its intrinsic molecular properties, but also on intermolecular interactions within the solid state and at the interface with the application media. Therefore, a complementary approach focuses on crystal and supramolecular chemistry to get a deeper understanding of the solid-state properties of the pigment particles. This enables us to better control the performance of different pigments.

3.2 Rhombic polymorph: Structural investigation

The structural information derived from solid-state NMR measurements for the rhombic crystals is compared to its X-ray crystal structure [Deroover]. For this purpose, the ^{1}H and ^{13}C solid-state chemical shifts are compared to their corresponding solution state values (in brackets) in Table 3.1 (see also spectra, Figure 3.3 and 3.9). Deviations of $\geq$ 0.5 ppm between the solid-state and the corresponding solution state chemical shift values point at significant

Table 3.1: Solid-state ^{1}H and ^{13}C chemical shifts of the rhombic crystal from ^{1}H-^{13}C REPT-HSQC correlation spectra and CP experiments. Solution-state NMR data in brackets. The^{1}H π-shifts (Δ) are derived from the difference between solution- and solid-state chemical shift values.

	δ^{13}C [ppm] solid-state	δ^{13}C [ppm] solution	δ^1H [ppm] solid-state	δ^1H [ppm] solution	$\rightarrow \Delta$ [ppm] π-shift
1 (CH_2)	14.0	(13.8)	0.5	(0.98)	
2 (CH_2)	17.6	(19.7)	1.7	(1.65)	
3 (CH_2)	28.8	(27.2)	2.7	(2.63)	
4 (CH)	151.5	(150.5)	*	(7.71)	
5a (arom CH)	136.1	(137.2)	$\sim$ 9.3	(8.45)	+0.85
5b (arom CH)	140.1		7.0		-1.45
6a (arom CH)	114.7	(112.3)	$\sim$ 7.5	(6.79)	+0.71
6b (arom CH)	110.2		5.3		-1.49
7a (NCH_2)	53.4	(52.6)	4.2, 6.0	(4.43)	-0.23, +1.57
7b (NCH_2)	51.8		4.9, 3.2		+0.47, -1.23
8a,b (OCH_2)	66.6	(66.4)	3.9	(4.05)	
9a,b (CH_2)	22.2	(21.6)	1.4	(1.59)	
10a (CH_3)	10.6	(10.3)	-0.1	(0.88)	-0.98
10b (CH_3)	9.9		0.2		-0.68
quaternary carbons					
I	171.6	(170.0)	-	-	
II	111.1	(111.9)	-	-	
III	165.5	(164.9)	-	-	
IV	123.2	(122.6)	-	-	
V	154.3	(153.2)	-	-	
VI	169.5	(169.5)	-	-	

* signal intensity too weak

π-shift effects induced by neighboring molecules.[1] Similar to the well-known ring-current effect, π-electrons of double bonds also induce local fields, see e.g. [Atkins 99], which lead to regions with shielding or deshielding effects. This is illustrated by the nucleus independent chemical shift (NICS) map depicted in Figure 3.10 [Sebastiani 03]), calculated using density functional theory [Sebastiani 01], see also Section 2.5. In this way, the observed π-shift effects (up- and downfield) of individual protons can be explained. Comparing the solid-state chemical shifts with the solution state values and the NICS map of the molecule, the following points are then apparent:

(i) The two ^{13}C groups (7a and 7b) can be distinguished in the solid state ($\delta(^{13}C)$ = 53.4 ppm and 51.8 ppm, Figure 3.3 (top) and 3.4 (bottom left)). Furthermore, the two protons of each NCH_2 group are inequivalent. They have different chemical shifts (7a: 4.2 ppm and 6.0 ppm, 7b: 4.9 ppm and 3.2 ppm, Figure 3.4 (bottom left)). Comparing these values to the solution-state value (4.43 ppm) it becomes clear that one proton of the NCH_2 group 7a is shifted to higher frequencies, while one proton of the NCH_2 group 7b is shifted to lower frequencies. The other two NCH_2 protons do not experience a very significant shift. Looking

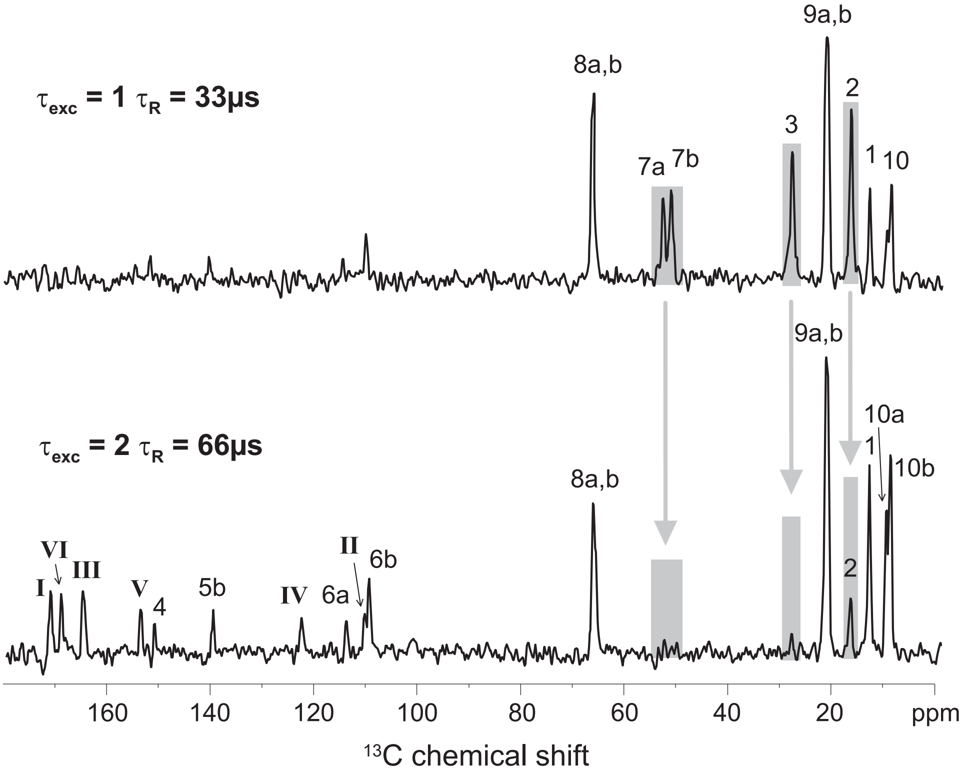

Figure 3.3: *One-dimensional ^1H-^{13}C TEDOR spectra of rhombic crystals obtained under MAS at 30 kHz, with τ_{rcpl} = 1 τ_R (top), τ_{rcpl} = 2 τ_R (bottom). The grey bars indicate a CH_2 signal-loss at τ_{rcpl} = 2 τ_R, which is explained in Section 3.4.1.*

---

[1] Deviations between solid and solution state chemical shift values can of course also be due to intermolecular hydrogen bonds, but in the case of the Yellow Filter Dye molecule no intermolecular hydrogen bonds are present.

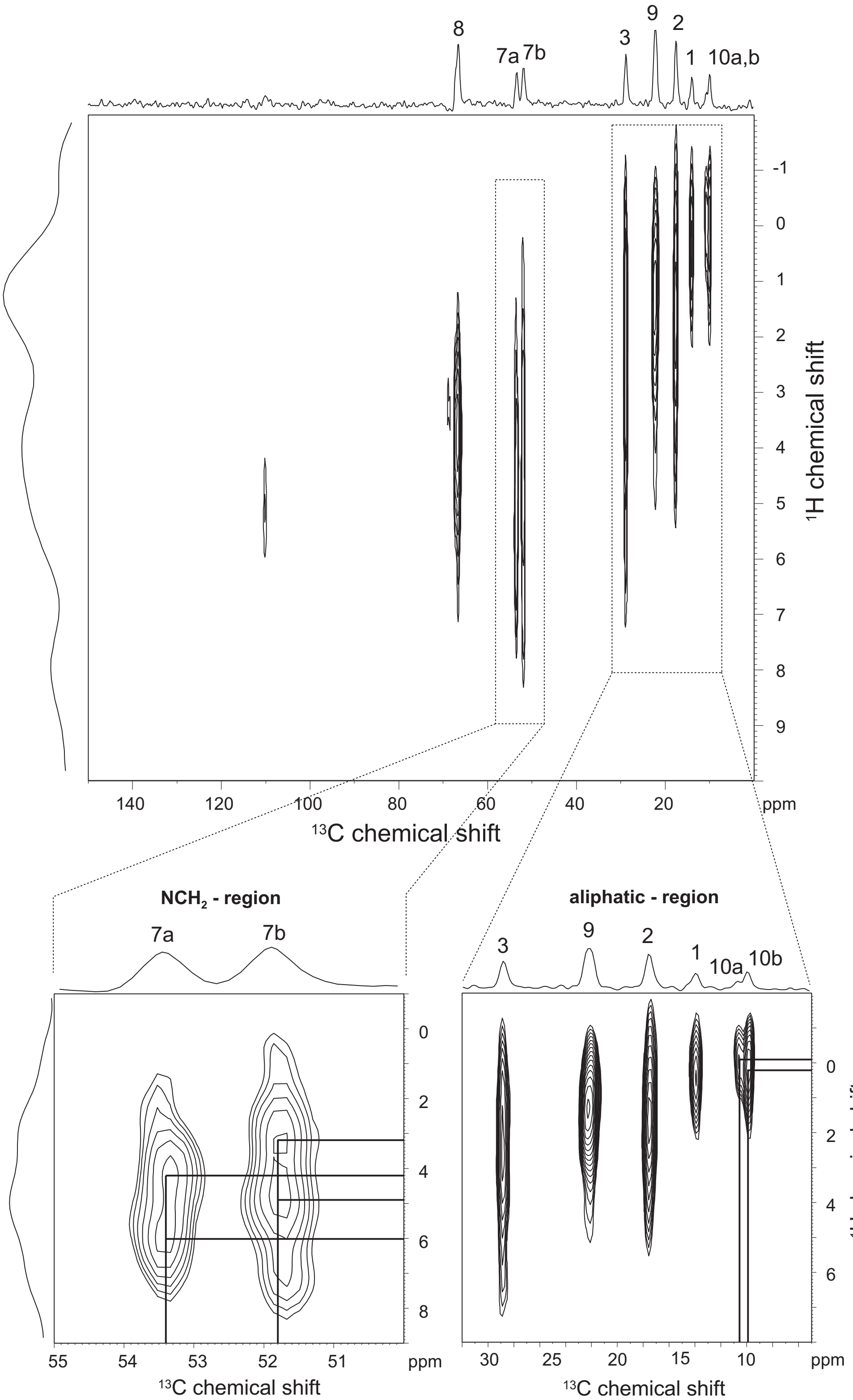

Figure 3.4: *Two-dimensional ^{1}H-^{13}C REPT-HSQC spectrum of rhombic crystals obtained under MAS at 30 kHz and τ_{rcpl} = 1 τ_R (top). The NCH$_2$- and the aliphatic region are enlarged at the bottom.*

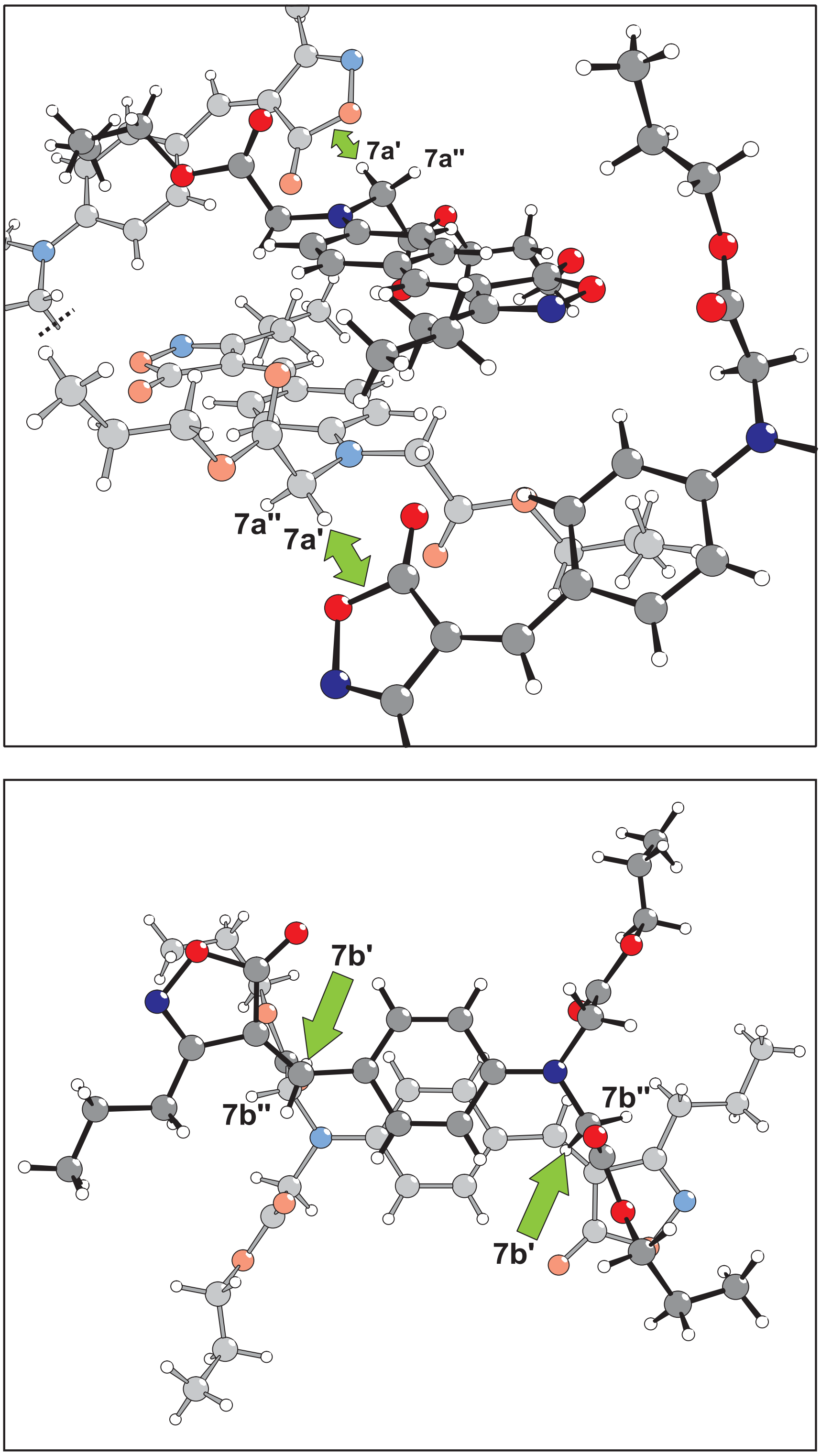

Figure 3.5: *X-ray crystal structure of the rhombic polymorph. Shielding and deshielding effects experienced by the* NCH_2 *groups 7a', 7a" (top) and 7b', 7b" (bottom).*

at the X-ray structure, the two NCH_2 groups clearly have a different chemical environment (Figure 3.5). Proton 7b' (as indicated by the arrow) is located ~3.0 Å underneath a double bond of the π-electron system of the adjacent molecule, while proton 7a' lies at a distance of ~2.7 Å beside the isoxazol-5-on ring. On locating these positions on the chemical shift maps in Figure 3.10, it is apparent that proton 7a' would lie in the dark red (deshielded) region (top picture) while proton 7b' would lie in a light green (shielded) region (bottom picture). Hence, expected effects on their chemical shifts are +1.0 to +1.5 ppm and -1.0 to -1.5 ppm, respectively. This is in good agreement to the experimentally observed chemical shifts (see Figure 3.4 and Table 3.1), where proton 7a' is shifted by ~1.6 ppm to higher frequencies (δ(7a') = 6.0 ppm), while proton 7b' is shifted by ~1.2 ppm to lower frequencies (δ(7b') = 3.2 ppm). The other two protons (7a" and 7b") of the CH_2 group remain basically unaffected, because they are too far away from the adjacent molecule to experience much shielding or deshielding effects from the π-electrons.

(ii) The two CH_3 groups 10a and 10b also have different ^{13}C chemical shifts (10.6 ppm and 9.9 ppm, Figure 3.3 and 3.4 (bottom right)). This is not surprising since the crystal structure shows that the two $-NCH_2COOCH_2CH_2CH_3$ branches of the molecule have a different chemical environment. The corresponding proton resonances are shifted to lower frequencies. This is due to the shielding effects of the π-electron system. The CH_3 protons 10b lie at a distance of ~ 3.5 Å underneath the phenylene ring of an adjacent molecule, while CH_3 10a is located

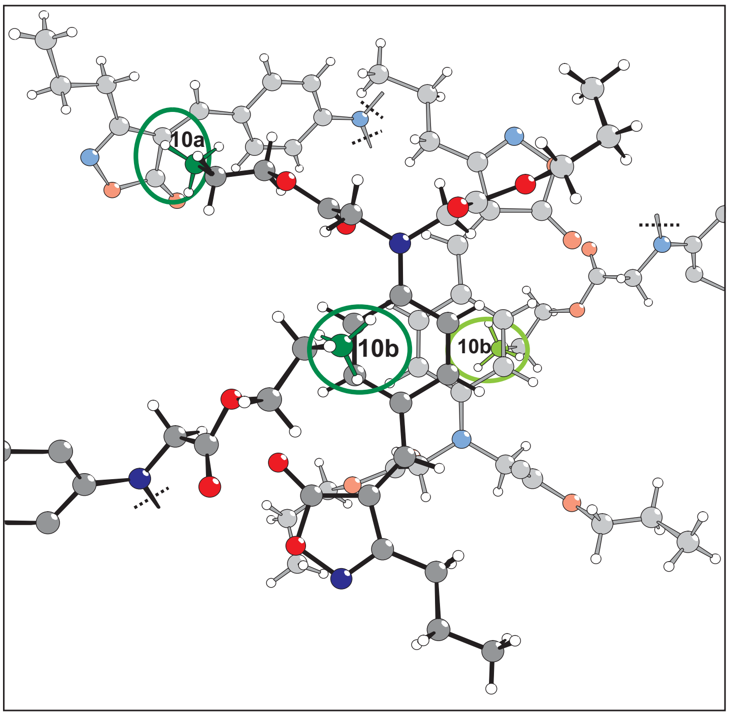

Figure 3.6: *X-ray crystal structure of the rhombic polymorph. Shielding and deshielding effects experienced by the CH_3 groups 10a and 10b.*

$\sim$ 3.5 Å underneath the isoxazol-5-on ring of a different neighboring molecule (Figure 3.6). For the CH_3 groups 10a and 10b shifts to lower frequencies of approximately 1.0 and 0.7 ppm, respectively are observed (Figure 3.4 and Table 3.1), which correspond well to the shifts predicted from the chemical shift maps in Figure 3.10 (bottom).

(iii) The other two CH_2 groups in the branches of the molecule (8a,b and 9a,b) only show one ^{13}C chemical shift each (Figure 3.3 and 3.4), despite the different chemical environment of the two branches mentioned above. Here, the difference in chemical shift for position a and b is not large enough to be resolved in the spectra and, hence, only an average peak is observed for 8a,b and 9a,b at 66.6 ppm and 22.2 ppm, respectively.

(iv) In the solid state the aromatic carbons 5a and 5b have a different chemical environment and hence different ^{13}C chemical shifts (136.1 ppm and 140.1 ppm, Figure 3.3). The same applies to the aromatic carbons 6a and 6b (114.7 ppm and 110.2 ppm, Figure 3.3). The signal for the aromatic protons is very weak in the 2D REPT-HSQC spectrum (Figure 3.4). 2D ramped CP experiments were carried out to assign the aromatic ^{1}H chemical shift values (Figure 3.8). Comparing the aromatic ^{1}H chemical shifts in the solid state to the solution state values, protons 5a and 6a are shifted to higher ppm values by Δ = +0.85 ppm and +0.71 ppm, respectively. Protons 5b and 6b are shifted to lower frequencies, Δ = -1.45 ppm and Δ = -1.49 ppm, respectively. These shifts can easily be explained in terms of ring-current effects and hydrogen bonding. In the solid-state proton 5a undergoes intramolecular hydrogen bonding interactions to the carbonyl group of the isoxazol-5-on ring. This explains its high chemical shift value of 9.3 ppm. Proton 5b is not affected by hydrogen bonding in the solid-state, therefore its chemical shift value is lower (7.0 ppm). In solution the isoxazol-5-on ring rotates with respect to the phenylene ring so that protons 5a and 5b are exposed to an average environment and have the same chemical shift value (8.45 ppm). This effect alone could in principle explain the shift to higher and lower frequencies for the two protons 5a and 5b. Looking however at the other two aromatic protons (6a and 6b), it will become clear, that π-shift effects also play a significant role. It is obvious, that protons 6a and 6b cannot be involved in hydrogen bonding, which is also reflected in their lower solution state value of 6.79 ppm. Nevertheless, in the solid state protons 6a and 6b are shifted to higher and lower frequencies, respectively. The shift to lower frequencies can be explained in terms of ring-current effects of the molecule below. Looking at the X-ray crystal structure in Figure 3.7, it becomes apparent that always two molecules form sandwich-type pairs with their aromatic moieties nearly parallel but shifted vertically with respect to each other. The distance between the molecular planes is $\sim$ 3.5 Å, which is the typical distance between two stacked π-electron systems. Therefore the aromatic proton 6b lies $\sim$ 3.5 Å above the aromatic ring of the adjacent molecule. Figure 3.10 shows the shielding effects and the resultant chemical shifts to lower frequencies induced by the aromatic ring within its molecular plane and $\sim$ 3 Å above its plane. Correspondingly, proton 6b would be shifted by -1.0 to -1.5 ppm, because it is located in the dark green region above the phenylene ring in the bottom picture of Figure 3.10. This is in

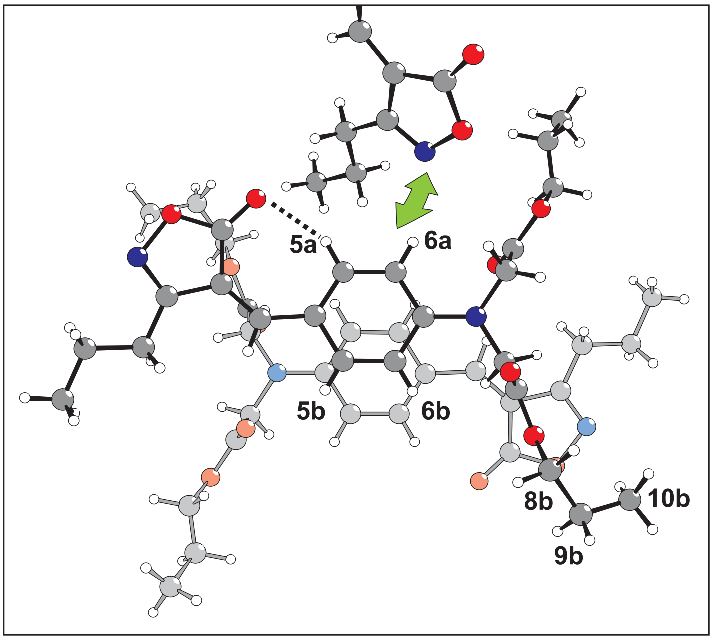

Figure 3.7: *X-ray crystal structure of the rhombic polymorph. "Sandwich"-type pair of molecules with their phenylene rings parallel but shifted "vertically" with respect to each other. The plane of the phenylene rings is parallel to the plane of the page.*

pretty good agreement with the experimentally observed shift of Δ = -1.49 ppm. Similarly, proton 5b should also be affected by the shielding effects of the phenylene ring below. Here the expected shift lies between -0.5 and -1.0 ppm as indicated by the lighter green region in the bottom NICS map in Figure 3.10. This clearly shows that the experimental shift of Δ = -1.49 ppm for proton 5b is not explained in terms of hydrogen bonding alone (mentioned above) but also by the shielding effects of the neighboring phenylene ring. Turning to the aromatic proton 6a and locating its position on the chemical shift map in Figure 3.10 (bottom), it is clearly in the orange region and is therefore not affected by the π-shift effects of the molecule below. Consequently the shift to higher frequencies must be induced by another neighboring molecule. As indicated by the arrow in Figure 3.7, the isoxazol-5-on ring of a neighboring molecule is indeed quite close to the aromatic proton 6a. The lone electron pairs of this isoxazol-5-on ring induce strong deshielding effects of Δ = +0.5 to +1.5 ppm, shown by the large red region in Figure 3.10 (top). Remarkably, these deshielding effects are stronger and of much longer range than the deshielding effects known from ring current effects of aromatic rings. (The latter only occur in a very confined region of about 1 Å around the aromatic ring and are $\leq$ +1.0 ppm, as was explained in Section 2.5). For the isoxazol-5-on ring, Figure 3.10 clearly shows that deshielding effects of Δ = +0.5 to +1.0 ppm are still present at 3 Å above/below the plane of the molecule and that they range over a distance of $>$ 4 Å within the plane. Thus, the shift of proton 6a to higher ppm values (Δ = +0.71 ppm) is easily explained. Proton 5a is a little further away from the isoxazol-5-on ring but might still experience some deshielding effects (compare Figure 3.7). Therefore its shift of Δ = +0.85 ppm is caused by

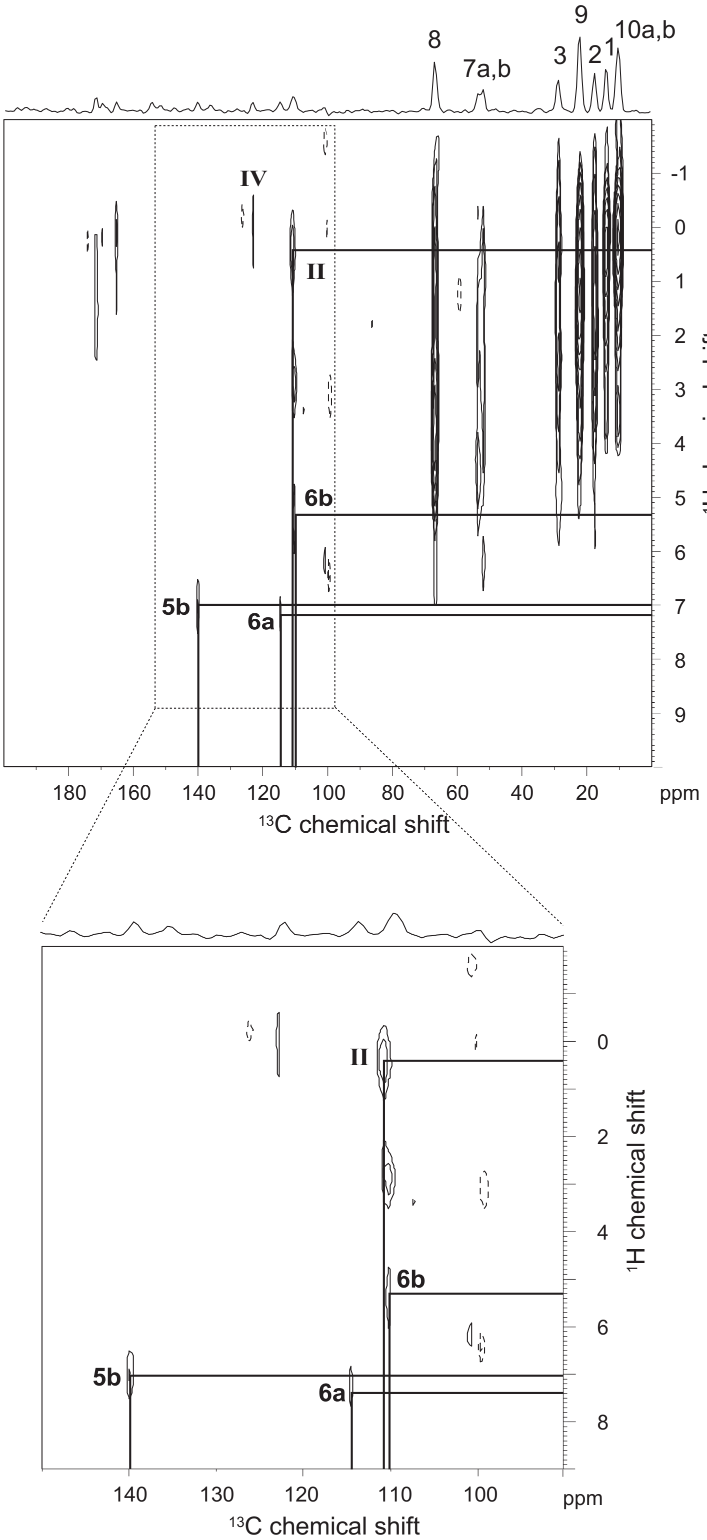

Figure 3.8: *Two-dimensional CP-spectrum of rhombic crystals obtained under MAS at 30 kHz (top), the aromatic region is enlarged at the bottom.*

a combination of intramolecular hydrogen bonding to the carbonyl group and the deshielding effects of the isoxazol-5-on ring of a neighboring molecule.

(v) The 2D ^{1}H DQ MAS spectrum in Figure 3.9 shows through space proton-proton proximities. Considering first the high-field region, the observed peaks can be explained by the alkyl groups 10, 9 and 8, which can be assigned to the SQ peaks at 0.2 ppm, 1.4 ppm and 3.9 ppm, respectively. (The alkyl groups 1 and 2 will, of course, also contribute to the observed signals.) A cross peak is observed between the CH_3 group (10) and the neighboring CH_2 group (9) as expected. The cross peak between the CH_3 group (10) and the CH_2 group (8) is also not surprising, because the two groups are still close enough in space with a distance of approximately 2.5 Å or less, as can be extracted from the crystal structure (Figure 3.7). Two aromatic proton resonances, 5a and 5b, can be clearly observed at 9.3 ppm and 7.0 ppm, respectively, together with two shoulders at about 7.5 and 5.3 ppm corresponding to the protons 6a and 6b. As expected, crosspeaks between the neighboring aromatic protons 5a and 6a as well as between 5b and 6b are observed. The weak crosspeaks between 6a and 5b as well as

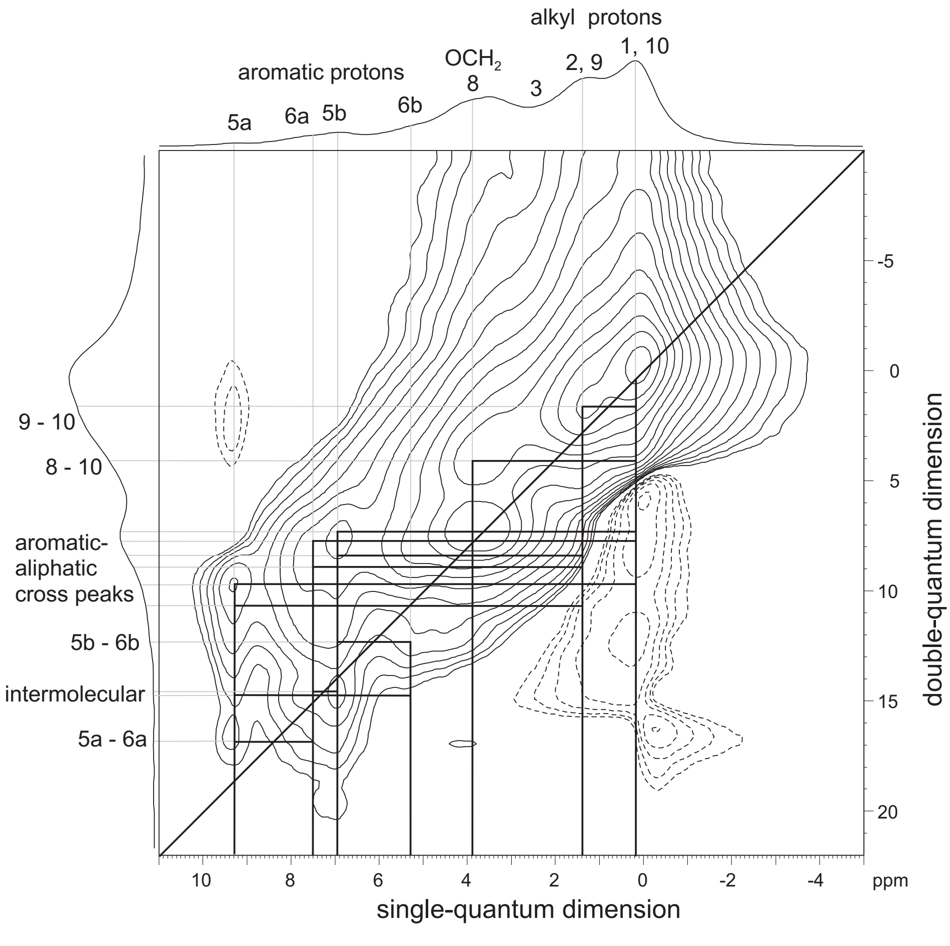

Figure 3.9: *Two-dimensional DQ-spectrum of rhombic crystals obtained under MAS at 30 kHz and* τ_{exc} = *1* τ_R.

6b and 5a must be of intermolecular origin: Looking at the X-ray crystal structure the closest proximity between these protons is ~ 3.8 Å. Usually the ^{1}H-^{1}H dipolar coupling at distances > 3.5 Å is too weak to be detected in a 2D DQ spectrum at one rotor period excitation. The immobility of the Yellow Filter dye molecules in the crystal could, however, explain why dipole-dipole couplings of slightly larger distances can still be observed. Furthermore, there are also crosspeaks observed between the aromatic protons and the aliphatic protons. These are also due to intermolecular proximities. The close packing of the molecules in this case allows distances as low as 2.7 Å between aromatic protons and alkyl chains of neighboring molecules.

Conclusion:

- The two branches of the molecule -$NCH_2COOCH_2CH_2CH_3$ do not have the same chemical environment. This becomes apparent in solid-state NMR when looking at the different ^{13}C chemical shifts of the two NCH_2 or the two CH_3 groups.
- The high and low frequency shifts observed for the phenylene protons can be explained in terms of intramolecular hydrogen bonding as well as shielding and deshielding effects induced by the π-electrons of adjacent molecules.
- Intermolecular spatial proximities of 2.5–3.5 Å between the π-electrons of the chromophore system and the NCH_2 and CH_3 moieties cause shielding and deshielding effects. These correspond well to the chemical shifts obtained from the nucleus independent chemical shift (NICS) map. Proximities between aromatic and aliphatic moieties, in general, are also evident from the 2D ^{1}H DQ experiment.
- The molecule is essentially rigid on the NMR time scale, so that the two protons of the NCH_2 groups do not show one average proton resonance (as in solution), but two distinct proton resonances. (A more detailed investigation of the dynamic properties can be found in Section 3.4.1.)
- The agreement of the NMR-results with the X-ray crystal structure and the NICS map is very good. Thus, the observed ^{1}H chemical shift effects can be directly related to certain structural features and packing phenomena of the molecules.

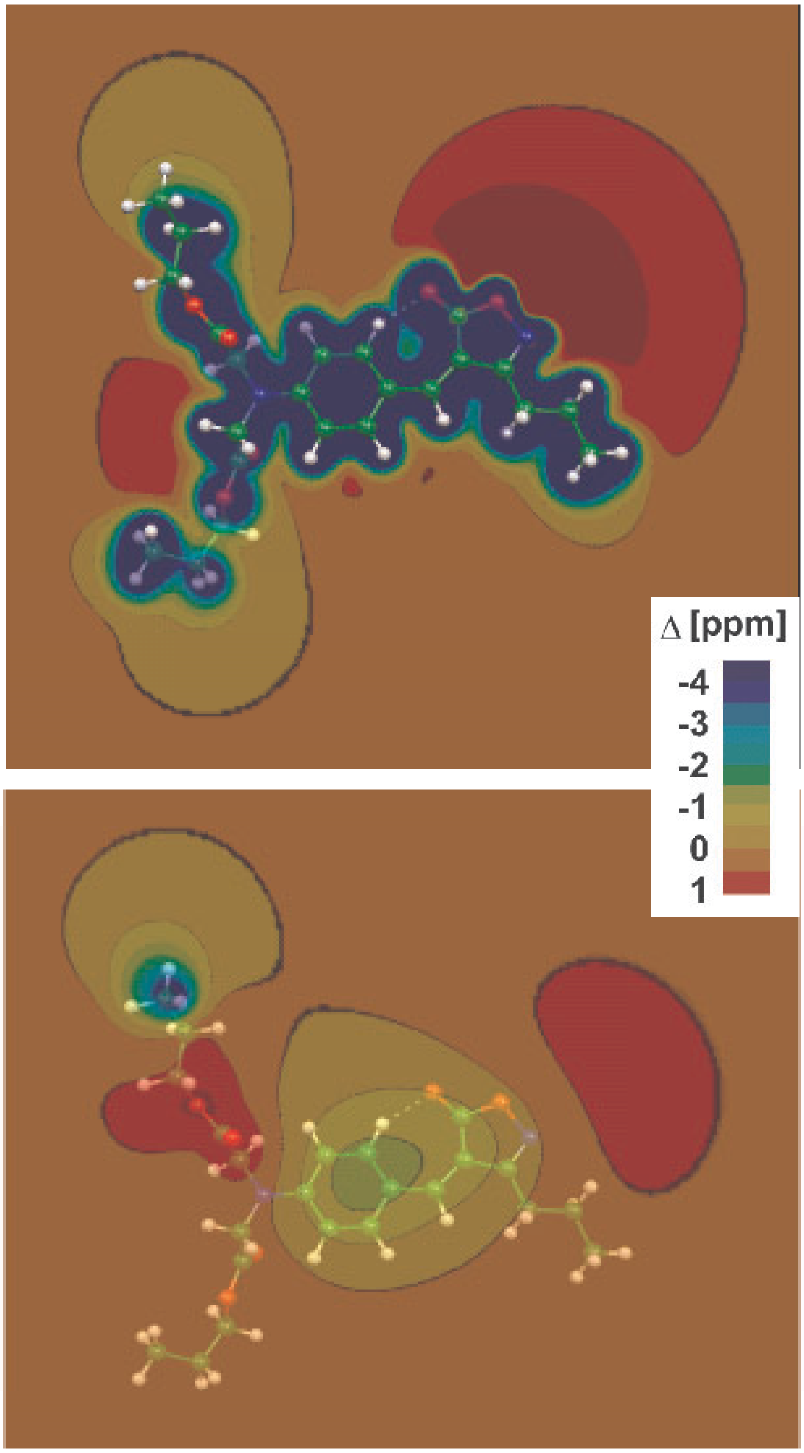

Figure 3.10: *Nucleus independent chemical shift (NICS) map of the Yellow Filter Dye molecule [Sebastiani 03] calculated using density functional theory with BLYP exchange correlation functional [Becke 88, Lee 88] and the CPMD code [CPMD]. The color code reflects the chemical-shift changes a nucleus would experience when placed at the respective position within the chromophore plane (top) and ∼ 3 Å above or below the plane of the molecule (bottom).*

3.3 Needle polymorph: Structural investigation

The crystal structure of the needles could not be easily derived from X-ray diffraction. The needles turn out to be a little too thin for a detailed analysis. Nevertheless the dimension and the angles of the unit cell could be determined. In combination with molecular modeling the crystal structure could eventually be solved, at least for the chromophore part of the molecule [Deroover]. For the alkyl branches, there is still some uncertainty. A comparison with the NMR-results is made below, as well as a comparison of the NMR results of needle and rhombic crystals.

For the two samples, a significant difference in the NMR signal-to-noise ratio obtainable for ^{13}C is observed. Compared to the rhombic crystal, the 1D ^{1}H-^{13}C TEDOR spectra of the needles show very strong aromatic signals for an excitation time of one rotor period (τ_{exc} = 1 τ_R = 33.3 μs), see Figure 3.3 and 3.11. The gain in aromatic signal intensity is related to the fact that the T_1 relaxation time of the aromatic protons is significantly shorter in the needles (T_1 = 1.9 s) than in the rhombic crystal (T_1 = 4.3 s) (see Appendix B). For a shorter proton T_1, more ^{1}H magnetization can be transferred to ^{13}C in each transient of the experiment. Commonly, shorter T_1 values result from a lower degree of order and a higher degree of segmental or local mobility. The dynamical properties of the needles are discussed in more detail in Section 3.4.2.

A comparison of ^{1}H and ^{13}C solid-state chemical shifts of the needles with the rhombic crystal as well as with the corresponding solution state values (in brackets) is given in Table 3.2 (see also spectra, Figure 3.11 and 3.12). Most of the ^{13}C and ^{1}H chemical shifts of the two samples are comparable. However the following important differences between the two samples are apparent:

(i) In the needle morphology the two CH_3 groups 10a and 10b have the same ^{1}H chemical shift (0.8 ppm, Figure 3.12 (bottom right)), which is not shifted to lower frequencies, as in the rhombic crystals (0.0, 0.2 ppm), but close to the solution state value (0.88 ppm). Hence, there is no influence of π-shift effects on these CH_3 groups in the needles. This can be easily understood when looking at the crystal structure in Figure 3.13, where no spacial proximity between the alkyl branches of one molecule and the chromophore moiety of another molecule is observed. This stands in clear contrast to the rhombic crystal structure.

(ii) There is also no difference observed in the ^{13}C chemical shifts of the two CH_3 groups 10a and 10b (11.0 ppm, Figure 3.11 and 3.12). Hence the two -$NCH_2COOCH_2CH_2CH_3$ branches of the molecule have a more similar environment in the needle crystals than in the rhombic one. This is also apparent when looking at the other resonances of the branch: For the CH_2 group 8a,b (65.4 ppm) a narrower peak is observed for the needles than for the rhombic crystal (Figure 3.3 and 3.11). Looking at the NCH_2 groups 7a and 7b (Figure 3.11 and 3.12), the two peaks are less well separated (needles: $\Delta\ \delta^{13}$C(7a-7b) = 1.0 ppm vs. rhombic:

Table 3.2: Solid-state ^{1}H and ^{13}C chemical shifts of rhombic and needle-shape crystals from ^{1}H-^{13}C REPT-HSQC correlation spectra and CP experiments. Solution-state NMR data in brackets.

	rhombic	**needle**		**rhombic**	**needle**	
	δ^{13}C [ppm] solid-state	δ^{13}C [ppm] solid-state	δ^{13}C [ppm] solution	δ^1H [ppm] solid-state	δ^1H [ppm] solid-state	δ^1H [ppm] solution
1 (CH_2)	14.0	14.5	(13.8)	0.5	0.7	(0.98)
2 (CH_2)	17.6	21.0	(19.7)	1.7	1.6	(1.65)
3 (CH_2)	28.8	27.6	(27.2)	2.7	2.1	(2.63)
4 (CH)	151.5	149.3	(150.5)	*	6.7	(7.71)
5a (arom CH)	136.1	135.0	(137.2)	~ 9.3	9.3	(8.45)
5b (arom CH)	140.1	140.0		7.0	7.2	
6a (arom CH)	114.7	115.1	(112.3)	~ 7.5	7.1	(6.79)
6b (arom CH)	110.2	111.8		5.3	6.4	
7a (NCH_2)	53.4	54.1	(52.6)	4.2, 6.0	4.5	(4.43)
7b (NCH_2)	51.8	53.1		4.9, 3.2	3.7	
8a,b (OCH_2)	66.6	65.4	(66.4)	3.9	3.9	(4.05)
9a,b (CH_2)	22.2	22.5	(21.6)	1.4	1.2	(1.59)
10a (CH_3)	10.6	11.0	(10.3)	-0.1	0.8	(0.88)
10b (CH_3)	9.9			0.2		
quaternary carbons						
I	171.6	171.6	(170.0)	-	-	-
II	111.1	111.8	(111.9)	-	-	-
III	165.5	165.3	(164.9)	-	-	-
IV	123.2	124.2	(122.6)	-	-	-
V	154.3	152.5	(153.2)	-	-	-
VI	169.5	169.1	(169.5)	-	-	-

* signal intensity too weak

Δ δ^{13}C(7a-7b) = 1.6 ppm). Comparing these observations to the X-ray crystal structure in Figure 3.13, it is evident that the chemical environment for the two -$NCH_2COOCH_2CH_2CH_3$ branches is indeed very similar in the needle morphology. The molecules stack on top of each other in such a way, that the following molecule is only flipped “horizontally”, so that the alkyl branches lie on top of each other in the stack and only the carbonyl group of the isoxazol-5-on ring points in the opposite direction for each molecule. Remembering the rhombic crystal (Figure 3.7), always two molecules “sandwich” together, where one molecule is not only flipped “horizontally” but also “vertically” with respect to the other, so that some kind of centrosymmetry results for the "sandwich" and the two -$NCH_2COOCH_2CH_2CH_3$ branches experience a more different chemical environment.

(iii) The two NCH_2 groups have different proton chemical shift, but in contrast to the rhombic polymorph the two protons of each NCH_2 group are equivalent in the needles (Figure 3.12 bottom left). For NCH_2 7b both protons are shifted by ~0.7 ppm to lower frequencies (3.7 ppm), while for 7a they remain almost unshifted (4.5 ppm), (see Table 3.2). Again, this indicates a more similar environment for the two alkyl branches and less influence of the π-electron systems of the neighboring molecules. Looking at the X-ray crystal structure in Figure 3.14 (top), the NCH_2 group 7b is located approximately 3.0 Å above the aromatic ring of the adjacent molecule. Locating this position on the chemical shift map in Figure 3.10 (bottom), a shift of approximately -1.0 ppm would be expected, which corresponds quite well to the experimental value of -0.7 ppm. For the protons of the NCH_2 group 7a, no shielding or deshielding effects are expected, because they are located in the orange region of the chemical shift map (Figure 3.10 (bottom)). The equivalence in proton chemical shift of the two protons of each NCH_2 group could, in principle, also be enhanced by a greater mobility of the NCH_2 groups in the needles. A local motion can lead to some degree of averaging of the different environments. This is, however, not the case here, as will be explained in Section 3.4.

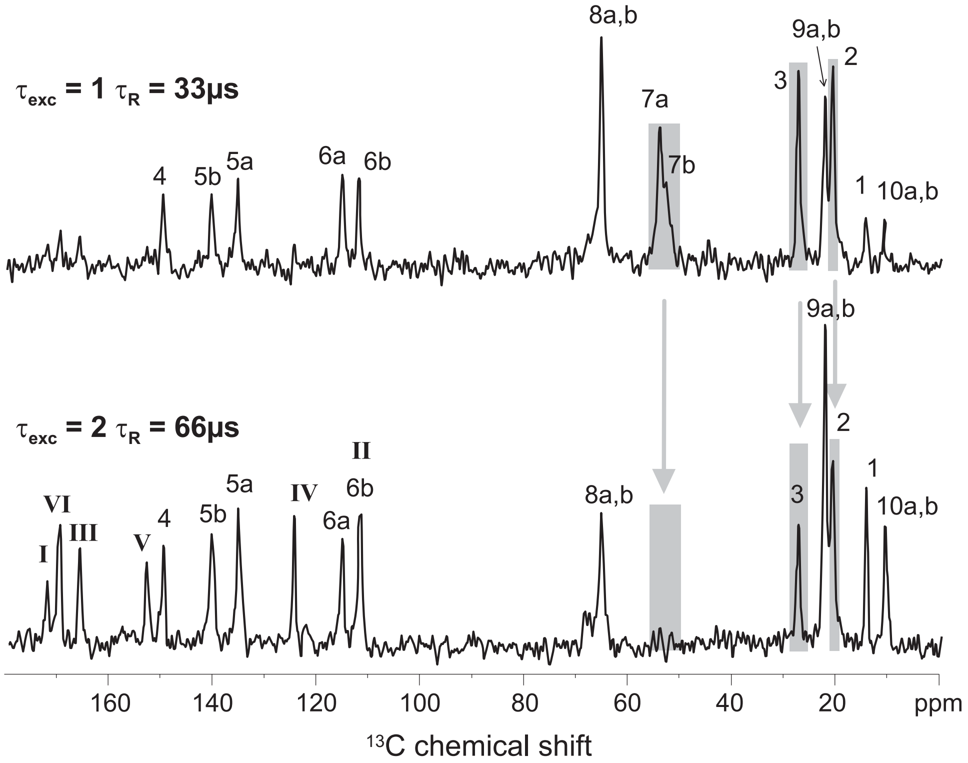

Figure 3.11: *One-dimensional ^{1}H-^{13}C TEDOR spectra of the needles obtained under MAS at 30 kHz, with τ_{rcpl} = 1 τ_R and τ_{rcpl} = 2 τ_R. The grey bars facilitate a comparison of selected CH_2 signal intensities at 1 and 2 τ_R recoupling, which is explained in Section 3.4.2.*

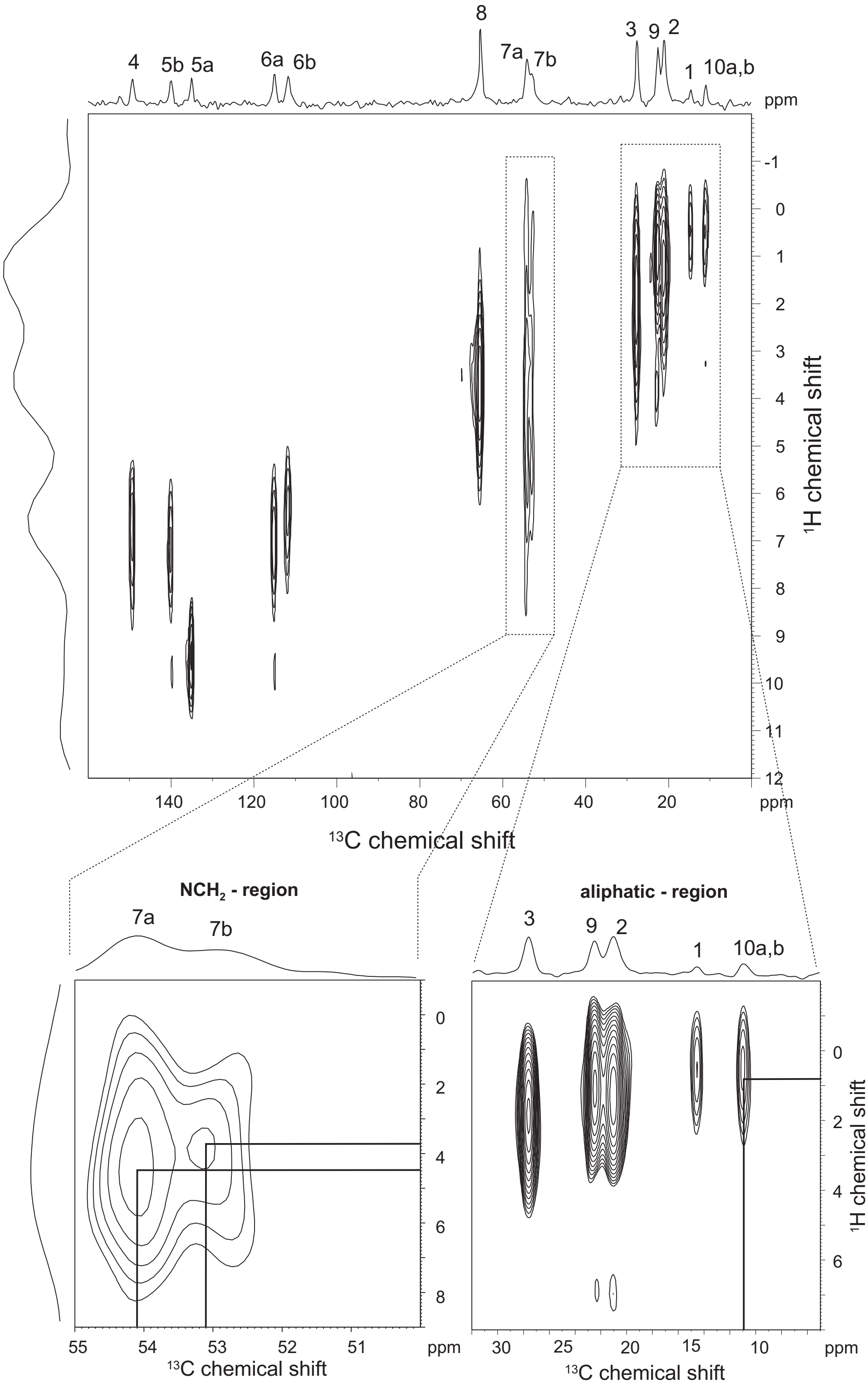

Figure 3.12: *Two-dimensional ^{1}H-^{13}C REPT-HSQC spectrum of the needles obtained at 30 kHz MAS and τ_{rcpl} = 1 τ_R (top). The NCH$_2$- and the aliphatic region are enlarged at the bottom.*

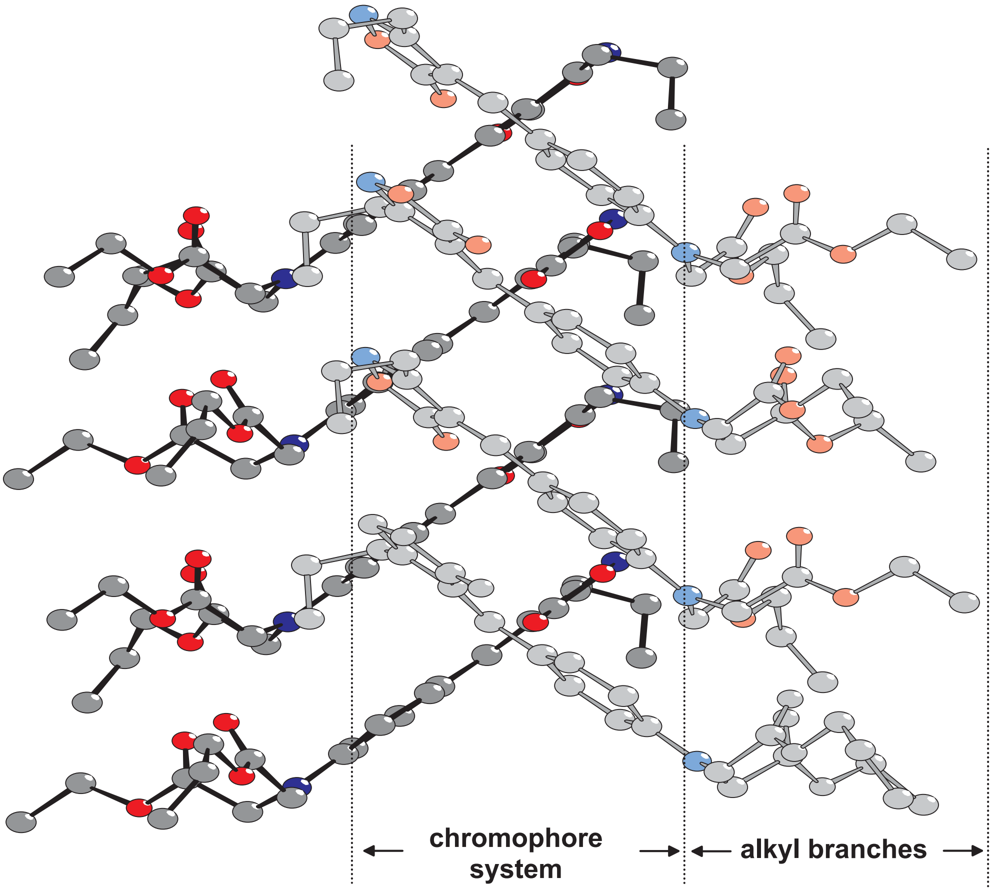

Figure 3.13: *X-ray crystal structure of the needle polymorph. The Yellow Filter Dye molecules build stacks, where one stack is tilted* $\sim$ *90° with respect to the next.*

(iv) The aromatic ^{1}H and ^{13}C resonances of the two crystal structures are somewhat similar, but not the same (see Table 3.3 and 3.2). It is possible to estimate the π-shift effects for the phenylene protons in both crystal structures ((a) rhombic and (b) needle) with the chemical shift maps depicted in Figure 3.10. These estimated chemical shift differences are in surprisingly good agreement with the experimentally observed values. In this way, the small differences in proton chemical shift can be explained rather well by the different crystal structure.

(a) As mentioned above in Section 3.2, the phenylene protons are shifted in the solid-state because of hydrogen bonding as well as shielding and deshielding effects of π-electrons of neighboring molecules. While protons 5b and 6b experience shielding effects from the aromatic ring below and are shifted to lower frequencies, protons 5a and 6a are under the influence of deshielding effects from the neighboring isoxazol-5-on ring and are therefore shifted to higher frequencies. In addition proton 5a also undergoes hydrogen-bonding to the carbonyl group in the solid-state, while proton 5b cannot experience any hydrogen-bonding effects any more (as suppose to solution). This effect also contributes to their respective high and low frequency shifts.

Table 3.3: Comparison of aromatic ^{1}H chemical shifts in solution and the solid-state and the resultant chemical shift differences (Δ) for the rhombic crystal and the needles.

(a) rhombic

δ^1H (solid-state)	5a: $\sim$9.3 ppm	6a: $\sim$ 7.5 ppm
	Δ(5a-5) $\approx$ +0.85 ppm	Δ(6a-6) $\approx$ +0.71 ppm
δ^1H (solution)	5: 8.45 ppm	6: 6.79 ppm
	Δ(5b-5) = -1.45 ppm	Δ(6b-6) = -1.49 ppm
δ^1H (solid-state)	5b: 7.0 ppm	6b: 5.3 ppm

(b) needle

δ^1H (solid-state)	5a: 9.3 ppm	6a: 7.1 ppm
	Δ(5a-5) = +0.85 ppm	Δ(6a-6) = +0.31 ppm
δ^1H (solution)	5: 8.45 ppm	6: 6.79 ppm
	Δ(5b-5) = -1.25 ppm	Δ(6b-6) = -0.39 ppm
δ^1H (solid-state)	5b: 7.2 ppm	6b: 6.4 ppm

(b) In the case of the needles, protons 5b and 6b are also shifted to lower, and 5a and 6a to higher, frequencies (Figure 3.12, Table 3.3 and 3.2). The hydrogen-bonding is expected to contribute to the high and low frequency shifts of 5a and 5b to the same extent than in the rhombic crystal, because in both polymorphs the chromophore is fully immobile. Hence, the shift differences between rhombic and needle shape crystals must be induced by a different packing. Looking at the X-ray crystal structure of the needles in Figure 3.13 we observe stacks of molecules as suppose to the "sandwiches" observed for the rhombic crystal. The molecules in the stacks are at a distance of $\sim$ 3.3 Å. Figure 3.14 (top) shows three adjacent molecules in such a stack. It is apparent that the phenylene rings are twisted and shifted "horizontally" as well as "vertically" with respect to each other (in the plane of the paper). Therefore the phenylene protons in the needles must experience π-shift effects somewhat different from the rhombic form. Taking into account the ring-current effects of the molecule above and the one below and locating the respective positions of the phenylene protons on the chemical shift map in Figure 3.10 (bottom) a shift to lower frequencies of $\Delta \approx$ -0.5 is expected for protons 5b and 6b. For proton 6b this agrees rather well with the experimentally observed value of Δ = -0.39 ppm, for 5b with Δ = -1.25 ppm the "loss" of hydrogen-bonding effect accounts for the "remaining" low-frequency shift difference. Protons 5a and 6a remain unaffected by the π-shifts of the molecules above and below, but both experience deshielding effects of about Δ = +0.5 ppm induced by the isoxazol-5-on rings in the neighboring stack (depicted in Figure 3.14 (bottom)). Proton 5a in addition undergoes hydrogen-bonding, which explains its larger chemical shift difference (already mentioned above).

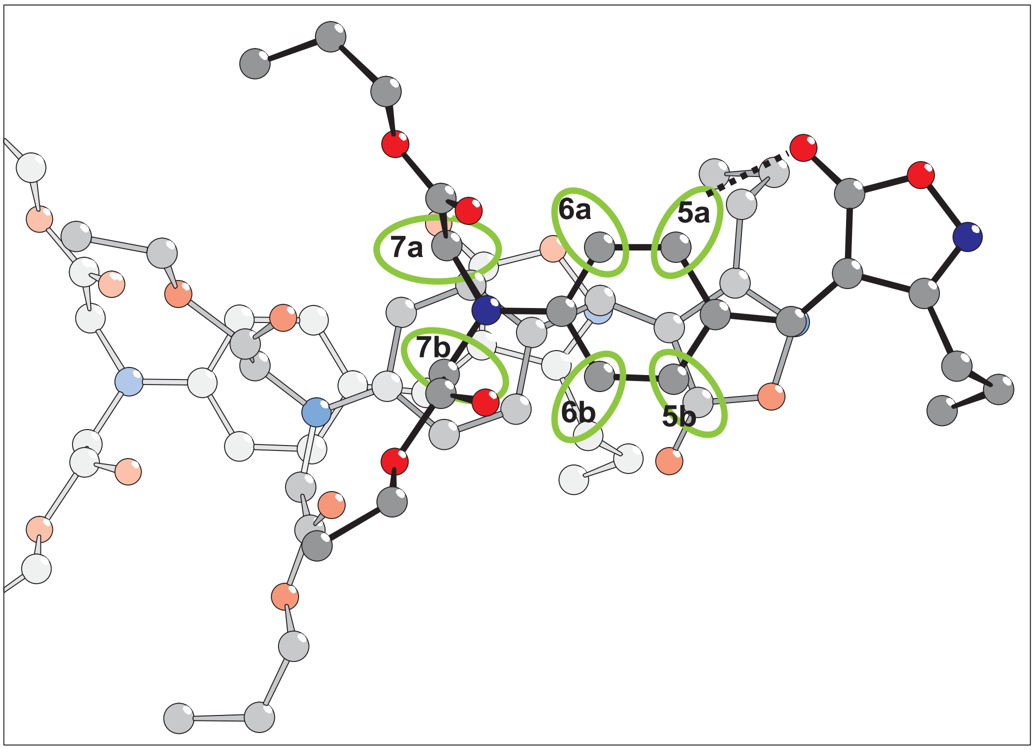

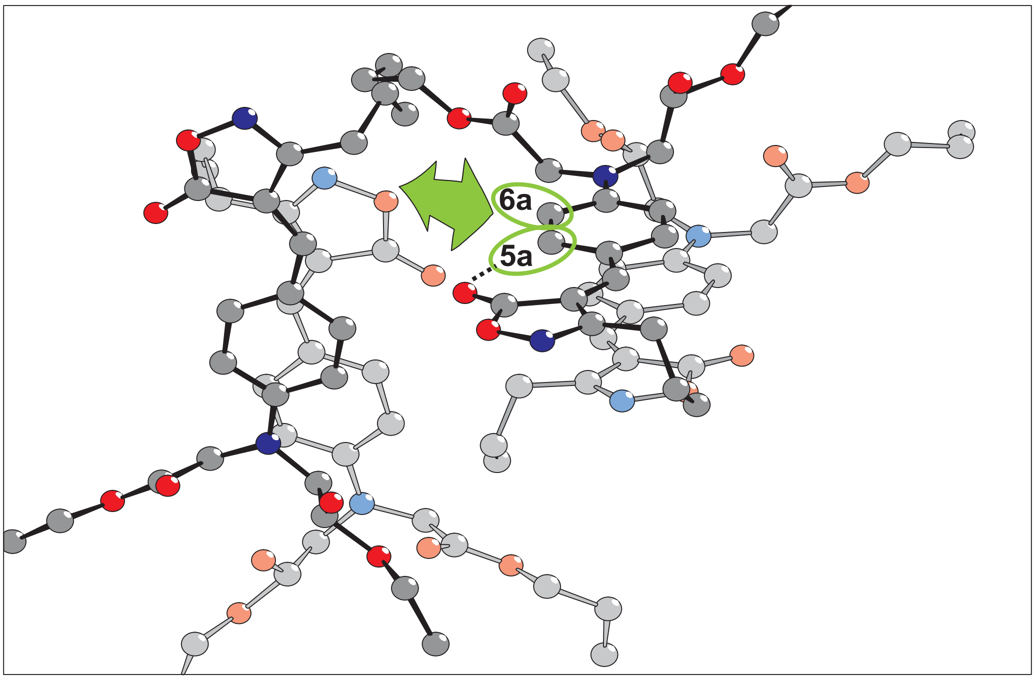

Figure 3.14: *X-ray crystal structure of the needle polymorph. Three adjacent molecules in a stack (top). Two neighboring stacks, each with only two molecules depicted.*

Conclusion:

- The two -$NCH_2COOCH_2CH_2CH_3$ branches of the molecule have a more similar chemical environment in the needles than in the rhombic crystal. This becomes apparent when looking at the ^{13}C chemical shifts of the CH_3 and the CH_2 groups of the two branches and is confirmed by the different crystal structures.
- Due to the different packing of the molecules, less shielding and deshielding effects are observed for the NCH_2 groups in the needles and no such effects for the protons of the CH_3 groups. Moreover the protons of each NCH_2 group are equivalent. This is solely an effect of the different packing in the needles, as confirmed by the ^{1}H chemical shifts taken from the nucleus independent chemical shift (NICS) map of the molecule, and is not influenced by potential local dynamics.
- The differences in ^{1}H chemical shifts for the phenylene protons in the needle polymorph as compared to the rhombic polymorph, can be explained by the different packing of the molecules in the two polymorphs.
- The agreement of the NMR-results with the crystal structure and the nucleus independent chemical shift map of the molecule is very good. It shows that the different packing of the molecules in the two morphologies is reflected in characteristic changes of ^{1}H and/or ^{13}C chemical shifts.

3.4 Molecular Dynamics of Yellow Filter Dye Polymorphs

With solid-state NMR it is possible to obtain also dynamical information in addition to structural information. Motions of molecular building blocks, such as CH, CH_2 or CH_3 groups, on a time scale faster than $\sim 10^{-6}$ s can easily be detected via dipole-dipole couplings. Qualitative information about the mobility of CH_2 groups is directly obtainable from one-dimensional ^{1}H-^{13}C TEDOR spectra recorded with a recoupling time of $\tau_{rcpl} \geq 2\ \tau_R$ for MAS frequencies of 25–30 kHz [Fischbach 02]. Under these conditions the ^{13}C signal of rigid CH_2 groups disappears. Dynamic processes, however, lead to the re-appearance of the respective ^{13}C resonance, as was explained in Chapter 2, Section 2.3.3. To extend this qualitative to a quantitative investigation, the local dynamics of different CH_n-groups in a molecule can be determined by measuring C-H dipole-dipole couplings using spinning sideband patterns arising from rotor-encoding of the recoupled dipolar Hamiltonian. Looking for immobile segments, such as CH, CH_2 or CH_3 or an aromatic ring with known C-H bondlengths, the dipole-dipole couplings can easily be calculated. Using a C-H bondlength of 113 pm a coupling of $D_{CH}/\ 2\pi$ = 21.0 kHz results [Saalwächter 00]. Under the influence of motion this coupling is reduced. Conversely, from the reduction factor of the residual dipole-dipole coupling the degree of molecular mobility can be determined. Defining a dynamical order parameter S_{het}, the measured (reduced) heteronuclear ^{1}H-^{13}C dipolar coupling of an individual segment can be related to the calculated one for the immobile case. Hence, an experimentally determined coupling of $D_{CH}/\ 2\pi$ = 21.0 kHz results in an order parameter of S_{het} = 100%.

3.4.1 Local Dynamics of Rhombic Polymorph

Qualitative investigation of local molecular dynamics. Looking at Figure 3.3 no signal intensity is observed for $\tau_{exc} = 2\ \tau_R$ at $\delta(^{13}C)$ = 28.8 ppm, which corresponds to the CH_2 group 3, while for CH_2 group 2 at 17.6 ppm some signal is present. Since for ^{1}H-^{13}C TEDOR spectra with $\tau_{exc} = 2\ \tau_R$ and $\tau_R \leq 25$ kHz virtually no signal is observed for rigid CH_2 groups (see above), the CH_2 group 3 must be rigid, while CH_2 2 displays some mobility. Hence, the propyl chain at the isoxazol-5-on ring is almost but not fully immobile. This is not too surprising, because the sample is of course crystalline, which implies a rigidness of the molecules, but some motion of alkyl chain ends can still be present. This effect is also observed for the -$NCH_2COOCH_2CH_2CH_3$ branches of the molecule. The signal intensity at $\tau_{exc} = 2\ \tau_R$ has disappeared for the NCH_2 groups (7a,b) at $\delta(^{13}C)$ = 53.4–51.8 ppm, while the signals at $\delta(^{13}C)$ = 66.6 ppm and 22.2 ppm, corresponding to 8a,b and 9a,b, respectively, have not disappeared (Figure 3.3). Hence, the molecule must allow for some motion in the propyl-ends of the two -$NCH_2COOCH_2CH_2CH_3$ branches, while the NCH_2 groups are rather immobile, as are the aromatic ring and the isoxazol-5-on ring. The latter must be very rigid to allow for the delocalization of the π-electrons, to successfully build the chromophore system. A quantitative investigation of the mobility of the different CH_2 groups is made below with REREDOR spinning sideband patterns [Saalwächter 02b]. The dynamic properties of the aromatic protons are investigated also with REPT-HDOR spinning sideband patterns [Saalwächter 01a].

Quantitative investigation of the CH_2 group dynamics. For a quantitative analysis of the dynamical properties of the molecule spinning sideband patterns are used. For CH_2 groups REREDOR sidebands are most suitable. Looking at the -$NCH_2COOCH_2CH_2CH_3$ branches we can investigate the mobilities of the NCH_2 (7a,b), the OCH_2 (8a,b) and $OCH_2\mathit{CH_2}$ (9a,b) groups (see Figure 3.15). The best fit for the REREDOR sideband pattern of the NCH_2 group (7a,b) gives a residual dipole-dipole coupling of $D_{CH}/\ 2\pi$ = 19.0 kHz, which corresponds to an order parameter of S_{het} = 90%. Hence, the NCH_2 groups must be almost rigid, as already mentioned above. Looking at the OCH_2 groups (8a,b) we observe a residual dipole-dipole coupling of $D_{CH}/\ 2\pi$ = 17.5 kHz with an order parameter of S_{het} = 83% and for the CH_2 group 9a,b $D_{CH}/\ 2\pi$ = 11.5 kHz with an order parameter of S_{het} = 55%. Clearly, the -$NCH_2COOCH_2CH_2CH_3$ branches of the Yellow Filter Dye molecule display some mobility towards their chain-ends. This explains why the two CH_2 groups 8a,b and 9a,b each only show one ^{13}C chemical shift (Figure 3.3), despite the different chemical environment of the two branches. The mobility of 8a,b and 9a,b is with $D_{CH}/\ 2\pi$ = 17.5 kHz and $D_{CH}/\ 2\pi$ = 11.5

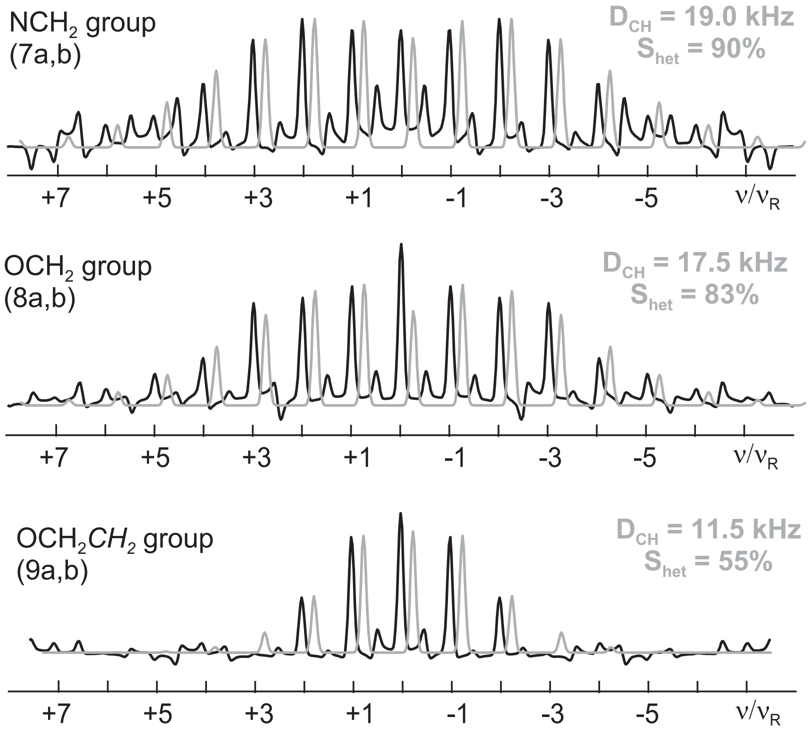

Figure 3.15: *REREDOR spinning sideband patterns of the rhombic polymorph. Residual dipole-dipole couplings of the NCH_2 (top) and the OCH_2 groups (middle) at a MAS frequency of 25 kHz and of the $OCH_2\boldsymbol{CH_2}$ groups at a MAS frequency of 30 kHz (bottom), all recorded with τ_{rcpl} = 2 τ_R (black line = experimental, grey line = calculated).*

kHz, respectively, large enough to reduce the difference in chemical shift for position a and b so that it cannot be resolved any more in the spectra and only one averaged peak is observed for each CH_2 group (mentioned above in Section 3.2). Now the question arises, why different ^{13}C chemical shifts are observed for the CH_3 group 10a and 10b, although they must be even more mobile than the CH_2 group 9a,b. If the alkyl groups were immobile, the difference in chemical shift observed for CH_3 10a and 10b would be a lot larger than for 9a and b or 8a and b, because the different chemical environment for the two branches is a lot more pronounced for the CH_3 groups (10a and b) than for the CH_2 groups (9a,b and 8a,b). Therefore a motion of the CH_3 groups does not fully average the chemical shifts for position a and b, but only reduces their chemical shift difference.

Looking at the propyl chain attached to the isoxazol-5-on ring, the -$CH_2\mathrm{CH_2CH_3}$ group 3 is with $\mathrm{D}_{CH}/\ 2\pi$ = 19.0 (S_{het} = 90%) almost rigid (similar to the $\mathrm{NCH_2}$ groups), while the -$\mathrm{CH_2}CH_2\mathrm{CH_3}$ group 2 does display some mobility ($\mathrm{D}_{CH}/\ 2\pi$ = 15.0 kHz, S_{het} = 71%), see Figure 3.16. Therefore also the propyl chain, similar to the -$\mathrm{NCH_2COOCH_2CH_2CH_3}$ branches, is not stiff on the NMR time scale.

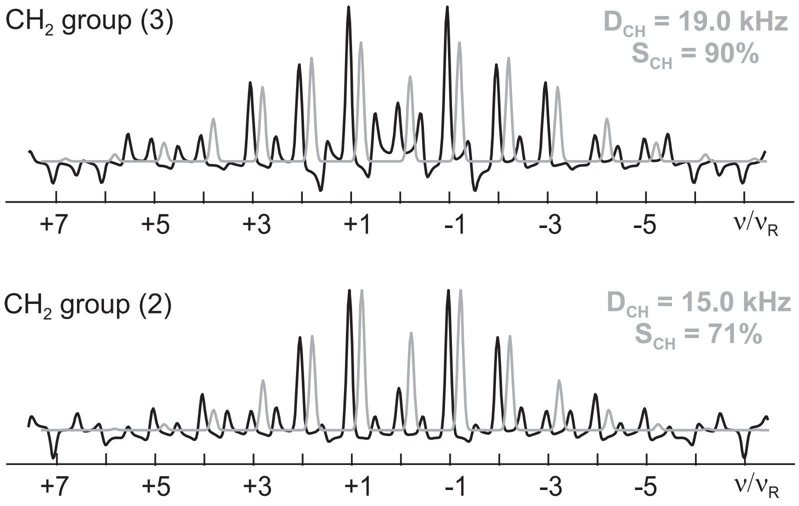

Figure 3.16: *REREDOR spinning sideband patterns of the rhombic polymorph. Residual dipole-dipole couplings of the propyl chain at the isoxazol-5-on ring:* -$\boldsymbol{CH_2}CH_2CH_3$ *group (3) (top) and* $CH_2\boldsymbol{CH_2}CH_3$ *group (2) (bottom), recorded under MAS at 30 kHz and* τ_{rcpl} = 2 τ_R *(black line = experimental, grey line = calculated).*

Quantitative investigation of the phenylene ring dynamics. The aromatic ring and the isoxazol-5-on ring are expected to be rigid to allow for the delocalization of the π-electrons. Looking for example at the REPT-HDOR spinning sideband pattern of the aromatic proton 6b, we observe a residual dipole-dipole coupling of $\mathrm{D}_{CH}/\ 2\pi$ = 21.4 kHz (Figure 3.17). This corresponds to an order parameter of S_{het} = 102% (using again a C-H bond length of 113 ppm, which leads to a dipole-dipole coupling of $\mathrm{D}_{CH}/\ 2\pi$ = 21.0 kHz for a perfectly immobile aromatic C-H group). It becomes clear, that the aromatic moiety of the molecule is indeed completely stiff, while the alkyl chains display some mobility towards their ends.

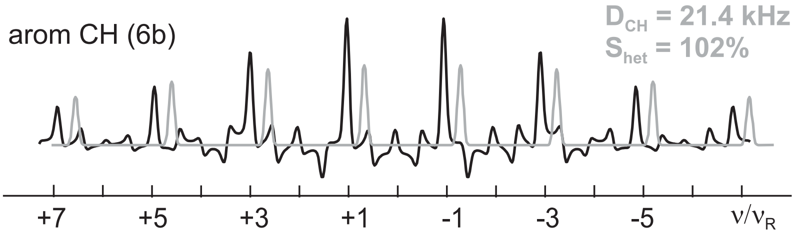

Figure 3.17: *REPT-HDOR spinning sideband pattern of the rhombic polymorph. Residual dipole-dipole couplings of the aromatic CH group (6b) recorded under MAS at 30 kHz and* τ_{rcpl} = 4 τ_R, *(black line = experimental, grey line = calculated).*

3.4.2 Local Dynamics of Needle polymorph

Qualitative investigation of local molecular dynamics. Comparing the TEDOR spectra of the two samples at two rotor periods excitation (Figure 3.3 and 3.11), there is significant signal intensity for the CH_2-groups 8 and 9 of the needle polymorph, similar to the rhombic sample. Therefore the propyl-ends of the -$NCH_2COOCH_2CH_2CH_3$ branches of the needle polymorph also display some mobility. A quantitative investigation, comparing the REREDOR spinning sideband patterns of the two samples, will point out some minor differences in the dynamic behavior of these alkyl branches. Looking at the propyl arm of the isoxazol-5-on ring (CH_2 group 2 and 3) there is significant CH_2 signal for the needles, in particular position 3 (Figure 3.11), while for the rhombic sample most signal-intensity is lost (Figure 3.3). This shows that the propyl chain in the needles is more mobile than in the rhombic sample.

Quantitative investigation of the CH_2 group dynamics. For the NCH_2 groups (7a,b) the same residual dipole-dipole coupling ($D_{CH}/2\pi$ = 19.0 kHz, S_{het} = 90%) is observed in the needles (Figure 3.18) than in the rhombic polymorph (Figure 3.15). Remembering that the two protons of the NCH_2 groups have equal proton chemical shifts in the needles, but not in the rhombic crystal (see Section 3.3), it is now clear, that this cannot be an effect of increased molecular motion of the NCH_2 groups, but is rather caused by the more uniform environment of the alkyl branches in the needles. The CH_2 groups 8a,b and 9a,b, on the other hand, are more mobile in the needle morphology. They are with $D_{CH}/2\pi$ = 14.5 kHz and $D_{CH}/2\pi$ = 8.5 kHz, respectively, by a factor of 1.2–1.3 more mobile than in the rhombic polymorph.

As mentioned above for the ^1H-^{13}C TEDOR spectra, the propyl chain at the isoxazol-5-on ring is expected to be significantly more mobile in the needle morphology than in the rhombic polymorph. Looking at Figure 3.19, the residual dipole-dipole coupling of the CH_2 groups 3 and 2 is $D_{CH}/2\pi$ = 14.0 kHz and $D_{CH}/2\pi$ = 10.0 kHz, respectively, which corresponds to an order parameter of S_{het} = 67% and S_{het} = 48%. Comparing these values to the ones determined for the rhombic polymorph in Figure 3.16, it is apparent, that the propyl chain at the isoxazol-5-on ring is by a factor of 1.4–1.5 more mobile in the needles. This increase in mobility for all alkyl chains of the molecule confirms the idea of a less well ordered packing of the molecules in the kinetically controlled needle polymorph, which was already mentioned in Section 3.3.

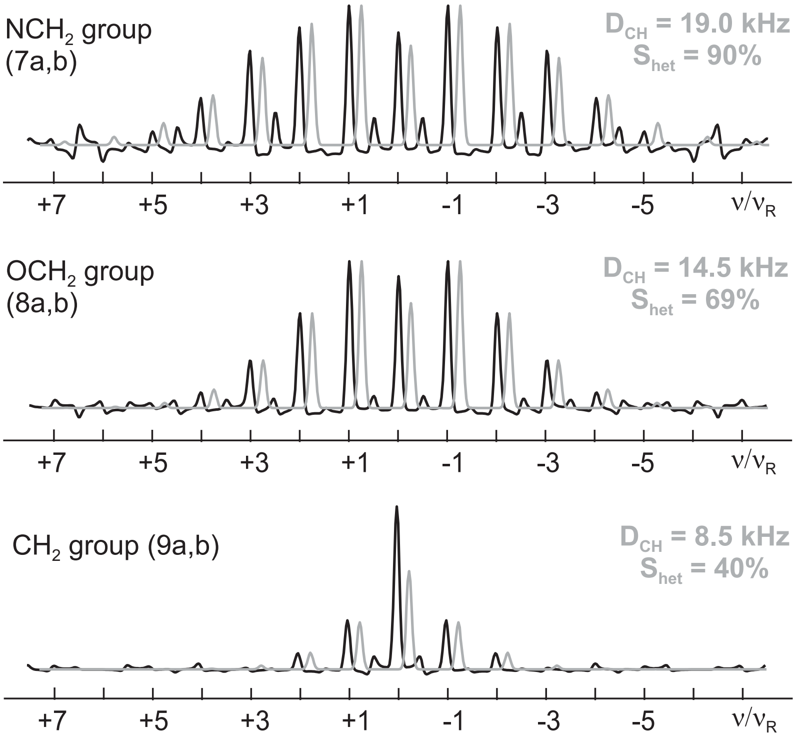

Figure 3.18: *REREDOR spinning sideband patterns of the needle polymorph. Residual dipole-dipole couplings of the NCH$_2$ (top), the OCH$_2$ groups (middle) and the OCH$_2$**CH$_2$** groups (bottom) recorded under MAS at 30 kHz and τ_{rcpl} = 2 τ_R (black line = experimental, grey line = calculated).*

Quantitative investigation of the phenylene ring dynamics. Despite the increased segmental dynamics of the alkyl chains in the needles, the aromatic and the isoxazol-5-on moiety should remain stiff, to ensure optimum π-electron delocalization of the chromophore system. The mobility of the aromatic CH groups is investigated with REPT-HDOR and REREDOR spinning sideband patterns. For rigid CH groups, both pulse sequences generate spinning sidebands equally well, as can be seen in Figure 3.20. The residual dipole-dipole couplings extracted from REPT-HDOR and REREDOR sidebands are in good agreement within the error margin of $\leq$ 1 kHz. The dipole-dipole couplings extracted for the aromatic protons are between $D_{CH}/ 2\pi$ = 20.5 and 22.1 kHz, which corresponds to order parameters between S_{het} = 98–105% (Figure 3.20). (The REPT-HDOR sideband patterns of the aromatic CH group 6b is neglected, because the signal-to-noise ratio was rather poor and no additional information is expected from its residual dipole-dipole coupling).

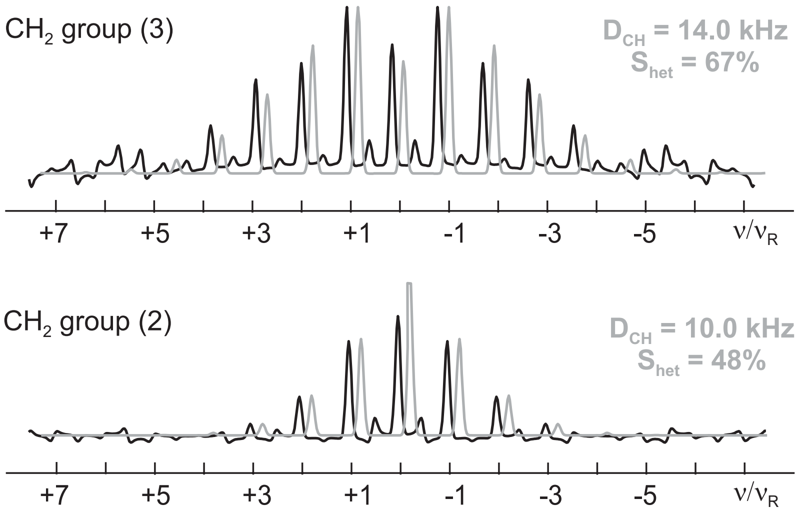

Figure 3.19: *RERDOR spinning sideband patterns of the needle polymorph. Residual dipole-dipole couplings of the propyl chain at the isoxazol-5-on ring:* -$\boldsymbol{CH}_2CH_2CH_3$ *group (3) (top) and* $CH_2\boldsymbol{CH}_2CH_3$ *group (2) (bottom), recorded under MAS at 30 kHz and* $\tau_{rcpl} = 2\ \tau_R$ *(black line = experimental, grey line = calculated).*

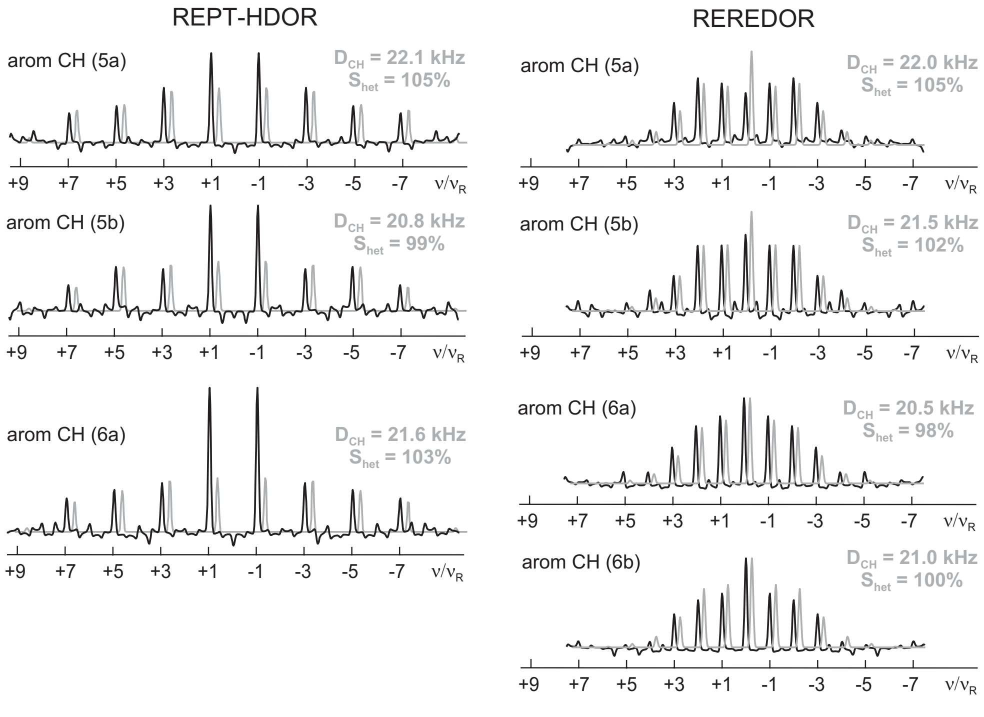

Figure 3.20: *REPT-HDOR and RERDOR spinning sideband patterns of needle polymorph. Residual dipole-dipole couplings of the aromatic CH groups of the needles recorded under MAS at 30 kHz with* $\tau_{rcpl} = 4\ \tau_R$ *for the REPT-HDOR sidebands and* $\tau_{rcpl} = 2\ \tau_R$ *for RERDOR (black line = experimental, grey line = calculated).*

3.4.3 Conclusion

- The Yellow Filter Dye molecules pack less well in the needle morphology than in the rhombic crystal. Therefore, the crystal structure of the needles allows for a significantly higher degree of local molecular mobility of the alkyl chains. This observation agrees well with the fact that the rhombic morphology is the thermodynamically preferred structure, while the formation of the needle polymorph is kinetically controlled.
- The propyl chain at the isoxazol-5-on ring and the ends of the -$NCH_2COOCH_2CH_2CH_3$ branches are by a factor ~ 1.5 and ~ 1.3, respectively, more mobile in the needle polymorph than in the rhombic crystal.
- The phenylene rings, in contrast, are completely rigid on the NMR time scale in both morphologies, to allow for an optimal π-electron delocalization of the chromophore system.

From a NMR-methodological point of view it should be added that:

- For rigid CH groups REPT-HDOR and REREDOR spinning-sideband patterns work equally well.
- For CH_2 groups (especially more mobile ones) REREDOR spinning sideband patterns yield a much better signal-to-noise ratio and are therefore preferable over REPT-HDOR patterns.

Chapter 4

Heteronuclear NMR investigation of helical shape-persistent dendritic macromolecules

Determining the structure as well as identifying the structure-driving and structure-directing features of supramolecular systems represent an important challenge for modern characterization techniques [Steed 00, Ciferri 00, Atwood 96, Brundveld 01, Moore 99]. In this Chapter it is demonstrated how advanced solid-state NMR methods under fast MAS can provide very useful and detailed information about the structure and dynamics of fairly large supramolecular systems. MAS frequencies of 25 – 30 kHz combined with dipolar ^{1}H-^{1}H or ^{1}H-^{13}C recoupling techniques give insight into the local structure of several related self-assembling columnar structures. These superstructures are formed by polymer molecules consisting of a polymethacrylate (PMA) or polystyrene (PS) backbone with large dendritic side-groups. In particular, site-specific information about the local dynamics of different CH$_n$ units is obtained, which allows the identification of the structure-driving and structure-determining elements in the self-assembly process of such systems. The following five related polymers were investigated [Percec 98a, Percec 98b, Percec 93, Percec 94]:

(A) Poly(3',4',5'-Tris[4''-(n-dodecyl-1-oxy)benzyloxy]benzyl methacrylate), henceforth referred to as **G1-PMA,**

(B) Poly(4-ethylbenzyl3',4',5'-Tris[4''-(n-dodecyl-1-oxy)benzyloxy]benzoate), henceforth referred to as **G1-PS,**

(C) Poly(3',4',5'-Tris[3'',4'',5''-Tris(n-dodecyl-1-oxy)benzyloxy]benzyl methacrylate), henceforth referred to as **G2-PMA,**

(D) Poly(3',4',5'-Tris[3'',4'',5''-Tris[4'''-(n-dodecyl-1-oxy)benzyloxy]benzyloxy]benzyl methacrylate), henceforth referred to as **Benz-G2-PMA,**

(E) Poly{2-[2-[2-(2-methacryloylethoxy)ethoxy]ethoxy]ethyl-3',4',5'-tris[4"-(n-dodecyl-1-oxy) benzyloxy] benzoate}, henceforth referred to as **G1-4EO-PMA.**

The dendrons are attached to a polymer backbone with a short and inflexible -CH_2OCO- / -$COOCH_2Ph$- linking unit or with a more extended and flexible -$(OCH_2CH_2)_4OCO$- unit (see Figure 4.1). They self-organize in a columnar fashion in the solid state, as has been investigated by scanning force microscopy [Percec 98a]. G1-4EO-PMA has also been studied in great detail by small and wide angle X-ray diffraction [Chvalun 96, Chvalun 97]. G1-PMA, G1-PS and G1-4EO-PMA display a glass transition temperature, while G2-PMA and Benz-G2-PMA do not (they decompose before melting at ~250°C). The T_g of G1-PMA and G1-PS is ~70°C, for G1-4EO-PMA it is 5°C. G1-PMA and G1-PS enter the isotropic phase at ~130°C and G1-4EO-PMA at 105°C. The observed liquid crystalline phase is hexagonal columnar Φ_h [Percec 98a], which shows that the highly organized columnar structure is observed below as well as above T_g.

In the following, the structural features and segmental dynamics (above and below T_g) of G1-PMA (see Figure 4.1 A) are studied by analyzing ^{1}H NMR chemical shifts as well as ^{1}H-^{13}C and ^{1}H-^{1}H dipolar sideband patterns. In particular, the aromatic rings and the -CH_2O- linking units within the dendrons are investigated in detail. Based on the high degree of local order found within the dendrons, they are identified as the structure-directing moieties of the columnar architecture. Subsequently, the results obtained for G1-PMA are systematically compared to materials with characteristic differences, i.e., a different polymer backbone (G1-PS, see Figure 4.1 B), a larger dendritic side-group (G2-PMA and Benz-G2-PMA, see Figures 4.1 C and D) and, finally, a longer and more flexible linker between backbone and dendron (G1-4EO-PMA, see Figure 4.1 E).

4.1 Structural features of G1-PMA below T_g: 2D ^{1}H-^{13}C correlation spectrum

Figure 4.2 shows the two-dimensional ^{1}H-^{13}C correlation spectrum, obtained using the REPT-HSQC experiment described in Chapter 2. It allows the resonances of carbons and their attached protons to be assigned for the different CH_n groups of G1-PMA. A comparison of selected solid-state chemical shifts with the corresponding solution-state values (in brackets) is given in Table 4.1. In the 2D REPT-HSQC spectrum, three regions can be distinguished: the aromatic, the OCH_2, and the aliphatic region. No peaks of quaternary carbons are observed, because the REPT-HSQC experiment, when performed with short recoupling times of τ_{rcpl} = τ_R = 40 μs (at 25 kHz MAS), is selective for carbons that couple to a directly bonded proton.

In the aromatic region, two peaks are observed at 114 and 130 ppm, which belong to the three outer phenylene rings of the dendron, as indicated in the inset in Figure 4.2. The CH

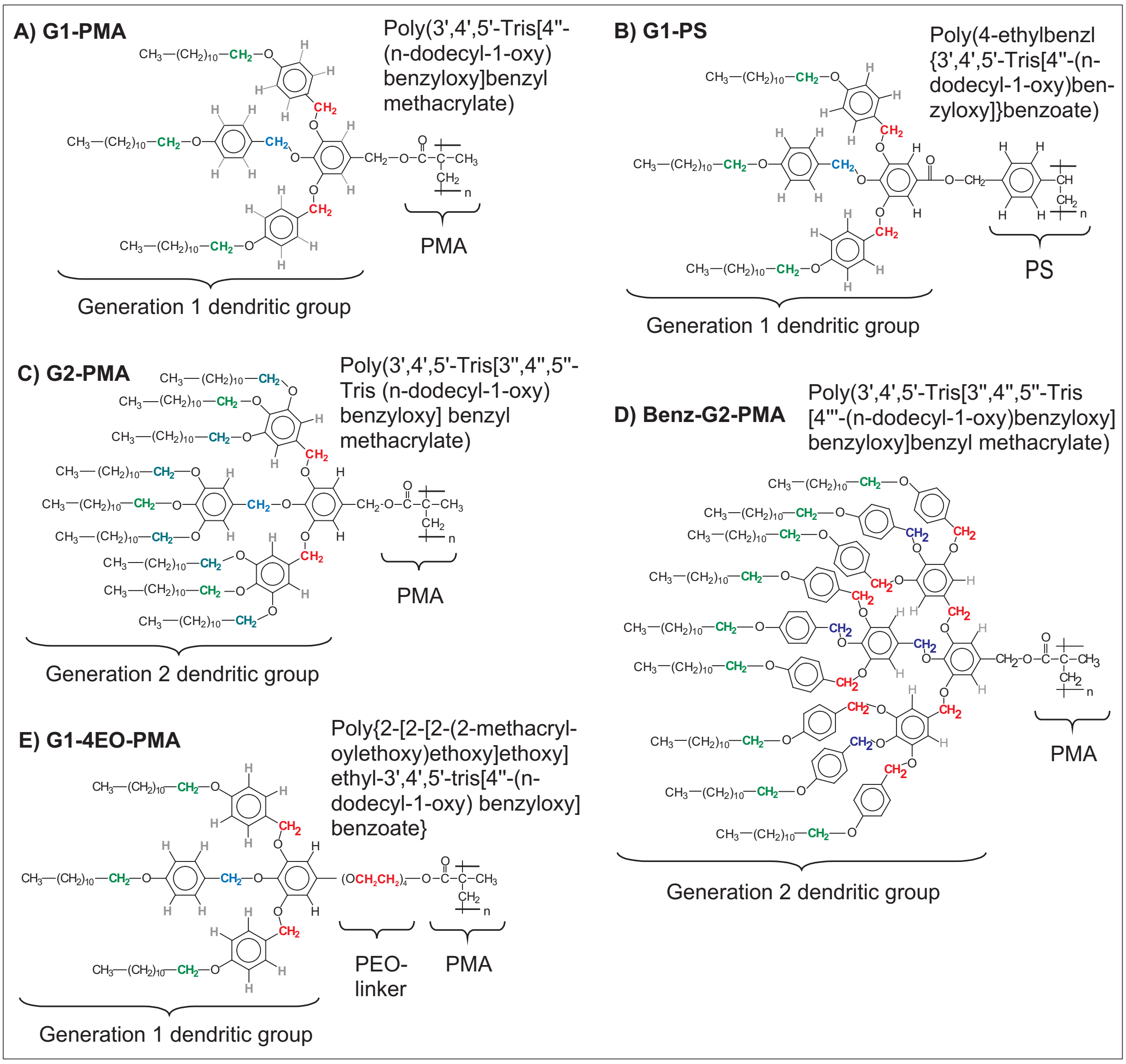

Figure 4.1: *Systems investigated in this Chapter. All consist of a polymer backbone (PMA or PS), to which dendrons of first and second generation (G1 and G2) are attached. The side-groups are responsible for a columnar supramolecular arrangement of the molecules.*

signal of the inner aromatic ring is expected at a carbon chemical shift of $\delta(^{13}\mathrm{C}) = 109$ ppm, but was only observed as a very weak signal in a conventional cross polarization (CP) MAS spectrum which is plotted above the sum projection of the carbon-dimension in Figure 4.2. Thus, no corresponding proton chemical shift can be assigned for the inner aromatic rings, but from the rather broad shape of the ^{13}C peak (covering a spectral range from 100 to 115 ppm) a similarly broad distribution of the ^{1}H resonances can be assumed.

In the OCH_2 region, different types of groups can be distinguished, corresponding to the molecular structure of G1-PMA (depicted in Figure 4.1 A): OCH_2R groups in the dodecyl chain (with R = $C_{11}H_{23}$), OCH_2Ph between the aromatic rings, and a $(COO)CH_2Ph$ group

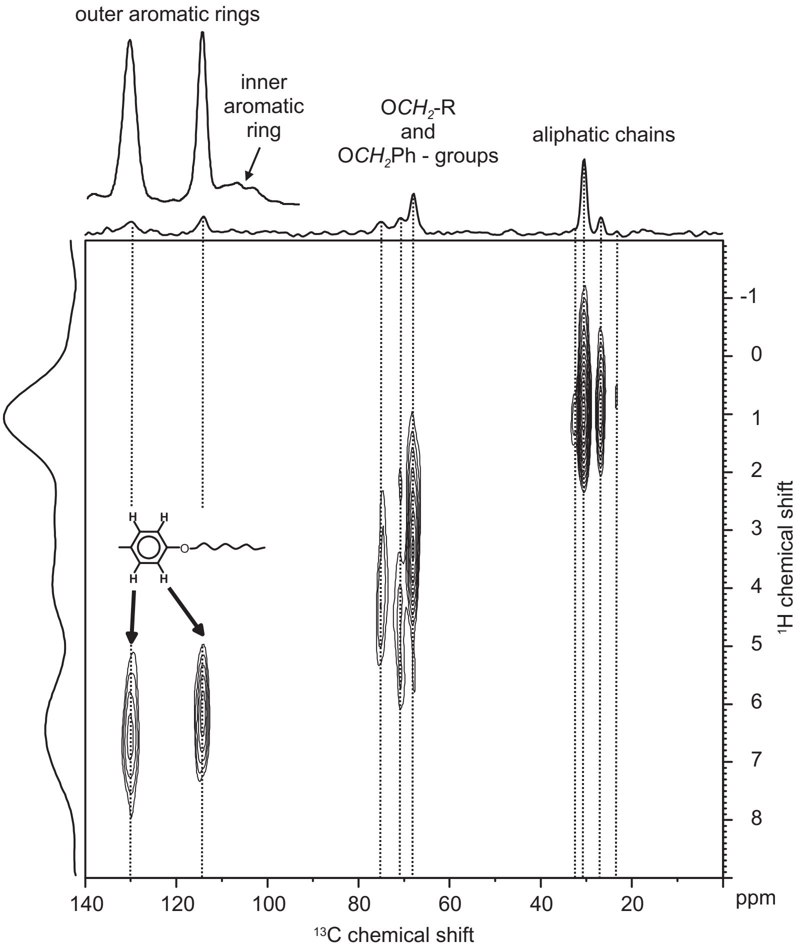

Figure 4.2: *2D ^{1}H-^{13}C REPT-HSQC correlation spectrum of G1-PMA, obtained at 25 kHz MAS using short dipolar recoupling periods of $\tau_{rcpl} = \tau_R = 40\ \mu s$. The one-dimensional spectra plotted at the top and the left are the sum-projections for the carbon and proton dimension, respectively.*

that attaches the dendron to the polymer backbone. The latter, however, is not visible in our NMR spectra because it is of weak intensity and, moreover, it is covered by the low-frequency wing of the 4-OCH_2R peak. On the basis of symmetry consideration, the OCH_2Ph groups in the 4-position of the aromatic ring can be expected to exhibit different properties than those in the 3- and 5-positions. Therefore, a distinction is made according to 4-OCH_2Ph (blue), 3,5-OCH_2Ph (red), while the 4-OCH_2R groups are shown in green. The aliphatic region is dominated by the dodecyl chains of the dendron. However, this region is not of major interest in this study, as the aliphatic side-chains do not play a significant role in the self-assembling process of the dendritic polymer.

For the structure of G1-PMA and, in particular, for the molecular dynamics of the dendritic moieties, the OCH_2 units play a central role as they link the different moieties. Therefore, they deserve a more detailed consideration, and the respective region of the 2D REPT-HSQC spectrum is enlarged in Figure 4.3 A. Three different carbon resonances are observed at

Table 4.1: ^{1}H and ^{13}C chemical shifts of G1-PMA from ^{1}H-^{13}C REPT-HSQC solid-state correlation spectra and solution-state NMR (in brackets).

	G1-PMA			
	δ^{13}C [ppm]		δ^{13}C [ppm]	
	solid-state	solution-state*	solid-state	solution-state*
4-OCH$_2$R	67.8	(69.1)	3.4	(3.8)
(COO)CH$_2$Ph	~67.8	(67.7)	***	(4.7)
3,5-OCH$_2$Ph	70.6	(70.4)	2.3	(4.7)
	”	”	4.3	(4.7)
	”	”	5.5	(4.7)
4-OCH$_2$Ph	75.0	(76.1)	4.4	(4.7)
outer phenylene CH, meta	114.0	(114.0-114.8)	6.3	(6.6)
outer phenylene CH, ortho	130.0	(129.0-130.5)	6.7	(7.0)
inner aryl CH	109.0	(109.0)	?**	(6.6)

* Solution-state chemical shifts taken from [Percec 98a].

** The signal intensity in the 2D REPT-HSQC spectrum is too low to reliably determine the ^{1}H chemical shifts.

*** The ^{1}H resonance is concealed by the high frequency wing of the 4-OCH$_2$R peak.

67.8 (green), 70.6 (red), and 75.0 ppm (blue), they are assigned to the 4-OCH$_2$R, 3,5-OCH$_2$Ph, and 4-OCH$_2$Ph group, respectively, based on solution-state NMR data (see also Appendix C). The corresponding proton resonances range from 2.3 to 5.5 ppm (Table 4.1) and deviate noticeably from their solution-state values. Such effects can be attributed to ring currents of nearby aromatic moieties, which have been discussed in Chapter 2, Section 2.5. Three ^{1}H resonances can be differentiated in Figure 4.3 A, which are all correlated to the ^{13}C peak at 70.6 ppm (see also Table 4.1). Hence, the four protons of the two 3,5-OCH$_2$Ph groups do not have the same chemical environment, but experience ring current effects to different degrees. Based on Figure 2.12 in Chapter 2, the low-frequency shift to 2.3 ppm (relative to a solution-state value of ~4.7 ppm, i.e., Δ = -2.4 ppm) can be explained by an aromatic ring located at a distance of (2.5±0.5) Å above or below the respective proton, while the high-frequency shift to 5.5 ppm (corresponding to Δ = +0.8 ppm) suggests that this proton is placed beside an aromatic ring at a distance of ~3 Å (relative to the center of the ring).

To interpret these observations, possible scenarios of CH$_2$ groups with π-shifted protons are considered in the following, depicted schematically in Figure 4.4. Ignoring signal intensities, the simplest scenario a) would be represented by three different CH$_2$ groups whose protons have different chemical shifts: $H^{(+)}$-C-$H^{(+)}$, $H^{(0)}$-C-$H^{(0)}$, $H^{(-)}$-C-$H^{(-)}$, where the

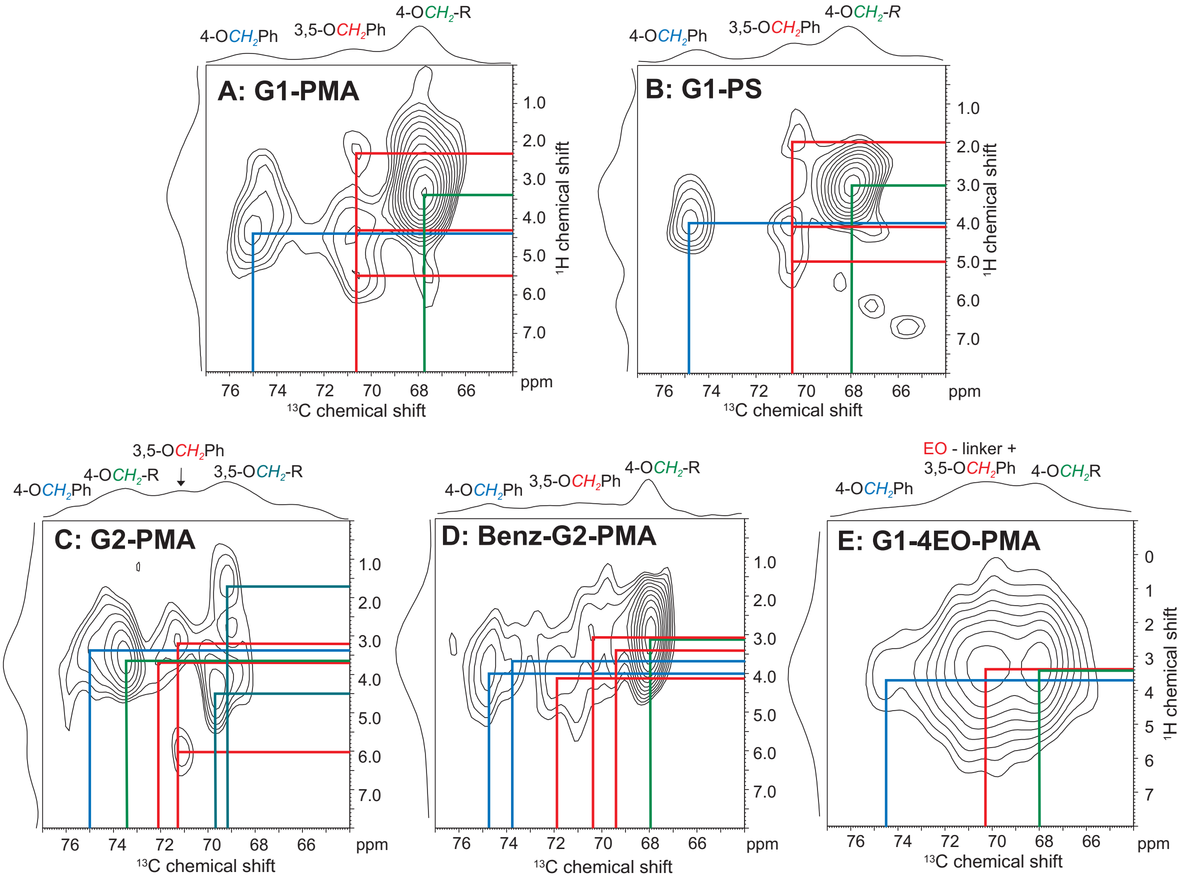

Figure 4.3: *OCH_2 region of 2D ^1H-^{13}C REPT-HSQC correlation spectrum of A: G1-PMA with τ_{exc} = 1 τ_R = 40 μs, B: G1-PS with τ_{exc} = 1 τ_R = 33 μs, C: G2-PMA with τ_{exc} = 1 τ_R = 40 μs, D: G1-4EO-PMA with τ_{exc} = 1 τ_R = 33 μs.*

superscripts (+), (0) and (-) denote high-frequency shift, no shift and low-frequency shift, respectively. While an unaffected group, $H^{(0)}$-C-$H^{(0)}$, can obviously be understood very easily, it appears unlikely that both protons of a CH_2 group can be located relative to an aromatic ring in such a way that they are subject to equal ring currents at the same time, given the geometrical requirements and spatial restrictions for noticeable shift effects (see Figure 2.5 in Chapter 2). Therefore, $H^{(+)}$-C-$H^{(+)}$ and $H^{(-)}$-C-$H^{(-)}$ are unlikely situations. Moreover, the three different proton resonances are expected to arise from two OCH_2 groups not from three. A second possibility b) is based on two OCH_2 groups, where the protons of one are not shifted, $H^{(0)}$-C-$H^{(0)}$, and the protons of the other are up- and downfield shifted, $H^{(+)}$-C-$H^{(-)}$. The combination of up- and down-field shifted protons on one CH_2 group can, however, also be excluded, because Figure 2.5 shows that the regions, where the ring current of a single phenyl ring would cause the observed shifts in both directions, are spatially separated by $>$ 2.5 Å. This distance is far too large for a single CH_2 group with a proton-proton distance of only 1.8 Å. Consequently, the CH_2 groups need to consist of a shifted ($H^{(+)}$ or $H^{(-)}$) and an unshifted proton ($H^{(0)}$), which leads us to two different types of CH_2 groups, namely $H^{(+)}$-C-$H^{(0)}$ and $H^{(-)}$-C-$H^{(0)}$, depicted in Figure 4.4c. This scenario also concurs with the observation that the peak at 4.3 ppm (i.e. $H^{(0)}$ with $\Delta \approx 0$ ppm) is stronger than the shifted ones at 2.3 ppm ($H^{(-)}$) and 5.5 ppm ($H^{(+)}$).

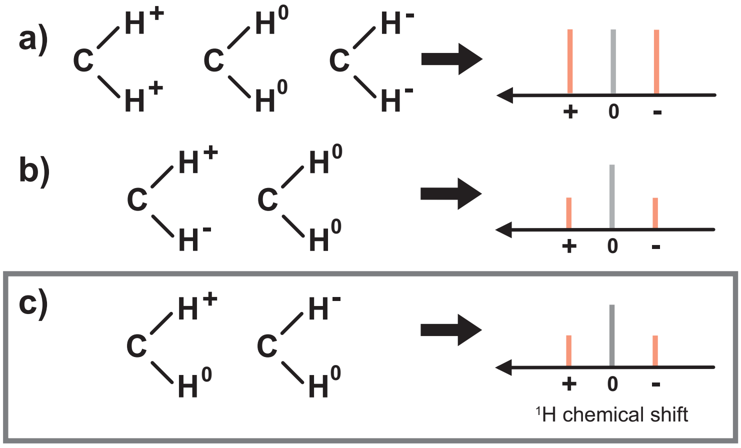

Figure 4.4: *Schematic representation of three possible scenarios of CH_2 groups with π-shifted protons. The superscripts (+), (0) and (-) denote a high-frequency shift, no shift or low-frequency shift of the respective proton. Scenario c) is the one observed for the 3,5-OCH_2Ph protons in G1-PMA.*

Turning to the question which aromatic rings are responsible for the shifts, we first note that the observed effects cannot be caused by the aromatic rings attached to either side of the -OCH_2- units alone. On the OCH_2-Ph side, the effect is already included in the solution-state chemical shift, while on the Ph-OCH_2 side, the possible positions of the OCH_2 protons with respect to the aromatic ring allow for π-shift effects of only $0 \text{ ppm} < \Delta < +0.2$ ppm, which is significantly less than the observed $\Delta = +0.8$ ppm. Thus, the shift effects can be attributed to aromatic rings of neighboring dendritic side-chains (or other segments of the same dendritic side-chain, but this possibility will be excluded later), depicted schematically in Figure 4.5. The aromatic rings are arranged next to the 3,5-OCH_2Ph groups according to the two distance constraints derived above: (i) a neighboring aromatic ring is located above or below one of the two 3,5-OCH_2Ph groups at a distance of (2.5±0.5)Å, such that one of its two protons points toward the center of the ring ("face-on"-type arrangement), which leads to a low-frequency shift of $\Delta = -2.4$ ppm; (ii) the other 3,5-OCH_2Ph group of the dendron is oriented such that one of its protons is placed at a distance of ~3 Å beside another aromatic ring ("edge-on"-type arrangement) resulting in a high-frequency shift of $\Delta = +0.8$ ppm. The respective regions are highlighted in red in Figure 4.5. In both cases, only one of the two CH_2 protons experiences additional ring currents, while the other proton remains essentially unaffected. The features displayed in Figure 4.5 should, however, only be taken as suggestions for local packing phenomena. These local features belong to an overall structure which can, as a whole, not be determined by NMR experiments alone. In particular, it is not known whether each dendron is involved in "edge-on" and "face-on type" arrangements at the same time (as shown in Figure 4.5) or whether there are different types of dendrons packed in face-on, edge-on and mixed arrangements. Finally, from the observation of three distinct chemical shifts it is evident that the 3,5-OCH_2Ph groups are rather immobile on the NMR time scale (i.e., 10 μs to 1 ms) so that the ^{1}H chemical-shifts are not motionally averaged. In fact, the presence of only one (average) ^{1}H chemical-shift of the 4-OCH_2Ph groups can be attributed to motional effects. This point will also be addressed in the discussion of CH_2 dynamics in the following Section, where structural features derived above will be combined with features of segmental motion.

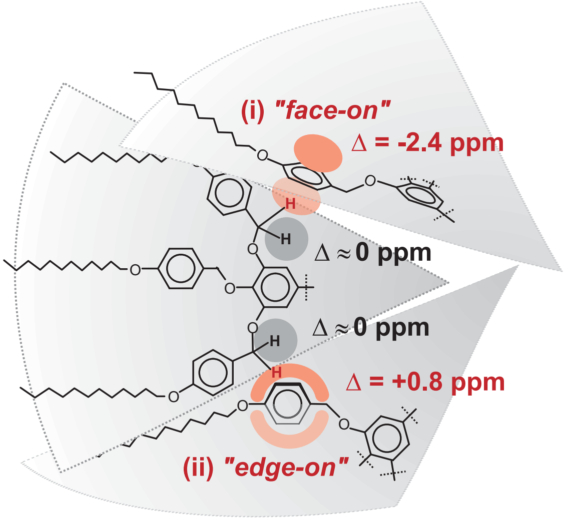

Figure 4.5: *Characteristic features of the packing of the dendrons in G1-PMA. From the*^{1}*H chemical-shift effects observed for the 3,5-*OCH_2Ph *groups, "face-on" and "edge-on" types of contacts between dendrons can be derived. The Figure should only be taken as a schematic visualization of principal structural features, rather than a part of the actual structure.*

4.2 Segmental dynamics of G1-PMA below T_g: ^{1}H-^{13}C and ^{1}H-^{1}H sideband patterns

Turning to the molecular dynamics of G1-PMA, qualitative information can be straightforwardly obtained from one-dimensional ^{1}H-^{13}C TEDOR spectra recorded with a recoupling time of $\tau_{rcpl} = 2\ \tau_R$ for MAS frequencies of 25 – 30 kHz (as described above), because under these experimental conditions the ^{13}C signal of immobile CH_2 groups vanishes. Considering the CH_2 groups of G1-PMA, only the peak at 71 ppm disappears; therefore, only the 3,5-OCH_2Ph groups are rigid (Figure 4.6 A). For $\tau_{rcpl} = 4\ \tau_R$, the 4-OCH_2Ph group has disappeared, too; obviously, it fulfills the condition for signal cancellation at longer recoupling times due to weaker dipole-dipole couplings. Therefore, it must be a little more mobile than the 3,5-OCH_2Ph groups, but still a lot less mobile than the 4-OCH_2R groups in the alkyl chains, as their signal at 68 ppm clearly persists at $\tau_{rcpl} = 4\ \tau_R$.

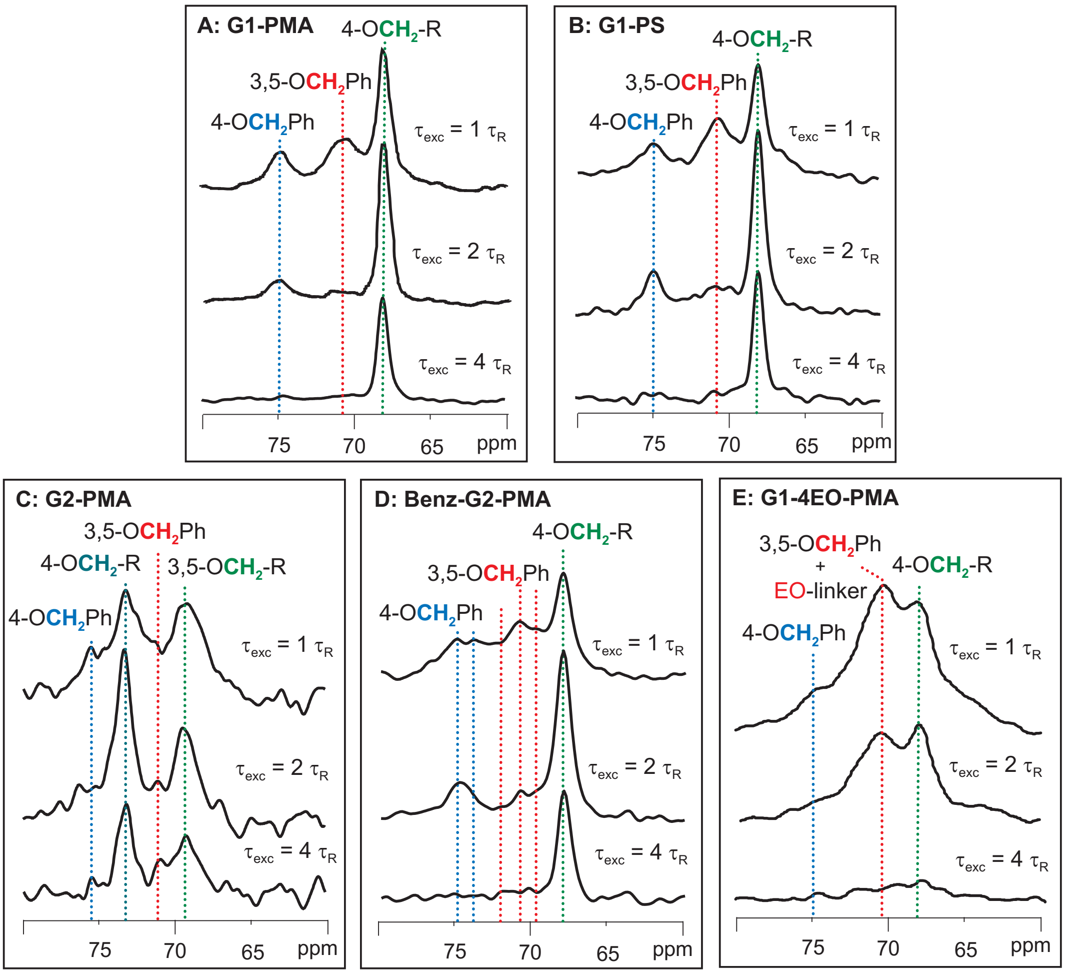

Figure 4.6: *OCH_2 region of one-dimensional ^1H-^{13}C TEDOR spectra of A: G1-PMA, B: G1-PS, C: G2-PMA, D: G1-4EO-PMA at ω_R = 33 kHz.*

To extend from this qualitative understanding to a quantitative investigation, the segmental dynamics of a molecule can be determined by means of spinning sideband patterns which arise from heteronuclear (^{1}H-^{13}C) or homonuclear (^{1}H-^{1}H) dipole-dipole couplings according to the rotor-encoding mechanisms described in Section 2.4 of Chapter 2. Based on internuclear distances from known bond lengths and angles, the dipole-dipole coupling of an immobile segment, such as CH, CH_2, CH_3 or a phenylene ring, can be easily calculated. Using a C-H bond length of 113 pm, a coupling of $D_{CH}/2\pi = 21.0$ kHz results [Saalwächter 00], which is reduced in the case of molecular motions occurring on a time scale $< 1\mu$s. Similarly, the homonuclear coupling of two neighboring protons on a phenylene ring with a distance of 247 pm [Ochsenfeld 02] is $D_{HH}/2\pi = 8.0$ kHz According to conventional definitions, a dynamic order parameter S can then be determined locally for individual segments by relating the measured (reduced) coupling and the one calculated for the immobile case. Effectively, the parameter S reflects the motion of the internuclear vector (C-H or H-H) in terms of its reorientation with respect to the external magnetic field vector B_0. Recalling the cancellation effects observed in ^{1}H-^{13}C TEDOR spectra, it should be noted that ^{1}H-^{13}C REPT experiments and their sideband patterns are not suited for measuring couplings of relatively rigid CH_2 groups, because the 2D REPT sequences are extended versions of the TEDOR experiment and therefore equally suffer from signal losses. Instead, rigid CH_2 groups are investigated by REREDOR experiments and their sideband patterns.

When fitting REPT-HDOR and DQ sideband patterns, the first order sidebands are always neglected, because their intensity is usually too high due to couplings to remote protons. Similarly, the centerband of REREDOR sideband patterns is excluded from the evaluation, as its intensity is strongly affected by relaxation processes [Saalwächter 02b]. The error margin of the residual dipole-dipole couplings extracted from the relative intensities of the sidebands predominantly depends on the signal-to-noise ratio of the experiment. For the REPT-HDOR and DQ sideband patterns shown below, it can be estimated to be about $\Delta D_{ij}/2\pi \approx 0.5$ kHz. Since the signal intensity in REREDOR experiments is spread over a larger number of sidebands, the error margin is about twice as large, i.e. $\Delta D_{ij}/2\pi \approx 1.0$ kHz.

For G1-PMA below T_g, Figure 4.7 and 4.8 A show ^{1}H-^{13}C REREDOR and REPT-HDOR patterns, of CH groups of the inner and outer aromatic rings, respectively. Figures 4.9 A depicts the ^{1}H-^{1}H DQ sideband patterns for the outer aromatic rings, while the REREDOR sideband patterns of the OCH_2 groups are shown in Figure 4.10. These results are discussed below.

Motions of aromatic rings. Comparing Figures 4.7 and 4.8 A, the best fit for the sideband pattern of the inner and outer aromatic ring gives heteronuclear couplings of $D_{CH}/\ 2\pi = 21.0$ kHz and 6.1 kHz, corresponding to order parameters of $S_{het} = 100\%$ and 29%, respectively. Thus, the inner aromatic ring of the dendrons is fully immobile, while the outer ones are highly mobile. For the outer aromatic rings the homonuclear coupling between the two neighboring aromatic protons can be measured, too, where a coupling of $D_{HH}/\ 2\pi = 4.9$ kHz, corresponding to $S_{hom} = 61\%$, is determined (Figure 4.9 A).

For phenylene rings, the comparison of homo- and heteronuclear dipole-dipole couplings is informative, since local flip or rotation motions of the phenylene segment can be distinguished from motions of the whole side-chain including the phenylene group. Only the heteronuclear coupling is affected by a flip or a rotation of the aromatic rings, while the homonuclear coupling between the two aromatic protons remains unaffected, because the dipolar coupling vector lies parallel to the rotation axis. Therefore, a reduction of the homonuclear coupling must be due to a motion of the whole dendritic side-chain, while the heteronuclear dipole-dipole coupling can be reduced by both, the side-chain movement and a ring-flip. The reduced homonuclear coupling ($D_{HH}/\ 2\pi = 4.9$ kHz, $S_{hom} = 61\%$) can be related to a side-chain motion which effectively occurs within a cone-shaped volume with an opening angle of $\pm$ 20 (see below, Figure 4.11). The angular restriction can be estimated directly from the residual order parameter $S_{hom} \approx 60\%$ [Schmidt-Rohr 94, Hentschel 81].

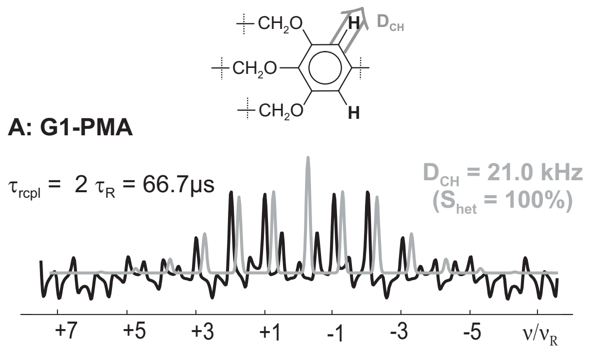

Figure 4.7: *REREDOR spinning sideband pattern. Residual heteronuclear dipole-dipole coupling of the inner aromatic rings of G1-PMA, recorded under MAS at 30 kHz and* τ_{exc} *= 2* τ_R *= 67* μ*s, (black line = experimental, grey line = calculated). The coupling vector is indicated in the inset above.*

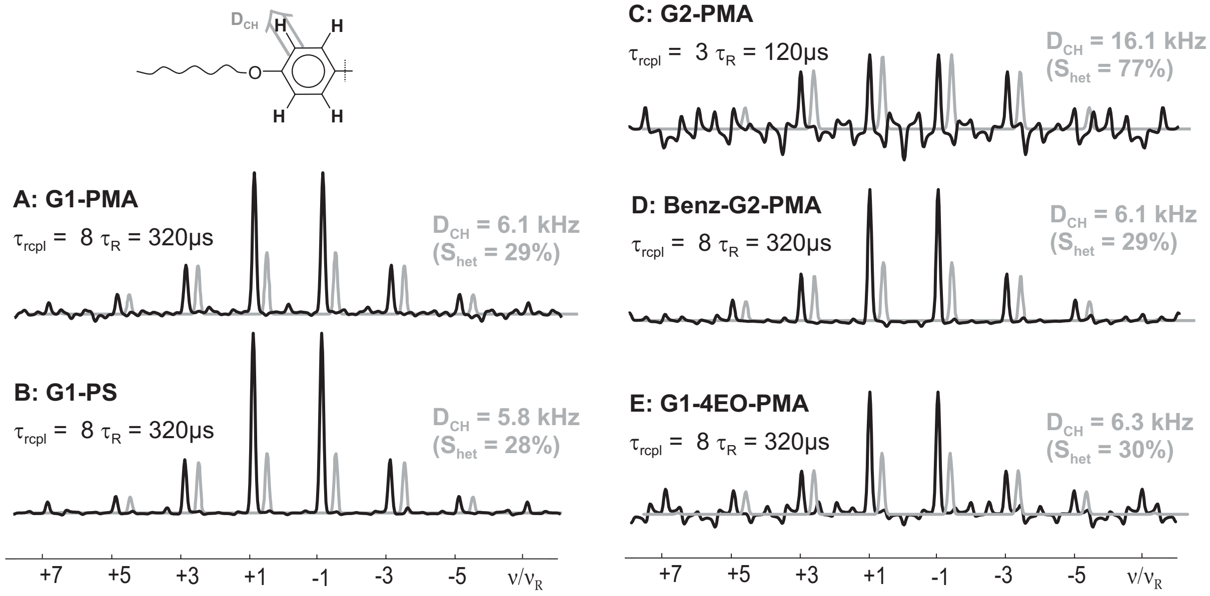

Figure 4.8: *REPT-HDOR spinning sideband patterns. Residual heteronuclear dipole-dipole couplings of the outer phenylene rings of G1-PMA, recorded under MAS at 25 kHz, (black line = experimental, grey line = calculated). The coupling vector is indicated in the inset above.*

In the heteronuclear experiment, a lower order parameter of S_{het} = 29% is found, which indicates a phenylene ring-flip that occurs in addition to the side-chain motion. A pure 180°-flip would result in an order parameter of S_{het} = 62% for the C-H coupling [Macho 01]. When flip and side-chain motions are considered independent of each other, the effective heteronuclear order parameter can be calculated according to S_{het} = S_{hom} × 62% = 38%, which would correspond to $D_{CH}/ 2\pi$ = 7.9 kHz (see Table 4.2). These numbers are slightly higher than the ones observed experimentally ($D_{CH}/ 2\pi$ = 6.1 kHz, S_{het} = 29%), which points

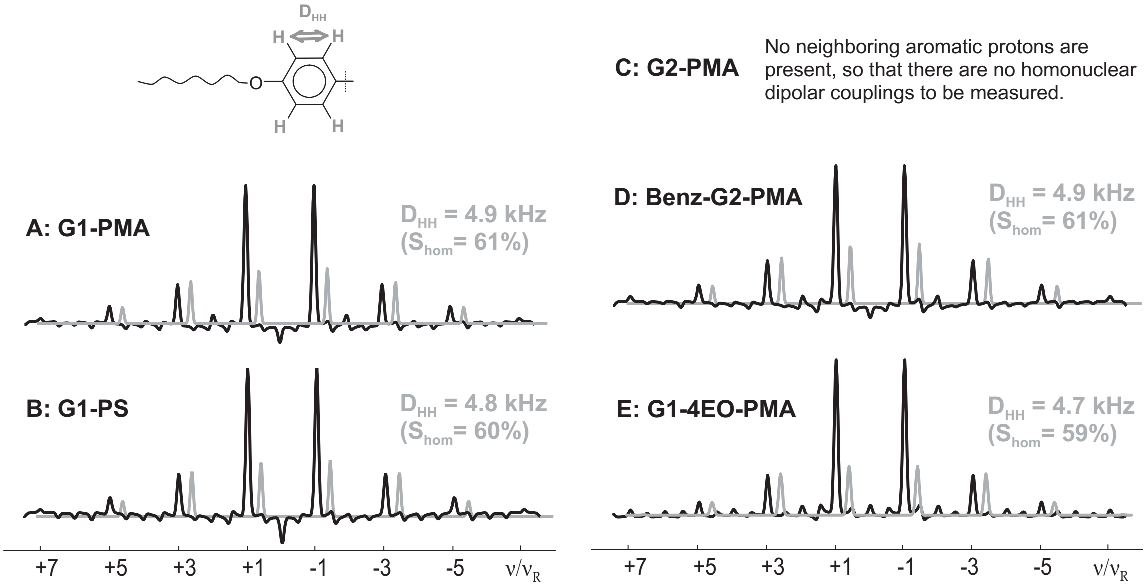

Figure 4.9: *DQ spinning sideband patterns. Residual homonuclear dipole-dipole couplings of the outer phenylene rings below* T_g*, recorded under MAS at 30 kHz and* $\tau_{exc} = 8\,\tau_R = 267\ \mu s$*, (black line = experimental, grey line = calculated). The coupling vector is indicated in the inset above.*

at a librating small-angle motion of the aromatic rings on top of the 180° ring-flip. However, a full ring rotation can be excluded, because the resulting coupling would then be much lower ($D_{CH}/\ 2\pi$ = 2.6 kHz, S_{hom} = 12%) [Macho 01] than the experimental one, not even taking into account the side-chain motion.

These results show very clearly that there is a pronounced mobility gradient among the aromatic moieties of the dendron with order parameters changing from S = 100% to 61% (29% including the ring-flip) between the inner and outer aromatic rings.

Motions of OCH_2 groups. In the qualitative study, it has already been noted that 4-OCH_2R groups are significantly more mobile than the PhOCH_2Ph groups (see Figure 4.6). The exact residual dipole-dipole couplings, as obtained from the REREDOR sideband patterns shown in Figure 4.10, are listed in Table 4.3.

Since the ^{13}C resonance lines of the 4-OCH_2Ph and 3,5-OCH_2Ph groups are separated, their mobility can be determined independently. It is then apparent that the 4-OCH_2Ph segment is more mobile (S_{het} = 57%) than the ones in position 3 and 5 (S_{het} = 81%). This effect is most likely due to steric hindrances from neighboring dendritic groups, which affect the chains in 3 and 5 position more severely. The extent to which this effect is also present for the outer aromatic rings and the 4-OCH_2R groups cannot be determined, because the chemical shifts can no longer be distinguished. Rather, the value of S_{het} = 36% determined for 4-OCH_2R, as well as the values S_{hom} = 61% and S_{het} = 29% determined above for the phenylene rings, represent averages over all three rings. Based on the OCH_2Ph results, however, it

Table 4.2: Experimental and calculated residual dipole-dipole couplings for the possible motions of the outer aromatic rings in G1-PMA.

calculated/ **experimental** couplings and order parameters	homonuclear H-H $D_{HH}/ 2\pi$ (S_{hom})*	heteronuclear C-H $D_{CH}/ 2\pi$ (S_{het})**
rigid aromatic ring	8.0 kHz (100%)	21.0 kHz (100%)
180° ring-flip	8.0 kHz (100%)	13.1 kHz (62%)
full ring rotation	8.0 kHz (100%)	2.6 kHz (12%)
only chain motion	**4.9 kHz (61%)**	⇒ 12.8 kHz (61%)
chain motion plus 180° ring-flip		⇒ 7.9 kHz (38%) **6.1 kHz (29%)**

* Calculated using r_{HH}= 2.47 Å according to [Ochsenfeld 02].

** Calculated using r_{CH}= 1.13 Å according to [Saalwächter 00].

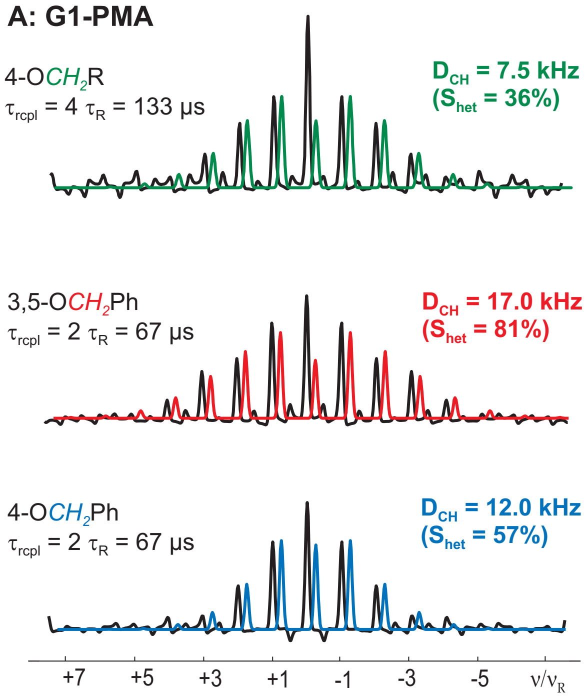

Figure 4.10: *REREDOR spinning sideband patterns. Residual homonuclear dipole-dipole couplings of the different OCH_2 groups of G1-PMA, recorded under MAS at 30 kHz, (black line = experimental, colored line = calculated).*

can be assumed that the chain in the 4 position is more mobile, as a whole, than the other two chains.

On going from the outer phenylene rings (S_{hom} = 61%) to the attached 4-OCH_2R groups (S_{het} = 36%), the segmental mobility increases by a factor of ∼1.7, which can only be at-

Table 4.3: Residual dipole-dipole couplings of OCH_2 groups of G1-PMA from REREDOR experiments.

experimental couplings and order parameters	heteronuclear C-H $D_{CH}/ 2\pi$ (S_{het})
4-OCH_2R	**7.5 kHz (36%)**
3,5-OCH_2Ph	**17.0 kHz (81%)**
4-OCH_2Ph	**12.0 kHz (57%)**

tributed to a liberating effect of the –O– segment between the phenylene ring and the CH_2 group. A similar effect is also observed when comparing the inner aromatic ring and the attached OCH_2Ph groups. Correspondingly, the –O– segment leads to an increase in the segmental mobility by factors of 1.2 – 1.8.

Figure 4.11 schematically summarizes the information gained about the dynamics of the dendrons in G1-PMA. A clear mobility gradient is observed along the dendrons, ranging from the immobile inner aromatic rings to the mobile ends of the aliphatic chains. The order parameter of the terminating methyl groups at the alkyl chains could be estimated to $S < 4\%$ by means of REREDOR experiments with long recoupling times (sideband patterns not shown). The order parameter $S \approx 60\%$ of the outer phenylene rings can be understood in terms of an angular motion by which the chain covers a cone-shaped volume with an opening angle of approximately $\pm 20^\circ$ (as indicated in Figure 4.11) [Schmidt-Rohr 94, Hentschel 81]. In addition, the outer phenylene rings undergo a 180° flip.

Some conclusions concerning the structure of the dendrons and their packing have already been drawn in Section 4.1. Combining these with the results on the molecular dynamics, some additional features of the dendron packing can be derived. As discussed above, the shift effects allow the CH_2 protons of the 3,5-OCH_2Ph groups to be located either above/below or beside an aromatic ring (according to Δ = -2.4 ppm or Δ = +0.8 ppm, respectively). The respective regions are relatively small and restricted (highlighted in red in Figure 4.5), so that the aromatic ring causing the shifts has to be relatively immobile. Otherwise, motional averaging would lead to less pronounced shift effects. This kind of situation is observed in the case of the 4-OCH_2Ph groups, where a combination of $\Delta \approx 0$ ppm and S = 57% is found. Consequently, the phenylene rings belonging to the chains in the 4-position can hardly cause the ^{1}H shift effects of the 3,5-OCH_2Ph groups. Following the mobility argument, the inner and immobile aromatic ring needs to be considered for the π-shifts, but there is only one such inner aromatic ring per dendron and, in addition, there are considerable steric hindrances, in particular for the “edge-on”-type arrangement beside the aromatic ring. It cannot be excluded that the inner aromatic ring contributes to the Δ = -2.4 ppm shift effect in the “face-on”-type arrangement, but it is most likely that the outer phenylene rings in the 3- and 5-positions of

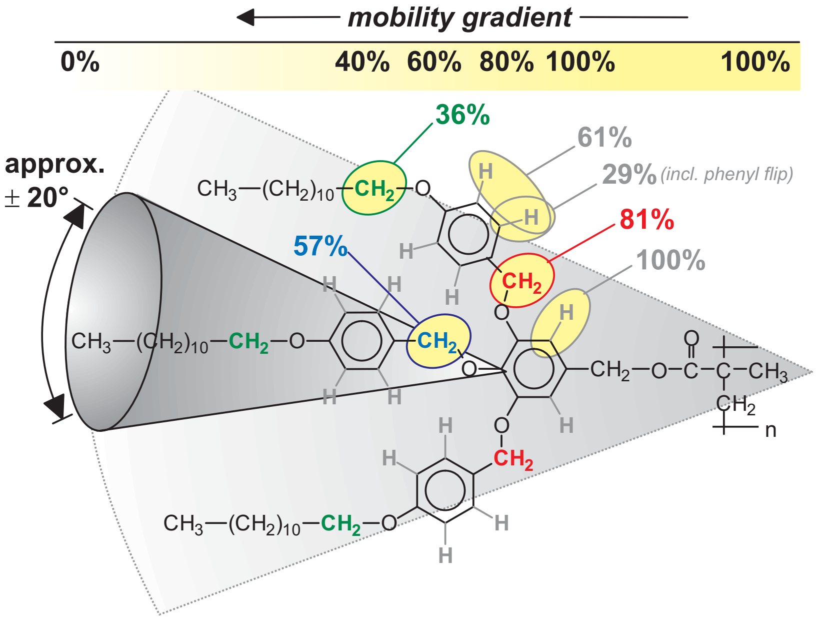

Figure 4.11: *Characteristic features of the molecular dynamics of the dendrons in G1-PMA. A mobility gradient along the dendrons is obvious from the local order parameters. Based on S ≈ 60%, the motion of the three linear chains occurs within a cone with an opening angle of approximately ±20° [Schmidt-Rohr 94, Hentschel 81].*

neighboring dendrons dominate the ^{1}H shift effects of the 3,5-OCH$_2$Ph groups, which was schematically depicted in Figure 4.5.

4.3 Segmental dynamics of G1-PMA above T_g – intermediate motional regime

Above T_g, the system enters the hexagonal-columnar liquid-crystalline phase. Of course, the motion of the dendritic side-groups increases above the phase transition, but the interactions are still strong enough to force the polymer into a helical arrangement, so that the columnar structure persists [Percec 98a].

The NMR signal intensity above T_g is very poor for all recoupling experiments, which indicates that the molecular motions in the system occur on the time scale of the NMR experiment, i.e. with motional correlation times of 10 μs – 1 ms. This regime is commonly referred to as the intermediate motional regime [Saalwächter 02a] and characterized by pronounced signal cancellation effects. An attempt to measure residual proton-proton couplings of the outer aromatic rings in the LC phase at T = 108 °C, despite the poor signal, results in a value of $D_{HH}/2\pi \leq 2.4$ kHz, corresponding to $S_{hom} \leq 30\%$ (see Figure 4.12). Heteronuclear ^{1}H-^{13}C studies were not feasible at all due to a lack of ^{13}C signal.

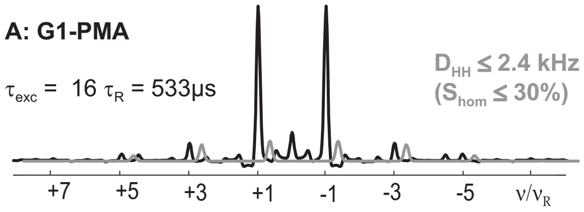

Figure 4.12: *DQ spinning sideband patterns. Residual homonuclear dipole-dipole couplings of the outer phenylene rings of G1-PMA above* T_g *(T = 108 °C), recorded under MAS at 30 kHz and* τ_{exc} = *16* τ_R = *533* μ*s, (black line = experimental, grey line = calculated).*

4.4 G1-PS vs. G1-PMA

G1-PS has the same dendritic side-group as G1-PMA, but attached to a polystyrene backbone instead of a polymethacrylate one. G1-PS self-assembles into a columnar structure similar to G1-PMA and also exhibits a hexagonal liquid crystalline phase above T_g. Comparing the local structure and dynamics of the two supramolecular systems provides insight into the role the polymer backbone plays in the self-assembly process of the columnar structure.

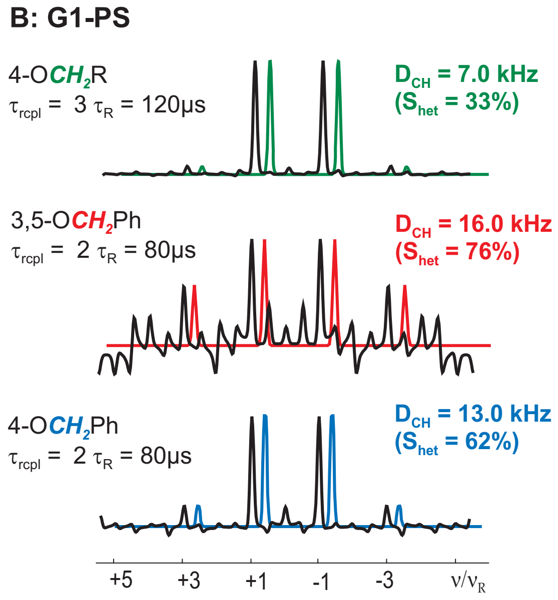

Figure 4.13: *REPT-HDOR spinning sideband patterns. Residual heteronuclear dipole-dipole couplings of the different* OCH_2 *groups of G1-PS, recorded under MAS at 25 kHz (black line = experimental, colored line = calculated).*

Figure 4.3 B shows the OCH_2 region of the ^{1}H-^{13}C REPT-HSQC spectrum of G1-PS. Comparing this spectrum to the one of G1-PMA (Figure 4.3 A), similar ^{1}H chemical shifts are observed, which indicates that similar π-shifts are present in both systems. This observation suggests that the inner OCH_2 groups and the outer aromatic rings arrange in a similar fashion in both systems. Consequently, the polymer backbone does not have a pronounced influence on the structure adopted by the system, which is rather driven by the steric requirements as well as the π-π interactions of the dendron. This conclusion is further supported by the local dynamics of the dendritic side-groups of G1-PS. The ^{1}H-^{13}C TEDOR spectra (Figure 4.6 B) as well as the REPT-HDOR sideband patterns of the OCH_2 groups (Figure 4.13) prove that the dynamical properties of G1-PS are very similar to G1-PMA. Moreover, the residual dipole-dipole couplings and order parameters observed for the outer aromatic rings (^{1}H-^{13}C and ^{1}H-^{1}H couplings in Figure 4.8 B and 4.9 B, respectively) are practically identical, too. The values are listed in Table 4.4. Thus, not only the local structure but also the dynamics of G1-PMA and G1-PS are largely identical despite the different polymer backbones.

Table 4.4: Residual dipole-dipole ^{1}H-^{13}C couplings of G1-PS and G1-PMA from REPT-HDOR and REREDOR spinning sideband patterns as well as residual homonuclear ^{1}H-^{1}H couplings from DQ sideband patterns.

experimental couplings and order parameters	**G1-PS** heteronuclear C-H $D_{CH}/2\pi$ (S_{het})	**G1-PMA** heteronuclear C-H $D_{CH}/2\pi$ (S_{het})
inner aromatic ring	not measured	**21.0 kHz (100%)**
3,5-OCH_2Ph	**16.0 kHz (76%)**	**17.0 kHz (81%)**
4-OCH_2Ph	**13.0 kHz (62%)**	**12.0 kHz (57%)**
outer phenylene rings *homonuclear H-H* $D_{HH}/2\pi$ (S_{hom})	**5.8 kHz (28%)** *4.8 kHz (55%)*	**6.1 kHz (29%)** *4.9 kHz (56%)*
4-OCH_2R	**7.0 kHz (33%)**	**7.5 kHz (36%)**

From an NMR-methodological point of view it should be added, that the determination of the local dynamics of the OCH_2 groups with REPT-HDOR spinning sideband patterns, as shown in Figure 4.13, is not the best approach. It is difficult to extract the residual dipole-dipole couplings from the REPT-HDOR spinning sideband patterns in Figure 4.13 accurately, because only weak third order sidebands are generated. Longer excitation times, in principle, should give higher order sidebands, but in the case of rather rigid OCH_2 groups the signal intensity is lost, which can be seen from the TEDOR spectra in Figure 4.6 B and was explained in Chapter 2, Section 2.3.3. As was mentioned above, REREDOR spinning sideband patterns do not suffer from such signal losses, so that much more reliable sideband patterns can be generated (see e.g. Figure 4.10) at comparable experimental times. Thus, the REREDOR technique is clearly superior to REPT-HDOR experiments if CH_2 group dynamics are to be investigated.

4.5 G2-PMA vs. G1-PMA

The G1-PMA and G1-PS systems discussed so far contain dendrons of the first generation. To study the influence of the generation on the supramolecular arrangement, the results obtained for G1-PMA are now compared to those for G2-PMA where there is a PMA backbone and dendritic side-groups of the second generation. In the solid phase, G2-PMA also self-assembles in a columnar structure, but no pronounced glass transition nor an isotropic phase is observed before the compound decomposes at 250 °C.

Chemical shifts. A comparison of selected solid-state chemical shifts of G2-PMA with the corresponding solution-state values (in brackets) and the values of G1-PMA is given in Table 4.5. On the basis of the solution-state NMR data, the ^{13}C resonances between 69 and 75 ppm, as observed in the ^{1}H-^{13}C correlation spectrum (Figure 4.3 C), could be assigned to the different OCH_2 groups. As mentioned above for G1-PMA and G1-PS, the 4-OCH_2 groups (blue in Figure 4.3 C) are expected to have a different ^{13}C chemical shift than the 3,5-substituted ones (red in Figure 4.3 C). Accordingly, in G2-PMA, 4-OCH_2R (green) and 3,5-OCH_2R (dark green) are also expected to have different ^{13}C chemical shifts. However, there are two more ^{13}C chemical shifts present: For the 3,5-OCH_2Ph and the 3,5-OCH_2R groups pairs of resonances are observed (71.3/72.1 ppm and 69.2/69.7 ppm, respectively). This could either mean that in G2-PMA the 3-OCH_2 and 5-OCH_2 groups have a slightly different environment or that the organization of the 3,5-OCH_2 groups is not fully identical throughout the macromolecule. With respect to the structure, however, the observation of more than one ^{1}H resonance for the 3,5-OCH_2 groups is more significant. Similar to G1-PMA, the 3,5-OCH_2Ph protons are found to be shifted by π-electron effects to higher and lower frequencies, i.e. 6.0 and 3.2 ppm compared to the solution-state value of 4.8 ppm. Based on Figure 2.12 in Chapter 2, the shift changes of Δ = +1.2 and -1.6 ppm can be converted to proton locations at distances of $\sim$ 3 Å beside and (3.0 ± 0.5) Å above/below the center of an aromatic ring, respectively. In G2-PMA, the shifts tend to slightly higher frequencies than in G1-PMA, and all OCH_2Ph protons experience π-shifts of nearby aromatic rings, so that no chemical shift close to the solution-state value is observed. This can be attributed to the higher density of phenyl systems in G2-PMA. For the 3,5-OCH_2R groups, similar π-shifts lead to two different ^{1}H resonances at 4.5 and 1.7 ppm, compared to the solution-state value of 3.6 ppm (i.e., Δ = +0.9 and -1.9 ppm). These values correspond to proton locations at distances of $\sim$ 3 Å beside and (3.0 ± 0.5) Å above/below the center of an aromatic ring, respectively. These findings bear similarities to the 3,5-OCH_2Ph segments in G1-PMA. From a structural point of view, 3,5-OCH_2Ph in G1-PMA and 3,5-OCH_2R in G2-PMA play a similar role in the dendrons, since both units link a linear side-chain to a 3,4,5-substituted aromatic ring.

Considering the chemical shifts in G1- and G2-PMA, it is evident that the dendrons of first and second generation exhibit similar general features and can thus be expected to pack in a similar fashion. The local arrangement of the aromatic rings and OCH_2 groups, however, bears some differences, because in G2-PMA the local density of aromatic rings is obviously higher around the OCH_2 groups, which leads to more pronounced π-shift effects.

Table 4.5: ^{1}H and ^{13}C chemical shifts of G1-PMA and G2-PMA from ^{1}H-^{13}C REPT-HSQC solid-state correlation spectra and solution-state NMR (in brackets).

	G1-PMA		G2-PMA	
	δ^{13}C [ppm]	δ^{1}H [ppm]	δ^{13}C [ppm]	δ^{1}H [ppm]
3,5-OCH_2R	–*	–*	69.2 (68.5)	1.7 (3.6)
	–*	–*	69.7 (68.5)	4.5 (3.6)
4-OCH_2R	67.8 (69.1)	3.4 (3.8)	73.5 (73.1)	3.7 (3.8)
3,5-OCH_2Ph	70.6 (70.4)	2.3 (4.7)	71.3 (71.2)	3.2 (4.9)
	”	4.3 (4.7)	”	6.0 (4.9)
	”	5.5 (4.7)	72.1 (71.3)	3.7 (4.9)
4-OCH_2Ph	75.0 (76.1)	4.4 (4.7)	75.0 (74.8)	3.4 (4.8)
aromatic CHs:				
outer (meta)	114.0 (114.0-114.8)	6.3 (6.6)	–*	–*
outer (ortho)	130.0 (129.0-130.5)	6.7 (7.0)	106.0 (105.7-106.3)	6.4 (6.5)
inner	109.0 (109.0)	?** (6.6)	110.0 (110.1)	?** (6.7)

* No such group is present in the molecule

** The signal intensity in the 2D REPT-HSQC spectrum is too low to reliably determine the ^{1}H chemical shifts.

Molecular dynamics. The dynamical properties of G2-PMA are somewhat different from G1-PMA, as will be discussed in the following. Starting with the outer aromatic rings, Figure 4.8 C shows a ^{1}H-^{13}C REPT-HDOR sideband pattern from which a coupling of $D_{CH}/ 2\pi$ = 16.1 kHz is determined, corresponding to S_{het} = 77%. Hence, the outer aromatic rings in G2-PMA are a lot less mobile than in G1-PMA and G1-PS ($S_{het} \approx 30\%$ and 60% with and without the phenylene flip, respectively). This is not too surprising, because the outer rings in G2-PMA are centers of dendritic units (with a 3,4,5-substitution), while in G1-PMA the outer ring is only part of a linear side-chain (only 4-substitution). The coupling value of $D_{CH}/ 2\pi$= 16.1 kHz also shows that the aromatic ring-flip is inhibited, as such a flip would be associated with a reduction of the coupling to 13.1 kHz. Obviously, the 3,4,5 substitution of the rings places higher energetical demands on a flip process of the outer aromatic rings in G2-PMA, while in G1-PMA the outer phenylenes can flip without affecting the overall packing due to the linearity of the chain and the para-substitution of the rings. In comparison to the inner aromatic ring in G1-PMA (with S_{het} = 100%), however, the outer rings in G2-PMA are more mobile (S_{het} = 77%). This is due to the fact that the outer rings in G2-PMA carry only linear alkyl side-chains, but no phenylene rings which would be capable of π-π stacking.

Turning to the OCH_2 groups, the 1D TEDOR spectra in Figures 4.6 C and A, show similar dynamical properties for G2-PMA and G1-PMA, where the OCH_2R groups are significantly more mobile than the OCH_2Ph groups. The 4-OCH_2Ph groups are more mobile than the 3,5-OCH_2Ph groups, as described above for G1-PMA, similarly the 4-OCH_2R groups of G2-PMA are more mobile than the 3,5-OCH_2R groups. An analysis of the dynamics of the 4-OCH_2R groups of G2-PMA with REREDOR spinning sideband patterns gives the same dipole-dipole couplings $D_{CH}/2\pi$ = 7.5 kHz and order parameters S_{het} = 36% as found for the 4-OCH_2R groups in G1-PMA (see Figure 4.10 and 4.14). Thus, the dynamics of these CH_2 groups appears to be dominated by the dynamics of the alkyl chain, rather than by the inner part of the dendron. Obviously, the –O– linker provides efficient mechanical decoupling from the aromatic ring, whose dynamics is considerably different in G1-PMA and G2-PMA.

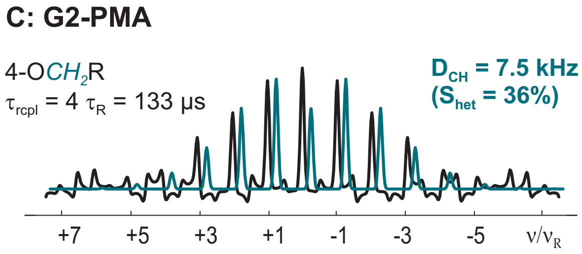

Figure 4.14: *REREDOR spinning sideband patterns. Residual heteronuclear dipole-dipole couplings of a OCH_2 group of G2-PMA, recorded under MAS at 30 kHz, (black line = experimental, green line = calculated).*

4.6 Benz-G2-PMA vs. G1-PMA and G2-PMA

The properties of an even larger G2 dendritic side-group are investigated in this Section, comparing the Benz-G2-PMA macromolecule to G2-PMA and G1-PMA. Benz-G2-PMA has three different types of aromatic rings, one inner, three middle and nine outer ones, depicted in Figure 4.1 D. The inner and the middle aromatic rings are centers of dendritic units (with 3,4,5-substitution), similar to G2-PMA. The outer aromatic rings, however, are part of the linear alkyl chain (4-substituted), as in G1-PMA. In the solid phase Benz-G2-PMA also self-assembles in a columnar fashion, but does not undergo any phase transition before it decomposes at 260 °C, similar to G2-PMA.

Chemical shifts. A comparison of selected ^{13}C and ^{1}H solid-state NMR chemical shifts with the corresponding solution state values and the values of G1-PMA is given in Table 4.6. The ^{13}C chemical shift values between 68 and 75 ppm could be assigned to the different OCH_2 groups. Looking at Figure 4.3 D, the chemical shifts at 74.7 and 73.8 ppm correspond to the

4-OCH$_2$Ph groups (blue), while the other three resonances (69.4, 70.4 and 71.9 ppm) belong to the 3,5-OCH$_2$Ph groups (red). Comparing the signal intensities of the two 4-OCH$_2$Ph resonances, the peak at 73.8 ppm appears to be a little weaker, so that the resonance at 73.8 and 74.7 are assigned to the inner and and middle 4-OCH$_2$Ph groups, respectively. With respect to 3,5-OCH$_2$Ph groups, it seems likely that two of the three resonances belong to the middle 3,5-OCH$_2$Ph groups and only one to the inner groups. The exact assignment, however, is not entirely clear.

In the 2D ^{1}H-^{13}C REPT-HSQC spectrum in Figure 4.3 D only one ^{1}H-resonance is observed for each carbon resonance. With respect to the 3,5-OCH$_2$Ph groups, this stands in clear contrast to G1-PMA, G1-PS and G2-PMA (Figure 4.3 A – C). The distribution of 3,5-OCH$_2$Ph ^{1}H chemical shifts in Benz-G2-PMA, however, is rather broad ranging from 2.0 – 5.5 ppm. This suggests a distribution of arrangements of the different 3,5-OCH$_2$Ph groups with respect to their neighboring aromatic rings, with a preferred arrangement resulting in ^{1}H chemical shifts of 3.4 – 4.2 ppm (Table 4.6). Considering the large size of the dendron such a distribution is not very surprising. Comparing these numbers to the chemical shift in solution, π-shifts of Δ = (-0.6) – (-1.5) ppm are determined. Thus, most of the 3,5-OCH$_2$ protons should, on average, be located at 3.0 – 6.0 Å above or below a neighboring aromatic ring (see Figure 2.5). At distances of $\sim$5–6 Å it is, however, not very realistic, to consider only one neighboring aromatic ring. The observed low-frequency shifts should rather be seen as a combination of π-shift effects from several adjacent aromatic ring.

Turning to the aromatic rings, the ^{1}H and ^{13}C chemical shift values observed are similar to their solution-state values as well as to G1-PMA. For the inner and middle aromatic rings only one broad ^{13}C resonance is observed at 107.0-108.2 ppm with a rather weak signal intensity, so that only an approximate ^{1}H chemical shift value, $\sim$7.0 ppm, can be extracted from the ^{1}H-^{13}C 2D REPT-HSQC spectrum (not shown).

Molecular Dynamics. The dynamical properties of Benz-G2-PMA turn out to be more similar to G1-PMA than to G2-PMA. Starting with the outer phenylene rings, a homo- and heteronuclear dipole-dipole coupling of $D_{HH}/\ 2\pi$ = 4.9 kHz (S_{hom} = 61%) and $D_{CH}/\ 2\pi$ = 6.1 kHz (S_{het} = 29%), respectively, is extracted from the sideband patterns in Figure 4.8 D and 4.9 D. The same values were observed for G1-PMA (Figure 4.8 A and 4.9 A). Therefore the dynamics of the outer phenylene rings do not seem to be influenced by the actual size of the dendron (G1 or G2). In other words, an aromatic ring at the periphery of a dendritic side-group, which is part of a linear side-chain displays similar dynamical properties, independent of the generation of the dendron.

Since the ^{13}C resonances of the inner and the middle aromatic rings cannot clearly be distinguished, their segmental dynamics cannot be determined independently. The average dipole-dipole coupling extracted from the spinning sideband pattern in Figure 4.15 is approximately $D_{CH}/\ 2\pi$ = (21.0$\pm$1.0) kHz ($S_{het} \approx$ 100%), showing that the inner and the middle

Table 4.6: ^{1}H and ^{13}C chemical shifts of G1-PMA and and Benz-G2-PMA from ^{1}H-^{13}C REPT-HSQC solid-state correlation spectra and solution-state NMR (in brackets).

	G1-PMA		**Benz-G2-PMA**	
	δ^{13}C [ppm]	δ^1H [ppm]	δ^{13}C [ppm]	δ^1H [ppm]
outer 4-OCH$_2$R	67.8 (69.1)	3.4 (3.8)	68.0 (68.0)	3.2 (3.8)
middle 3,5-OCH$_2$Ph	–*	–*	69.4 (70.7-71.1)	3.4 (4.8-4.9)
			71.9 (70.7-71.1)	4.2 (4.8-4.9)
middle 4-OCH$_2$Ph	–*	–*	74.7 (74.8-75.3)	4.1 (4.8-4.9)
inner 3,5-OCH$_2$Ph	70.6 (70.4)	2.3 (4.7)	70.4 (70.7-71.1)	3.4 (5.0)
	”	4.3 (4.7)		
	”	5.5 (4.7)		
inner 4-OCH$_2$Ph	75.0 (76.1)	4.4 (4.7)	73.8 (74.8-75.3)	3.9 (5.0)
aromatic CHs:				
outer (meta)	114.0 (114.0-114.8)	6.3 (6.6)	114.1 (114.1-114.9)	6.0 (6.5)
outer (ortho)	130.0 (129.0-130.5)	6.7 (7.0)	130.1 (129.1-130.0)	6.5 (6.8)
middle	–*	–*	} 107.0-108.2	} ~7.0
inner	109.0 (109.0)	?** (6.6)	(106.8-107.6)	(6.6-6.8)

* No such group is present in the molecule.

** The signal intensity is too low to reliably determine the ^{1}H chemical shifts.

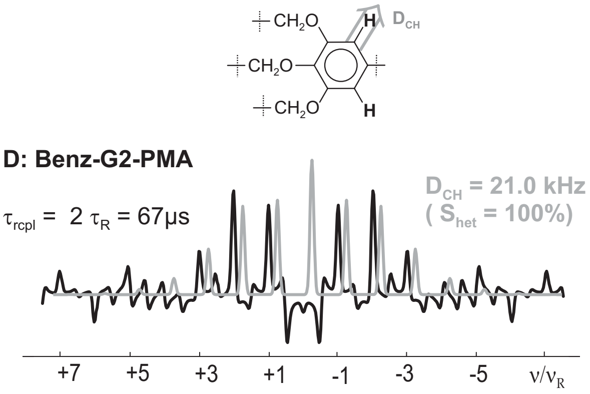

Figure 4.15: *REREDOR spinning sideband patterns. Residual heteronuclear dipole-dipole couplings of the inner and middle aromatic groups of Benz-G2-PMA, recorded under MAS at 30 kHz, (black line = experimental, grey line = calculated).*

aromatic rings are both immobile. From a structural point of view, the middle aromatic rings of Benz-G2-PMA correspond to the outer ones in G2-PMA, because they both represent the second branching point (3,4,5-substitution) in the dendron. The outer aromatic rings in G2-

PMA, however, are not fully immobile (S_{het} = 77%, Figure 4.8 C), which can be explained by the “missing” 4-substituted phenylene rings at the beginning of the alkyl chains. These are capable of π-π stacking, and thus immobilize the middle 3,4,5-substituted aromatic rings in Benz-G2-PMA.

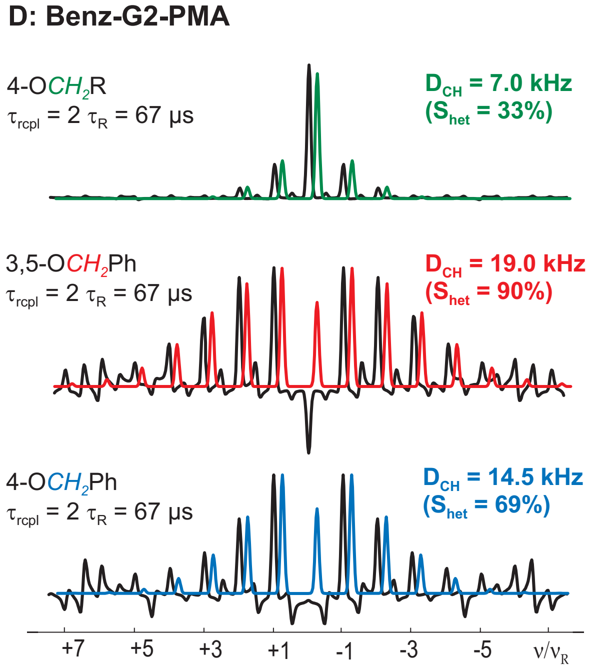

Figure 4.16: *REREDOR spinning sideband patterns. Residual heteronuclear dipole-dipole couplings of the OCH_2 groups of Benz-G2-PMA, recorded under MAS at 30 kHz, (black line = experimental, colored line = calculated).*

Turning to the segmental dynamics of the OCH_2 groups in Figure 4.16, a residual dipole-dipole coupling of $D_{CH}/\ 2\pi$ = 7.0 kHz (S_{het} = 33%) is observed for the 4-OCH_2R groups, which is rather similar to the values observed for G1-PMA and G2-PMA $D_{CH}/\ 2\pi$ = 7.5 kHz, S_{het} = 36%, Figure 4.10). As already explained in Section 4.5 for G2-PMA, the –O– segment provides efficient decoupling, so that the segmental dynamics of the OCH_2R groups are dominated by the alkyl chains. The residual dipole-dipole couplings of the inner and middle 3,5-OCH_2Ph and 4-OCH_2Ph groups cannot be determined independently, because the resolution and signal-to-noise ratio both are rather poor. The average residual dipole-dipole coupling for the inner and middle 3,5-OCH_2Ph and 4-OCH_2Ph groups is $D_{CH}/\ 2\pi$ = 19.0 kHz (S_{het} = 90%) and $D_{CH}/\ 2\pi$ = 14.5 kHz (S_{het} = 69%), respectively. These values are 2–2.5 kHz higher than the ones determined for G1-PMA ($D_{CH}/\ 2\pi$ = 17.0 kHz and 12.0 kHz for 3,5-OCH_2Ph and 4-OCH_2Ph, respectively, Section 4.2), which can be explained in terms of the average that is taken over the inner and middle OCH_2Ph groups. As described above, the middle aromatic rings are immobile, so that the inner OCH_2Ph groups are expected to be immobile, too ($D_{CH}/\ 2\pi$ = 21.0 kHz, S_{het} = 100%). Thus, the six middle 3,5-OCH_2Ph groups should have a coupling of $D_{CH}/\ 2\pi$ = 18.3 kHz, according to ($2_{inner} \times$ 21.0 kHz +

$6_{middle} \times ?) / 8 = 19.0$ kHz → ? = 18.3 kHz. Similarly for 4-OCH_2Ph, the inner OCH_2 group is expected to be immobile while the middle ones are not, so that a residual dipole-dipole coupling of $D_{CH}/2\pi = 12.3$ kHz results for the middle 4-OCH_2Ph. These numbers are very similar to the ones observed for G1-PMA. The residual dipole-dipole couplings of Benz-G2-PMA are summarized in Table 4.7. The comparison of the segmental dynamics to G1-PMA clearly shows a very similar dynamical behavior of the two dendritic units. In both molecules the 3,4,5-substituted aromatic rings are perfectly immobile and a similar mobility gradient is observed along the rest of the dendron.

Table 4.7: Residual dipole-dipole ^1H-^{13}C couplings of Benz-G2-PMA and G1-PMA from REPT-HDOR and REREDOR spinning sideband patterns as well as residual homonuclear ^1H-^1H couplings from DQ sideband patterns.

experimental couplings and order parameters	**G1-PMA** heteronuclear C-H $D_{CH}/2\pi$ (S_{het})	**Benz-G2-PMA** heteronuclear C-H $D_{CH}/2\pi$ (S_{het})	**exp.** couplings and order parameters
		21.0 kHz (100%)	inner aromatic ring
		21.0 kHz (100%)	inner 3,5-OCH_2Ph
		21.0 kHz (100%)	inner 4-OCH_2Ph
inner aromatic ring	**21.0 kHz (100%)**	**21.0 kHz (100%)**	middle aromatic rings
3,5-OCH_2Ph	**17.0 kHz (81%)**	**18.3 kHz (87%)**	middle 3,5-OCH_2Ph
4-OCH_2Ph	**12.0 kHz (57%)**	**12.3 kHz (59%)**	middle 4-OCH_2Ph
outer phenylene rings	**6.1 kHz (29%)**	**6.1 kHz (29%)**	outer phenylene rings
homonuclear H-H			*homonuclear H-H*
$D_{HH}/2\pi$ (S_{hom})	*4.9 kHz (56%)*	*4.9 kHz (56%)*	$D_{HH}/2\pi$ (S_{hom})
4-OCH_2R	**7.5 kHz (36%)**	**7.0 kHz (33%)**	4-OCH_2R

4.7 G1-4EO-PMA vs. G1-PMA

The G1-4EO-PMA macromolecule is very similar to G1-PMA, with the only difference being a linker of four ethoxy (EO) groups between the polymethacrylate backbone and the G1 dendron. G1-4EO-PMA also self-assembles into columns, but the EO linker chain has significant influences. Its impact on the supramolecular structure is quite pronounced, because G1-4EO-PMA displays a higher long-range order than the molecules without EO linker unit, so that thorough small- and wide-angle X-ray diffraction studies could be carried out [Chvalun 96, Chvalun 97, Chvalun 99, Chvalun 01]. From comparing the solid-state NMR data of G1-4EO-PMA and G1-PMA more insight can be gained into the effects of the linker unit on the local arrangement and dynamics of the aromatic rings. These properties can be considered as the actual source of the increased long-range order.

Table 4.8: ^{1}H and ^{13}C chemical shifts of G1-PMA and and G1-4EO-PMA from ^{1}H-^{13}C REPT-HSQC solid-state correlation spectra and solution-state NMR (in brackets).

	G1-PMA		**G1-4EO-PMA**	
	δ^{13}C [ppm]	δ^{1}H [ppm]	δ^{13}C [ppm]	δ^{1}H [ppm]
4-OCH$_2$R	67.8 (69.1)	3.4 (3.8)	68.0 (68.1)	3.5 (3.9)
3,5-OCH$_2$Ph	70.6 (70.4)	2.3 (4.7)	70.3 (71.3)	3.5 (5.0)
	”	4.3 (4.7)		
	”	5.5 (4.7)		
4-OCH$_2$Ph	75.0 (76.1)	4.4 (4.7)	74.5 (74.8)	3.7 (5.0)
EO-linker	–*	–*	70.3 (70.8)	3.5 (3.6)
aromatic CHs:				
outer (meta)	114.0 (114.0-114.8)	6.3 (6.6)	114.0 (114.0-114.6)	6.1 (6.7-6.4)
outer (ortho)	130.0 (129.0-130.5)	6.7 (7.0)	130.7 (129.4-130.3)	6.6 (7.2-7.3)
inner	109.0 (109.0)	?** (6.6)	107.8 (109.6)	6.8 (7.4)

* No such group is present in the molecule.

** The signal intensity in the 2D REPT-HSQC spectrum is too low to reliably determine the ^{1}H chemical shifts.

Chemical shifts. In Table 4.8 selected solid-state chemical shifts of G1-4EO-PMA are compared with the corresponding solution-state values (in brackets), as well as with values of G1-PMA. Similar to G1-PMA, the ^{13}C resonances at 68.0 and 74.5 ppm could be assigned to the 4-OCH$_2$R and the 4-OCH$_2$Ph group, respectively. There is only one more resonance observed at 70.3 ppm, which has to be assigned to the 3,5-OCH$_2$Ph group as well as to the EO linker. Unfortunately these groups turn out to have the same ^{13}C chemical shifts. Based on the solution-state values in Table 4.8, different ^{1}H chemical shifts would be expected for 3,5-OCH$_2$Ph and the linker unit in the solid-state, but basically only a broad ^{1}H resonance at 3.4 – 3.8 ppm is observed for the different OCH$_2$ groups in the 2D ^{1}H-^{13}C REPT-HSQC spectrum (shown in Figure 4.3 E). This is in significant contrast to the observation of many different ^{1}H chemical shifts in G1-PMA, G1-PS and G2-PMA (see Figures 4.3 A–C) and leads to the conclusion that the EO linker introduces some degree of flexibility into the system, thereby allowing for a distribution of conformations and, as a consequence of this, a distribution of ^{1}H chemical shifts. Correspondingly, a broad Gaussian-type lineshape is found, which reflects the homogeneous distribution of local conformations. It should be noted that the protons of the linker do not experience aromatic ring currents at all, but remain at their resonance position. Hence, the EO linker and the aromatic units are spatially separated in the columns.

Molecular Dynamics. Turning to the dynamics of G1-4EO-PMA, the TEDOR spectra in Figure 4.6 D show that the signal of the 4-OCH_2R group disappears at a recoupling time of four rotor periods, while the corresponding signal is still present in the case of G1-PMA (Figure 4.6 A). Hence, the 4-OCH_2R group is less mobile in G1-4EO-PMA than in G1-PMA. Moving toward the inner part of the dendron, the 4-OCH_2Ph group remains basically as mobile as the 4-OCH_2R group. The peak at 70.3 ppm is dominated by the EO linker rather than the 3,5-OCH_2R group, and its mobility appears comparable to 4-OCH_2R. This observation is proven by REREDOR spinning sideband patterns (Figure 4.17), which yield a residual heteronuclear coupling of $D_{CH}/ 2\pi$ = 11.5 kHz and 11.0 kHz for the EO linker and the 4-OCH_2R group, respectively, corresponding to order parameters $S_{het} = 52 - 55\%$. Thus, considering all OCH_2 segment mobilities, it can be concluded that G1-4EO-PMA exhibits basically no mobility gradient through its dendritic side-groups.

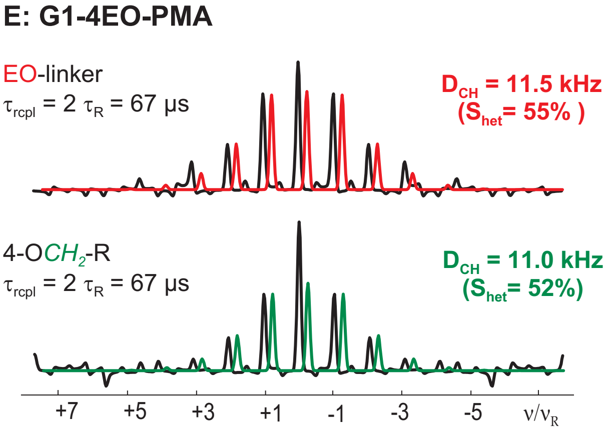

Figure 4.17: *REREDOR spinning sideband patterns. Residual heteronuclear dipole-dipole couplings of a OCH_2 group of G1-4EO-PMA below T_g (T = 15 °C), recorded under MAS at 30 kHz, (black line = experimental, green line = calculated).*

For the outer phenylene rings, residual homo- and heteronuclear couplings of $D_{HH}/ 2\pi$ = 4.7 kHz (Figure 4.9 D) and $D_{CH}/ 2\pi$ = 6.3 kHz (Figure 4.8 D), respectively, are measured, which are similar to G1-PMA (Figures 4.9 A and 4.8 A). Therefore the outer phenylene rings of G1-4EO-PMA undergo a 180° flip in addition to a motion of the whole side-chain with a chain order parameter of $S_{hom} \approx 60\%$, as was found for G1-PMA above. This value is not significantly higher than the one determined for the EO linker ($S_{het} = 55\%$) and the 4-OCH_2R group ($S_{het} = 52\%$), which again shows that the dendrons of G1-4EO-PMA exhibit a very uniform motion, in contrast to G1-PMA. Obviously, the EO linker mechanically decouples the polymer backbone from the dendron such that the immobility of the backbone no longer induces a mobility gradient through the dendron. In this way, the aromatic units of the dendrons gain motional flexibility which allows them to unperturbedly arrange in a favorable fashion.

4.8 Conclusion

Dipolar ^{1}H-^{1}H and ^{1}H-^{13}C recoupling NMR methods under fast MAS allow a detailed analysis of the local structure and the local molecular dynamics in supramolecular dendritic polymers. This Chapter focuses on how dendritic side-groups attached to a polymer backbone arrange in a supramolecular fashion, and how the local molecular packing and dynamics of this assembly are influenced by (i) the polymer backbone, (ii) the generation of dendritic side-groups or (iii) the type and size of linkers. All five polymers investigated self-assemble in a columnar fashion, which is well organized below as well as above T_g.

High local order parameters of up to S = 100%, as obtained from ^{1}H-^{13}C and ^{1}H-^{1}H dipolar recoupling experiments, and pronounced aromatic ring-current effects on ^{1}H chemical shifts, as observed in ^{1}H-^{13}C correlation spectra, provide evidence for a high degree of order in the packing of the dendrons. The pronounced local order among the aromatic moieties implies that these parts play a structure-directing role in the systems. Using aromatic ring current effects on ^{1}H chemical shifts as distance constraints, "edge-on" and "face-on"-type arrangements can be identified as characteristic features of the dendron packing. Within the dendrons (except for G1-4EO-PMA, see below), large mobility gradients are found to range from $S_{het} \approx 100\%$ for the inner aromatic rings to $S_{het} \approx 30\%$ for the outer ones. Hence, the core of the column consists of a helical polymer backbone which is surrounded by the inner, well-organized and relatively rigid part of the dendrons. At the outer part of the dendrons, mobile dodecyl chains build an additional flexible layer toward the surface of the columns, which further stabilizes them.

Besides these common general features, a more detailed study of the individual properties of the dendritic polymers reveals further similarities as well as a few significant differences among them. G1-PMA and G1-PS generally exhibit very similar overall properties: They do not differ much in their T_g value and their melting temperature, and a very similar arrangement of the dendritic moieties of G1-PMA and G1-PS is observed. The π-shifts experienced by the OCH_2Ph protons are largely identical for both systems, which indicates similar ring-current effects and, thus, implies that the arrangement of the aromatic rings and OCH_2 groups must be essentially the same for G1-PMA and G1-PS. This is further confirmed by the similar dynamical properties observed for both systems. From this comparison, it becomes very obvious that the polymer backbone does not have a significant influence on the structure adopted by the system. Rather, the aromatic moieties in the dendrons are the driving force in the self-assembly process, inducing a helical arrangement of both the PS and the PMA chain.

Comparing dendrons of first and second generation (i.e., G1-PMA vs. G2-PMA and Benz-G2-PMA), the OCH_2 groups and aromatic rings of the G2-dendron arrange in a fashion comparable to G1. In G2-PMA, however, more pronounced π-shifts are observed, which indicate a higher density of aromatic rings around the OCH_2 groups, while the much larger number of aromatic rings present in Benz-G2-PMA leads to a distribution of arrangements of the different OCH_2 groups with respect to their neighboring aromatic rings. Turning to the dynamic properties, very similar segmental mobilities are observed for G1- and G2-dendrons. The 4-OCH_2R groups of G2-PMA and Benz-G2-PMA turn out to be as mobile as in G1. Obviously, the dynamics of the long alkyl chain is, even at the α-CH_2 position, remarkably independent of the phenylene dynamics, which are different for G2-PMA as compared to G1-PMA and Benz-G2-PMA. This decoupling effect can be attributed to the –O– segment between the alkyl chain and the phenylene ring. As a general estimate, the local order parameter is found to drop by a factor of $\sim$ 1.5 behind the –O– linker. The 4-substituted phenylene groups in Benz-G2-PMA (not present in G2-PMA) are also as mobile as in G1-PMA, despite the much larger size of the G2-dendron. In the case of 3,4,5-substituted aromatic rings some segmental mobility is observed if linear O-dodecyl chains (without 4-substituted phenylene rings) are attached, as in G2-PMA. Otherwise the 3,4,5-substituted aromatic rings are perfectly immobile, no matter if they are the first or second branching point in the dendron (Benz-G2-PMA). Thus, the dynamical properties of the different segments are largely independent of the size of the dendron, so that a similar mobility gradient is observed for G1- and G2-dendrons.

G1-4EO-PMA deviate significantly from the other three materials. With regard to its macroscopic properties, G1-4EO-PMA exhibits a higher long-range order below T_g. This effect can be attributed to the flexible EO linker unit, which allows for a uniform degree of mobility (as reflected in the uniform order parameter S_{het} = 52%-55%) throughout the dendron instead of a mobility gradient, which is observed, for example, within the G1-PMA dendron. In analogy to the –O– segment mentioned above, the EO linker unit is capable of providing efficient mechanical decoupling between the polymer backbone and the attached dendron, such that the latter can arrange in a favorable fashion instead of being forced to mediate between the rigid backbone and the flexible alkyl chains. The different arrangement of the G1-dendrons in G1-PMA and G1-4EO-PMA is also reflected by the very different ring current effects on the ^{1}H chemical shifts detected for the two systems.

In conclusion, this investigation shows how advanced solid-state NMR experiments can elucidate the local structure of supramolecular architectures as well as the site-specific dynamics of different molecular building blocks in large complex systems. In this way, valuable information is provided which helps to quantify local interactions, to identify structure-directing elements and to understand principal order phenomena, which all together determine the self-assembly process of supramolecular systems.

Chapter 5

Homonuclear ^{1}H NMR investigation on dendritic molecules forming columnar structures with a polycyclic aromatic core

In contrast to Chapter 4, the dendritic molecules investigated in this Chapter are not part of a polymer chain, but individual molecules with a pyrene or naphthalene ring attached via a linker [Percec 02b]. These molecules also self-organize in a columnar fashion, where the polycyclic aromatic units build π-stacks in the center of the column and are surrounded by dendritic units with partially fluorinated alkyl chains. This columnar structure is observed below as well as above T$_g$, and the liquid crystalline phase is hexagonal columnar Φ_h, similar to the molecules described in the previous Chapter. The columns are of nanometer scale, and the fluorinated periphery shields the core of the columns from external influences such as moisture. The π-stacks of aromatic donor molecules in the center of these columns exhibit charge carrier mobilities of μ_{hole} = 9.4$\times$10^{-4}–1.5$\times$10^{-3} cm^{2}V^{-1}s^{-1} in the liquid crystalline phase [Percec 02b]. Since molecules of this type are promising in terms of electronic and optoelectronic applications, a detailed knowledge about their structural and dynamical properties is desirable. In the following, it is demonstrated how simple one-dimensional ^{1}H solid-state NMR spectra recorded under fast MAS (30 kHz) can already provide valuable information with respect to the local structure of the supramolecular assembly. In addition it is shown, how ^{1}H Double Quantum (DQ) spectra and DQ spinning sideband patterns can give a more detailed insight into structural and dynamical similarities and differences of the molecules under investigation. The properties of the following six molecules are investigated:

(A) 2{1-[(pyrylacetyl)oxy]ethoxy}ethyl 3,4,5-Tris(5,5,6,6,7,7,8,8,9,9,10,10,11,11,12,12-heptadecafluoro-dodecyl-1-oxy)benzoate, henceforth referred to as **G1-2EO-pyr,**

(B) 2{1-[(naphtylacetyl)oxy]ethoxy}ethyl 3,4,5-Tris(5,5,6,6,7,7,8,8,9,9,10,10,11,11,12,12-heptadecafluoro-dodecyl-1-oxy)benzoate, henceforth referred to as **G1-2EO-napht,**
(C) 2-(1-naphthyl)butyl 3,4,5-Tris(5,5,6,6,7,7,8,8,9,9,10,10,11,11,12,12-heptadecafluoro-dodecyl-1-oxy)benzoate, henceforth referred to as **G1-4Me-pyr,**
(D) 2-(1-naphthyl)ethyl 3,4,5-Tris(5,5,6,6,7,7,8,8,9,9,10,10,11,11,12,12-heptadecafluoro-dodecyl-1-oxy)benzoate, henceforth referred to as **G1-2Me-napht,**
(E) 4-(1-naphthyl)butan-1-ol, henceforth referred to as **pyr-OH,**
(F) 2-(1-naphthyl)ethanol, henceforth referred to as **napht-OH**

The four molecules (A), (B), (C) and (D) are depicted in Figure 5.1. They all have a dendritic group of generation 1 with partially fluorinated alkyl chains -O$(CH_2)_4(CF_2)_7CF_3$, but differ in their polycyclic aromatic core and linker-unit. The latter connects the polycyclic aromatic core to the dendron. (A) G1-2EO-pyr and (C) G1-4Me-pyr both have a pyrene-core, but they differ in their linker-unit, where the -$CH_2COO(CH_2CH_2O)_2CO$- linker is more flexible than the -$(CH_2)_4OCO$- one. (B) G1-2EO-napht and (D) G1-2Me-napht, in contrast, both have a naphthalene-core instead of a pyrene-core, while their linker-units are similar to the ones of (A) G1-2EO-pyr and (C) G1-4Me-pyr, respectively. The properties of these four molecules ((A) – (D)) are also compared to a pyrene (E) and a naphthalene (F) ring with linker, but without a dendritic group attached, to gain more insight into the role the dendritic group plays in the stacking of the pyrene and naphthalene rings. The phase transition temperatures are summarized in Table 5.1.

Table 5.1: *Phase transition temperatures of molecules (A) – (D) and (E) –(F) from DSC measurements (2^{nd} heating, with a scanning rate of 10°C/min) [Percec 02a] and ^{1}H NMR measurements, respectively.*

	solid → LC (Φ_h)	LC → melt
(A) G1-2EO-pyr	17 °C	98 °C
(B) G1-2EO-napht	24 °C	74 °C
(C) G1-4Me-pyr	13 °C	82 °C
(D) G1-2Me-napht	26 °C	81 °C
(E) pyr-OH	–	~60 °C
(F) napht-OH	–	~50 °C

5.1 Structural investigation

Considering the proton spectra in Figure 5.2, the resolution of the spectra increases with temperature going from the solid state via the hexagonal columnar liquid crystalline (LC) phase to the melt. Of course, this is due to an increase in the mobility of the molecules with temperature, leading to a decrease in the effective dipolar couplings (due to motional averaging) and

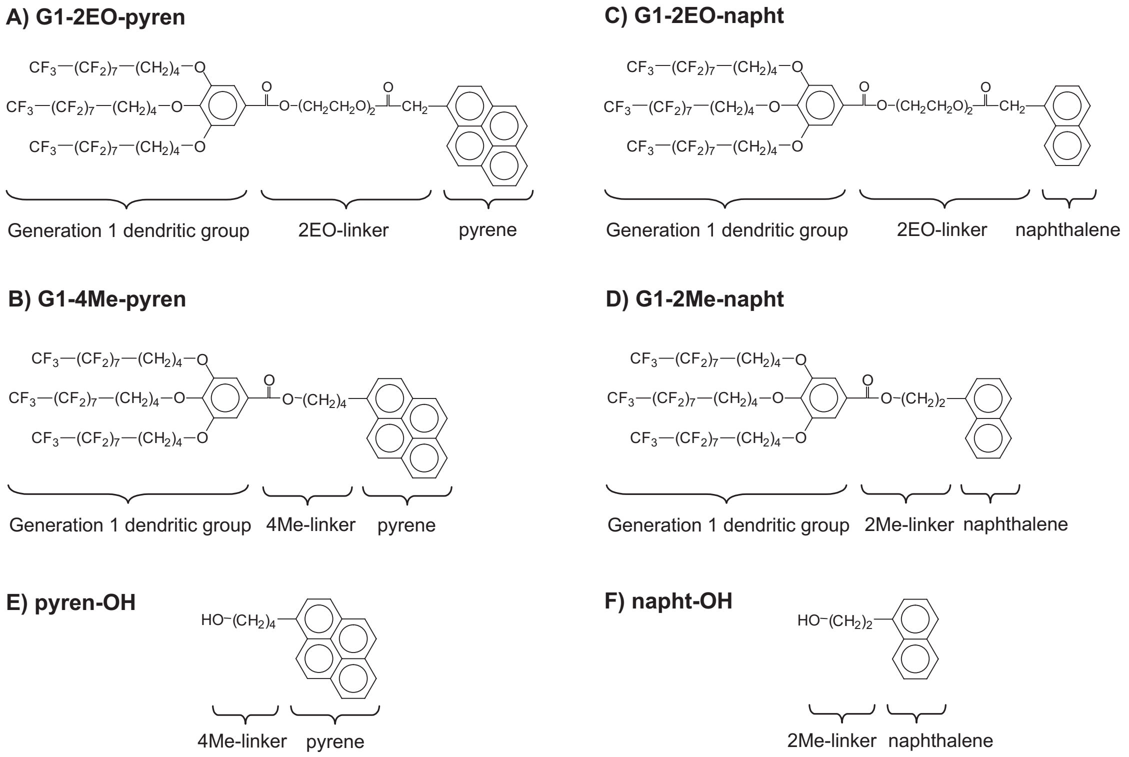

Figure 5.1: *Systems investigated in this Chapter. Molecules (A) – (D) consist of a dendron of generation 1 with fluorinated alkyl chains attached via a linker-unit to a pyrene or naphthalene core and self-assemble in a columnar structure. Molecules (E) and (F) do not have a dendritic group attached.*

hence causing less broadening of the resonance lines. Comparing the spectra in the LC phase, much narrower peaks are observed for G1-2EO-pyr and G1-2EO-napht than for G1-4Me-pyr and G1-2Me-napht. This difference in linewidth is also a striking feature of the 2D DQ spectra in Figure 5.4. It shows, that the longer and more flexible EO-linker allows for a greater mobility of the molecules in the LC-phase. This point will be discussed in more detail in the following Section.

Comparing the solution spectra to the bulk-spectra (solid, LC and melt), it becomes apparent that there are π-shifts present to lower frequencies for all ^{1}H resonances (aromatic, OCH_2 and alkyl) in all six molecules, as indicated by the white arrows in Figure 5.2. Generally, similar π-shifts mean similar π-electron densities surrounding the respective proton in a molecular assembly, pointing at a similar packing of the molecules. Comparing the π-shifts of the aromatic, OCH_2 and alkyl groups in each molecule for the melt, the LC (Φ_h) and the solid phase, two important points are to be noted: (i) For G1-2EO-pyr and G1-2EO-napht, the π-shifts observed for the aromatic and the OCH_2R protons increase when going from the solid to the LC phase, but remain similar for the transition to the melt. Therefore, the π-electron density of the LC phase and the melt must be comparable, suggesting a similar arrangement of the molecules in both phases. Hence, the columnar structure of the liquid crystalline phase

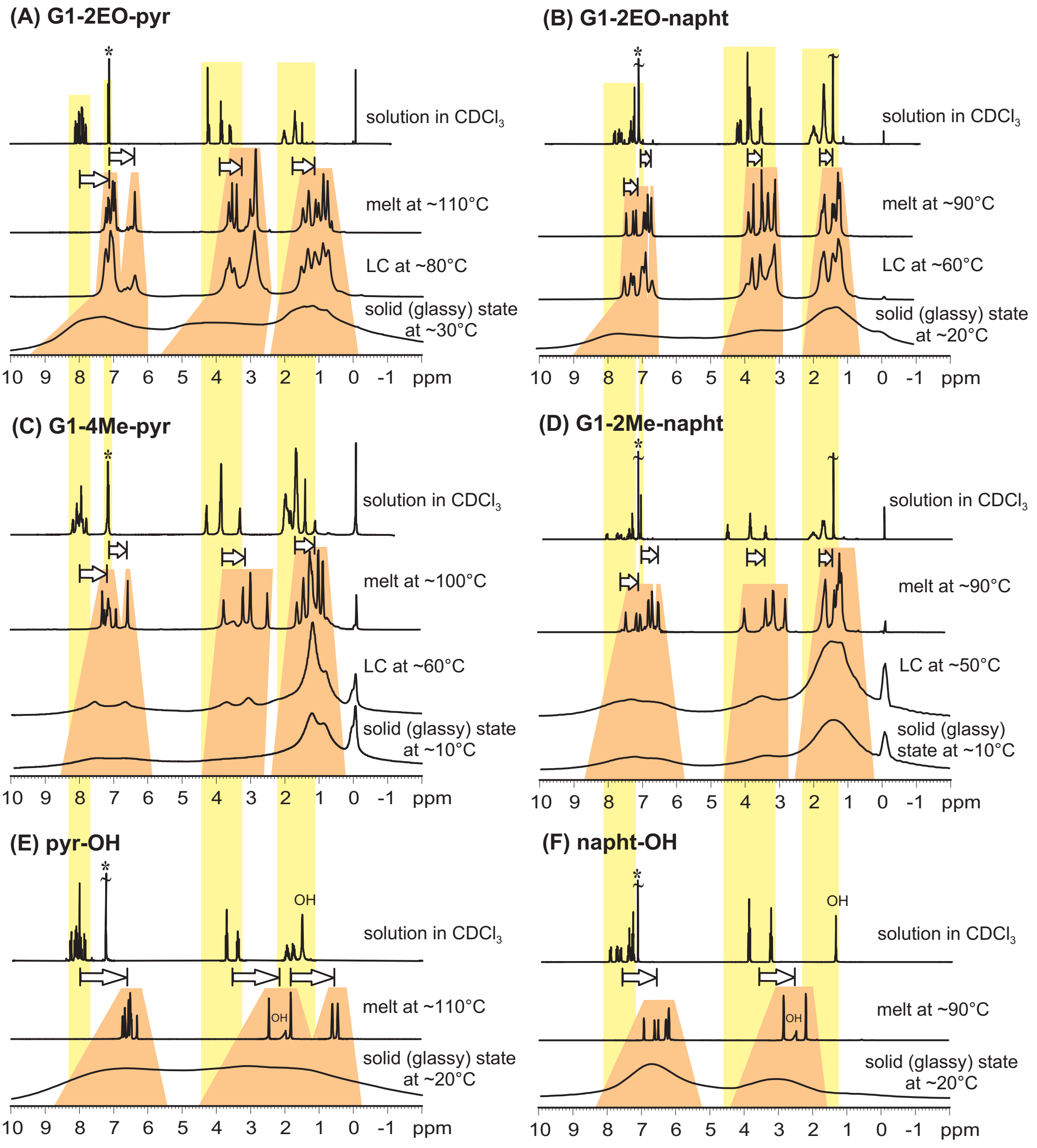

Figure 5.2: *^{1}H one-pulse spectra of molecules (A) – (F) in the solid glassy state, the hexagonal liquid crystalline phase and the melt recorded at 30 kHz MAS. The solution spectra were measured in CDCl$_3$. The white arrows indicate the π-shifts present in the solid-state, the liquid crystalline phase and the melt.*

is expected to persist in the melt. The difference in π-shifts observed for the solid and the LC phase can be explained in terms of a slightly different packing of the molecules in the column. In the solid phase, the assembly might be kinetically controlled, while in the LC phase the thermodynamically preferred arrangement is achieved. (ii) For G1-4Me-pyr and G1-2Me-napht the observed π-shifts are comparable for all three phases. Therefore, the π-electron density and, thus, also the molecular assembly in the column are similar in all three phases.

For a quantitative investigation of the π-shifts, it is necessary to compare the chemical shift of the individual CH_n group observed in solution with the corresponding chemical shift in the bulk. Therefore, assignment of the different peaks is required.

5.1.1 Assignment of ^1H chemical shifts

The assignment of the solution spectra is easily carried out, interpreting the relative intensities of the peaks and their J-splittings. In the LC phase, peak assignment was aided by 2D Double Quantum (DQ) spectra (Figure 5.4) in addition to the relative intensities of the peaks.

Taking G1-2EO-pyr as an example (see Figure 5.3), the resonances in solution between 7.8 and 8.2 ppm can be assigned to the pyrene protons. The aromatic protons of the dendron are observed at 7.2 ppm (almost at the same position as the solvent peak). The peaks at 3.9 ppm are assigned to the OCH_2R groups (green in Figure 5.3), while the two triplets at ~4.2 ppm and the multiplet at 3.6 ppm belong to the OCH_2CH_2-linker groups (marked blue). Finally, the singlet at 4.2 ppm corresponds to the CH_2 group attached to the naphthalene ring (marked pink).

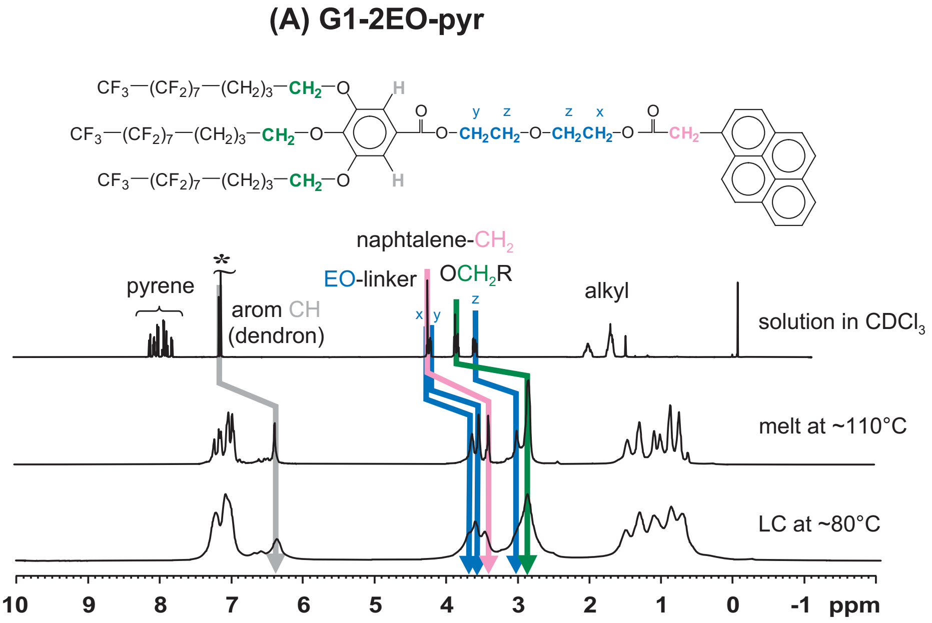

Figure 5.3: *Assignment of ^1H chemical shifts of G1-2EO-pyr in solution as well as in the LC-phase and the melt.*

Turning to the LC-phase, the two-dimensional DQ spectra in Figure 5.4 facilitate the assignment of the different resonances. Looking at the spectrum of (A) G1-2EO-pyr, it is apparent that the diagonal and cross peaks between 6.9 and 7.4 ppm must arise from the pyrene core of the molecule (marked purple in the spectrum), while the resonance at 6.4 ppm belongs to the two aromatic protons of the dendron. As expected, the latter show a cross-peak to the adjacent OCH_2R groups (2.9 ppm) of the alkyl chains (depicted in dark green) and, in addition, also a weak cross-peak to other CH_2 groups of the alkyl chains (depicted in light green). The cross-peaks marked in blue at 3.7–3.6 ppm and 3.0 ppm correspond

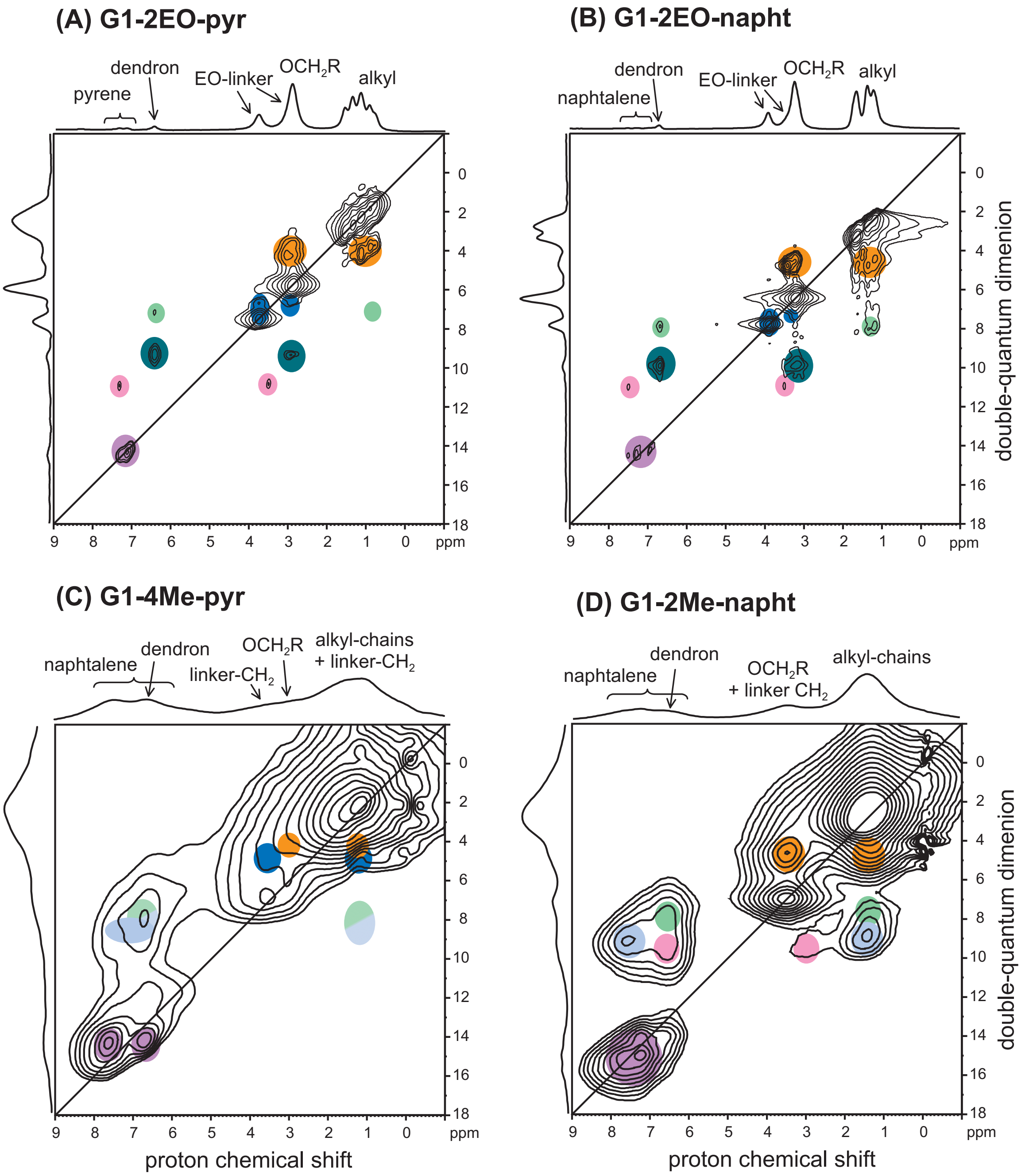

Figure 5.4: *Two-dimensional Double-Quantum (DQ) spectra of molecules (A) – (D), in the liquid crystalline phase, recorded at 30 kHz MAS with an excitation time of* $\tau_{exc} = 4\ \tau_R$ *and 2* τ_R *for molecules (A),(B) and (C),(D), respectively.*

to the resonances of the neighboring CH$_2$ groups in the linker (labeled as x, y and z in the ^{1}H spectrum in Figure 5.3). The orange region in the DQ spectrum indicates cross-peaks

Table 5.2: ^{1}H chemical shifts observed for the different CH and CH$_2$ groups of molecules (A) – (F) in solution and in the bulk and the resultant π-shifts.

	(A) G1-2EO-pyr			**(B) G1-2EO-napht**		
	solution $\delta(^1\mathrm{H})$ [ppm]	melt, LC $\delta(^1\mathrm{H})$ [ppm]	π-shift Δ [ppm]	solution $\delta(^1\mathrm{H})$ [ppm]	melt, LC $\delta(^1\mathrm{H})$ [ppm]	π-shift Δ [ppm]
pyrene/naphthalene	7.8-8.2	6.9-7.4	$\sim$**0.9**	7.2-7.8	6.8-7.5	$\sim$**0.4**
arom CH (dendron)	7.2	6.4	**0.8**	7.1	6.7	**0.4**
OCH$_2$R	3.9	2.9	**1.0**	3.9	3.1	**0.8**
OCH$_2$ (linker)	4.2	3.6	**0.6**	4.2	3.9	**0.3**
	4.2	3.7	**0.5**	4.1	3.8	**0.3**
	3.6	3.0	**0.6**	3.5	3.3	**0.2**
pyr-/napht-CH$_2$-	4.2	3.4	**0.8**	3.9	3.5	**0.4**

	(C) G1-4Me-pyr			**(D) G1-2Me-napht**		
	solution $\delta(^1\mathrm{H})$ [ppm]	melt, LC, solid $\delta(^1\mathrm{H})$ [ppm]	π-shift Δ [ppm]	solution $\delta(^1\mathrm{H})$ [ppm]	melt, LC, solid $\delta(^1\mathrm{H})$ [ppm]	π-shift Δ [ppm]
pyrene/naphthalene	7.7-8.2	6.9-7.4	$\sim$**0.8**	7.2-8.1	6.6-7.5	$\sim$**0.6**
arom CH (dendron)	7.2	6.6	**0.6**	7.0	6.5	**0.5**
OCH$_2$R	3.9	3.0, 3.2*	**0.9, 0.7***	3.8	3.1, 3.3*	**0.7, 0.5***
-OCO-CH$_2$-dendron	4.3	3.8	**0.6**	4.5	4.0	**0.5**
pyr-/napht-CH$_2$-	3.3	2.5	**0.8**	3.4	2.8	**0.6**

	(E) pyr-OH			**(F) napht-OH**		
	solution $\delta(^1\mathrm{H})$ [ppm]	melt $\delta(^1\mathrm{H})$ [ppm]	π-shift Δ [ppm]	solution $\delta(^1\mathrm{H})$ [ppm]	melt $\delta(^1\mathrm{H})$ [ppm]	π-shift Δ [ppm]
pyrene/naphthalene	7.8-8.3	6.3-6.8	**1.5**	7.2-8.0	6.2-7.0	**1.0**
CH$_2$ (“linker”)	3.5	2.1	**1.4**	3.5	2.5	**1.0**
	1.8	0.5	**1.3**			

* The first and second value correspond to the 3, 5 and 4-substituted OCH$_2$R groups on the aromatic ring, respectively.

between the OCH_2R and the other CH_2 groups of the alkyl chains. Finally, there is a weak cross-peak observed between the resonances at 8.4 ppm and 3.4 ppm (marked pink). Hence, 3.4 ppm must be the chemical shift belonging to the pyrene-CH_2 protons, since it is the only one expected to show a proximity to protons of the pyrene ring. Thus, all the resonances observed for the LC phase and the melt in the ^1H spectrum in Figure 5.3 could be assigned, and the result agrees well with the relative intensities of the proton peaks. The peaks of the other three molecules ((B) – (D)) have been assigned in an analogous manner. For pyr-OH and napht-OH the assignment is obvious. Table 5.2 summarizes the chemical shift values of the different CH_n groups and the resultant π-shifts for all six molecules (A) – (F).

5.1.2 Analysis of π-shifts

Starting with the π-shifts observed for the polycyclic aromatic protons (pyrene and naphthalene), listed in Table 5.2, the shifts observed for (A) G1-2EO-pyr and (C) G1-4Me-pyr (Δ = 0.9 and 0.8 ppm, respectively) are more pronounced than for (B) G1-2EO-napht and (D) G1-2Me-napht (Δ = 0.4 and 0.6 ppm, respectively). These π-shifts must be an effect of the stacking of the pyrene and naphthalene rings, as depicted schematically for pyrene in Figure 5.6a. Therefore, it is not surprising that the pyrene rings, being the larger polycyclic aromatic unit, induce stronger π-shifts than the naphthalene rings. Altogether, the core of the column consists of four parallel π-stacks [Percec 02b], schematically illustrated in Figure 5.6b. Larger π-shifts are also observed for pyr-OH (Δ = 1.5 ppm) as suppose to napht-OH (Δ = 1.0 ppm) listed in Table 5.2. When comparing pyr-OH and napht-OH with the respective dendritic molecules (A) – (D), however, significantly larger π-shifts are observed for pyr-OH and napht-OH, which can be explained in terms of a higher π-electron density. This arises from a different packing of the molecules, which is expected to be similar to the one shown in Figure 5.5 for pyrene and naphthalene and is clearly not columnar.

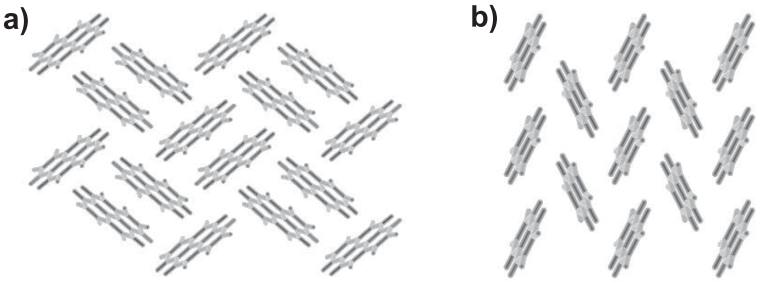

Figure 5.5: *Crystal structure of a) pyrene and b) naphthalene [CSD].*

Turning to the aromatic protons of the dendron, π-shifts similar to those of the polycyclic aromatic protons are observed. Again, they are a little larger for G1-2EO-pyr (A) and G1-4Me-pyr (C) (Δ = 0.8 and 0.6 ppm, respectively) than for G1-2EO-napht (B) and G1-2Me-napht (D) (Δ = 0.4 and 0.5 ppm, respectively). These π-shifts can hardly be induced by the polycyclic aromatic core, unless some sort of backfolding of the molecules takes place, the possibility of which will be discussed in the following Section. Without backfolding, the π-shifts observed for the aromatic protons of the dendron can only be induced by the aromatic rings of neighboring dendrons. In Section 2.5 of Chapter 2 the theoretical chemical-shift displacement was displayed, which a nuclear spin would experience when placed at a given position relative to a phenol molecule. Figure 2.12 shows that a shift of 0.8–0.4 ppm to lower frequencies can be induced by a single aromatic ring located above or below the respective proton, at a distance of 3.5–4.5 Å. This suggests a helical arrangement, as depicted in Figure 5.6b, for all four molecules (A) – (D). In this assembly one aromatic proton of the dendron is located underneath the aromatic ring of the adjacent dendron at an average distance of approximately 3.5–4.5 Å (depending on the molecule). The other aromatic proton lies above the aromatic ring of the neighboring dendron on the other side, also at an average distance of approximately 3.5–4.5 Å. It should be noted that Figure 5.6b is, of course, only a schematic visualization of principal structural features and should be taken as a suggestion, rather than a part of the actual structure.

The resonances between 2.8 and 4.5 ppm in Figure 5.2 correspond to the OCH_2R and the linker protons. Again, larger π-shifts are observed for the two molecules with a pyrene core than for the molecules with a naphthalene core. Comparing the different resonances listed in Table 5.2, it is apparent that the OCH_2R protons of the alkyl chains experience stronger π-

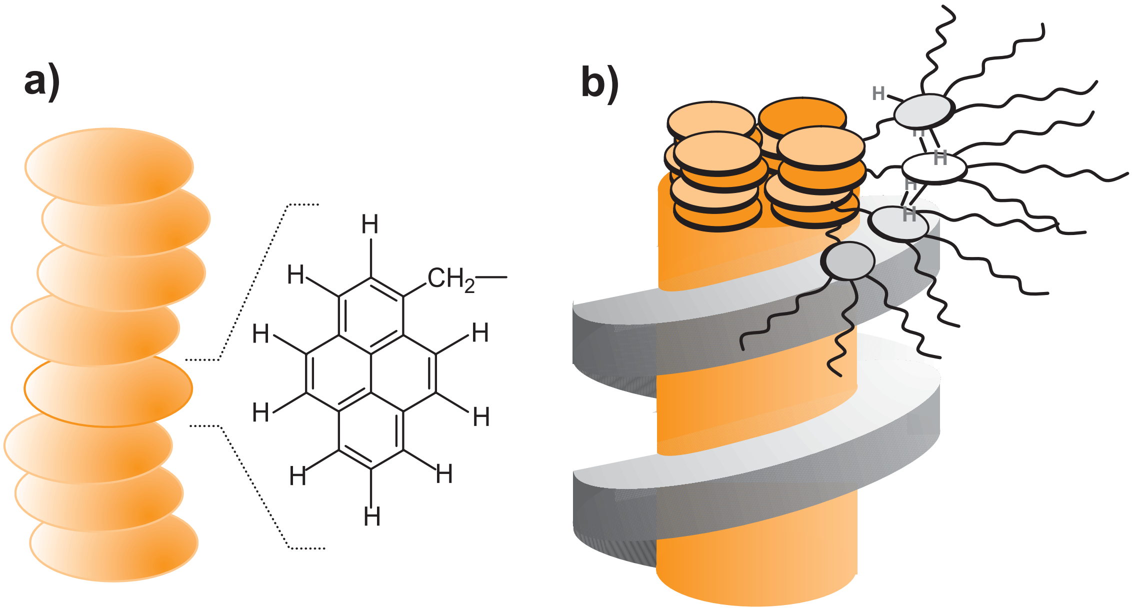

Figure 5.6: *Schematic visualization of the supramolecular columnar structure of molecules (A) – (D): a) Stacking of pyrene rings in the center of the column (similar for naphthalene rings). b) Helical arrangement of the dendrons in the column, such that the aromatic protons of the dendron are located above/ underneath the adjacent dendritic aromatic ring. The orange and grey disks represent the polycyclic aromatic core and the aromatic ring of the dendron, respectively.*

shifts than the linker protons. Out of the protons of the linker, the CH_2 group next to the pyrene or naphthalene ring (pyr-/napht-CH_2 in Table 5.2) experiences the most pronounced π-shifts. This is not surprising, because the pyrene and naphthalene rings are displaced with respect to each other in the column, so that the pyr-/napht-CH_2 groups are influenced by the shielding effects of the pyrene/naphthalene rings above and below. From a sterical point of view and neglecting backfolding effects, the OCH_2R groups can only experience ring-current effects from dendritic aromatic rings of neighboring molecules, while the CH_2 groups of the linker can also be influenced by the π-electrons of the polycyclic aromatic core. Nevertheless, the π-shifts observed for the linker groups are on average weaker. Therefore, the linker unit must be spatially separated to a large extent from the polycyclic aromatic core and the dendritic unit, which is discussed in more detail in Section 5.1.3.

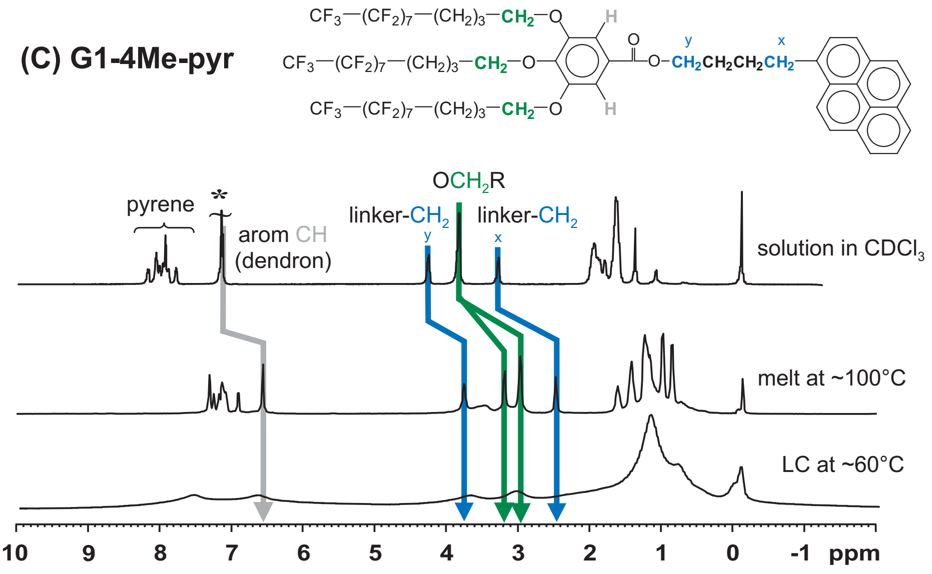

Figure 5.7: *Assignment of ^1H chemical shifts of G1-4Me-pyr in solution as well as in the LC-phase and the melt. Two different ^1H chemical shifts are observed for the OCH_2R protons in the melt and LC phase (marked green).*

With respect to the OCH_2R groups another interesting feature should be mentioned. The ^1H spectra of G1-4Me-pyr and G1-2Me-napht show two different resonances for the OCH_2R groups in the melt and LC-phase (Figure 5.7 and Table 5.2), while for G1-2EO-pyr and G1-2EO-napht only one resonance is observed (Figure 5.3 and Table 5.2). These two resonances can be attributed to different π-shifts experienced by the OCH_2R groups in 3,5 and 4-position on the dendritic aromatic ring. This inequivalence of 3,5- and 4- substituted OCH_2R groups has already been observed for the dendritic polymer G2-PMA in the last Chapter. The present case shows that it is strongly dependent on the linker unit. Short and rigid linker units, as in G1-4Me-pyr and G1-2Me-napht, lead to an arrangement of the dendrons in the column where the 3,5 and 4-OCH_2R protons experience different π-shifts from neighboring aromatic rings, while longer and more flexible linkers, as in G1-2EO-pyr and G1-2EO-napht, give rise to an arrangement of the dendritic groups where all OCH_2R groups experience the same π-shifts. Another explanation could be a larger mobility of the dendritic units in G1-2EO-pyr and G1-2EO-napht, leading to an average π-shift experienced by all three OCH_2R protons. Since the splitting of the OCH_2R resonances for G1-4Me-pyr and G1-2Me-napht is already observed in the melt, an explanation in terms of different mobilities can, however, be ruled out.

5.1.3 Separation of aromatic and aliphatic region

A helical-type arrangement of the molecules as depicted schematically in Figure 5.6, suggests a spacial separation of the polycyclic aromatic core from the dendritic groups. This picture is supported by the relatively weak π-shifts observed for the linker-protons mentioned above. For G1-4Me-pyr and G1-2Me-napht there are however indications of a backfolding of molecules in the column, which is not observed for G1-2EO-pyr and G1-2EO-napht.

In the 2D DQ spectra of G1-2Me-napht in Figure 5.4 two different cross peaks can be distinguished between aromatic and aliphatic protons. The cross peak depicted in light green can be explained by a spacial proximity of the aromatic protons of the dendron and the alkyl chain, analogous to G1-2EO-pyr and G1-2EO-napht. The cross peak marked light blue, however, indicates a proximity between the naphthalene protons and the alkyl chain. Such a proximity could arise from a backfolding of some molecules. In the case of G1-4Me-pyr (Figure 5.4) only one cross peak is observed between the aromatic and the alkyl protons. This could either arise from a proximity of the dendritic aromatic protons and the alkyl chains (light green) or the pyrene protons and the alkyl chains (light blue) or a superposition of both.[1] Again, this indicates the possibility of a backfolding of some molecules in the column. The properties of the columnar assembly, however, do not seem to be influenced very significantly by such a backfolding of molecules. Also, the backfolding of G1-4Me-pyr and G1-2Me-napht has no measurable influence on the π-shifts observed for the aromatic protons of the dendron and the OCH_2R groups (Section 5.1.2). If it did, the proximity to the polycyclic aromatic core would cause larger π-shifts than in G1-2EO-pyr and G1-2EO-napht (not subject to backfolding effects) and not smaller ones (Table5.2). Nevertheless, it is quite clear that a longer and more flexible linker unit, as in G1-2EO-pyr and G12EO-napht provides a much better spatial separation of the dendritic and polycyclic aromatic moieties of the molecules and prevents backfolding phenomena much more efficiently.

---

[1] The corresponding cross peaks on the alkyl side of the 2D DQ spectrum is missing. This is a phenomenon often observed in the tail region of strong aliphatic peaks. It can be attributed to spectral distortions due to a mobility of the alkyl chains on then NMR time-scale [Schnell 98, Brown 00b].

Conclusion:

- For each dendritic molecule (A) – (D), similar π-shifts are observed in the LC-phase and the melt, suggesting that the columnar structure of the solid and LC-phase persists in the melt, despite the increase in mobility of the system.

- For pyrene and naphthalene without a dendritic group (pyr-OH and napht-OH) even larger π-shifts are observed. These can be explained in terms of a higher π-electron density caused by a different (not columnar) packing of the molecules, showing that the columnar structure is induced primarily by the dendrons and not the polycyclic aromatic rings.

- The pyrene and naphthalene rings stack on top of each other in the center of the column. They are somewhat displaced with respect to each other, so that their π-electrons shift the protons of the ring above and below to lower frequencies.

- Pyrene rings induce larger π-shifts than naphthalene rings, simply because pyrene is the larger polycyclic aromatic unit.

- The aromatic protons in the dendron experience significant ring-current-effects from aromatic rings of neighboring dendrons. This suggests a helical arrangement of the molecules in the column.

- The CH_2 groups of the linker-units experience significantly weaker π-shifts than the OCH_2R protons of the alkyl chains. Therefore the linker-units must be pretty much spatially separated from the polycyclic aromatic core and the dendron, while the OCH_2R groups are strongly influenced by the π-electrons of the neighboring dendritic aromatic rings.

- The more flexible EO linker in G1-2EO-pyr and G1-2EO-napht allows for a greater mobility of the molecules in the LC phase, as compared to G1-4Me-pyr and G1-2Me-napht. This is reflected in the much narrower peaks in the ^1H spectra of G1-2EO-pyr and G1-2EO-napht. Also, it prevents backfolding effects of the molecules in the column more efficiently than a shorter and more rigid linker.

5.2 Investigation of molecular dynamics

With homonuclear and heteronuclear MAS NMR spinning sideband patterns, the molecular dynamics of the polycyclic aromatic ring and the dendrons are investigated for all four molecules (A)–(D).

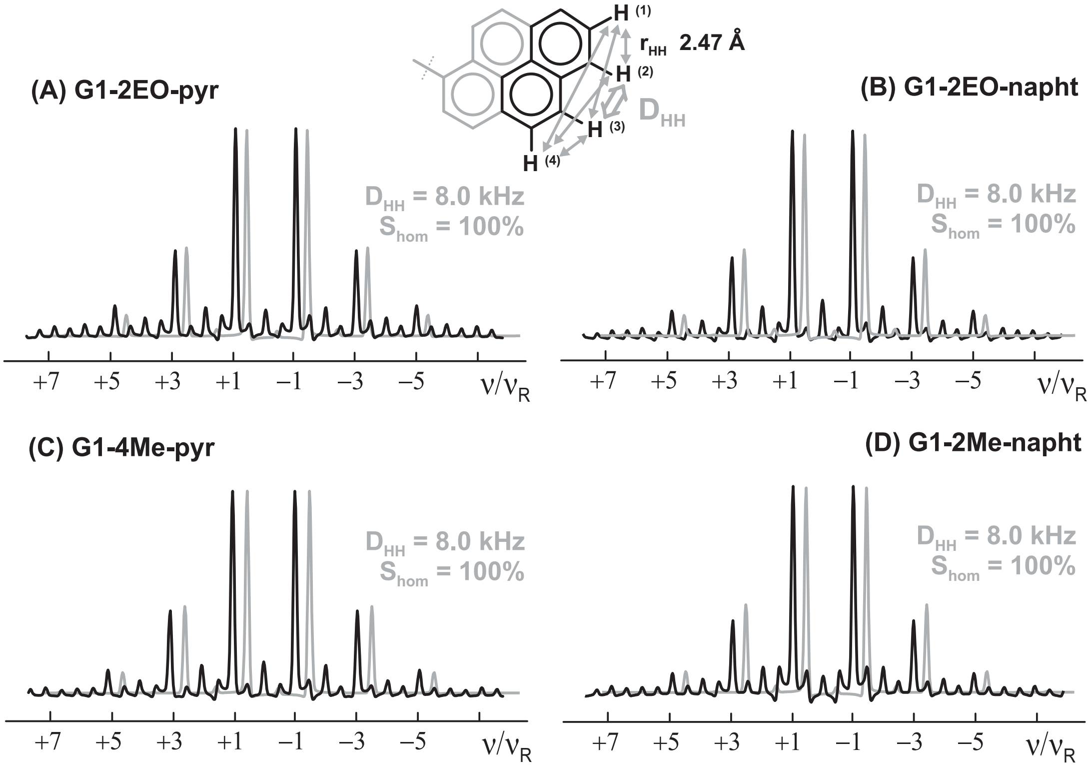

Figure 5.8: *^{1}H-^{1}H DQ spinning sideband patterns of the polycyclic aromatic core (pyrene/ naphthalene) of molecules (A) – (D) in the solid phase at 10°C, recorded under MAS at 30 kHz and τ_{exc} = 4 τ_R. (black line = experimental, grey line = 4-spin calculation). The inset schematically depicts the dipole-dipole couplings between four ^{1}H spins in a pyrene or naphthalene ring.*

Starting with ^{1}H-^{1}H DQ-spinning sideband patterns in the solid phase (Figure 5.8), similar patterns are observed for the pyrene or naphthalene protons of the four molecules. A coupling of $D_{CH}/2\pi$ = 8.0 kHz is extracted which corresponds to the full dipole-dipole coupling expected for two neighboring protons ($r_{HH} \approx 2.47$ Å). This yields an order parameter of S_{hom} = 100%. On the NMR time scale the pyrene or naphthalene rings are therefore perfectly immobile in their stack. The fitted sideband patterns, in this case, are not obtained from analytical spin-pair calculation but from numerical 4-spin calculations using the Simpson program [Bak 00]. In a pyrene or naphthalene ring, the distances between neighboring protons are all similar ($r_{HH} \approx 2.47$ Å, taking the value determined for a phenylene ring [Ochsenfeld 02]), therefore the ^{1}H dipole-dipole couplings (D_{HH}) are similar. Thus, the assumption of one strongest dipole-dipole coupling which determines the sideband pattern cannot be valid here, and more than two spins need to be considered to calculate the sideband pattern (see also Section 2.4.4). To determine the dipole-dipole coupling of two adjacent protons (2) and (3) in a pyrene or naphthalene ring (marked by the large grey arrow in the inset of Figure 5.8), the couplings to the neighboring protons on either side (1) and (4) also must be taken into account (indicated by the small grey arrows in Figure 5.8). Thus, a four-spin system with dipole-dipole couplings of D_{HH} = 8.0 kHz for neighboring protons ($\mathrm{H}^{(1)}$–$\mathrm{H}^{(2)}$, $\mathrm{H}^{(2)}$–$\mathrm{H}^{(3)}$ and $\mathrm{H}^{(3)}$–$\mathrm{H}^{(4)}$), D_{HH} = 1.3 kHz for every next neighbor ($\mathrm{H}^{(1)}$–$\mathrm{H}^{(3)}$ and $\mathrm{H}^{(2)}$–$\mathrm{H}^{(4)}$) and D_{HH} = 0.4 kHz for $\mathrm{H}^{(1)}$–$\mathrm{H}^{(4)}$ is calculated for an excitation time of τ_{exc} = 4 τ_R, yielding the sideband patterns depicted in grey in Figure 5.8. These are in very good agreement to the experimental patterns. Recording DQ sideband patterns with longer excitation times, e.g. τ_{exc} = 6 τ_R (not shown here), even more than 4 spins need to be considered to account for all sideband intensities including the first order (see Section 2.4.4).

Knowing that the polycyclic aromatic rings are immobile in the solid phase, a heteronuclear dipole-dipole coupling of $\mathrm{D}_{CH}/\ 2\pi$ = 21.0 kHz is expected for the pyrene and naphthalene CH groups. Indeed, couplings of $\mathrm{D}_{CH}/\ 2\pi$ = (20.5±0.5) – (21.4±0.5) kHz are extracted from the REPT-HDOR spinning sideband patterns (Figure 5.9), corresponding to order parameters of S_{het} = 98–102%. For (A) G1-2EO-pyr similar dipole-dipole coupling is expected, but no heteronuclear sideband pattern was recorded, because the measuring time would have been exceedingly long due to only little sample amounts available.

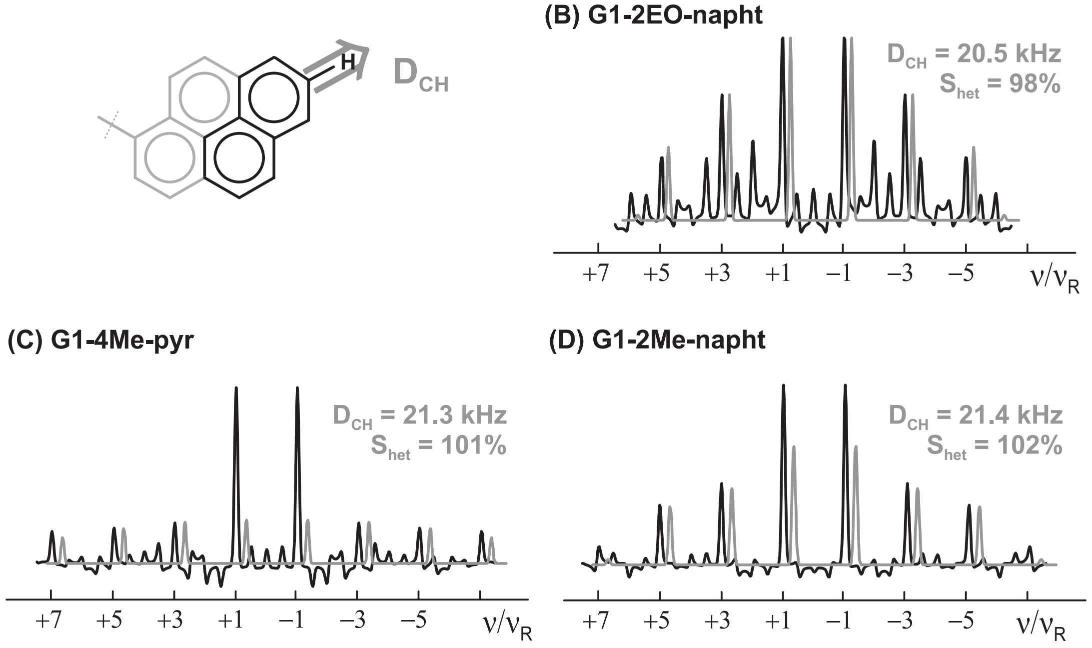

Figure 5.9: *^{1}H-^{13}C REPT-HDOR spinning sideband patterns of the polycyclic aromatic core (pyrene/ naphthalene) of molecules (B)–(D) in the solid phase at 10°C, recorded under MAS at 30 kHz and τ_{rcpl} = 3 τ_R for molecule (B) and (D) and 4 τ_R for molecule (C). The black and grey lines represent experimental and calculated data, respectively. The coupling vector is indicated in the inset above.*

For the aromatic CH group of the dendron, dipole-dipole couplings of $D_{CH}/ 2\pi$ = 19.0 – 21.0 kHz are determined for molecules (B)–(D) below T_g, as shown in Figure 5.10. These couplings correspond to order parameters of S_{het} = 90–100%. Quite clearly, not only the polycyclic aromatic rings, but also the dendritic units must be rather immobile in the solid phase.

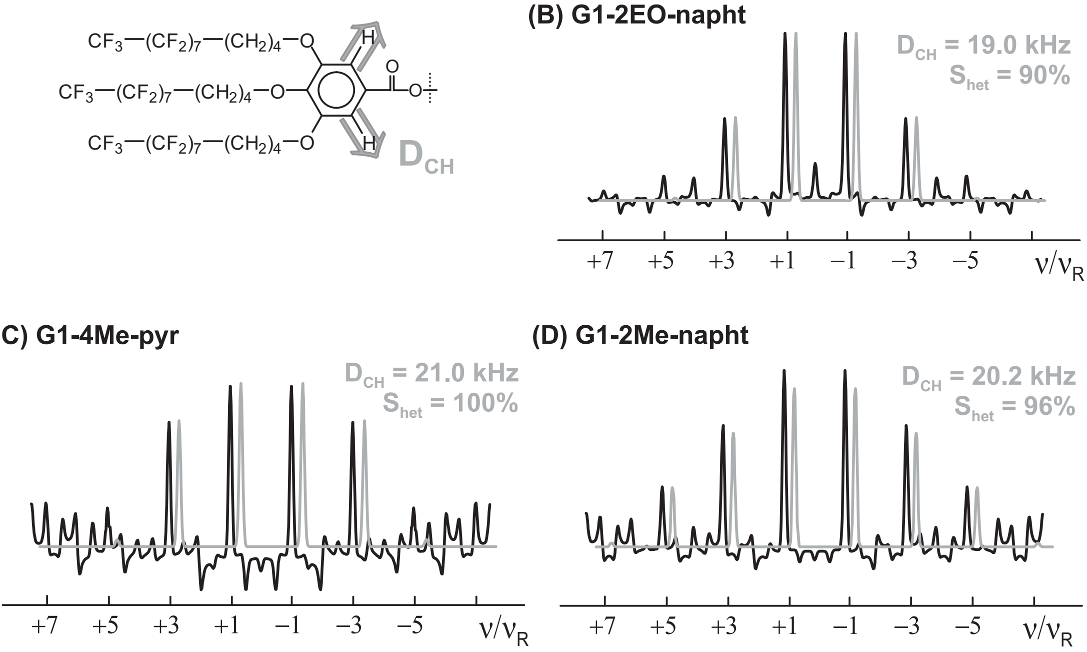

Figure 5.10: *^{1}H-^{13}C REPT-HDOR spinning sideband patterns of the aromatic CH groups of the dendron of molecules (B)–(D) in the solid phase at 10°C, recorded under MAS at 30 kHz and $\tau_{rcpl} = 2\ \tau_R$ for molecule (B) and (C) and $3\ \tau_R$ for molecule (D). The black and grey lines represent experimental and calculated data, respectively. The coupling vector is indicated in the inset above.*

Turning to the liquid crystalline phase, only homonuclear but no heteronuclear spinning sideband patterns could be recorded due to the poor ^{13}C signal intensity. From the DQ spinning sideband patterns in Figure 5.11, recorded at ∼60°C, it can be seen, that the pyrene and naphthalene rings are not immobile any more in the stack. For (C) G1-4Me-pyr and (D) G1-2Me-napht a residual ^{1}H dipole-dipole coupling of $D_{HH}/ 2\pi$ = 5.1 kHz and 5.3 kHz is extracted, respectively. This corresponds to a dynamic order parameter of $S_{hom} \approx 65\%$, showing that the pyrene and naphthalene rings of G1-4Me-pyr and G1-2Me-napht display some mobility in the π-stack. A fast axial rotation of the molecules in the stack can be excluded, because it would yield an order parameter of S = 50%, as discussed in reference [Brown 99]. Moreover, the dendritic moieties of the molecules are expected to stabilize the columnar packing significantly, which makes a rotation around the axis of the column highly unlikely anyway. Thus, the most probable motion of the polycyclic aromatic rings in the central stacks is a small angle motion covering a cone with an opening angle of approximately ±20° [Hentschel 81].

Looking at Figure 5.11 it is apparent, that the aromatic cores of (A) G1-2EO-pyr and

(B) G1-2EO-napht are a lot more mobile in the liquid crystalline phase than (C) G1-4Me-pyr and (D) G1-2Me-napht, which can be attributed to the different linker units. The residual ^{1}H-^{1}H dipole-dipole coupling extracted from the sidebands of G1-2EO-pyr and G1-2EO-napht is $D_{HH}/2\pi < 0.6$ kHz and results in an order parameter of $S_{hom} < 8\%$. Recalling the ^{1}H spectra in Figure 5.2 the higher mobility of molecules G1-2EO-pyr and G1-2EO-napht in the liquid crystalline phase, as compared to G1-4Me-pyr and G1-2Me-napht, is already apparent from the much narrower lines. Such a large mobility of the pyrene and naphthalene rings cannot be explained by an axial rotation or some other in-plane motion, but must rather be due to a fairly large out of plane motion of the rings. Since the LC phase is hexagonal columnar [Percec 02b], this motion must occur within the stack, without destroying the columnar arrangement. Thus, the stability of the columns must be attributed to the dendritic units, while the π-interactions between pyrene and naphthalene molecules in the center of the column only play a minor role. In this way, a rather large out of plane motion of the pyrene and naphthalene rings can be explained, which does not affect the overall columnar structure because it is determined by the dendritic units. Such a defined packing of the dendritic units in the column certainly restricts the motions possible for the polycyclic aromatic rings in the core of the column, where a shorter and more rigid linker as in G1-4Me-pyr and G1-2Me-napht will restrict the

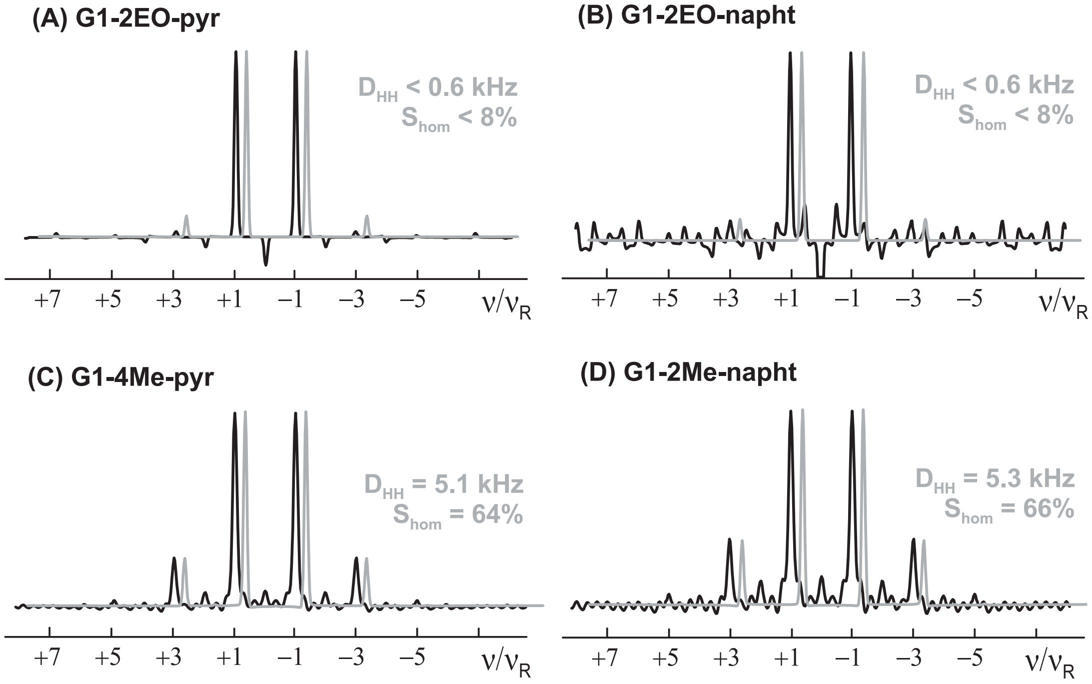

Figure 5.11: *^{1}H-^{1}H DQ spinning sideband patterns of the polycyclic aromatic core (pyrene/ naphthalene) of molecules (A)–(D) in the liquid crystalline phase at ∼60°C. The sideband patterns for molecule (A) and (B) were recorded at 20 kHz MAS with an excitation time of τ_{exc} = 32 τ_R, while the patterns for molecule (C) and (D) were recorded at 30 kHz MAS and τ_{exc} = 4 τ_R, (black line = experimental, grey line = 4-spin calculation).*

motion of the pyrene and naphthalene rings to a larger extent than a longer more flexible linker as in G1-2EO-pyr and G1-2EO-napht. In this way, the different linker units can account for the significantly different dynamical properties of the pyrene and naphthalene rings in the liquid crystalline phase of G1-4Me-pyr and G1-2Me-napht as compared to G1-2EO-pyr and G1-2EO-napht.

Conclusion

The columnar assembly is determined primarily by the dendrons, while the π-interactions between the polycyclic aromatic rings in the center of the column only play a minor role. This picture agrees well with the conclusions drawn for the dendritic polymers in the last Chapter, where the dendrons were identified as the driving force and structure determining unit of the columnar structure. In the solid phase the molecules are rather immobile in the column, while in the in the liquid crystalline phase the pyrene and naphthalene rings in the center of the column display significant mobility. The degree of segmental dynamics is dependent on the linker unit, where a longer and more flexible linker allows for a larger mobility of the polycyclic aromatic rings. A detailed understanding of the molecular dynamics of the polycyclic aromatic cores is helpful for designing stable columnar assemblies which exhibit promising charge carrier mobilities.

Chapter 6

Molecular dynamics of a liquid crystalline shape-persistent macrocycle with intraannular polar groups

Shape-persistent macrocycles, similar to discotic liquid crystals [Chandrasekhar 77, Bushby 02], are capable of forming supramolecular columnar structures. In contrast to discotic molecules, however, macrocycles form hollow columns, since they are non-collapsible. With functional groups attached to the inside of the macrocycles (intraannular substituents) intraannular functionalized nanotube can be constructed [Anderson 95, Tobe 98, Höger 99, Lehman 00, Höger 02]. It is well known that a stable thermotropic mesophase only arises in the case of a correct balance of stiff and flexible moieties in a molecule. On this basis, various extraannular alkyl and oligo-alkyl side-chains have been attached to rigid shape-persistent macrocycles, built from phenyl-ethynyl units [Höger 01]. None of these, however, forms a stable thermotropic mesophase. This observation leads to the assumption that the "void" inside the non-collapsible macrocycles might be responsible for this instability. Thus a macrocycle is investigated (see Figure 6.1a) which, in addition to the extraannular oligo-alkyl chains, also has intraannular polar groups to fill the "void" and, in this way, stabilize a columnar packing. With a correct balance of the stiff macrocyclic core and flexible extraannular alkyl chains, a stable thermotropic liquid crystalline phase results [Fischer 03]. Figure 6.1b schematically shows such a columnar packing.

The synthesis and characterization of the macrocycle are described in reference [Fischer 03], as are X-ray powder scattering experiments. Indeed, the molecule shows a stable mesophase between 82°C and 145°C. In addition, differential scanning calorimetry (DSC) shows a transition between 20°C and 40°C, which can be attributed to a transition of one solid phase into another. In the following, the dynamical properties of the shape-persistent macrocycle in the solid and the liquid crystalline phase are investigated with solid-state NMR

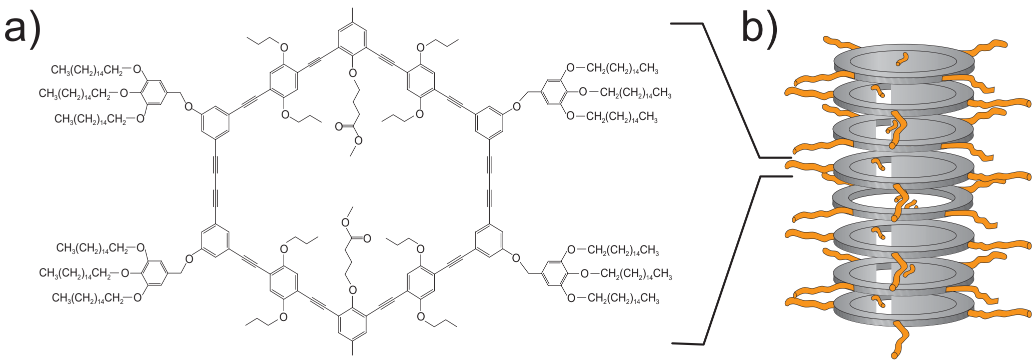

Figure 6.1: *Shape-persistent macrocycle with extraannular flexible oligo-alkyl chains and intraannular polar substituents (a), forming a thermotropic columnar mesophase (b).*

by means of ^{1}H-^{13}C MAS spinning sideband patterns. These sideband patterns are used as a sensitive measure for individual ^{1}H-^{13}C dipole-dipole couplings, which are then compared to coupling values of immobile segments, such as CH, CH$_2$, CH$_3$ or an aromatic ring, calculated from known ^{1}H-^{13}C bond lengths. Typically, an immobile C-H segment is characterized by a coupling of $D_{CH}/2\pi$ = 21.0 kHz (with a C-H bondlength of 1.13 Å) which is reduced when molecular motions occur on a time scale faster than $\sim 10^{-6}$ s. By relating the measured (reduced) dipole-dipole coupling to the one calculated for the immobile case, a dynamic order parameter S can be determined for individual segments, where S = 100% represents a perfectly immobile segment and S $\rightarrow$ 0% isotropic motion. From such order parameters the space requirements of molecular segments can be estimated in terms of an angular motion [Schmidt-Rohr 94, Hentschel 81].

6.1 Dynamical properties in the columnar liquid crystalline phase

The segmental dynamics of different types of aromatic rings and several methyl groups of the macrocyclic molecule are investigated in the liquid crystalline phase at ≥ 85°C with REPT-HDOR and REREDOR spinning sideband patterns. The assignment of the ^{13}C resonances is shown in Figure 6.2. Four different types of aromatic resonances can be distinguished at $\delta(^{13}C)$ = 133, 118, 115 and 108 ppm (marked dark green, blue, light green and purple, respectively). Two different OCH$_2$ resonances are observed at 73 and 69 ppm, depicted in red and light blue, respectively. The alkyl-CH_3 and the alkyl-CH_2CH$_3$ groups (marked grey and yellow, respectively) are observed at $\delta(^{13}C)$ = 11 ppm and 23 ppm, respectively, while the rest of the extraannular alkyl CH$_2$ groups is depicted in orange ($\delta(^{13}C)$ = 30–32 ppm). The resonances at 27 and 51 ppm belong to the OCH$_2$$CH_2CH_2COOCH_3$ groups of the intraannular substituent. All other CH, CH$_2$ and CH$_3$ groups of the molecule are not resolved due to the poor signal-to-noise ratio. The remaining resonances observed arise from quarternary carbons.

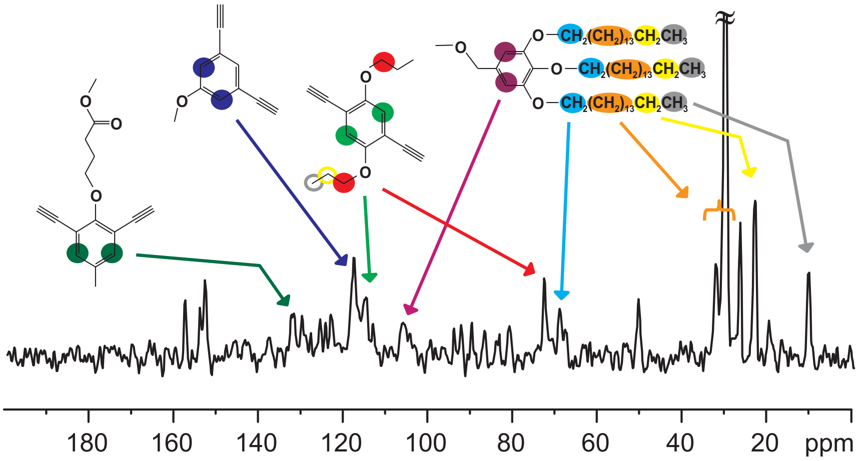

Figure 6.2: ^{13}*C NMR spectrum of the shape-persistent macrocycle.*

Considering first the aromatic rings of the molecule, Figure 6.3 shows REPT-HDOR spinning sideband patterns for the aromatic CH groups corresponding to $\delta(^{13}\mathrm{C})$ = 118 ppm (blue), 115 ppm (green) and 109 ppm (purple). (The resonance at 133 ppm is too weak to generate reliable sideband patterns). The residual dipole-dipole couplings extracted from the sideband patterns are significantly different, showing quite different segmental dynamics for the different moieties of the molecule. For the aromatic ring depicted in blue in Figure 6.2 and 6.3, a dipole-dipole coupling of $\mathrm{D}_{CH}/\ 2\pi$ = (21.5 ± 0.5) kHz is extracted from the respective spinning sideband pattern, which obviously agrees with the value of an immobile group. Hence, the aromatic ring is perfectly immobile on time scales below the millisecond range. In particular, there is no rotation of the macrocycles in the columnar LC phase.

Turning to the aromatic CH groups depicted in green in Figure 6.2 and 6.3, a reduced dipole-dipole coupling of $\mathrm{D}_{CH}/\ 2\pi$ = (16.4 ± 0.5) kHz is measured, corresponding to a dynamic order parameter of $\mathrm{S} \approx 80\%$. This parameter indicates a small-angle motion of the aromatic ring with a mean excursion of ± 15°. A full rotation or a flip of the aromatic ring can be excluded, because it would lead to dipole-dipole couplings significantly lower than the one observed ($\mathrm{D}_{CH}/\ 2\pi$ = 2.6 kHz and 12.8 kHz, respectively). The dynamics of the $\mathrm{OCH_2}$ group attached to the aromatic ring (marked red) result in a residual coupling of $\mathrm{D}_{CH}/\ 2\pi$ = (12.0 ± 1.0) kHz, corresponding to $\mathrm{S} \approx 55\%$ (Figure 6.4). When the motions of the aromatic ring and the $\mathrm{OCH_2}$ group are considered independent of each other, they can be separated by dividing the order parameters. Then, the $\mathrm{OCH_2R}$ segment exhibits an individual order parameter of $\mathrm{S} \approx 70\%$. This segmental dynamics can be rationalized in terms of a cone with an opening angle of ± 15°, which encompasses the core volume filled by the moving $\mathrm{OCH_2R}$ group and is illustrated in Figure 6.6.

Considering the oligo-alkyl substituents, a large mobility gradient is observed, starting with S = 100% at the immobile macrocyclic core and decreasing to $\mathrm{S} < 10\%$ at the terminus

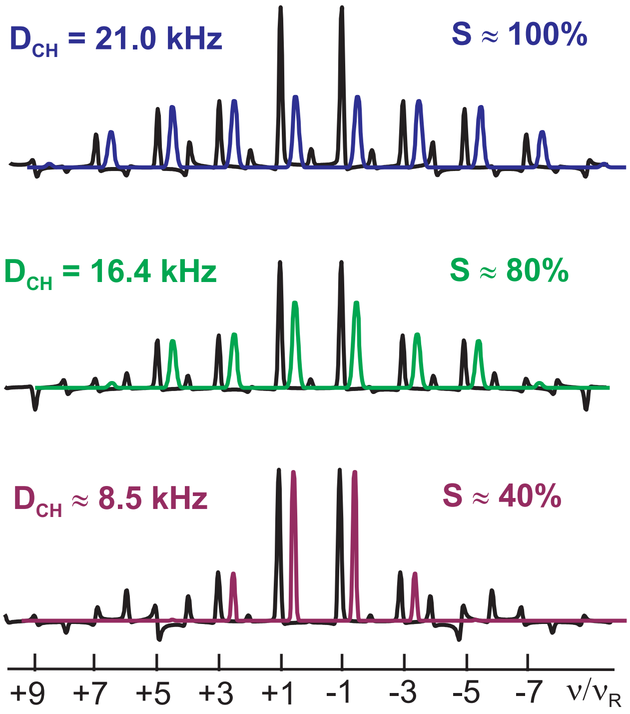

Figure 6.3: *^{1}H-^{13}C REPT-HDOR spinning sideband patterns of three different aromatic CH groups of the macrocycle are depicted, corresponding to $\delta(^{13}C)$ = 118 ppm (blue, top), 115 ppm (green, middle) and 109 ppm (purple, bottom). The black and colored lines represent experimental and calculated data, respectively. The spectra were recorded in the liquid crystalline phase at 92°C with a MAS spinning frequency of 15 kHz and $\tau_{rcpl} = 2\tau_R$.*

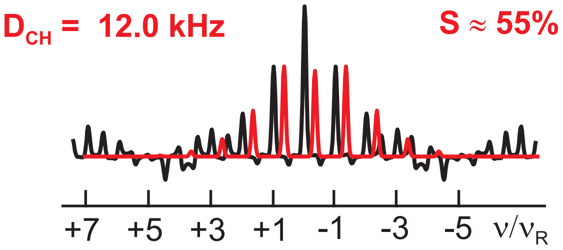

Figure 6.4: *^{1}H-^{13}C REREDOR spinning sideband pattern of the OCH$_2$ group, marked red ($\delta(^{13}C)$ = 73 ppm). The black and red line represent experimental and calculated data, respectively. The spectrum was recorded in the liquid crystalline phase at 85°C with a MAS spinning frequency of 30 kHz and $\tau_{rcpl} = 2\tau_R$.*

of the alkyl chains (see Figure 6.6). For the aromatic CH group within the substituent (marked purple) a residual dipole-dipole coupling of $D_{CH}/2\pi \approx 8.5$ kHz is determined (Figure 6.3). The corresponding dynamical order parameter, S ≈ 40%, can be related directly to a motion of the substituent as a whole, which occurs within a cone-shaped volume with an opening angle of ± 30°. For the main part of the alkyl chains, an order parameter of less than 25% is extracted from the sidebands shown in Figure 6.5.

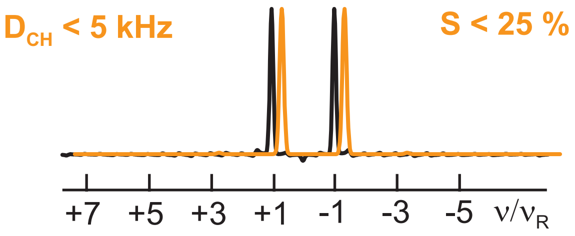

Figure 6.5: *^1H-^{13}C REPT-HDOR spinning sideband pattern of the $OCH_2\mathbf{CH}_{13}CH_2CH_3$ groups, marked orange ($\delta(^{13}C) \approx 30$ ppm), recorded in the liquid crystalline phase at 85°C with a MAS spinning frequency of 30 kHz at $\tau_{rcpl} = 4\ \tau_R$. The black and orange line represent experimental and calculated data, respectively.*

The different segmental dynamics of the macrocycle and its substituents in the liquid crystalline phase are summarized and schematically visualized in Figure 6.6. As mentioned above, the formation of a thermotropic liquid crystalline phase requires the correct ratio of rigid and flexible parts in a molecule. The degree of mobility of the different segments in the macrocycle has been determined with solid-state NMR, showing that the macrocyclic core, as expected, is rather rigid in the liquid crystalline phase and does not rotate within the column, while the substituents show significant mobility. In addition, the space requirements of the substituents can be estimated by the respective cone volumes (depicted in Figure 6.6). In this way, possible packing arrangements can be derived and phase stabilities, e.g. with respect to temperature, can be estimated for the material.

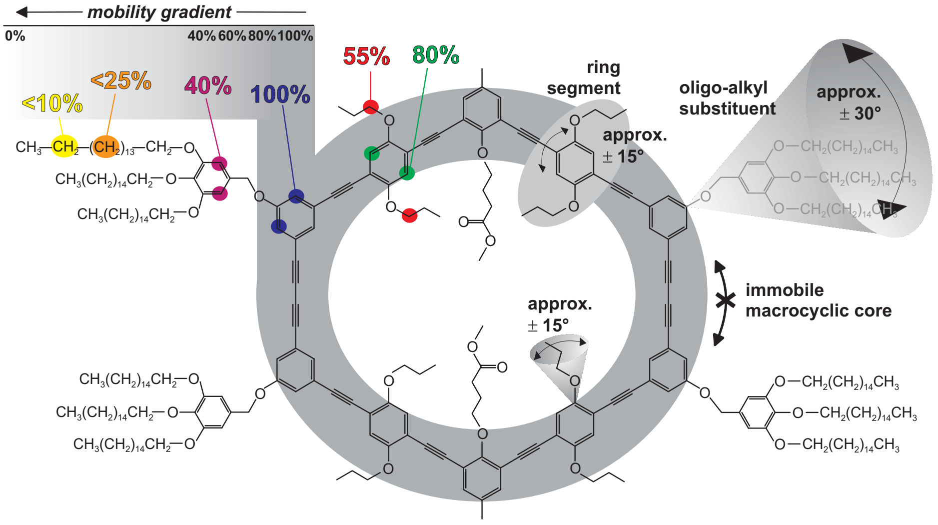

Figure 6.6: *Schematic representation of the segmental dynamics of the macrocycle. On the left, the degree of mobility for individual segments is given by the respective dynamic order parameters, S, in %, while on the right the corresponding motions are depicted.*

6.2 Dynamical properties of the extraannular oligo-alkyl chains in the solid phase

Within the solid phase a transition is observed between 20 and 40°C with differential scanning calorimetry (DSC). This can be explained in terms of a transition from one solid phase into another. Investigating the segmental mobility of the extraannular oligo-alkyl substituents with solid-state NMR at different temperatures, a significant change in the dynamical properties is observed at 20°C. Figure 6.7 shows ^{1}H-^{13}C REREDOR spinning sideband patterns of the alkyl CH_2 groups at 4, 20, 48 and 64°C. The residual dipole-dipole couplings extracted from the sideband patterns on the left (marked orange) represent an average coupling over thirteen CH_2 groups in the alkyl chain, all with a resonance frequency of about 30 ppm. At 20, 48 and 64°C an average residual dipole-dipole coupling of $D_{CH}/\ 2\pi$ = (8.0±1.0) kHz is determined, corresponding to an order parameter of S $\approx$ 40%, while at 4°C the observed coupling is $D_{CH}/\ 2\pi$ = 14.5 kHz, S $\approx$ 70%. The dynamic order parameter, S, reflects the displacement of the respective molecular segments, i.e. the space effectively filled by the moving groups. The reduction of the order parameter at 20°C, thus, corresponds to an increase in the segmental mobility of the alkyl chains, which marks the beginning of the transition from one solid phase to the other. Since a further increase in temperature (20–64°C), does not lead to a further reduction of the dynamic order parameter, the displacement of the alkyl-chain segments remains similar throughout the second solid phase. Nevertheless, the correlation time of the motion may well become smaller with increasing temperature, i.e. the motion faster. An order parameter of S $\approx$ 40% with respect to the oligo-alkyl-chains is therefore characteristic for the second solid phase, while the first solid phase displays an order parameter of S $\approx$ 70%.

On the right in Figure 6.7, depicted in yellow, the sideband patterns of the alkyl-CH_2CH_3 groups are shown. The same phenomenon is observed here. At 20°C and above a residual dipole-dipole coupling of about $D_{CH}/\ 2\pi$ = 6.5 kHz (S $\approx$ 30%) is extracted from the sidebands representing the properties of the second solid phase, while the first solid phase is characterized by a coupling of $D_{CH}/\ 2\pi$ = 12.0 kHz (S $\approx$ 60%). Comparing these values to the ones above for the main part of the alkyl chain, it is rather obvious that the mobility of the extraannular alkyl substituents, as expected, increases towards its chain end. This gradient of CH_2 mobility in the alkyl chain can, qualitatively, also be concluded from the sideband patterns of the $-OCH_2(CH_2)_{13}CH_2CH_3$ groups (left in Figure 6.7). Looking closely at the patterns at 20, 48 and 64°C, the higher order sidebands (4th to 6th order) do not match the calculated pattern, indicating that out of the thirteen CH_2 groups which contribute to the pattern, a few must be more rigid than the residual dipole-dipole coupling given by the fit.

On a time scale faster than $\sim 10^{-6}$ s, the transition from one solid phase into the other is characterized by a sudden increase in the segmental mobility of the alkyl chains by a factor of $\sim$ 1.2. The transition may of course also be accompanied by motional changes of the molecules on time scales slower than the microsecond range, but these were not investigated.

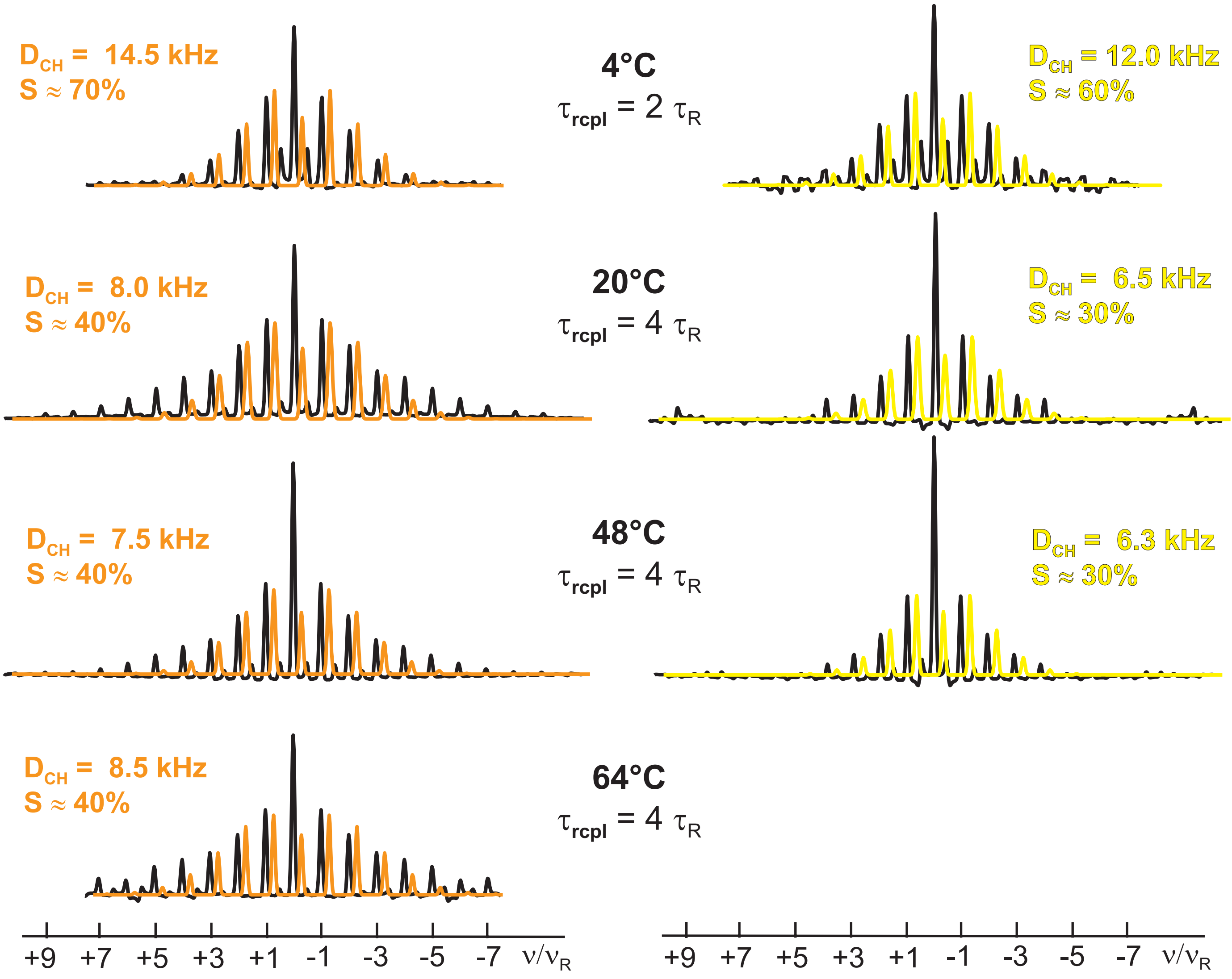

Figure 6.7: *^1H-^{13}C REREDOR spinning sideband patterns of the extraannular alkyl CH_2 groups in the solid phase between 4°C and 64°C. The sideband patterns on the left (depicted in orange) correspond to the -$OCH_2(\mathbf{CH_2})_{13}CH_2CH_3$ groups ($\delta(^{13}C) \approx 30$ ppm), the sidebands on the right correspond to -$OCH_2(CH_2)_{13}\mathbf{CH_2}CH_3$ ($\delta(^{13}C) = 23$ ppm). The black and colored lines represent experimental and calculated data, respectively. The spectra were recorded under MAS at 30 kHz and with $\tau_{rcpl} = 2\tau_R$ or $4\tau_R$.*

Chapter 7

Summary

Advanced solid-state NMR methods under fast MAS are very well suited to the study of the local structure and dynamics of large and complex supramolecular architectures. Dipolar ^{1}H-^{1}H and ^{1}H-^{13}C recoupling NMR methods, which do not rely on isotopic labeling, prove to be extremely powerful in this respect. The analysis of ^{1}H NMR chemical shift effects as well as dipolar ^{1}H-^{1}H and ^{1}H-^{13}C couplings provides site-specific information about the local structure and the segmental dynamics of different moieties of large molecules assembling in a supramolecular fashion. In combination with nucleus independent chemical shift (NICS) maps, relative changes of ^{1}H chemical shifts serve as distance constraints and allow protons to be positioned relative to π-electron systems. Moreover, local order parameters are selectively and precisely determined for different molecular building blocks from homo- and heteronuclear dipolar spinning sideband patterns arising from rotor-encoded recoupling. In this way, valuable information about structural and dynamical properties is gained, thus enabling the identification of structure-directing units within supramolecular systems and helping to understand the self-assembly process in general.

In Chapter 1, the fundamental aspects of supramolecular chemistry and NMR spectroscopy were explained, while Chapter 2 focused on a detailed description of the homo- and heteronuclear dipolar recoupling NMR methods used in this work. In particular, two-dimensional ^{1}H DQ and ^{1}H-^{13}C correlation experiments were described providing the theoretical background of spinning sideband patterns arising from rotor-encoding. The key feature is that the spinning sideband patterns allow ^{1}H-^{1}H and ^{1}H-^{13}C dipole-dipole couplings to be specifically and sensitively measured. These couplings are characteristically reduced by molecular motions on time scales $< 1\mu$s as compared to the couplings of rigid molecules. As a result, dynamic order parameters can be determined locally for individual molecular segments. In the subsequent Chapters, these NMR approaches were applied to systems forming supramolecular architectures with increasing degree of complexity. In addition, a short introduction to DFT calculations of nucleus independent chemical shift (NICS) maps was given.

Chapter 3 dealt with a so-called Yellow Filter Dye molecule which crystallizes in two different morphologies of known X-ray crystal structure. ^{1}H-^{13}C dipolar recoupling NMR experiments revealed ^{1}H chemical shift effects induced by the chromophore system of the molecule, which are not identical for the two polymorphs. These different π-shift effects could be explained by the different packing of the molecules in the two morphologies. The excellent agreement of the NMR results with the X-ray crystal structure in combination with the NICS map of the molecule confirmed the applicability of the methods. In addition, site-specific dynamic order parameters were obtained from dipolar spinning sideband patterns. Only the alkyl chain ends displayed some mobility, being slightly different for the two polymorphs, where the more stable thermodynamically controlled morphology showed less segmental motion. Thus, dipolar recoupling NMR methods can, indeed, determine π-π packing phenomena as well as segmental mobilities of different building blocks very precisely. The approach is not restricted to molecular crystals but can also be applied to study structural and dynamical properties of much larger and more complex supramolecular systems, as was described in the subsequent Chapters.

Chapters 4 and 5 focused on dendritic supramolecular systems which self-assemble in a columnar structure below as well as above T_g. In Chapter 4 the dendrons were attached to a polymer backbone via a linker unit. The analysis of π-shift effects provides site-specific insight into the local structure of the phenyl rings and –OCH_2– units within the dendron. In combination with a NICS map of a phenole ring, an arrangement of the OCH_2 protons with respect to the aromatic rings could be proposed for the G1-PMA macromolecule, as depicted in Figure 7.1. The dendritic units were identified as the driving force and structure determining segment of the columnar assembly.

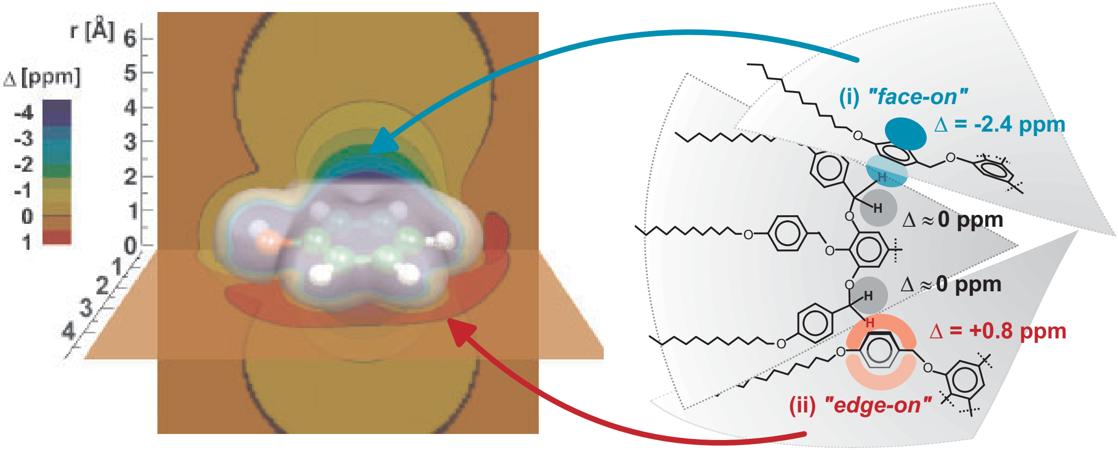

Figure 7.1: *Schematic representation of the OCH_2 proton positions with respect to the phenyl rings of the dendrons. The distance constraints were obtained from the relative changes of ^{1}H chemical shifts induced by neighboring aromatic rings.*

The studying of a representative selection of systems with characteristic differences, such as different polymer backbones, size of dendritic groups or length and flexibility of linker units, provided further insight into the role which the different moieties play in the self-assembly process. The polymer backbone was found to have virtually no effect on the overall structure, while the system is significantly affected by changing the linker unit. The dynamic order parameters of different phenyl and –OCH$_2$– groups could be determined by using dipolar spinning sideband patterns to measure individual ^{1}H-^{1}H and ^{1}H-^{13}C dipole-dipole couplings. These turn out to be largely independent of the generation of the dendron, as long as the same linker unit is used. Therefore, a similar mobility gradient was determined within the dendron for all molecules with a short and rigid linker unit, as depicted schematically in Figure 7.2a.

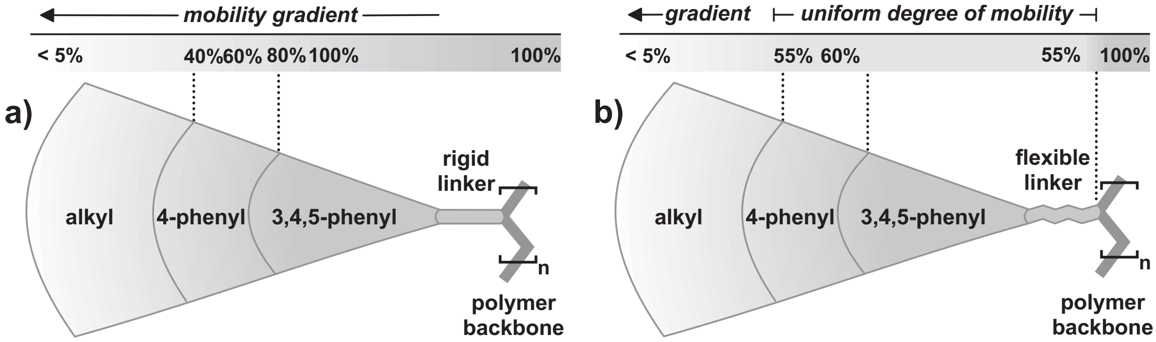

Figure 7.2: *Schematic representation of the segmental dynamics of a dendritic polymer with a) a short and rigid linker unit and b) a longer and more flexible linker unit.*

It was shown, that –O– segments provide very efficient mechanical decoupling such that, e.g., the dynamics of the OCH$_2$ groups of the alkyl chain are dominated by the alkyl chain rather than by the dynamics of the phenyl rings in the inner part of the dendron. This effect is even more pronounced for the more flexible EO linker unit, leading to a uniform degree of mobility in G1-4EO-PMA (Figure 7.2b), which stands in clear contrast to the mobility gradient discussed above. Thus, a more flexible linker unit has a significant impact on the segmental dynamics of the molecule. This behavior was also observed for the dendritic molecules investigated in Chapter 5.

Chapter 5 elucidated the dynamical and structural properties of dendrons which are attached to a polycyclic aromatic unit at their apex. Again, the columnar assembly is determined primarily by the dendrons and is basically independent of the polycyclic aromatic core, while the dynamic properties are influenced significantly by the type of linker unit. In the solid-state, the pyrene and naphthalene rings are immobile in all the systems investigated, while in the liquid crystalline phase a significantly higher mobility is observed for the molecules with a flexible EO linker. A good understanding of the molecular dynamics of the aromatic core is essential for designing self-assembling systems which combine stable columnar phases with sufficient charge carrier capabilities.

A very different columnar structure was investigated in Chapter 6, where macrocycles with extra- and intraannular substituents stack on top of each other to build hollow tubes.

The presence of intraannular polar groups in combination with the correct balance of stiff and flexible parts in the molecule enables the formation of a stable liquid crystalline phase. The degree of mobility in the system was determined from heteronuclear spinning sideband patterns. It was found that the macrocycles do not rotate on a μs timescale within the column, while the substituents are significantly more mobile. In addition, the space requirements of the substituents were estimated, thus allowing the columnar phase and packing behavior to be understood on a molecular level.

The results of this work contribute to the understanding of structural and dynamical properties induced by π-π interactions in different supramolecular systems and, in this way, promote the understanding as well as the chemical design of complex self-organizing materials.

Appendix

A Experimental details

All solid-state NMR measurements were carried out on 10–20 mg of as-synthesized samples. The data was collected on a Bruker DRX spectrometer with a 16.4 T magnet, operating at ^{1}H and ^{13}C Larmor frequencies of 700 and 176 MHz, respectively. A double resonance MAS probe supporting rotors of 2.5 mm outer diameter allowed the experiments to be performed at MAS frequencies of 25 kHz or 30 kHz. $\pi/2$ radiofrequency pulses were set to a lengths of 2 μs or 2.5 μs, and a recycle delay of 1–2 s was used. The spectra are referenced to adamantane (1.63 ppm for ^{1}H, and 38.5 ppm for ^{13}CH). If not stated otherwise, the spectra were recorded at room temperature, which, in combination with fast MAS, results in an effective sample temperature of (39 $\pm$ 2) °C and (48 $\pm$ 2) °C due to frictional heating at spinning frequencies of 25 kHz and 30 kHz, respectively [Langer 99]. All homo- and heteronuclear dipolar recoupling experiments were carried out with equal excitation and reconversion times. The rotor-synchronized ^{1}H-^{1}H DQ spectra were recorded with 40–64 slices in the indirect dimension and 64 transients averaged per slice. States-TPPI was applied in t_1 for phase sensitive detection [Marion 89]. The experimental time was about one hour. For the rotor-synchronized ^{1}H-^{13}C REPT-HSQC spectra a recoupling time equal to one rotor period was used and between 16 and 30 slices were recorded in t_1, with 1024–2048 transients averaged per slice, resulting in an experimental time of 5–17 hours. For the REPT-HDOR and REREDOR spinning sideband patterns a recoupling time between two and eight rotor periods was used and two full rotor periods were recorded in the indirect dimension, with the time increment set to 2.2 μs or 2.5 μs for 30 kHz or 25 kHz, respectively. Thus, 30 or 32 slices were recorded in the indirect dimension with 1024–5120 transients averaged per slice. The experimental time was between 10 and 60 hours.

B T_1 relaxation of Yellow Filter Dye molecules in the rhombic and the needle morphology

The T_1 relaxation of the Yellow Filter Dye molecules was measured for both morphologies with a saturation recovery experiment. Figure B.1 shows the signal intensity of the aromatic ^1H resonances plotted against the recovery time, t. Fitting the data points according to $S(^1H) = 1 - \exp(-t/T_1)$ yields relaxation times of T_1 = 4.3 s and 1.9 s for the rhombic and the needle polymorph, respectively.

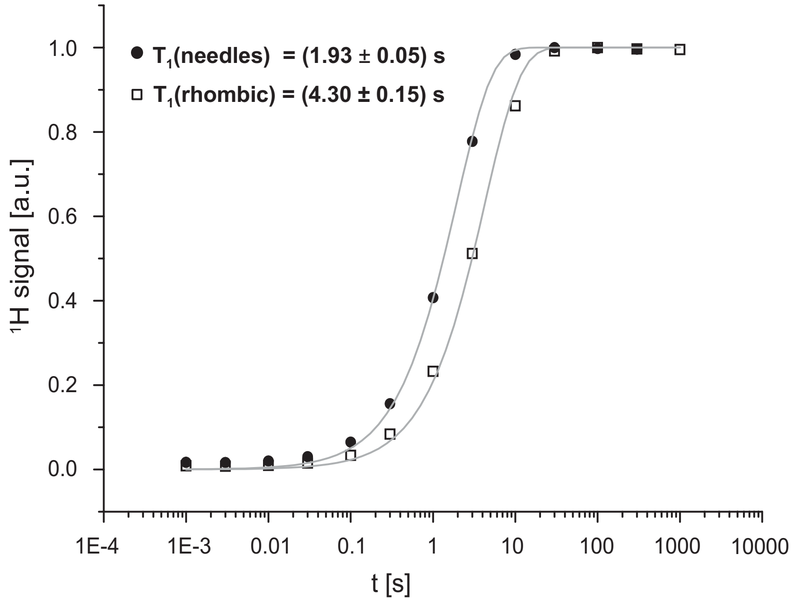

Figure B.1: *T_1 relaxation data for rhombic and needle polymorph.*

C G1-dendron – NOESY experiment

For the dendritic polymers described in Chapter 4 two different ^{13}C chemical shifts were observed for the OCH_2Ph groups (see Figure 4.3). The two resonances were attributed to a difference in chemical environment of the 3,5- and the 4-substituted OCH_2Ph groups in the dendron. In principle, one could also consider a scenario where e.g. the OCH_2 groups in 3 and 4 position are similar and the one in 5 position is different. That this is, however, not the case here is explained below on the basis of a NOESY spectrum, showing that the 4-OCH_2Ph group is, indeed, different from the two 3,5-OCH_2Ph groups.

Solubilizing a monomer of G1-4EO-PMA in $CDCl_3$, yields proton spectra with sufficiently narrow lines, so that two different proton resonances can be distinguished for the OCH_2Ph groups. In Figure C.1 a NOESY spectrum of the G1-dendron is shown [Thieme 02].

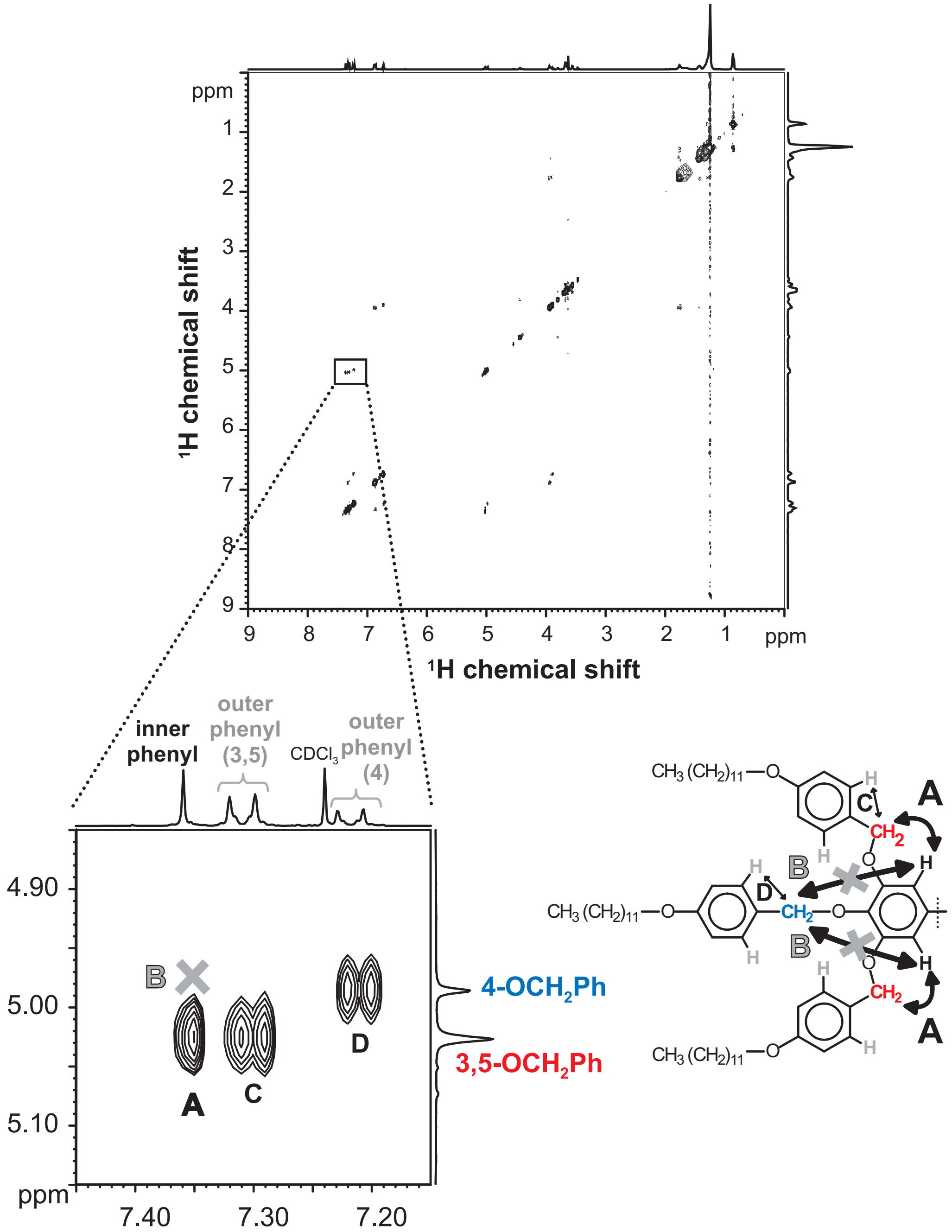

Figure C.1: *NOESY experiment of a G1-dendron (solubilized in $CDCl_3$), recorded with a mixing time of 1s [Thieme 02]. The cross peaks between the aromatic protons and the OCH_2Ph protons are enlarged. The grey cross indicates that the distance between the respective protons is too large to show a cross peak in the NOESY spectrum.*

NOESY experiments use the nuclear Overhauser effect (NOE) for correlation of protons. A cross-peak is observed if the respective protons are close enough in space (usually < 5 Å). The enlarged region in Figure C.1 shows the cross-peaks between the aromatic and the OCH_2Ph protons. Three aromatic resonances are observed between 7.2 and 7.4 ppm which are assigned to the inner aromatic ring ($\delta(^1\text{H})$ = 7.35 ppm) and the ortho-protons of the outer phenylene rings (doublets at $\delta(^1\text{H})$ = 7.30 and 7.21 ppm). The protons of the inner phenyl ring should only be able to couple to the 3,5-OCH_2Ph and not to the 4-OCH_2Ph protons, because the distance to the latter is too far. Indeed, only a cross-peak to the OCH_2Ph resonance at 5.3 ppm is observed (marked as A in Figure C.1) and not to the peak at 4.9 ppm (marked as B). Hence, the resonances at 5.3 and 4.9 ppm must correspond to the 3,5- and 4-OCH_2Ph protons, respectively. The remaining peaks in the spectrum, marked as C and D, correspond to the cross-peaks between the ortho protons of the outer phenylene rings and the OCH_2Ph protons in 3,5 and 4 position, respectively. Indeed, the middle strand in the dendron (4 position) can be distinguished from the outer ones (3,5 position).

Bibliography

[Abragam 61] A. Abragam. The Principles of Nuclear Magnetism. Oxford Univ. Press, Oxford (1961).

[Anderson 95] S. Anderson, U. Neidlein, V. Gramlich, F. Diederich. A new family of chiral binaphtyl-derived cyclophane receptors - complexation of pyranosides. *Angew. Chem. Int. Ed.* **34**, 1596–1600 (1995).

[Andrew 58] E. R. Andrew, A. Bradbury, R. G. Eades. Nuclear Magnetic Resonance Spectra from a Crystal Rotated at High Speed. *Nature* **182**, 1659 (1958).

[Atkins 99] P. W. Atkins. Physical Chemistry. Oxford University Press; 6th edition, Oxford (1999).

[Atwood 96] J. L. Atwood, J.-M Lehn. Comprehensive Supramolecular Chemistry. Vol. 9 and 10, Oxford: Pergamon Press (1996).

[Bak 00] M. Bak, J. T. Rasmussen, N. C. Nielsen. SIMPSON: A General Simulation Program for Solid-State NMR Spectroscopy. *J. Magn. Reson.* **147**, 296–330 (2000).

[Baldwin 90] R. L. Baldwin. Protein chemistry - Pieces of the folding puzzle. *Nature* **346**, 409–410 (1990).

[Bax 81] A. Bax, R. Freeman, T. A. Frenkiel. A NMR technique for tracing out the carbon sceleton of an organic molecule. *J. Am. Chem. Soc.* **103**, 2102–2104 (1981).

[Becke 88] A. D. Becke. Density-functional exchange-energy approximation with correct asymptotic behavior. *Phys. Rev. A* **38**, 3098–3100 (1988).

[Bennett 95] A. E. Bennett, C. M. Rienstra, M. Auger, K. V. Lakshmi, R. G. Griffin. Heteronuclear decoupling in rotating solids. *J. Chem. Phys.* **103**, 6951–6958 (1995).

[Bielecki 89] A. Bielecki, A. C. Kolbert, M. H. Levitt. Frequency-Switched Pulse Sequences: Homonuclear Decoupling and Dilute Spin NMR in Solids. *Chem. Phys. Lett.* **155**, 341–346 (1989).

[Bloch 46a] F. Bloch. Nulear Induction. *Phys. Rev.* **70**, 460–474 (1946).

[Bloch 46b] F. Bloch, W. W. Hansen, M. Packard. The Nulear Induction Experiment. *Phys. Rev.* **70**, 474–485 (1946).

[Bodenhausen 80] G. Bodenhausen, D. J. Ruben. Natural Abundance Nitrogen-15 NMR by Enhanced Heteronuclear Spectroscopy. *Chem. Phys. Lett.* **69**, 185–189 (1980).

[Branden 99] C.-I. Branden, J. Tooze. Introduction to Protein Structure. Garland Publishing; 2nd edition (1999).

[Brown 99] S. P. Brown, I. Schnell, J. D. Brand, K. Müllen, H. W. Spiess. An Investigation of $\pi - \pi$ Packing in a Columnar Hexabenzocoronene by Fast Magic-Angle Spinning and Double-Quantum ^{1}H Solid-State NMR Spectroscopy. *J. Am. Chem. Soc.* **121**, 6712–6718 (1999).

[Brown 00a] S. P. Brown, I. Schnell, J. D. Brand, K. Müllen, H. W. Spiess. A ^{1}H double quantum magic-angle spinning solid-state NMR investigation of packing and dynamics in triphenylene and hexabenzocoronene derivatives. *J. Mol. Struct.* **521**, 179–195 (2000).

[Brown 00b] S. P. Brown, I. Schnell, J. D. Brand, K. Müllen, H. W. Spiess. The competing effects of π-π packing and hydrogen bonding in a hexabenzocoronene carboxylic acid derivative: A ^{1}H solid-state MAS NMR investigation. *Phys. Chem. Chem. Phys.* **2**, 1735–1745 (2000).

[Brown 01a] S. P. Brown, T. Schaller, U. P. Seelbach, F. Koziol, C. Ochsenfeld, F. G. Klärner, H. W. Spiess. Structure and dynamics of the host-guest complex of a molecular tweezer: Coupling synthesis, solid-state NMR, and quantum-chemical calculations. *Angew. Chem. Int. Ed.* **40**, 717–720 (2001).

[Brown 01b] S. P. Brown, H. W. Spiess. Advanced Solid-State NMR Methods for the Elucidation of Structure and Dynamics of Molecular, Macromolecular, and Supramolecular Systems. *Chem. Rev.* **101**, 4125–4155 (2001).

[Brown 01c] S. P. Brown, X. X. Zhu, K. Saalwächter, H. W. Spiess. An Investigation of the Hydrogen-Bonding Structure in Bilirubin by ^{1}H Double-Quantum Magic-Angle Spinning Solid-State NMR Spectroscopy. *J. Am. Chem. Soc.* **123**, 4275–4285 (2001).

[Brundveld 01] L. Brundveld, B. J. B. Folmer, E. W. Meijer, R. P. Sijbesma. Supramolecular Polymers. *Chem. Rev.* **101**, 4071–4097 (2001).

[Burley 86] S. K. Burley, G. A. Petsko. Dimerization energetics of benzene and aromatic amino-acid side-chains. *J. Am. Chem. Soc.* **108**, 7995–8001 (1986).

[Bushby 02] R. J. Bushby, O. R. Lozman. Discotic liquid crystals 25 years on. *Curr. Opin. Colloid In.* **7**, 343–354 (2002).

[Caravetta 00] M. Caravetta, M. Eden, X. Zhao, A. Brinkmann, M. H. levitt. Symmetry principles for the design of radiofrequency pulse sequences in the nuclear magnetic resonance of rotating solids. *Chem. Phys. lett.* **321**, 205–215 (2000).

[Chandrasekhar 77] S. Chandrasekhar, S. Sadashiva, K. A. Suresh. Liquid crystals of disk-like molecules. *Pramana* **7**, 471–480 (1977).

[Chandrasekhar 98] S. Chandrasekhar. Handbook of Liquid Crystals, Volume 2B. Wiley-VCH, Weinheim (1998). Ed.: D. Demus, J. Goodby, G. W. Gray, H. W. Spiess and V. Vill.

[Chvalun 96] S. N. Chvalun, Y. K. Kwon, J. Blackwell, V. Percec. A Comparative Study of Supramolecular Self-Organization of Polymethacrylate Containing Bulky Side Substituents and its Monomer Precursor. *Polym. Sci. A* **38**, 1298–1304 (1996).

[Chvalun 97] S. N. Chvalun, J. Blackwell Y. K. Kwon, V. Percec. Small Angle X-Ray Analysis of the Effect of Temperature on the Self-Assembling Columnar Structures Formed by a Polymethacrylate with Highly Tapered Side Groups and by its Low Molar Mass Precursors. *Macromol. Symp.* **118**, 663–675 (1997).

[Chvalun 99] S. N. Chvalun, J. Blackwell, J. D. Cho, I. V. Bykova, V. Percec. A Second Columnar Liquid Crystalline Phase Formed by Polymers with Highly Tapered Side Chains. *Acta Polym.* **50**, 51–56 (1999).

[Chvalun 01] S. N. Chvalun, M. A. Shcherbina, I. V. Bykova, J. Blackwell, V. Percec, Y. K. Kwon, J.-D. Cho. The temperature behavior of self-assembling systems based on poly(methacrylates) with bulky side groups and theit macromonomers. *Polym. Sci. A* **43**, 33–43 (2001).

[Ciferri 00] A. Ciferri. Supramolecular Polymers. Dekker, New York (2000).

[Ciferri 02] A. Ciferri. Supramolecular polymerizations. *Macromol. Rapid. Comm.* **23**, 511–529 (2002).

[CPMD] CPMD: Computer pogramm CPMD V3.5, http://www.cpmd.org, © IBM Corp. 1990–2001. Max-Planck-Institut für Festkörperforschung, Stuttgart 1997–2001.

[CSD] CSD: Cambridge Structural Database, http://www.ccdc.cam.ac.uk.

[De Paul 00] S. M. De Paul, K. Saalwächter, R. Graf, H. W. Spiess. Sideband Patterns from Rotor-Encoded Longitudinal Magnetization in MAS Recoupling Experiments. *J. Magn. Reson.* **146**, 140–156 (2000).

[Deroover] G. Deroover, L. Timmermans (Agfa, Belgium). Personal communication.

[Desiraju 95a] G. R. Desiraju. Supramolecular synthons in crystal engineering - A new organic-synthesis. *Angew. Chem. Int. Ed.* **34**, 2311–2327 (1995).

[Desiraju 95b] G. R. Desiraju. The Crystal as a Supramolecular Entity. John Wiley & Sons (1995).

[Detken 02] A. D. Detken, B. H. Meier E. H. Hardy M. Ernst. Simple and efficient decoupling in magic-angle spinning solid-state NMR: the XiX scheme. *Chem. Phys. Lett.* **356**, 298–304 (2002).

[Dusold 00] S. Dusold, A. Sebald. Dipolar Recoupling under Magic-Angle Spinning Conditions. *Ann. Rep. NMR Spectr.* **41**, 185–262 (2000).

[Eden 99] M. Eden, M. H. Levitt. Pulse sequence symmetries in the nuclear magnetic resonance of spinning solids: Application to heteronuclear decoupling. *J. Chem. Phys.* **111**, 1511–1519 (1999).

[Ernst 87] R. R. Ernst, G. Bodenhausen, A. Wokaun. Principles of Nuclear Magnetic Resonance in One and Two Dimensions. Clarendon Press, Oxford (1987).

[Ernst 00] M. Ernst, H. Zimmermann, B. H. Meier. A simple model for heteronuclear spin decoupling in solid-state NMR. *Chem. Phys. Lett.* **317**, 581–588 (2000).

[Ernst 01] M. Ernst, A. Samoson, B. H. Meier. Low-power decoupling in fast magic-angle spinning NMR. *Chem. Phys. Lett.* **348**, 293–302 (2001).

[Feike 96] M. Feike, D. E. Demco, R. Graf, J. Gottwald, S. Hafner, H. W. Spiess. Broadband Multiple-Quantum NMR Spectroscopy. *J. Magn. Reson. A* **122**, 214–221 (1996).

[Fersht 99] A. Fersht. Structure and Mechanism in Protein Science: A Guide to Enzyme Catalysis and Protein Folding. W H Freeman & Co. (1999).

[Filip 99] C. Filip, S. Hafner, I. Schnell, D. E. Demco, H. W. Spiess. Solid-state nuclear magnetic resonance spectra of dipolar-coupled multi-spin systems under fast magic angle spinning. *J. Chem. Phys.* **110**, 423–440 (1999).

[Fischbach 02] I. Fischbach, T. Pakula, P. Minkin, A. Fechtenkötter, K. Müllen, H. W. Spiess, K. Saalwächter. Structure and dynamics in columnar discotic materials: A combined X-ray and solid-state NMR study of hexabenzocoronene derivatives. *J. Phys. Chem. B* **106**, 6408–6418 (2002).

[Fischer 03] M. Fischer, G. Lieser, A. Rapp, I. Schnell, W. Mamdouh, S. De Feyter, F. C. De Schryver, S. Höger. Shape-Persistent Macrocycles with Intraannular Polar Groups: Synthesis, Liquid Crystallinity and 2D Organization (2003). To be submitted to *J. Am. Chem. Soc.*

[Friedrich 98] U. Friedrich, I. Schnell, S. P. Brown, A. Lupulescu, D. E. Demco, H. W. Spiess. Spinning-sideband patterns in multiple-quantum magic-angle spinning NMR spectroscopy. *Mol. Phys.* **95**, 1209–1227 (1998).

[Fung 00] B. M. Fung, K. Ermolaev A. K. Khitrin. An improved broadband decoupling sequence for liquid crystals and solids. *J. Magn. Reson.* **142**, 97–101 (2000).

[Gan 97] Z. H. Gan, R. R. Ernst. Frequency- and phase-modulated heteronuclear decoupling in rotating solids. *Solid State Nucl. Magn. Reson.* **8**, 153–159 (1997).

[Gerstein 77] B. C. Gerstein, R. G. Pembleton, R. C. Wilson, L. M: J. Ryan. High-Resolution NMR In Randomly Oriented Solids with Homonuclear Dipolar Broadening - Combined Multiple Pulse NMR and Magic Angle Spinning. *Chem. Phys.* **66**, 361–362 (1977).

[Goedecker 96] S. Goedecker, M. Teter, J. Hutter. Separable dual-space Gaussian pseudopotentials. *Phys. Rev. B* **54**, 1703–1710 (1996).

[Goetz 97] J. M. Goetz, J. Schaefer. REDOR Dephasing by Multiple Spins in the Presence of Molecular Motion. *J. Magn. Reson.* **127**, 147–154 (1997).

[Goward 01] G. R. Goward, I. Schnell, S. P. Brown, H. W. Spiess, H.-D. Kim, H. Ishida. Investigation of an N$\cdots$H hydrogen bond in a solid benzoxazine dimer by ^{1}H–^{15}N NMR correlation techniques under fast magic-angle spinning. *Magn. Reson. Chem.* **39**, S5–S17 (2001).

[Graf 98] R. Graf, D. E. Demco, S. Hafner, H. W. Spiess. Selective residual dipolar couplings in cross-linked elastomers by ^{1}H double-quantum NMR spectroscopy. *Solid State Nucl. Magn. Reson.* **12**, 139–152 (1998).

[Gullion 89a] T. Gullion, J. Schaefer. Detection of Weak Heteronuclear Dipolar Coupling by Rotational-Echo Double-Resonance Nuclear Magnetic Resonance. *Adv. Magn. Reson.* **13**, 57–83 (1989).

[Gullion 89b] T. Gullion, J. Schaefer. Rotational-Echo Double-Resonance NMR. *J. Magn. Reson.* **81**, 196–200 (1989).

[Gullion 98] T. Gullion. Introduction to rotational-echo, double-resonance NMR. *Concepts Magn. Reson.* **10**, 277–289 (1998).

[Haeberlen 68] U. Haeberlen, J. S. Waugh. Coherent Averaging Effects in Magnetic Resonance. *Phys. Rev.* **175**, 453–467 (1968).

[Haiduc 99] I. Haiduc, F. T. Edelmann. Supramolecular Organometallic Chemistry. VCH, Weinheim (1999).

[Harris 86] R. Harris. Nuclear Magnetic Resonance Spectroscopy: A Physicochemical View. Longman, Harlow (1986).

[Hentschel 81] D. Hentschel, H. Sillescu, H. W. Spiess. Orientational Distribution of Polymer-Chains Studied by ^{2}H NMR Line-Shapes. *Polymer* **22**, 1516–1521 (1981).

[Hing 92] A. W. Hing, S. Vega, J. Schaefer. Transferred-Echo Double-Resonance NMR. *J. Magn. Reson.* **96**, 205–209 (1992).

[Hing 93] A. W. Hing, S. Vega, J. Schaefer. Measurement of Heternuclear Dipolar Coupling by Transferred-Echo Double-Resonance NMR. *J. Magn. Reson. A* **103**, 151–162 (1993).

[Höger 99] S. Höger, A.-D. Meckenstock. Template-directed synthesis of shape-persistent macrocyclic amphiphiles with convergently arranged functionalities. *Chem. Eur. J.* **5**, 1686–1691 (1999).

[Höger 01] S. Höger, K. Bonrad, A. Mourran, U. Beginn, M. Möller. Synthesis, aggregation, and adsorption phenomena of shape-persistent macrocycles with extraannular polyalkyl substituents. *J. Am. Chem. Soc.* **123**, 5651–5659 (2001).

[Höger 02] S. Höger, D. L. Morrison, V. Enkelmann. Solvent triggering between conformational states in amphiphilic shape-persistent macrocycles. *J. Am. Chem. Soc.* **124**, 6734–6736 (2002).

[Hohwy 00] M. Hohwy, C. P. Jaroniec, B. Reif, C. M. Rienstra, R. G. Griffin. Local Structure and Relaxation in Solid-State NMR: Accurate measurement of Amide N-H Bond Lengths and H-N-H Bond Angles. *J. Am. Chem. Soc.* **122**, 3218–3219 (2000).

[Hore 00] P. J. Hore, J. A. Jones, S. Wimperis. NMR: The Toolkit. Oxford University Press (2000).

[Hunter 90] C. A. Hunter, J. K. M. Sanders. The Nature of π-π interactions. *J. Am. Chem. Soc.* **112**, 5525–5534 (1990).

[Jeener 71] J. Jeener (1971). Ampère Summer School, Basko Polje, Yugoslavia.

[Klug 83] A. Klug. From Macromolecules to Biological Assemblies. *Angew. Chem. Int. Ed.* **22**, 565–582 (1983).

[Langer 99] B. Langer, I. Schnell, H. W. Spiess, A.-R. Grimmer. Temperature calibration under ultrafast MAS conditions. *J. Magn. Reson.* **138**, 182–186 (1999).

[Lee 65] M. Lee, W. I. Goldburg. Nuclear-Magnetic-Resonance Line Narrowing by a Rotating rf Field. *Phys. Rev. A* **140**, 1261–1271 (1965).

[Lee 88] C. T. Lee, W. T. Yang, R. G. Parr. Development of the Colle-Salvetti correlation-energy formula into a functional of the electron density. *Phys. Rev. B* **37**, 785–789 (1988).

[Lehman 00] U. Lehman, A. D. Schlüter. A shape-persistent macrocycle with two opposing 2,2':6',2''-terpyridine units. *Eur. J. Org. Chem.* **20**, 3483–3487 (2000).

[Lehn 95] J. M. Lehn. Supramolecular Chemistry: Concepts and Perspectives. VCH, Weinheim (1995).

[Lesage 97] A. Lesage, C. Auer, S. Caldarelli, L. Emsley. Determination of through-bond carbon-carbon connectivities in solid-state NMR using the INADEQUATE experiment. *J. Am. Chem. Soc.* **119**, 7867–7868 (1997).

[Lesage 99] A. Lesage, M. Bardet, Emsley. Through-bond carbon-carbon connectivities in disordered solids by NMR. *J. Am. Chem. Soc.* **121**, 10987–10993 (1999).

[Levitt 93] M. H. Levitt, A. C. Kolbert, A. Bielecki, D. J. Ruben. High-Resolution ^{1}H NMR In Solids with Frequency-Switched Multiple-Pulse Sequences. *Solid State Nucl. Magn. Reson.* **2**, 151–163 (1993).

[Lowe 59] I. L. Lowe. Free Induction Decays in Rotating Solids. *Phys. Rev. B* **2**, 285 (1959).

[Macho 01] V. Macho, L. Brombacher, H. W. Spiess. The NMR WEBLAB - An Internet Approach to NMR Lineshape Analysis, (http://www.mpip-mainz.mpg.de/weblab40/). *Appl. Magn. Reson.* **20**, 405–432 (2001).

[Marion 83] D. Marion, K. Wüthrich. Application of phase sensitive two-dimensional correlated spectroscopy (COSY) for measurements of ^{1}H-^{1}H spin-spin coupling-constants in proteins. *Biochem. Biophys. Res. Commun.* **113**, 967–974 (1983).

[Marion 89] D. Marion, M. Ikura, R. Tschudin, A. Bax. Rapid recording of 2D NMR-spectra without phase cycling – application to the study of hydrogen-exchange in proteins. *J. Magn. Reson.* **85**, 393–399 (1989).

[McElheny 00] D. McElheny, E. DeVita, L. Frydman. Heteronuclear Local Field NMR Spectroscopy under Fast Magic-Angle Sample Spinning Conditions. *J. Magn. Reson.* **143**, 3218–3219 (2000).

[Mehring 72] M. Mehring, J. S. Waugh. Magic-Angle NMR Experiment in Solids. *Phys. Rev. B* **5**, 3459 (1972).

[Mehring 83] M. Mehring. High Resolution NMR od Solids. Springer, Berlin (1983).

[Moore 99] J. S. Moore. Supramolecular Polymers. *Curr. Opin. Colloid In.* **4**, 108–116 (1999).

[Moulton 01] B. Moulton, M. J. Zaworotko. From molecules to crystal engineering: Supramolecular isomerism and polymorphism in network solids. *Chem. Rev.* **101**, 1692–1658 (2001).

[Munowitz 82] M. Munowitz, R. G. Griffin. Two-dimensional nuclear magnetic resonance in rotating solids: An analysis of line shapes in chemical shift-dipolar spectra. *J. Chem. Phys.* **76**, 2848–2858 (1982).

[Ochsenfeld 01] C. Ochsenfeld, S. P. Brown, I. Schnell, J. Gauss, H. W. Spiess. Structure Assignment in the Solid State by the Coupling of Quantum Chemical calculations with NMR Experiments: A Columnar Hexabenzocoronene Derivative. *J. Am. Chem. Soc.* **123**, 2597–2606 (2001).

[Ochsenfeld 02] C. Ochsenfeld, F. Koziol, S. P. Brown, T. Schaller, U. P. Seelbach, F.-G. Klärner. A Study of a Molecular Tweezer Host-Guest System by a Combination of Quantum-Chemical Calculations and Solid-State NMR Experiments. *Solid State Nucl. Magn. Reson.* **22**, 128–153 (2002).

[Percec 93] V. Percec, J. A. Heck, D. Tomazos, F. Falkenberg, H. Blackwell, G. Ungar. Self-Assembly of Taper-Shaped Monoesters of Oligo(ethylene oxide) with 3,4,5-Tris(p-dodecyloxybenzyloxy)benzoic Acid and of their Polymethacrylates into Tubular Supramolecular Architectures Displaying a Columnar Mesophase. *J. Chem. Soc. Perkin Trans.* **1**, 2799–2811 (1993).

[Percec 94] V. Percec, J. A. Heck, G. Johansson, D. Tomazos, G. Ungar. Towards Tobacco Mosaic Virus-Like Self-Assembled Supramolecular Architectures. *Macromol. Symp.* **77**, 237–265 (1994).

[Percec 98a] V. Percec, C.-H. Ahn, W.-D. Cho, A. M. Jamieson, J. Kim, T. Leman, Schmidt, M. Gerle, M. Möller, S. A. Prokhorova, S. Sheiko, S. Z. D. Cheng, A. Zhang, G. Ungar, D. J. P. Yeardley. Vizualizable Cylindrical Macromolecules with Controlled Stiffness from Backbones Containing Libraries of Self-Assembling Dendritic Side Groups. *J. Am. Chem. Soc.* **120**, 8619–9631 (1998).

[Percec 98b] V. Percec, C.-H. Ahn, G. Ungar, D. J. P. Yeardley, M. Möller, S. S. Sheiko. Controlling Polymer Shape through the Self-Assembly of Dendritic Side-Groups. *Nature* **391**, 161–164 (1998).

[Percec 02a] V. Percec, M. Glodde (2002). Personal communication.

[Percec 02b] V. Percec, M. Glodde, T. K. Bera, Y. Miura, I. Shiyanovskaya, K. D. Singer, V. S. K. Balagurusamy, P. A. Heiney, I. Schnell, A. Rapp, H. W. Spiess, S. D. Hudson, H. Duan. Self-organization of supramolecular helical dendrimers into complex electronic materials. *Nature* **419**, 384–387 (2002).

[Philp 91] D. Philp, J. F. Stoddart. Self-assembly in organic synthesis. *Synlett,* pp. 445–458 (1991).

[Purcell 46] E. M. Purcell, H. C. Torrey, R. V. Pound. Resonance Absorption by Nuclear Magnetic Moments in Solids. *Phys. Rev.* **69**, 37 (1946).

[Rapp 03] A. Rapp, I. Schnell, D. Sebastiani, S. P. Brown, H. W. Spiess. Supramolecular Assembly of Dendritic Polymers Elucidated by ^{1}H and ^{13}C Solid-State MAS NMR Spectroscopy. *J. Am. Chem. Soc.* (2003). submitted.

[Roberts 87] J. E. Roberts, G. S. Harbison, M. G. Munowitz, J. Herzfeld, R. G. Griffin. Measurement of Heteronuclear Bond Distances in Polycrystalline Solids by Solid-State NMR Techniques. *J. Am. Chem. Soc.* **109**, 4163–4169 (1987).

[Rossum 01] B. J. van Rossum, D. B. Steensgaard, F. M. Mulder, G. J. Boender, K. Schaffner, A. R. Holzwarth, H. J. M. H. J. M. de Groot. A Refined Model of the Chlorosomal Antennae of the Green Bacterium Chlorobium Tepidum from Proton Chemical Shift Constraints Obtained with High-Field 2D and 3D MAS NMR Dipolar Spectroscopy. *Biochemistry* **40**, 1587–1595 (2001).

[Saalwächter 00] K. Saalwächter. *Heteronuclear Recoupling Methods in Solid-State NMR*. Dissertation, Universität Mainz (2000).

[Saalwächter 01a] K. Saalwächter, R. Graf, H. W. Spiess. Recoupled Polarization-Transfer Methods for Solid-State ^{1}H-^{13}C Heteronuclear Correlation in the Limit of Fast MAS. *J. Magn. Reson.* **148**, 398–418 (2001).

[Saalwächter 01b] K. Saalwächter, H. W. Spiess. Heteronuclear ^{1}H-^{13}C multiple-spin correlation in solid-state NMR: combining REDOR recoupling and multiple-quantum spectroscopy. *J. Chem. Phys.* **114**, 5707–5728 (2001).

[Saalwächter 02a] K. Saalwächter, I. Fischbach. The Application of MAS Recoupling Methods in the Intermediate Motional Regime. *J. Magn. Reson.* **157**, 17–30 (2002).

[Saalwächter 02b] K. Saalwächter, I. Schnell. REDOR-Based Heteronuclear Dipolar Correlation Experiments in Multi-Spin Systems: Rotor-Encoding, Directing, and Multiple Distance and Angle Determination. *Solid State Nucl. Magn. Reson.* **22**, 154–187 (2002).

[Samoson 01a] A. Samoson, T. Tuherm, Z. Gan. High-Field High-Speed MAS Resolution Enhancement in ^{1}H NMR Spectroscopy of Solids. *Solid State Nucl. Magn. Reson.* **20**, 130–136 (2001).

[Samoson 01b] A. Samoson, T. Tuherm, J. Past. Ramped-Speed Cross Polarization MAS NMR. *J. Magn. Reson.* **149**, 264–267 (2001).

[Sauvage 99] J. P. Sauvage. Transition Metals in Supramolecular Chemistry. John Wiley & Sons (1999).

[Schleyer 96] P. Rague Schleyer, C. Maerker, A. Dransfeld, H. Jiao, van N. J. R. van Eikema Hommes. Nucleus-Independent Chemical Shifts: A Simple and Efficient Aromaticity Probe. *J. Am. Chem. Soc.* **118**, 6317–6318 (1996).

[Schmidt-Rohr 94] K. Schmidt-Rohr, H. W. Spiess. Multidimensional Solid-State NMR and Polymers. Academic Press, London (1994).

[Schnell 98] I. Schnell, S. P. Brown, H. Y. Low, H. Ishida, H. W. Spiess. An Investigation of Hydrogen Bonding in Benzoxazine Dimers by Fast Magic-Angle Spinning and Double-Quantum ^{1}H NMR Spectroscopy. *J. Am. Chem. Soc.* **120**, 11784–11795 (1998).

[Schnell 99] I. Schnell. *^{1}H-NMR-Spektroskopie im Festkörper: Schnelle Probenrotation und Mehrquantenkohärenzen*. Dissertation, Universität Mainz (1999).

[Schnell 01a] I. Schnell, B. Langer, S. H. M. Söntjens, M. H. P. van Genderen, R. P. Sijbesma, H. W. Spiess. Inverse Detection and Heteronuclear Editing in ^{1}H–^{15}N Correlation and ^{1}H–^{1}H Double-Quantum NMR Spectroscopy in the Solid State under Fast MAS. *J. Magn. Reson.* **150**, 57–70 (2001).

[Schnell 01b] I. Schnell, H. W. Spiess. High-Resolution ^{1}H NMR Spectroscopy in the Solid State: Very-Fast Sample Rotation and Multiple-Quantum Coherences. *J. Magn. Reson./Adv. Magn. Opt. Reson.* **151**, 153–227 (2001).

[Schnell 02a] I. Schnell, B. Langer, R. P. Sijbesma, M. H. P. van Genderen, H. W. Spiess. An Investigation of Hydrogen-Bonded Ureido-Pyrimidone Moieties in the Solid State by ^{1}H Double-Quantum MAS NMR Spectroscopy. *Phys. Chem. Chem. Phys.* **4**, 3750–3758 (2002).

[Schnell 02b] I. Schnell, K. Saalwächter. ^{15}N-^{1}H Bond Length Determination in Natural Abundance by Inverse Detection in Fast-MAS Solid-State NMR Spectroscopy. *J. Am. Chem. Soc.* **124**, 10938–10939 (2002).

[Sebastiani 01] D. Sebastiani, M. Parinello. A New ab-Initio Approach for NMR Chemical Shifts in Periodic Systems. *J. Phys. Chem. A* **105**, 1951–1958 (2001).

[Sebastiani 02] D. Sebastiani, G. R. Goward, I. Schnell, M. Parrinello. NMR chemical shifts in periodic systems from first principles. *Comput. Phys. Commun.* **147**, 707–710 (2002).

[Sebastiani 03] D. Sebastiani. Personal communication (2003).

[Sijbesma 99] R. P. Sijbesma, E. W. Meijer. Self-assembly of well-defined structures by hydrogen bonding. *Curr. Opin. Colloid In.* **4**, 24–32 (1999).

[Slichter 96] C. P. Slichter. Principles of Magnetic Resonance. Springer Verlag, Berlin (1996).

[Sommer 95] W. Sommer, J. Gottwald, D. E. Demco, H. W. Spiess. Dipolar Heteronuclear Multiple-Quantum NMR Spectroscopy in Rotating Solids. *J. Magn. Reson. A* **113**, 131–134 (1995).

[Steed 00] J. W. Steed, J. L. Atwood. Supramolecular Chemistry. Wiley (2000).

[Steiner 95] T. Steiner. Cooperative C-C-H$\cdots$C-C-H interactions: Crystal Structure of DL-Prop-2-ynylglycine and Database Study of Terminal Alkanes. *J. Chem. Soc. Chem. Commun.,* pp. 95–96 (1995).

[Takegoshi 01] K. Takegoshi, J. Mizokami, T. Terao. ^{1}H decoupling with third averaging in solid NMR. *Chem. Phys. Lett.* **341**, 540–544 (2001).

[Terao 86] T. Terao, H. Miura, A. Saika. Dipolar SASS NMR spectroscopy: Separation of heteronuclear dipolar powder patterns in rotating solids. *J. Chem. Phys.* **85**, 3816–3826 (1986).

[Thieme 02] K. Thieme. Personal communication (2002).

[Tobe 98] Y. Tobe, N. Utsumi, K. Kawabata, A. Nagano, K. Naemura. Synthesis and association behavior of [4.4.4.4.4.4]metacyclophanedodecayne derivatives with interior binding groups. *Angew. Chem. Int. Ed.* **37**, 1285–1287 (1998).

[Vinogradov 99] E. Vinogradov, P. K. Madhu, S. Vega. High-resolution proton solid-state NMR spectroscopy by phase-modulated Lee–Goldburg experiment. *Chem. Phys. Lett.* **314**, 443–450 (1999).

[Vinogradov 00]	E. Vinogradov, P. K. Madhu, S. Vega. A bimodal Floquet analysis of phase-modulated Lee–Goldburg high resolution proton magic angle spinning NMR experiments. *Chem. Phys. Lett.* **329**, 207–214 (2000).
[Waugh 68]	J. S. Waugh, L. M. Huber, U. Haeberlen. Approach to High-Resolution NMR in Solids. *Phys. Rev.* **20**, 180 (1968).
[Wind 02]	M. Wind, K. Saalwächter K, U. M. Wiesler, K. Müllen, H. W. Spiess. Solid-state NMR investigations of molecular dynamics in polyphenylene dendrimers: Evidence of dense-shell packing. *Macromolecules* **35**, 10071–10086 (2002).
[Yu 98]	Y. Yu, B. M. Fung. An efficient broadband decoupling sequence for liquid crystals. *J. Magn. Reson.* **130**, 317–320 (1998).